UNIVERSITÀ DEGLI STUDI DI TRIESTE

Dipartimento di Fisica

XXII CICLO DEL
DOTTORATO DI RICERCA IN
NANOTECNOLOGIE

Multiscale Molecular Simulation of Nanostructured Systems

(SSD ING-IND/24 – Principi di Ingegneria Chimica)

DOTTORANDA
Paola Posocco

DIRETTORE DELLA SCUOLA
Chiar.mo Prof. Maurizio Fermeglia (Università di Trieste)

SUPERVISORE
Chiar.mo Prof. Maurizio Fermeglia (Università di Trieste)

TUTORE
Chiar.mo Prof. Sabrina Pricl (Università di Trieste)

ANNO ACCADEMICO 2008/2009

ABSTRACT

Computational materials science based on multiscale approach is very promising in the domain of nanoscience. It gives the modeler a route from the atomistic description of the system to a trust-worthy estimate of the properties of a material, obtained from the underlying molecules in a quantifiable manner.

In this thesis we discuss general guidelines for its implementation in the field of nanomaterials and propose an alternative pathway to link effectively atomistic to mesoscopic scale and this, in turn, to the macroscopic scale. As proofs of concept for the reliability of the proposed approach, we consider several systems of industrial interest, ranging from polymeric nanocomposite materials, to epoxy resins, block copolymers, and gels for biomedical applications.

In this context, we ascertain that multiscale molecular modelling can play a crucial role in the design of new materials whose properties are influenced by the structure at nanoscale. The results suggest that the combination of simulations at multiple scales can unleash the power of modeling and yield important insights.

Le tecniche computazionali fondate su un approccio multiscala costituiscono uno strumento molto promettente nel campo della nanoscienza e dei nanomateriali. Esse forniscono al modellatore un percorso quantitativo che parte dalla descrizione atomistica fino alle proprietà finali del materiale.

In questo lavoro di tesi sono discusse le linee guida per l'implementazione della modellistica multiscala nel settore dei nanomateriali ed è proposta una strategia alternativa alle soluzioni attualmente esistenti per collegare la scala atomistica alla mesoscala e, successivamente, la mesoscala alla scala macroscopica. Per dimostrare la validità del metodo proposto, sono stati presi in esame differenti sistemi di interesse industriale, i quali comprendono materiali nanocompositi polimerici, resine epossidiche, copolimeri a blocchi, e gel per applicazioni biomediche.

In questo contesto, si è evidenziato come la modellistica multiscala possa svolgere un ruolo cruciale nella progettazione di nuovi materiali le cui proprietà sono influenzate dalla struttura a scala nanometrica. I risultati suggeriscono che la combinazione di simulazioni su scale multiple amplifica sinergicamente la potenza della modellazione e può fornire importanti intuizioni.

Table of Contents

List of Figures

List of Tables

Chapter 1

Introduction

In this Chapter we illustrate the motivation and relevance of the present research together with a brief summary of all systems investigated.

1.1 Motivation and relevance

Nanoscience and nanomaterials have been identified worldwide as the key to disclose a new generation of devices with revolutionary properties and functionalities. Considerable experimental and theoretical work has been performed in these fields so far. The increased interest is indicated by the growing number of individuals and groups active in these disciplines and the rising funding on nanotechnology related to R&D. The real burst in the commercialization of nanomaterials has occurred over the last 10 years, and trends indicate that the nanomaterials market will continue to grow significantly in the future.

The recognized priorities in nanotechnology by the scientific and industrial community are the following: a) synthesis and assembly, b) characterization tools, c) manufacturing and processing, and d) modeling and simulation.

Nanomaterials are challenging since they involve components at characteristic scales that are not common and thus conventional theories may fail. Understanding the behavior of materials at this scale is important both from the point of view of basic science and future applications.

In order to develop new materials and compositions with designed novel properties, it is essential that these properties be predicted before preparation, processing, and experimental characterization. Despite the tremendous advance made in the modeling of structural, thermal, mechanical and transport properties of materials at macroscopic level, there remains enormous uncertainty about how to predict many critical properties related to performance.

In recent years, the advent of ever more powerful, massively parallel computers, coupled with advances in the theoretical framework that describes materials, has enabled the development of new concepts and algorithms for the computational modeling of materials. As the field of computational materials science develops and matures, the conscience that

modeling efforts should be an integral part of interdisciplinary materials research and must include experimental validation progressively develops in both scientific and industrial community.

The ultimate, common aim is to develop models for nanomaterials processing and the ability to predict bulk properties of systems that contain nanomaterials. A challenge is to bridge models along different length and time scales in order to be able to pass from atoms to self-assembly and finally to realistic devices. In this multiscale modeling approach, the goal is to predict the performance and behavior of complex materials across all relevant length and time scales, starting from fundamental physical principles and experimental data.

The primary problem is that properties depend on the atomic level interactions and chemistry at the level of nanometers and picoseconds. The material designer needs answer from macroscopic modeling (finite element paradigm) of components having scales of centimetres and milliseconds or larger. To dramatically advance the ability to design useful high performance materials, it is essential that we insert the chemistry into the mesoscopic and macroscopic modeling.

The molecular dynamics level allows one to predict the structures and the properties for system ~10^5 times larger than quantum mechanics, permitting direct simulations for properties of many interesting systems. This leads to relevant and useful results in material design; however, many critical problems in material design require time and length scales too large for practical molecular dynamics. Consequently, it is essential to develop methods treating the mesoscale in between atomic length and time scales of molecular dynamics and the macroscopic length and time scales of continuum analysis. This linking through the mesoscale in which we can describe microstructure is probably the most challenging step toward the developing reliable first principles methods for practical material's design applications.

Only by establishing this connection from microscale to macroscale it is possible to built first principles methods for describing properties of new materials and composite and to play a direct role in material innovation and design.

To accomplish these challenging goals, we proposed here new strategies for a multiscale modeling approach of several systems of industrial interest. Our aim is to stress the possibilities that multiscale modeling offers in the understanding and controlling the nanomaterials properties and tailoring them for specific applications.

1.2 Overview

Materials modelling tools have become increasingly integrated in the R&D. The unique insights available through simulation of materials at a range of scales, from the quantum and molecular, via the mesoscale to the finite element level, can provide discontinuous scientific advances. These tools are well validated and produce reliable, quantitative information. A key demand of academic and industrial research is that these tools become ever more integrated: integrated at each length and time scale with experimental methods and knowledge as well as integrated across the spectrum of scales in order to capture the multiscale nature of organisation in many materials (see Figure 1.1).

This thesis will address our efforts in this direction. The principal focus will be on the derivation of accurate input parameters for mesoscale simulation, and the subsequent use of finite element modeling to provide quantitative information regarding the properties of the simulated mesoscale morphologies.

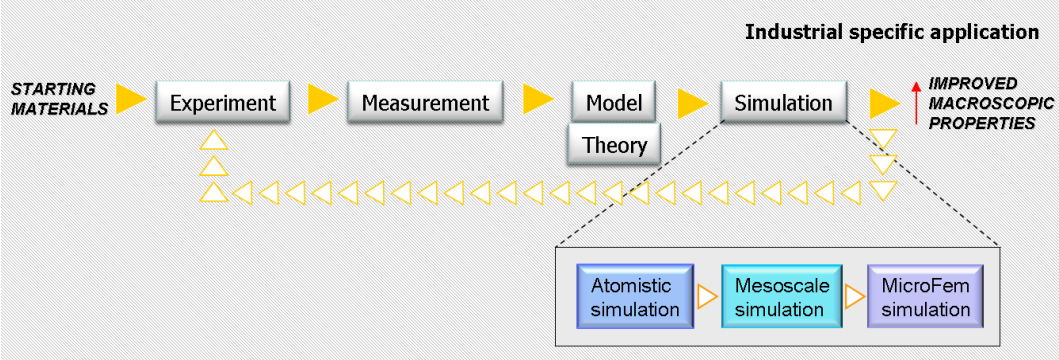

Figure 1.1. Pictorial scheme of the integrated process of developing and applying theoretical models and validation of experimental data.

In mesoscale modeling the familiar atomistic description of the molecules is coarse-grained, leading to beads of fluid (representing the collective degrees of freedom of many atoms). These beads interact through pair-potentials which crucially if meaningful data are to be obtained capture the underlying interactions of the constituent atoms. The use of atomistic modeling to derive such parameters will be discussed. The primary output of mesoscale modeling is phase morphologies with sizes up to the micron level. These morphologies are of interest, but little prediction of the material properties is available with the mesoscale tools. Finite element modeling can be used to predict physical and mechanical properties of arbitrary structures.

The systems analyzed belong to different fields, ranging from polymeric nanocomposite materials, to epoxy resins, block copolymers, and gels for biomedical applications, in order to demonstrate the broad applicability of the proposed methodology:

- In Chapter 3 we focused on water-based montmorillonite/poly(ethylene oxide) layered silicate nanocomposites; these materials are widely used in electronic applications, super capacitor, batteries, fuel cell applications. A multiscale procedure has been developed to calculate macroscopic properties of such materials, depending on concentration of silicate and quality of its dispersion and starting from molecular information of the material. According to the conceived computational recipe, no experimental data are required as input at any scale level. In addition, we analyzed the molecular interactions between the components of the system and assessed the impact of those on the final properties of the material, providing a tool for a better evaluation and a priori selection of each component.
- In Chapter 4 (poly(styrene)-poly(vinyl pyridine)) block copolymers filled with gold nanoparticles were explored. The morphology of the copolymer, when loaded with particles functionalized with one or both polymeric building blocks in different percentages, was predicted. In particular, the effect of concentration, degree and type of covering of the nanoparticle surface on the morphology of the final composite was assessed, highlighting the thermodynamic parameters that can be used to control the dispersion of the metal in the polymeric matrix. These materials find application in nanostructured solar cells, storage media, catalysts, sensors, just to name a few.
- In Chapter 5 a fully multiscale protocol for hybrid O/I materials based on cross-linked epoxy resin and zinc sulphide nanoparticles has been developed. A code

for the simulation of the crosslinked matrix was first developed; then, atomistic simulation of the composite has provided the necessary information to the mesoscale prediction of the morphology of the material and the dispersion of the metal varying the nanoparticle concentration. Finally, the mechanical properties of bulk material have been predicted via finite element calculation. Automotive, opto-electronic devices, displays, general and public lighting are the privileged applications for these hybrid systems.

- In Chapter 6 a systematic investigation of the main structural and physical factors influencing the ultimate morphology and properties of the poly (lactide) (PLA)-poly (ethylene oxide) (PEO) block copolymer nanoscopic aggregates was accomplished. In this work we report the results of a complete study on the self-assembly of PLA/PEO di/triblock copolymers in aqueous environment based on a multiscale molecular modeling recipe. Copolymers of PEO/PLA have generated broad interest in nanomedicine applications, like target therapy, drug delivery, and pharmaceutical applications. To test the ability of the adopted methodology to account for the effect of drug-loading on the nanocarrier aggregated morphology, further simulations were performed both on the di- and tri-block copolymer systems containing a model drug in concentration and composition intervals of pharmaceutical technology's interest.

Chapter 2 provides an overview of the multiscale molecular modelling, our combined strategy and a brief introduction to the computational techniques used in this work. Chapter 7 presents conclusions and future perspectives.

Chapter 2

Multiscale molecular modeling in nanomaterials science

Multiscale molecular modeling is a recent, fast developing and challenging scientific field with contributions from many scientific disciplines in an effort to assure materials simulation across length/time scales. In this Chapter we introduce the concept of multiscale approach of nanomaterials and present a brief description of the employed simulation methods based on time and length scales. Then, a hierarchical strategy of multiscale modeling to couple these techniques will be discussed.

2.1 Introduction to multiscale molecular modeling

In the last decades, modeling and computer simulation have increasingly become fundamental tools in many branches of science and engineering. As far as material science is concerned, modeling and simulation are generally intended for predicting properties of new materials before their synthesis as well as for investigating their inner structure. This approach can be very useful especially for those materials which present nanoscale features, as long as experimental characterization and manipulation at this scale represent an extremely difficult task.

There are many level at which modeling can be useful, ranging from the highly detailed *ab initio* quantum mechanics, through classical molecular modeling to process engineering modeling. These computations significantly reduce wasted experiments, allow products and processes to be optimized, and permit a large number of candidate materials to be screened prior to production.

Quantum mechanical (QM) methods have undergone enormous advances in the past 10 years, enabling simulation of systems containing several hundred atoms. Molecular mechanics is a faster and more approximate method for computing the structure and

behaviour of molecules or materials. It is based on a series of assumptions that greatly simplify chemistry, e.g., atoms and the bonds that connect them behave like balls and springs. The approximations make the study of larger molecular systems feasible, or the study of smaller systems, still not possible with QM methods, very fast. Using molecular mechanics (MM) force fields to describe molecular level interactions, molecular dynamics (MD) and Monte Carlo (MC) methods afford the prediction of thermodynamic and dynamic properties based on the principles of equilibrium and non equilibrium statistical mechanics.[1]

Mesoscale modeling uses a basic unit (an agglomeration of atoms, called bead, obtained through a coarse-graining procedure) just above the molecular scale, and is particularly useful for studying the behaviour of polymers and soft materials. It can model even larger molecular systems, but with the commensurate trade-off in accuracy. Examples of mesoscale theories are dynamic mean field density functional theory (Mesodyn) and *Dissipative Particle Dynamics* (DPD).[2] Furthermore, it is possible to transfer the simulated mesoscopic structure to finite elements modeling tools for calculating macroscopic properties for the systems of interest.[3]

Figure 2.1 shows the class of models that are available at each single scale.

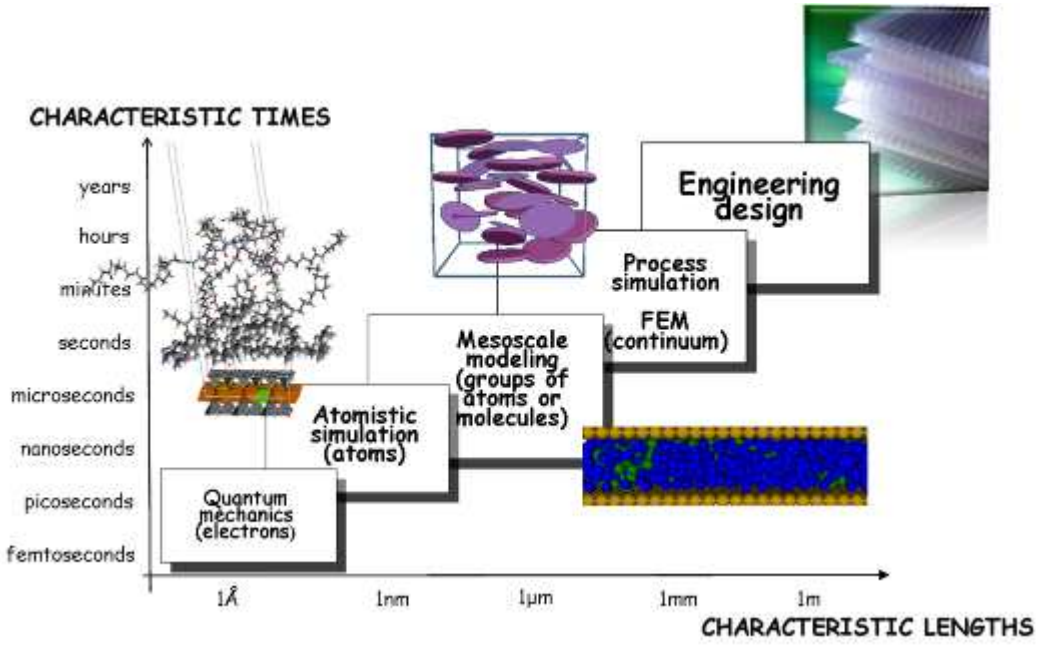

Figure 2.1. Multiscale molecular modeling: characteristic times and lengths.

QM, MM, MD and mesoscale techniques cover many decades of both length and time scale, and can be applied to arbitrary materials: solids, liquids, interfaces, self-assembling fluids, gas phase molecules and liquid crystals, to name but a few. There are a number of

[1] a) Allen, M. P.; Tildesley, D. J. *Molecular simulations of liquids*, Oxford: Oxford University Press, 1987; b) Gubbins, K. E.; Quirke, N. *Molecular simulations and industrial applications*, Amsterdam: Gordon & Breach 1996; c) Haile, J. M. *Molecular dynamics simulations*, New York, Wiley & Sons, 1992.

[2] a) Altevogt, P.; Evers, O. A.; Fraaije, J. G. E. M.; Maurits, N. M.; van Vlimmeren, B. A. C. *Journal of Molecular Structure* (Theochem) **1999**, *463*, 139–143; b) Fraaije, J. G. E. M.; van Vlimmeren, B. A. C.; Maurits, N. M.; Postma, M.; Evers, O. A.; Hoffman, C.; Altevogt, P.; Goldbeck-Wood G. *Journal of Chemical Physics* **1997**, *106*, 4260–4269; c) Groot, R. D.; Warren, P. B. *J Chem Phys* **1997**, *107*, 4423-4435.

[3] Gusev, A. A. *Macromolecules* **2001**, *34*, 3081-3093.

factors, however, which need to be taken care of to ensure that these methods can be applied routinely and successfully.

First and foremost of course are the validity and usability of each method on its own, followed by their interoperability in a common and efficient user environment. Of equal importance is the integration of the simulation methods with experiment. In modern materials research and development, one needs to be able to move almost seamlessly from experimental knowledge to simulation and back again, requiring multiple input-output relationships at a range of materials length and time scales.

Multiscale simulation can be defined as the enabling technology of science and engineering that links phenomena, models, and information between various scales of complex systems. The idea of multiscale modeling is straightforward: one computes information at a smaller (finer) scale and passes it to a model at a larger (coarser) scale by leaving out (i.e., coarse graining) degrees of freedom.[4]

The ultimate goal of multiscale modeling is then to predict the macroscopic behaviour of an engineering process from first principles, i.e., starting from the quantum scale and passing information into molecular scales and eventually to process scales.

Thus, based on accurate QM calculations, a force field (FF) is determined, which includes charges, force constants, polarization, van der Waals interactions and other quantities that accurately reproduce the QM calculations. With the FF, the dynamics is described with Newton's equations (MD), instead of the Schrödinger equation. The MD level allows predicting the structures and properties for systems much larger in terms of number of atoms than for QM, allowing direct simulations for the properties of many interesting systems. This leads to many relevant and useful results in materials design; however, many critical problems in this field still require time and length scales far too large for practical MD. Hence, we need to model the system at the mesoscale (a scale between the atomistic and the macroscopic) and to pass messages from the atomistic scale to the mesoscale and to the macroscale. This linking through the mesoscale in which the microstructure can be described is probably the greatest challenge to develop reliable first principles method for practical materials' design applications. Only by establishing this connection from microscale to mesoscale it is possible to build first principles method for describing the properties of new materials and (nano)composites.

The problem here is that the method of coarsening the description from atomistic to mesoscale or mesoscale to continuum is not as obvious as it is going from electrons to atoms.[5] For example, the strategy for polymers seems quite different than for metals, which seem different from ceramics or semiconductors. In other words, the coarsening from QM to MD relies on basic principles and can be easily generalized in a method and in a procedure, while the coarsening at higher scales is system specific.

One of the first breakthrough examples of multiscale modeling of materials is the linking of quantum and classical molecular methods with continuum methods to study crack propagation in silicon.[6] Here tight-binding MD was carried out near the crack tip, classical MD was employed farther away, and finite element calculations were performed far enough from the crack that a continuum approximation was valid. By developing clever schemes to link the three methods together both spatially and temporally, the entire hybrid simulation

[4] a) Goddard, W. A. III; Cagin, T.; Blanco, M.; Vaidehi, N.; Dasgupta, S.; Floriano, W. et al. *Computational and Theoretical Polymer Science* **2001**, *11*, 329–338; b) Doi, M. *Journal of Computational and Applied Mathematics* **2002**, *149*, 13–25; c) McGrother, S.; Golbeck Wood, G.; Lam, Y. M. *Lecture Notes in Physics* **2002**, *642*, 223–230.

[5] Glotzer, S. C.; Paul, S. C. *Annual Review of Materials and Research* **2002**, *32*, 401–436.

[6] Abraham, F. F.; Broughton, J. Q.; Bernstein, N.; Kaxiras, E. *Computers in Physics* **1998**, *12*, 538–544.

could be carried out with all three techniques operating simultaneously in the appropriate areas.

Multiscale simulation poses, in some sense, greater challenges for polymer materials than for metallic and ceramic systems due to the larger range of length and time scales that characterize macromolecules.

In this respect, for example, Doi[4b)] has developed a suite of state-of-the-art simulation tools that model polymers at the molecular and mesoscale level. Although each tool performs calculations using only one technique, the output from one level can be used directly as input for another, allowing an off-line bridging of length and time scales. To achieve what he and others refer to as "seamless zooming", namely the ability to spawn higher resolution simulations using more detailed methods where needed, will require additional theoretical and computational advances.

Along similar lines, off-line multiscale simulations of nanofilled polymers using coarse-grained molecular dynamics, mesoscopic time dependent Ginsburg–Landau theory, and macroscopic continuum finite element techniques have been carried out. Significant advances in uniquely mapping atomistic models of polymers onto coarse-grained models have been made in recent years, in some cases providing nearly exact quantitative agreement between the two models for certain quantities, but these mappings, too, are performed off-line, and the various methods are not linked within a single simulation.

Scale integration in specific contexts can be done in different ways. Any 'recipe' for passing information from one scale to another (upper) scale is based on the definition of multiscale modeling which consider 'objects' that are relevant at that particular scale, disregard all degrees of freedom of smaller scales and summarize those degrees of freedom by some representative parameters.

All approaches are initially based on the application of a force field that transfers information from quantum chemistry to atomistic simulation.

From atomistic simulation to mesoscale model, essential features of the system have to be maintained while reducing the degree of freedom. So far, the features chosen for the reproduction by coarse-grained models have been mainly structural, thermodynamical or both, with structure prevailing.[7]

As mesoscale simulation typical result is the morphology and the structure of the matter at nanoscale level at the desired conditions of temperature, composition and shear.

For the description of flow of polymeric materials on a processing scale, one must employ a hydrodynamic description and incorporate phenomena occurring on mesoscopic to macroscopic length and time scales. For example, to capture the non-Newtonian properties of polymer flow behaviour one can either use special models for the materials stress tensor, or obtain it from a molecular simulation using the instantaneous flow properties of the hydrodynamic fields as input. In the area of high-performance materials and devices, polymer composites are finding a widespread application, and the modeling of these materials was until recently done primarily through finite element methods (FEM), and are beyond the realm of application of molecular modeling approaches. Nonetheless, a real problem in using FEM is the definition of the physical property of a complex material such as a polymer blend with phase segregation and/or a polymer with microinclusions of nanosized platelets.[8]

[7] Müller-Plathe, F. *ChemPhysChem* **2002**, *3*, 754-769.

[8] a) Gusev, A. A. *Journal of the Mechanics and Physics of Solids* **1997**, 45, 1449–1459; b) Gusev, A. A.; Lusti, H. R. *Advanced Materials* **2001**, *13*, 1641–1643; c) Gusev, A. A. *Physical Review Letters* **2004**, *93*, 34302–34304.

Mesoprop is a method based on finite elements for estimating properties of a complex material starting from the density distribution at mesoscale. The method uses the results of a mesoscale simulation under the form of three-dimensional density maps, and transforms such information into a fixed grid that is used for the integration of the equations to determine macroscopic properties. Palmyra is a different method that allows the simulation at FEM level with a variable grid methodology that allows extending the size of the system studied.

In the next Chapters we will show hierarchical procedures for bridging the gap between atomistic and macroscopic modeling passing through mesoscopic simulation. In particular, we will present and apply to some cases of industrial interest the concept of "message-passing" multiscale modeling. The strategy described is based on an overlapping array of successively coarser modelling techniques. At each plateau (a range of length and time scales), the parameters of the coarse description are based on the representative results of the immediately finer description.

2.2 Simulation methods

Several methods suitable for particular length and time scales are available to treat aspects of materials phenomena that operate only over those scales. In the following we present briefly the main characteristics of the methods we principally employed in this thesis and how they are combined within multiscale modeling strategies.

2.2.1 Atomistic methods

The modeling and simulation methods at molecular level usually employ atoms or small atom clusters (in coarse-grain approaches) as the basic units considered. Beyond Quantum Mechanical methods (which incorporate quantum effects and are applicable only to very small systems due to their computational cost), the most popular methods include molecular mechanics, Molecular Dynamics and Monte Carlo simulations.

Classical molecular dynamics (MD)

MD is a computer simulation technique that allows one to predict the time evolution of a system of interacting particles (e.g., atoms, molecules) and estimate the relevant physical properties.[9] It generates information as atomic positions, velocities and forces from which the macroscopic properties (e.g., pressure, energy, heat capacities) can be derived by means of statistical mechanics. MD simulation usually consists of three main constituents: (i) a set of initial conditions (e.g., initial positions and velocities of all particles in the system); (ii) the interaction potentials to represent the forces among all the particles; (iii) the evolution of the system in time by solving a set of classical Newtonian equations of motion for all particles in the system.

The equation of motion is generally given by

$$F_i(t) = m_i \frac{d^2 r_i}{dt^2} \tag{2.1}$$

[9] a) Allen, M. P.; Tildesley, D. J. *Computer simulation of liquids*, Oxford: Clarendon Press; 1989; b) Frenkel, D.; Smit, B. *Understanding molecular simulation: from algorithms to applications*, 2nd ed. San Diego: Academic Press; 2002.

where $\boldsymbol{F}_i$ is the force acting on the *i*th atom or particle at time *t* which is obtained as the negative gradient of the interaction potential *U*, m_i is the atomic mass and $\boldsymbol{r}_i$ the atomic position. A physical simulation involves the proper selection of interaction potentials, numerical integration, periodic boundary conditions, and the control of pressure and temperature to mimic physically meaningful thermodynamic ensembles.

The interaction potentials together with their parameters, i.e., the so-called *force fields*, describe in detail how the particles in a system interact with each other, i.e., how the potential energy of a system depends on the particle coordinates. Such a force field may be obtained by quantum methods, empirical methods or quantum-empirical method. The criteria for selecting a force field include the accuracy, transferability and computational speed.

A typical interaction potential *U* may consist of a number of bonded and nonbonded interaction terms, which can be calculated for each of the N particles

$$U(r_1, r_2, ...r_N) = U_{bond} + U_{angle} + U_{torsion} + U_{inversion} + U_{vdw} + U_{electrostatic} \quad (2.2)$$

The first four terms represent bonded interactions, i.e., bond stretching U_{bond}, bond-angle bend U_{angle}, dihedral angle torsion $U_{torsion}$ and inversion interaction $U_{inversion}$, while the last two terms are non bonded interactions, i.e., van der Waals energy U_{vdw} and electrostatic energy $U_{electrostatic}$.

Usually, equations of motion are integrated applying one of the many algorithms using finite difference methods. MD simulations can be performed in many different ensembles, such as grand canonical (μVT), microcanonical (*NVE*), canonical (*NVT*) and isothermal–isobaric (*NPT*). The constant temperature and pressure can be controlled by adding an appropriate thermostat and barostat.

2.2.2 Mesoscopic methods

Mesoscale methods aim at linking microscale methods, i.e. atom based simulations, with macroscale methods based on continuum models. Various simulation methods have been proposed to study the mesoscale structures, the most common being Brownian Dynamics (BD), *Dissipative Particle Dynamics* (DPD), Lattice Boltzmann (LB), time–dependent Ginsburg–Landau (TDGL) theory, and Dynamic Density Functional Theory (DDFT).

In these methods, a molecule is usually treated with a field description or microscopic particles that incorporate molecular details implicitly. Therefore, they are able to simulate the phenomena on length and time scales currently inaccessible by the classical MD methods.

Dissipative Particle Dynamics (DPD)

In 1992, Hoogerbrugge and Koelman introduced a mesoscale technique to simulate hydrodynamic behavior, called *Dissipative Particle Dynamics* (DPD).[10] DPD is a computational tool for simulating soft matter, on mesoscopic length and time scales. Similar to molecular dynamics (MD) or Brownian dynamics (BD), DPD is a particle-based method. However, in a DPD simulation, the elementary unit is not an atom, but groups of atoms or molecules,

[10] a) Hoogerbrugge, P. J.; Koelman, J. M. V. A. *Europhys. Lett.* **1992**, *19*, 155-160; b) Koelman, J. M. V. A.; Hoogerbrugge, P. J. *Europhys. Lett.* **1993**, *21*, 363-368.

referred to as beads. The DPD interaction is mesoscopic since the internal degrees of freedom of the fluid elements are ignored and only their center of mass motion is resolved.

If the mass of all particles is set equal to unity, the time evolution of the positions ($\boldsymbol{r}_i$(t)) and momenta ($\boldsymbol{p}_i$(t)) is governed by Newton's equations

$$\frac{d\mathbf{r}_i}{dt} = \mathbf{v}_i(t) \quad \frac{d\mathbf{v}_i}{dt} = \mathbf{f}_i(t) \tag{2.3}$$

where the mass of each particle *i* is set to unity, and $\boldsymbol{r}_i$, $\boldsymbol{v}_i$, and $\boldsymbol{f}_i$ are the position vector, velocity, and total force, acting on particle *i* , respectively.

The total force exerted on a bead *i* contains three parts, each of which is pair-wise additive: a conservative ($\boldsymbol{F}_{ij}^{C}$), a dissipative ($\boldsymbol{F}_{ij}^{D}$), and a random ($\boldsymbol{F}_{ij}^{R}$) force. Accordingly, the effective force $\boldsymbol{f}_i$ acting on a particle *i* is given by

$$\mathbf{f}_i = \sum_{i \neq j} \left(\mathbf{F}_{ij}^{C} + \mathbf{F}_{ij}^{D} + \mathbf{F}_{ij}^{R} \right) \tag{2.4}$$

where the sum extends over all particles within a given distance r_c from the *i*th particle. This distance practically constitutes the only length scale in the entire system. The conservative force is a soft repulsion, given by

$$\mathbf{F}_{ij}^{C} = \begin{cases} a_{ij}\left(1 - r_{ij}\right)\hat{\mathbf{r}}_{ij} & \left(r_{ij} < 1\right) \\ 0 & \left(r_{ij} \geq 1\right) \end{cases} \tag{2.5}$$

where a_{ij} is the maximum repulsion between particles *i* and *j*, $\boldsymbol{r}_{ij}$ is the magnitude of the particle-particle vector $\boldsymbol{r}_{ij} = \boldsymbol{r}_i - \boldsymbol{r}_j$, and $\hat{\boldsymbol{r}}_{ij}$ is the unit vector joining particles *i* and *j*. The other two forces, $\boldsymbol{F}_{ij}^{D}$ and $\boldsymbol{F}_{ij}^{R}$, are both responsible for the conservation of the total momentum in the system, and incorporate the Brownian motion into the larger length scale. They are given by the following expressions

$$\begin{aligned} \mathbf{F}_{ij}^{D} &= -\gamma\, \omega^{D}(r_{ij})\left(\hat{\mathbf{r}}_{ij} \cdot \mathbf{v}_{ij}\right)\hat{\mathbf{r}}_{ij} \\ \mathbf{F}_{ij}^{R} &= \sigma\, \omega^{R}(r_{ij})\theta_{ij}\, \hat{\mathbf{r}}_{ij} \end{aligned} \tag{2.6}$$

where $\boldsymbol{v}_{ij} = \boldsymbol{v}_i - \boldsymbol{v}_j$, ω^D and ω^R are r-dependent weight functions tending to zero for r = $\boldsymbol{r}_c$, and ϑ_{ij} is a randomly fluctuating variable with zero mean and unit variance. Español and Warren have shown that one of the two weight functions in Equation 2.6 can be chosen arbitrarily, thereby fixing the other weight function.[11] However, the weight function and constants should obey

$$\left[\omega^{R}(r)\right]^2 = \omega^{D}(r) \quad , \quad \sigma^2 = 2\gamma k_B T \tag{2.7}$$

where k_B is the Boltzmann constant.

[11] Espanol, P.; Warren, P. B. *Phys. Rev. E* **1995**, *52*, 1734-1742.

Further incorporation of chain molecules simply requires the addition of a harmonic spring force between the beads allowing them to interconnect to highly complex topologies

$$\mathbf{F}_{ij}^{spring} = K(\mathbf{r}_{ij} - r_{eq}) \tag{2.8}$$

where K is the spring constant and $\boldsymbol{r}_{eq}$ is the equilibrium spring length.

Many different formulations of the DPD method have been proposed, i.e. with inclusion of angle potentials and electrostatics.[2c), 12]

2.2.3 Macroscopic methods

Within the framework of material multiscale modeling, we refer to macroscale methods as those modeling and simulation techniques which allow the calculation of some specific macroscopic property (i.e. Young's modulus, electrical conductivity, gas permeability, …) of a material by considering a continuous distribution of its components throughout its volume, ignoring discrete atomic and molecular structures and their influence on system behaviour. The final aim basically consists in representing a heterogeneous material as an equivalent homogeneous one. According to some authors,[13] such a description could be as well suited for the definition of micromechanics whose objective basically consists in bridging and determining relationship between microstructures and macroscopic (mechanical) properties. On the other hand, other authors consider micromechanics as just one of the possible methods for obtaining macroscopic properties starting from a representative model of the material.[14]

In any case, the fundamental concept of these methods consists in the choice of a model which is representative of the whole material. Thus, the model has to be a *Representative Volume Element* (RVE) for the system, i.e. a sample which is entirely typical of the whole mixture on average. Defining RVE and its minimum dimensions is obviously a non trivial task and amenable of different interpretations. Besides setting the RVE, macroscale methods usually involve the definition of appropriate constituent laws and implementation of relationships between structural features and macroscopic properties.

Continuum equations, typically in the form of deterministic or stochastic partial differential equations, are at the pinnacle of the coarse-graining hierarchy. Differential equations are formulated from basic physical principles, such as the conservation of energy or momentum, etc. Such methods permit to examine macroscopic regions in space over extended periods of time. Possible macroscale modeling strategies can be grouped into methods: analytical models, which directly calculate overall properties from system parameters, like the well known Halpin-Tsai or Mori-Tanaka models of composite materials, and computational methods, the best known of which is the Finite Element (FE) method.

Finite Element Methods (FEM)

In this approach the region of interest is covered with a mesh determined by contiguous components called 'elements' and the solution of the differential equation is discretized on the mesh points, called nodes, and interpolated within the elements. A partial (ordinary)

[12] a) Espanol, P.; Warren, P. B. *Europhys. Lett*. **1995**, *30*, 191-196; b) Espanol, P. *Europhys. Lett.* **1997**, *40*, 631-636; c) Bonet Avalos, J.; Mackie A.D. *Europhys. Lett.* **1997**, *40*, 141-146; d) Groot, R.D. *J. Chem. Phys.* **2003**, *118*, 11265-11278; e) Travis, K.P.; Bankhead, M.; Good, K.; Owens S. L. *J. Chem. Phys.* **2007**, *127*, 014109, *12 pages*.

[13] a) Zohdi, T. I.; Wriggers, P. *Introduction to Computational Micromechanics*, Springer Verlag, 2005; b) Bohm, H. J. *Mechanics of Microstructured Materials*, Springer Verlag, 2004.

[14] Zeng, Q. H.; Yua, A. B.; Lu G. Q. *Prog Polym Sci* **2008**, 33,191-269.

differential equation is thereby replaced by a set of coupled ordinary (algebraic) equations and solved numerically at the nodal points. The energy in FE method is taken from the theory of linear elasticity and thus the input parameters are simply the elastic moduli and the density of the material.

In the following we will referred only to the specific form of the method based on the work of Gusev and its implementation in the software Mesoprop and Palmyra by Matsim GmbH.[3,15]

This FEM approach consists in a constant-strain-tetrahedra displacement-based technique with an iterative solver. An adaptative (Palmyra)/fixed (Mesoprop) mesh is built using specific criteria to model particle – matrix interface effectively in the RVE. For calculation of thermo-mechanical properties, six different infinitesimally small deformations are applied to the composite mesh and the total strain energy for each of these deformations is minimized using the conjugate gradient method in order to calculate the elastic composite properties. To calculate thermal expansion of the composite a seventh "deformation" (an increase of temperature by 1 Kelvin) is applied in order to obtain the linear thermal expansion coefficients. For other physical properties such as conductivities, dielectric constants, and transport properties a Laplace solver is used, that applies a field in the three main directions to the finite element mesh and minimizes the energy of the composite.

Palmyra and Mesoprop software have been developed to be able to perform FEM analysis also on the density fields generated using the mesoscale techniques. Importing the morphology of the composite as obtained from mesoscale simulation in form of 3-D density distribution of each constituent, FE calculation is performed, so realizing a complete multiscale approach to the prediction of macroscopic properties of nanomaterials.

2.3 Linking atomistic to mesoscale and macroscopic models

As already mentioned, the linking of the atomistic to the macroscopic scale through the mesoscale is probably the greatest challenge to develop reliable first principles method for practical materials' design applications. Only by establishing this connection from microscale to mesoscale it is possible to build first principles method for describing the properties of new materials and (nano)composites.

The main problem here is that the method of coarsening the description from atomistic to mesoscale or mesoscale to continuum is not as obvious as it is going from electrons to atoms.[5] For example, the strategy for polymers seems quite different than for metals, which seem different from ceramics or semiconductors. In other words, the coarsening from QM to MD relies on basic principles and can be easily generalized in a method and in a procedure, while the coarsening at higher scales is system specific.

Given this concept, one of unresolved issue so far is how effectively linking the molecular interaction energies with mesoscale interaction energies. This is particularly critical if one desire to use a *Dissipative Particle Dynamics* approach.

In DPD chemical interactions are described via a conservative force $\boldsymbol{F}_c$. This conservative force between two particles *i* and *j*, as mentioned previously in this Chapter, is a soft repulsion acting along the line of the particle centers, and is given in absolute value and within the cut-off radium r_c by the Equation 2.5.

The interaction parameter a_{ij} has been linked to the χ-parameter in a Flory-Huggins type model by Groot and Warren[2c)], or with the bead size by Maiti and McGrother.[16]

[15] Gusev, A. A. *J Mech Phys Solids* **1997**, *45*, 1449-1459.

In this work, we propose an alternative route, in which the interaction repulsive DPD parameters are coupled to the energies values resulting from the atomistic molecular dynamics simulations. An internal consistency is established by comparing the density fields obtained from DPD and MD on the same system. Accordingly, the derivation of the conservative repulsion form a lower scale (i.e. atomistic) modeling constitutes a bottom-up, multiscale approach to the simulation of complex systems. Further, the proposed strategy is not system dependent and can be applied in principle to polymer, polymer solution, systems featuring solid inclusions, and so on.

The multiscale molecular modeling strategy developed relied on several, consecutive steps (see Figure 2.2):

- generate and optimize the three-dimensional model for each system component.
- Map the atomistic model to the mesoscale model reproducing thermodynamic or structural properties, like stiffness (i.e. through Kuhn segment), geometrical quantities, which can be intramolecular (distance between two adjacent super-atoms, angles between three subsequent super-atoms, dihedral angles between four subsequent super-atoms, principal values of radius of gyration tensor, and so forth) or intermolecular (distances between super-atoms belonging to different chains, distances between the centers of mass of different chains or chains fragment, and so on).[7,17] Which one actually being used depends on the intended purpose of the coarse-grained model. Here, choices have to be made, as eliminating the degree of freedom necessarily leads to models which reproduce fewer characteristics of the molecules. Then, mesoscale topology and mesoscale chemical specie for each component are known.
- Calculate molecular dynamics energies and the nonbonded interaction energies among each mesoscale species. The choice of using only the nonbonded interactions stems from the fact that they represent the most appropriate choice to describe the DPD conservative force $\boldsymbol{F}_c$ as derived by Groot and Warren.[2c)] Considering a system made up of single particles *i* and *j*, the total energy of the system is given, in the hypothesis of neglecting the ternary contribution to interaction, by

$$E_{system}^{tot} = n_{ii}E_{ii} + n_{jj}E_{jj} + n_{ij}Ei_{j} + n_{ji}E_{ji} \tag{2.9}$$

where

$$n_{ii} = \frac{n_{ii}\left(n_{ii} - 1\right)}{2} \tag{2.10}$$

is the number of contacts between the n_i particles of type *i*, and

$$n_{ij} = \frac{n_i n_j}{2} \tag{2.11}$$

[16] Maiti, A.; McGrother, S. *J. Chem Phys.* **2004**, *120*, 1594-1601.

[17] Scocchi, G.; Posocco, P.; Handgraaf, J.–W.; Fraaije, J. G. E. M.; Fermeglia, M.; Pricl S. *Chem. Eur. J.* **2009**, *15*, 7586-7592.

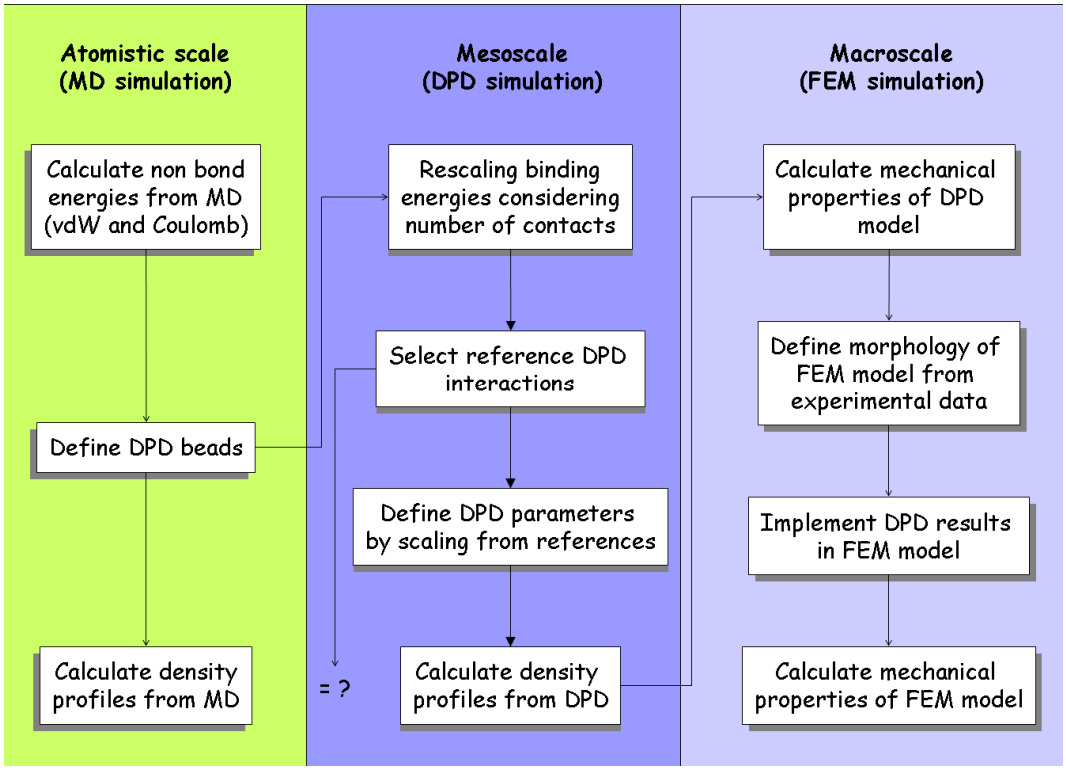

Figure 2.2. Pictorial scheme describing the proposed strategy to link atomistic simulation to mesoscale simulation and mesoscale simulation to macroscale analysis.

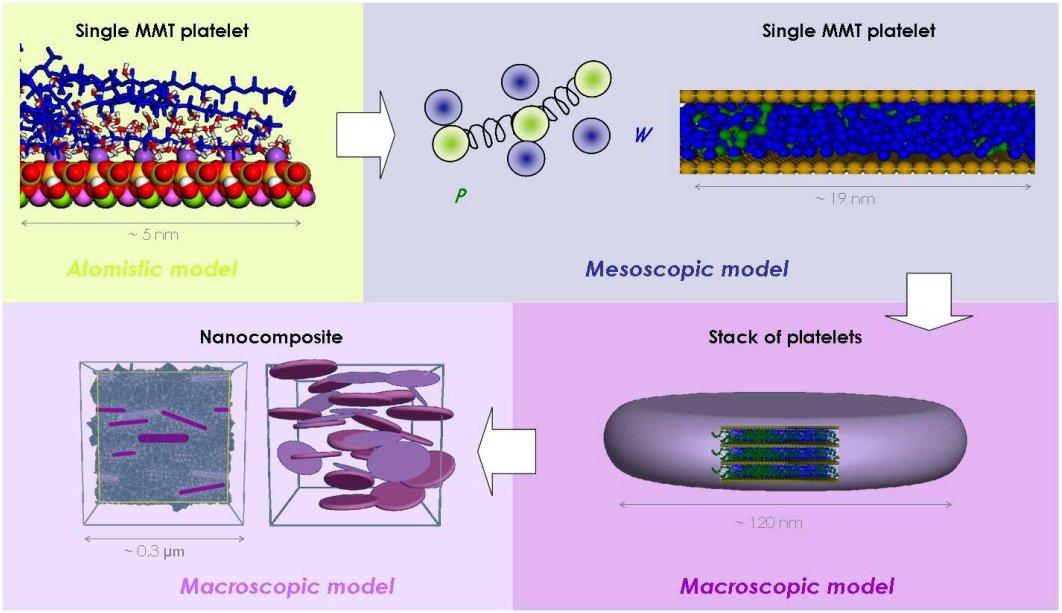

Figure 2.3. Proposed scheme to integrate atomistic to mesoscale simulation and mesoscale to macroscopic simulation. A layered nanocomposite system has been taken here as a proof of concept.

is the number of contacts between n_i particles of type *i* and n_j particles of type *j*. Since the mixed energy terms (E_{ij} and E_{ji}) and the number of contacts (n_{ij} and n_{ji}) are the same, the expression for the total system energy becomes

$$E_{system}^{tot} = n_{ii}E_{ii} + n_{jj}E_{jj} + 2ni_jEi_j \quad (2.12)$$

- The values of the self-interaction energies (E_{ii} and E_{jj}) are easily obtainable dividing the corresponding molecular value by the appropriate number of contacts, while the value of the system total energy is derived straightforwardly from MD. Accordingly, the remaining mixed energy term, E_{ij}, is calculated by applying Equation 2.12.
- Select two reference DPD interactions. Having fixed these two parameters, their values are associated with the corresponding values of the DPD energies rescaled from MD simulations. All the remaining DPD interaction parameters are derived using this reference relationship. An internal consistency is established by comparing the density fields obtained from DPD and MD on the same system using the obtained interaction parameters.
- Export density fields of each mesoscale specie to FE calculation, choosing fixed and/or variable grid according to the complexity and the morphology of the system. Finally, calculate mechanical properties of interest. I.e., in the case of water/PEO nanocomposite (Chapter 3), first, the properties of a single MMT platelet were calculated importing the 3-D density profiles as derived from mesoscale simulations and employing a fixed mesh grid. Then, the calculated properties were used to predict the properties of the overall composite applying a variable adaptative grid mesh (see Figure 2.3).

Chapter 3

Water-based montmorillonite/poly(ethylene oxide) nanocomposites

In this Chapter we present a multiscale computational approach to probe the behavior of polymer/clay nanocomposites based on poly (ethylene oxide) (PEO)/montmorillonite (MMT) as obtained from water intercalation. In details, our modeling recipe is based on four sequential steps: a) atomistic molecular dynamics simulations to derive interaction energy values among all system components; b) mapping of these values onto mesoscale *Dissipative Particle Dynamics* parameters; c) mesoscopic simulations to determine system density distributions and morphologies (i.e., intercalated vs. exfoliated); and d) simulations at finite-element levels to calculate the relative macroscopic properties. The entire computational procedure has been applied to four PEO/MMT systems with PEO chains of different molecular weight (750, 1100, 2000, and 5000 Da), and thermal and electrical characteristics were predicted in excellent agreement with the available experimental data. Importantly, the methodology constitutes a truly integrated multiscale modeling approach, in which no "learning against experiment" has been performed in any step of the computational recipe.

This work is published in Toth, R.; Voorn, D.-J.; Handgraaf, J.-W.; Fraaije, J. G. E. M.; Fermeglia, M.; Pricl, S.; Posocco, P. *Macromolecules* **2009**, *42*, 8260-8270.

3.1 Introduction

In recent years, polymer nanocomposites based on layered silicates, or polymer-clay nanocomposites (PCNs), have attracted great industrial and academic interest as they often exhibit remarkable improvement in materials properties with respect to virgin polymers or conventional micro/macro composites. These enhanced features include high mechanical moduli, increased strength and heat resistance, decreased gas permeability and

flammability, and increased biodegradability in case of biodegradable polymers.[1] Fabricating polymer clay nanocomposites (PCNs) in an efficient and cost-effective manner, however, poses significant synthetic challenges. As the ultimate properties of these hybrid systems commonly depend on their structure, it is of particular interest to establish the morphology of the final composite. To this purpose, the development of theories and the application of computer simulation techniques have opened avenues for the design of these materials, and the *a priori* prediction/optimization of their structures and properties.[2]

The commonly used clay materials for the preparation of PCNs belong to the same general family of 2:1 layered silicates, or phyllosilicates, montmorillonite (MMT) being a prime example of these minerals. Their crystal structure consists of layers made up of two tetrahedrally coordinated silicon atoms fused to an edge-shared octahedral sheet of either aluminum or magnesium hydroxide. The layer thickness is around 1 nm, and the lateral dimension may vary from 30 nm up to several microns or larger, depending on the particular mineral. Stacking of the layers leads to a regular van der Waals gap between the layers called the interlayer space or gallery. Isomorphic substitution within the layers (for example, Al^{3+} replaced by Mg^{2+} or Fe^{2+}, or Mg^{2+} replaced by Li^{+}) results in an excess of negative charge, which is counterbalanced by alkali and alkaline earth cations located inside the galleries. This type of layered silicate is characterized by a moderate surface charge known as the cation exchange capacity (CEC), generally expressed as mequiv/100 g.

Generally speaking, mixing a polymer and a clay may not result in a nanocomposite material.[1] Indeed, in their pristine state layered silicates are only directly miscible with hydrophilic polymers, such as poly(ethylene oxide) (PEO),[3] or poly(vinyl alcohol) (PVA).[4] To render layered silicates compatible with other polymer matrices, one must convert the normally hydrophilic silicate surface to an organophilic one, making the intercalation of many engineering polymers possible. Depending on the strength of interfacial interactions between the polymer matrix and the clay (modified or not), two main types of PCNs can be thermodynamically achieved: i) intercalated nanocomposites, in which the insertion of a polymer matrix into the clay galleries occurs in a crystallographically regular fashion, regardless of the clay to polymer ratio; and ii) exfoliated nanocomposites, where the individual clay layers are separated in a continuous polymer matrix by an average distances that depends on clay loading. The two architectures described above can be practically produced by i) *in situ* polymerization of a given monomer in the presence of the layered silicate, ii) solution intercalation, where both the polymer matrix and clay are dispersed in a common solvent followed by precipitation, or iii) melt processing, which involves the mechanical mixing of the polymeric matrix and the inorganic filler.[1b)]

MMT/PEO-based PNCs are hybrid structures with improved electrical properties for electronic applications in solid-state electrolyte batteries.[5,6,7] The intercalation of water-soluble PEO molecules between the clay galleries can be obtained by mixing the clay with an

[1] a) Pinnavaia, T. J.; Beall, G. W. *Polymer-clay nanocomposites*, John Wiley & Sons Ltd., Chichester, England, 2001; b) Biswas, M.; Sinha Ray, S. *Adv. Polym. Sci.* **2001**, *155*, 167–221; c) Sinha Ray, S.; Okamoto, M. *Prog. Polym. Sci.* **2003**, *28*, 1539–1641; d) Utraki, L. A. *Clay-containing polymeric nanocomposites*, Rapra Technology: Shrewsbury, England, 2004; e) Zeng, Q. H.; Yu, A. B.; Lu, G. Q.; Paul, D. R. *J. Nanosci. Nanotechnol.* **2005**, *5*, 1574-1592; f) Balazs, A. C.; Emrick T.; Russell, T. P. *Science* **2006**, *314*, 1107-1110; g) Pavlidou, S.; Papaspyrides, C. D. *Prog. Polym Sci.* **2008**, *33*, 1119-1198; h) Paul, D. R.; Robeson, L. M. *Polymer* **2008**, *49*, 3187-3204.

[2] Zeng, Q. H.; Yu, A. B.; Lu, G. Q. *Progr. Polym. Sci.* **2008**, *33*, 191–269.

[3] Aranda, P.; Ruiz-Hitzky, E. *Chem. Mater.* **1992**, *4*, 1395–1403.

[4] Greenland, D.J. *J. Colloid Sci.* **1963**, *18*, 647–664.

[5] Kim, S.; Hwang, E.-J.; Jung, Y.; Han, M.; Park, S.-J. *Colloids and Surfaces A: Physicochem. Eng. Aspects* **2008**, *313-314*, 216–219.

[6] Wu, J.; Lerner, M. M. *Chem. Mater.* **1993**, *5*, 835–838.

[7] Aranda, P.; Ruiz-Hitzky, E. *Chem. Mater.* **1992**, *4*, 1395–1403.

aqueous dispersion of PEO (i), or by direct intercalation from the melt (ii).[8] In the latter case, the organic component is inserted between the clay layers such that the interlayer spacing is expanded to an extent at least sufficient to replace the water of hydration associated with the exchangeable cations in the galleries.[9] An alternative method for the preparation of PEO nanocomposites is the dispersion of completely exfoliated clay particles within the polymer matrix. Under these conditions, the observed behavior is rather different with respect to the one described above: indeed, the addition of an adsorbing polymer to the clay colloidal dispersion can cause flocculation at low surface coverage, and steric stabilization when the particle surface is saturated with the polymer.[10] As stated above, PCNs offer a wide range of promising applications because of their enhanced properties with respect to the polymeric matrix *per se*. However, further development of such nanomaterials depends on the fundamental understanding of their hierarchical structures and behaviours, a goal which requires multiscale modeling and simulation strategies to provide seamless coupling among various length and time scales. Several computational approaches, spanning different length/time scale domains have been proposed in recent years for the characterization of polymer-clay nanocomposites, including atomistic molecular dynamics (MD) and Monte Carlo (MC), mesoscale, and finite element simulations.[2]

As concerns PEO-based PCNs, it has been more than 20 years since PEO was first suggested as a suitable polymeric matrix for these systems.[11] Accordingly, a plethora of MD-based simulations have been successfully applied to study, for example, the mobility of ions in PEO matrices,[12] segmental motion of polymer backbone in PEO melts,[13] influence of the polarizability in PEO solid electrolytes,[14] and the effect of temperature,[12b),15,16] concentration,[15] solvent,[16] and salt[12b),17] on the dynamics of PEO segments. Further, the effect on polymer dynamics exerted by the addition of methoxy-terminated PEO side-chains with different lengths and separations to an amorphous long-chain PEO backbone has also been studied using MD techniques.[18] As concerns the resulting PCN systems, Aabloo et al. have studied the molecular behavior at the interface between PEO and an inorganic double-layered gel by a molecular mechanics/molecular dynamics (MM/MD) approach.[19] Similarly, PEO inorganic nanocomposites were subject to MM/MD experiments aimed at characterizing the effect of the nanoparticle filler, its concentration and temperature on the motion of ions in the polymer host.[15,20] In spite of these efforts devoted to the simulation of PEO-based systems, there is still a lack of studies dealing with computational modeling and simulations of PEO nanocomposites, with special mention to those systems obtained from solution.

Here we present a hierarchical procedure for bridging the gap between atomistic and finite element calculations via mesoscale simulations (MS) in polymer-clay nanocomposite

[8] Vaia, R. A.; Vasudevan, S.; Krawiec, W.; Scanlon, L. G.; Giannelis, E. P. *Adv. Mater.* **1995**, *7*, 154–156.
[9] Chaiko, D. J. *Chem. Mater.* **2003**, *15*, 1105–1110.
[10] Pozzo, D. C.; Walker, L. M. *Colloids Surf. A.* **2004**, *240*, 187–197.
[11] Armand, M. B.; Chabagno, J. M.; Duclot, M. J. In Fast ionic transport in solids, Vashishta M., editor. Elsevier: Amsterdam, The Netherlands, 1979.
[12] a) Aabloo, A.; Thomas, J. *Solid State Ion.* **2001**, *143*, 83–87; b) Catlow, C. R. A.; Mills, G. E. *Electrochim. Acta* **1995**, *40*, 2057–2062; c) Ferreira B. A.; Müller-Plathe F.; Bernardes A. T.; De Almeida, W. B. *Solid State Ion.* **2002**, *147*, 361–366.
[13] de Leeuw, S. W.; van Zon, A.; Bel, G. J. *Electrochim. Acta* **2001**, *46*, 1419–1426.
[14] de Jonge, J. J.; van Zon, A.; de Leeuw, S.W. *Solid State Ion.* **2002**, *147*, 349–359.
[15] Kasemägi, H.; Klintenberg, M.; Aabloo, A.; Thomas, J. O. *Electrochim. Acta* **2003**, *48*, 2273–2278.
[16] Ferreira, B. A.; Dos Santos, H. F.; Bernardes, A. T.; Silva, G. G.; De Almeida, W. B. *Chem. Phys. Lett.* **1999**, *307*, 95–101.
[17] van Zon, A.; Mos, B.; Verkerk, P.; de Leeuw, S.W. *Electrochim. Acta* **2001**, *46*, 1717–1721.
[18] Karo, J.; Aabloo, A.; Thomas, J. O. *Solid State Ion.* **2005**, *176*, 3041–3044.
[19] Aabloo, A.; Klintenberg, M.; Thomas, J. O. *Electrochim. Acta* **2000**, *45*, 1425–1429.
[20] a) Kasemägi, H.; Aabloo, A.; Klintenberg, M. K.; Thomas J. O. *Solid State Ion.* **2004**, *168*, 249–254; b) Kasemägi, H.; Klintenberg, M. K.; Aabloo, A.; Thomas J. O. *Solid State Ion.* **2002**, *147*, 367–375.

design. According to the proposed computational recipe, the Dissipative Particle Dynamics (DPD)[21] was adopted as the mesoscale simulation technique, and the interaction parameters of the mesoscopic model were estimated by mapping interaction energy values obtained from atomistic MD simulations. Finally, the morphologies and density distributions of the PCN system components were used as input for finite element calculations to estimate the most relevant macroscopical properties.

This work is organized as follows. First, we aimed at studying the interactions which occur at a molecular level near the surface of MMT platelets in PEO aqueous systems. In particular, we focused our attention on the effects of polymer molecular weight, and presence of water molecules on the interactions between individual PCN components. Secondly, we expanded the information obtained from the atomistic simulations by employing mesoscale models for density profiles and morphology predictions. To this purpose, the resulting MD data were mapped onto the corresponding mesoscale models, and the results generated at both length scales were compared for consistency. Lastly, the density profiles and the morphologies resulting from the MS simulations were imported into a finite element code and some characteristic macroscopic properties of these systems - e.g. thermal expansion coefficients and electrical conductivity as functions of PEO molecular weight and clay loading - were predicted and compared with the corresponding experimental values available in the current literature.

To the best of our knowledge, this is the first attempt to study the behavior of water molecules in nanocomposites at mesoscale level, and to estimate macroscopic properties for water-based PEO PCNs via multiscale molecular modeling procedures.

3.2 Computational methodology

3.2.1 Atomistic models and simulations

All atomistic simulations were performed using *Materials Studio* (v.4.4, Accelrys, San Diego, USA). The starting structure of sodium montmorillonite (MMT) was taken from a previous work of our group.[22] As mentioned above, one of the major goals of this work was to estimate the interaction energies between all system elements accurately. Since these quantities are highly sensitive to the nonbonded components of the force field (FF) employed (e.g., atomic charges and van der Waals parameters), here we adopted the *ad hoc* force field developed by Heinz and coworkers.[23] As demonstrated by the authors for sodium MMT and other phyllosilicatesqq, this accurately derived FF is able to describe, among many other properties, the thermodynamics of surface processes more reliably by reducing deviations of 50-500% in surface and interface energies to less that 10%, which constitutes a fundamental step towards quantitative modeling of interface processes involving layered silicates. Accordingly, the resulting lattice of our MMT model is monoclinic, with space group

[21] a) Hoogerbruge, P. J.; Koelman, J. M. V. A. *Europhys. Lett.* **1992**, *18*, 155–160; b) Koelman, J. M. V.A.; Hoogerbruge, P. J. *Europhys. Lett.* **1993**, *21*, 363.

[22] a) Fermeglia, M.; Ferrone, M.; Pricl, S. *Fluid Phase Eq.* **2003**, *212*, 315-329; b) Toth, R.; Coslanich, A.; Ferrone, M.; Fermeglia, M.; Pricl, S.; Miertus, S.; Chiellini, E. *Polymer* **2004**, *45*, 8075–8083; c) Fermeglia, M.; Ferrone, M.; Pricl, S. *Mol. Simul.* **2004**, *30*, 289-300; d) Scocchi, G.; Posocco, P.; Danani, A.; Pricl, S.; Fermeglia, M. *Fluid Phase Eq.* **2007**, *261*, 366-374; e) Scocchi, G.; Posocco, P.; Handgraaf, J.-W.; Fraaije, J. G. E. M.;Fermeglia, M.; Pricl, S. *Chem. Eur. J.* **2009**, *15*, 7586-7592.

[23] a) Heinz, H.; Suter, U. W. *J. Phys. Chem. B* **2004**, *108*, 18341-18352; b) Heinz, H.; Koerner, H.; Anderson, K. L.; Vaia, R. A.; Farmer, B. L. *Chem. Mater.* **2005**, *17*, 5658-5669.

C2/m, and characterized by the following lattice parameters: a = 5.20 Å, b = 9.20 Å, c = 10.13 Å, and α = 90°, β = 99°, γ = 90°, in excellent agreement with the available literature.[23b),24]

The generation of PEO chains was conducted following a well-validate procedure,[22] according to which the constitutive repeating unit (CRU) of the polymer was first built and its geometry optimized by energy minimization. Hence, the CRU was polymerized to a given degree of polymerization (DP). Four different values of DP were considered in order to study the influence of PEO molecular weight (M_W) on the interaction energies of the corresponding PCN systems: DP = 19, 28, 56, and 113, approximately corresponding to a M_W of 750 Da, 1100, 2000, and 5000, respectively. The Rotational Isomeric State (RIS) algorithm,[25] as modified by Theodorou and Suter,[26] was used to create the initial polymer conformations at T = 300 K. Explicit hydrogens were used in all model systems. In order to obtain a reasonable sampling of the polymer conformational space, we built and energy minimized 10 different PEO configurations for each DP considered. A conformational search was then carried out using a well-validated combined molecular mechanics/molecular dynamics simulated annealing (MDSA) protocol,[22,27] in which the relaxed molecular structure is subjected to five repeated temperature cycles using constant volume/constant temperature (*NVT*) MD conditions. At the end of each annealing cycle, the structure is again energy minimized, and only the structure corresponding to the minimum energy is used for further modeling.

Resorting to atomistic MD simulations in the canonical ensemble allows retrieving important information on the interaction and binding energy values between the different components of a PCN system.[20,22,27f),28,29,30,31] The technique basically consists in simulating the interface between the exfoliated clay, polymer and water by building a cell that is "stretched" along the c-direction. Accordingly, a MMT supercell of 10 × 5 × 2 (≈ 5.2 nm × 4.6 nm × 2.3 nm) was first constructed. For each of the 10 different PEO conformations obtained in correspondence of a given DP, we copied six PEO chains with DP = 19, four chains with DP = 28, two chains with DP = 56, and 1 chain with DP 113 in 10 identical MMT supercells, thus obtaining 40 different binary model systems (10 for each DP) overall. This choice allowed for an approximately constant number of polymer atoms in each simulation cell, a condition necessary for energy comparison. Each resulting (MMT/PEO) binary system was shortly energy minimized to relieve close contacts. To avoid crystal structure deformation during minimization, both montmorillonite layers were treated as rigid bodies by fixing all cell dimensions, and all atoms in the interlayer space including the cations were allow to move without any constraint.

---

[24] a) Brown, G. The X-ray *Identification and Crystal Structures of Clay Minerals*, Mineralogical Society: London, 1961; b) Reviews in Mineralogy; Bayley, S. W., Ed.; Mineralogical Society of America, Chelsea, MI, 1988; Vol. 19. See also http://www.webmineral.com; c) Tsipurski, S. I.; Drits, V. A. *Clay Mineral.* **1984**, *19*, 177-193; d) The exact crystal structure of MMT depends on the nature of the cations (e.g., Na+, K+, Ca++), charge density, and the presence of crystal water. However, mainly the parameters c (approx. 9.9-13 Å) and β (approx. 95-100°) are affected.

[25] Flory, P. J. *Principles of Polymer Chemistry*, Cornell University Press: Ithaca, 1974.

[26] Theodorou D. N.; Suter U. W. *Macromolecules* **1986**, *19*, 139-154.

[27] a) Fermeglia, M.; Pricl, S. *AIChE J.* **1999**, *45*, 2619-2627; b) Fermeglia, M.; Ferrone, M.; Pricl, S. *Bioorg. Med. Chem.* **2002**, *10*, 2471-2478; c) Felluga, F.; Pitacco, G.; Valentin, E.; Coslanich, A.; Fermeglia, M.; Ferrone, M.; Pricl, S. *Tetrahedron: Asymmetry* **2003**, *14*, 3385-3399; d) Pricl, S.; Fermeglia, M; Ferrone, M.; Asquini, A. *Carbon* **2003**, *41*, 2269-2283; e) Metullio, L.; Ferrone, M.; Coslanich, A.; Fuchs, S.; Fermeglia, M.; Paneni, M.S.; Pricl, S. *Biomacromolecules* **2004**, *5*, 1371-1378; f) Toth, R.; Ferrone, M.; Miertus, S.; Chiellini, E.; Fermeglia, M.; Pricl, S. *Biomacromolecules*, **2006**, *7*, 1714–1719; g) Fermeglia, M.; Cosoli, M.; Ferrone, M.; Piccarolo, S.; Mensitieri, G.; Pricl, S. *Polymer* **2006**, *47*, 5979-5989; h) Posocco, P.; Ferrone, M.; Fermeglia, M.; Pricl, S. *Macromolecules* **2007**, *40*, 2257-2266; i) Mensitieri, G.; Larobina, D.; Guerra, G.; Venditto, V.; Fermeglia, M.; Pricl, S. *J. Polym. Sci. B: Polym. Phys.* **2008**, *46*, 8-15; j) Cosoli, P.; Scocchi, G.; Pricl, S.; Fermeglia, M. *Micropor. Mesopor. Mater.* **2008**, *1*, 169-179.

[28] Tanaka, G.; Goettler, L. A. *Polymer* **2002**, *43*, 541-553.

[29] Gardebien, F.; Bredas, J.-L.; Lazzaroni, R. *J. Phys. Chem. B* **2005**, *109*, 12287–12296.

[30] Katti, K. S.; Sikdar, D.; Katti D. R.; Ghosh, P.; Verma, D. *Polymer* **2006**, *47*, 403-414.

[31] Paul, D. R.; Zeng, Q. H.; Yu, A. B.; Lu, G. Q. *J. Colloid Interface Sci.* **2005**, *292*, 462-468.

For the construction of the water-based systems, the SPC/E model was chosen to represent water molecules.[32] Each ternary simulation model consists of a MMT unit cell, the PEO chain(s) with a given DP, and a suitable number of water molecules. Water molecules were added according to the following procedure:[33] first, a MMT cell with a interlayer spacing of 17.6 Å with the PEO chain(s) inserted in the interlayer space was created, and a short (50 ps) MD simulation was performed to equilibrate the polymer configuration within the MMT gallery. Then water was adsorbed through a grand canonical Monte Carlo (GCMC) simulation, in which chemical equilibrium was established by imposing vapour pressure of 100 kPa (1 atm). The corresponding hydrated system was equilibrated with another, short *NVT* MD run. The water molecules were subsequently deleted and re-adsorbed through a second GCMC run that ensured the accurate amount of adsorbed water.[34]

To generate a mineral surface apt for the simulation, the top silicate sheet, along with the appropriate number of alkali ions, was moved along the *c* cell axis up to 150 Å.[22,27f),28] This extension in the *c*-direction, being quite larger than the maximum system length, results in an effective 2D (x,y) periodic system,[35] which allows the use of the *NVT* ensemble for successive molecular dynamics (MD) simulations instead of the alternative constant-pressure constant-temperature (*NPT*) ensemble. As pointed out by previous studies,[36] the small difference in the pressure component along the z axis (P_{zz}), relative to the *NPT* ensemble, is negligible; furthermore, the uncertainties in selecting the correct barostat are eliminated, and the required computational time is reduced. The new equilibrium position of the remaining Na^+ counterions on the remaining MMT sheet were determined following the procedure suggested by Heinz et al.[23b)] Accordingly, half of them were placed 1 nm away on one side, and the remaining half 1 nm away on the other side of the MMT layer in 10 different arrangements; molecular mechanics energy minimizations were then performed to convergence, keeping all other MMT atoms fixed, and the structure with the lowest energy was finally selected for further simulations. In this configuration, the Na^+ ions are found at about 1.8 Å from the center of the surface oxygen atoms, or about 4.8 Å from the central plane of the metal atoms, in excellent agreement with previous simulations,[33] and experimental NMR data.[37] In fact, surface lattice cavities are characteristic of the oxygen network in all 2:1 layer silicates, and in cations primarily reside partially inserted within these cavities.

Subsequently, 500 ps of *NVT* MD experiments were run at 300 K for each system, using the Verlet algorithm and an integration step of 1 fs. The Ewald summation method[38] was applied for treating both van der Waals and electrostatic interactions. Temperature was controlled using the Nosé thermostat (Q ratio = 1).[39] In order to reduce computational time, during each MD both montmorillonite layers were treated as rigid bodies by fixing all cell dimensions, and all atoms in the interlayer space including the cations were allow to move without any constraint. The total number of ternary systems generated was 40, ten for each PEO DP value considered.

The procedure used to calculate the interaction energies and, hence, the binding energy values E_{bind} between all system components, is well estabilished.[22a-d),27f)] By definition, the binding energy E_{bind} is the negative of the interaction energy. As an example, to calculate the

[32] Berendsen, H.J.C.; Grigera, J.R.; Straatsma, T.P. *J. Phys. Chem.* **1987**, *91*, 6269-6271.
[33] Hackett, E.; Manias, E.; Giannelis, E. P. *Chem. Mater.* **2000**, *12*, 2161-2167.
[34] Bujdak, J.; Hackett, E.; Giannelis, E. P. *Chem. Mater.* **2000**, *12*, 2168-2174.
[35] Misra, S.; Fleming, P. D. III; Mattice, W.L. *J. Comp. Aided. Mater. Des.* **1995**, *2*, 101-112.
[36] Heinz, H.; Paul, W.; Suter, U. W.; Binder, K. *J. Chem. Phys.* **2004**, *120*, 3847-3854.
[37] Yang, D.-K.; Zax, D. B. *J. Chem. Phys.* **1999**, *110*, 5325-5336.
[38] Ewald, P. P. *Ann. Phys.* **1921**, *64*, 253-287.
[39] Nosé, S. Pr*og. Theor. Phys., Suppl.* **1991**, *103*, 1-46.

binary binding energy term E_{bind}(PEO/H_2O), we can first created a PEO–H_2O system deleting the MMT platelet and the Na^+ ions from one of the equilibrated MD trajectory frames, and then calculated the potential energy of the system $E_{PEO/H2O}$. Next, we deleted the water molecules, leaving the PEO chain alone, and thus calculated the energy of the PEO molecule, E_{PEO}. Similarly, we deleted the PEO molecules from the PEO–H_2O system, and calculated E_{H2O}. Then, the binding energy E_{bind}(PEO/H_2O) is simply obtained from the following equation:

$$E_{bind}\left(PEO/H_2O\right) = E_{PEO} + E_{H_2O} - E_{PEO/H_2O} \tag{3.1}$$

The remaining binding energy terms E_{bind}(PEO/MMT) and E_{bind}(MMT/H_2O), can be calculated in an utterly analogous fashion from the corresponding energy components.

As the MD frames choice is concerned, we decided to calculate the system energies at 300, 350, 400, 450, and 500 ps. We considered these as representative energy values, since every energy component was well equilibrated after approximately 100 ps of simulation. All data collected have then been averaged over the 10 different model systems for each PEO DP.

Importantly, the binding energies between the individual components of each nanocomposite system estimated using the procedure outlined above will also constitute the input parameters for the higher level, mesoscale simulations, as described in the next section.

In order to investigate the arrangement of PEO and water molecules in the silicate galleries along a plane normal to the mineral surfaces, and to compare these with the corresponding morphology resulting from mesoscale simulations, we applied an original procedure to simulate PEO chains intercalation into the clay galleries. For the simulations, we used the same molecular models employed in the *NVT* binding energies calculations described above. Starting from the 10 ×5 × 2 MMT supercell, we performed a geometry optimization of the system, keeping all cell parameters fixed except for the c distance, and using a convergence criterion of 10^{-4} kcal/(mol Å). The resulting configuration was then subjected to the MDSA procedure, in order to sample as many system configurations as possible. The total simulation lasted 25 ps, with a time step of 1 fs, and consisted of 5 annealing cycles with a starting temperature of 300 K, a mid-cycle temperature of 1500 K, and 5 heating ramps per cycle. The Ewald method[38] was again employed for treating the nonbonded energy components, and the Nosé thermostat[39] was chosen for temperature control. After each cycle, a molecular geometry optimization was run with the same criteria described before. Finally, the lowest potential energy conformation from the 5 different frames obtained as output from the described procedure was selected for further modeling. This frame was used as an initial configuration for the polymer chain/water molecules insertion. To this purpose, we used the different PEO chains built as reported in the previous section, and the same water adsorption recipe. After each polymer chain/s and water insertion, we performed the optimization procedure described above. The final systems were subjected to the last *NVT* annealing run, from which we selected the lowest potential energy frames from the trajectory files and used them as starting configurations to perform productive 300 ps *NVT* runs. Once the simulations were completed, 30 frames were extracted from the corresponding trajectory files, and on each one we performed the density profile calculations within the interlayer spaces.

3.2.2 Mesoscale models and simulations

In order to obtain the morphology of polymer and water molecules between the montmorillonite layers, and to evaluate and compare the influence of the polymer molecular weight at a mesoscopic level, *Dissipative Particle Dynamics* (DPD)[21] simulations were carried out using the *DPD module* of the Culgi modeling suite (Culgi B.V., Leiden, The Netherlands).

As described in Chapter 2, in the *Dissipative Particle Dynamics* simulation method, a set of particles moves according to Newton's equation of motion, and interacts dissipatively through simplified force laws. Also, in the DPD model individual atoms or molecules are not represented directly, but are coarse-grained into beads. These beads, or particles, constitute local "fluid packages" able to move independently.

The force acting on the beads, which is pairwise additive, can be decomposed into three elements: a conservative ($\boldsymbol{F}_{ij}^{C}$), a dissipative ($\boldsymbol{F}_{ij}^{D}$), and a random ($\boldsymbol{F}_{ij}^{R}$) force.[40] Accordingly, the effective force $\boldsymbol{f}_i$ acting on a particle *i* is given by:

$$\mathbf{f}_i = \sum_{i \neq j} \left(\mathbf{F}_{ij}^{C} + \mathbf{F}_{ij}^{D} + \mathbf{F}_{ij}^{R} \right) \tag{3.2}$$

where the sum extends over all particles within a given distance r_c from the *i*th particle. This distance practically constitutes the only length scale in the entire system. Therefore, it is convenient to set the cutoff radius r_c as a unit of length (i.e., r_c = 1), so that all lengths are measured relative to the particles radius.[40]

In the framework of a multiscale approach to PCN simulation, the conservative interaction parameters *a* needed as input for the mesoscale level DPD calculations can be obtained by a mapping procedure of the binding energy values between different species obtained from simulations at a lower (atomistic) scale.[41,22d)] The first step necessary for determination of the DPD input parameters generally consists of defining the DPD bead dimensions, thus implicitly defining characteristic length of the system (r_c). The interaction range r_c sets the basic length scale of the system; in other terms, r_c can be defined as the side of the cube containing an average number ρ of beads. Therefore,

$$r_c = \left(\rho \, V_b \right)^{1/3} \tag{3.3}$$

where V_b is the volume of a DPD bead. It is important to recall here that, even in a heterogeneous system consisting of several different species such as a PCN, a basic DPD assumption is that all bead types (each representing a single species) must be of a comparable volume, V_b.

Starting mesoscale model generation with the polymer chain, the basic strategy to calculate the volume of a DPD bead V_b consists in mapping the real polymer chain onto a chain consisting of Kuhn segments. Consequently, each DPD bead represents a statistically correlated unit or Kuhn segment of the polymer. A DPD chain should, therefore, be made up of N_{DPD} beads, where:

$$N_{DPD} = \frac{N_{mon}}{C_\infty} \tag{3.4}$$

[40] Groot, R. D.; Warren, P. B. *J. Chem. Phys.* **1997**, *107*, 4423-4435.
[41] Scocchi, G.; Posocco, P.; Fermeglia, M.; Pricl, S. *J. Phys. Chem. B* **2007**, *111*, 2143–2151.

where N_{mon} is equal to the degree of polymerization of the molecular chain DP, and C_∞ its characteristic ratio. If so, the mesoscale simulations should capture in a reliable way two essential features of a given polymer chain, namely its dimension (given by N_{mon}) and flexibility (given by C_∞). When a flexible macromolecules is modeled as a Gaussian chain, however, C_∞ represents also the number of monomers making up a Kuhn segment (i.e., contained in a single DPD bead). Therefore, the bead volume V_b can be simply obtained multiplying the characteristic ratio C_∞ by the monomer volume V_{mon}, here estimated to be equal to 52.68 Å^3 by the Connolly algorithm.[42]

For a polymeric chain, the characteristic ratio is defined as:

$$C_\infty = \frac{\left\langle R_0^2 \right\rangle}{N l^2} \tag{3.5}$$

where R_0 is the unperturbed mean-square end-to end distance, N is the total number of skeletal bonds, and l^2 is the mean-square bond length. In the case of PEO, N is three times the degree of polymerization, and l^2 is calculated to be equal to 2.14 Å by simply applying:

$$l^2 = \frac{l^2(C-C) + 2l^2(C-O)}{3} \tag{3.6}$$

where $C-C$ = 1.53 Å and $C-O$ = 1.43 Å.[43,44] A conformation-related property such as C_∞ can be experimentally estimated, for example, in dilute polymer solution under unperturbed or θ-conditions or calculated, as done in this work, using a molecular dynamics procedure based on the Rotational Isomeric State (RIS) method.[45,46] Generally speaking, for a given polymer at low degree of polymerization the characteristic ratio varies with N. According to our simulations, we found that for PEO C_∞ is only weakly varying with molecular weight, and the average value resulting from the application of the RIS procedure is equal to 4.9. This finding is in good agreement with the corresponding values available in the literature both from experiments and simulation.[43,44,47,48]

The resulting values of the calculated bead volume V_b, the corresponding number of beads for each PEO chain N_{DPD}, and the cut-off radius r_c used in the DPD simulations are listed in Table 3.1.

V_b[a] (Å^3)	r_c[b] (Å)	N_{DPD}[c]			
		PEO19	PEO28	PEO56	PEO113
262	9.23	4	6	11	23

Table 3.1. Characteristics of the DPD beads and chains. [a]DPD bead volume. [b]Cut-off radius. [c]Total number of DPD beads in each PEO chain.

[42] Connolly, M.L. *J. Am. Chem. Soc.* **1985**, *107*, 1118-1124.
[43] Kawaguchi, S.; Imai, G.; Suzuki, J.; Miyahara, A.; Kitano, T.; Ito, K. *Polymer* **1997**, *38*, 2885-2891.
[44] Smith, G. D.; Yoon, D. Y.; Jaffe, R. L.; Colby, R. H.; Krishnamoorti, R.; Fetters, L. J. *Macromolecules* **1996**, *29*, 3462-3469.
[45] Blomqvist, J.; Mietila, L.-O.; Mannfors, B. *Polymer* 2001, ***42***, 109-116.
[46] Maly, M.; Posocco, P.; Pricl, S.; Fermeglia, M. *Ind. Eng. Chem. Res.* **2008**, *47*, 5023-5038.
[47] Annis, B. K.; Kim, M.-H.; Wignall, G. D.; Borodin, O.; Smith, G. D. *Macromolecules* **2000**, *33*, 7544-7548.
[48] Dong, H.; Hyun, J.-K.; Durham, C.; Wheeler, R. A. *Polymer* **2001**, *42*, 7809-7817.

Having determined the bead size, and fixed the system density to ρ=3, the characteristic dimension of the mesoscopic system could be calculated from Equation (3.3) as r_c = 9.23 Å. As said, this value represents the soft potential cut-off distance, but also sets the length of the DPD simulation box. Our overall DPD system was chosen to be constituted by 20 × 20 × 3 unit cells, and hence was characterized by effective dimensions of 18.5 nm × 18.5 nm × 2.8 nm.

At this point, the number of DPD beads of each individual system component (i.e., MMT, PEO, and H_2O) must be estimated. To this purpose, the PEO-based PCN can be devised as composed of three different species of beads: one for the polymer chains (*P*), one for the water molecules (*W*), and one for the MMT surface (*M*). The modeling of the MMT layers in the context of DPD has been addressed by freezing locally the particles representing the silicate solid boundaries. These particles behave as fluid particles but maintain a fixed position and possess zero velocity. Therefore, these MMT walls interact with each bead in the system with a potential of the same form as the bead-bead conservative force. This force is short-ranged, so the system beads are not strictly forbidden from passing through the barrier. To prevent particles from entering the wall region, several methods have been proposed. In this work, we decided to apply the bounce-forward reflection approach[49] in all calculations. Lastly, the number of individual polymer (Table 3.1) and water beads can be easily obtained from the atomistic polymer/water molecular volume ratio.

The next, important issue of a DPD simulation is the determination of the bead interaction parameters. The detailed procedure for obtaining these mesoscale interaction parameters from atomistic molecular dynamics binding energies is reported Chapter 2. Adapting this recipe to the present system, the bead-bead interaction parameter for water-water interaction was set equal to a_{WW} = 25, in agreement with the correct value for a density value of ρ = 3.[40] The clay-water interaction parameter was set to a lower value (i.e., a_{MW} = 15), in order to mimic the good affinity between the silicate and water. Once these two parameters were set, and their values associated with the corresponding values of the self and mixed rescaled DPD energies, all the remaining bead-bead interaction parameters for the DPD simulation could be easily obtained, starting from the atomistic binding energy values, as described in Chapter 2. The entire set of DPD interaction parameters employed in this work are summarized in Table 3.2.

	P					
a_{ij}	PEO19	PEO28	PEO56	PEO113	*W*	*M*
P	29.7	30.4	30.8	31.2		
W	24.1	26.0	28.1	30.0	25	
M	17.4	16.0	14.6	12.8	15	0

Table 3.2. Bead-bead interaction parameters obtained for water-based PEO-MMT nanocomposites.

In the framework of a multiscale modeling approach, one of the most important outputs of the mesoscale level calculations is the obtainment of the three-dimensional density profiles for each type of bead or, in other words, the system morphology. In fact, these density profiles constitute the input information for the last recipe step: the finite element calculations to estimate macroscopical properties.

[49] Lavallee P.; Boon J. P.; Noullez A. *Physica D* **1991**, *47*, 233–240.

3.2.3 Finite element simulations

Prediction of macroscopic properties of the PEO/MMT PCNs considered in this work, as a function of polymer molecular weight and clays loading, constitutes the final step of our multiscale modeling recipe. To this purpose, finite element (FE) simulations at ordinary temperature were performed using the software Palmyra (v. 2.5, MatSim, Zürich, CH). This software has been validated on different composite material morphologies by several authors,[22d),e),50,51] yielding reliable results. FE calculations were applied in order to analyze both platelet stacks and overall nanocomposite properties, using fixed and variable grid, respectively. In particular, thermal expansion coefficients and electrical conductivity were the macroscopic properties of election, since it is in these performances that lies most of the industrial interest towards these new materials. The properties of the pure system components (i.e., silicate, polymer, and water) were taken from the available literature.[52]

One of the major concerns in creating a suitable model for FE calculations is the definition of an appropriate reactive volume element (RVE), which could be representative of the different morphologies characterizing such complex materials as PCNs. Since most of the effects exerted by layered silicate addition is generally observed at low clay contents, we decided to adopt the following values for clay loading: 1%, 2%, 3%, 4%, and 5% w/w. Given the PEO and MMT experimental density values (1.14 g/cm^3 and 2.71 g/cm^3, respectively),[52,53] these amounts correspond to clay volume fraction V_f range from 2.2% to 0.42%. Relying on previous studies,[22d),e)] and on extensive trials, we selected to simulate an RVE made up of 48 MMT particles, grouped in stacks of different size, representing both the exfoliated and intercalated states (*vide infra*).

MMT particles (both single particles and stacks) were modelled as disks with a toroidal rim. Each platelet thickness was defined by the height of the corresponding symmetry axis h and diameter d, thus being characterized by an aspect ratio of $a = d/h$. By setting d = 120 nm and h = 1 nm for each single particle, the aspect ratio a was equal to 120, a value in agreement with common literature data for layer silicates.[1] According to these settings, the volume of a single MMT platelet is $V_p = 11.3 \times 10^3$ nm^3; this information, coupled with the MMT V_f values for each loading and the number of MMT sheets in each model box, was used to retrieve the dimensions of the FE cubic calculation cells.

The mixed nature of intercalation and exfoliation of PEO/MMT PCNs was accounted for by grouping some MMT platelets in stacks; in other words, the models contained two different elements: single MMT sheets, representing exfoliated nanoparticles, and polymer intercalated MMT sheets (or stacks). Stacks were modelled using the same particle representation employed for MMT isolate sheets, but varying the platelet thickness according to the number of sheets characterizing each stack element. As PEO/MMT systems are known to be highly intercalated,[52,54] based on our previous studies[22d),e)], and on the d-spacing of stacks resulting from our lower-scale simulations, we convene to represent a PCN characterized by a low exfoliation/high intercalation morphology according to the conditions

[50] Osman, M. A.; Mittal, V.; Lusti, H. R. *Macromol. Rapid Commun.* **2004**, *25*, 1145-1149.

[51] Heggli, M.; Etter, T.; Wyss, P.; Uggowitzer, P. J.; Gusev, A. A. *Adv. Eng. Mater.* **2005**, *7*, 225-229.

[52] a) Fripiat, J. J.; Jelli, A.; Poncelet, G.; André, J. *J. Phys. Chem.* **1965**, 69, 2185-2196; b) McGowan, J. C. *Polymer* **1969**, *10*, 841-848; b) Wu, J.; Lerner, M. M. *Chem. Mater.* **1993**, *5*, 835-838; c) Shanmukaraj, D.; Murugan, R. *J. Polym. Sci.* **2005**, *149*, 90-95; d) Wang, W.; Yang, X.; Fang, Y.; Ding, J.; Yan, J. *Appl. Energy* **2009**, *86*, 1196-1200; e) Sengwa, R. J.; Choudhary, S.; Sankhla, S. *Colloid Surface A* **2009**, *336*, 79-87.

[53] Fornes, T. D.; Hunter, D. L.; Paul, D. R. *Macromolecules* **2004**, *37*, 1793-1798.

[54] a) Krishnamoorti, R.; Vaia, R. A.; Giannelis, E. P. *Chem. Mater.* **1996**, *8*, 1728-1734; b) Harris, D. J.; Bonagamba, T. J.; Schmidt-Rohr, K. *Macromolecules* **1999**, *32*, 6718-6724; c) Shen, Z.; Simon, G. P.; Cheng, Y. - B. *Polymer* **2002**, *43*, 4251-4260; d) Chaiko, F. J. *Chem. Mater*. **2003**, *15*, 1105-1110; e) Reinholdt, M. X.; Kirkpatrick, R. J.; Pinnavaia, T. J. *J. Phys. Chem. B* **2005**, *109*, 16296-16303; f) Chen, B.; Evans, J. R. G. *J. Phys. Chem. B* **2004**, *108*, 14986-14990; g) Sun, L.; Ertel, E. A.; Zhu, L.; Hsiao, B. S.; Avila-Orta, C. A.; Sics, I. *Langmuir* **2005**, *21*, 5672-5676.

reported in Table 3.3. Single particles and stacks were then oriented in the FE simulation box according to a method reported previously.[22d)]

Particle type	n. of particles	*a*
single	4	120
2-stack	8	15
4-stack	4	7.5
6-stack	2	5

Table 3.3. Platelet stacking parameters *a* and relative aspect ratio for a low exfoliation/high intercalation morphology of PEO/MMT PCN systems. The term particle designates both single, exfoliated clay sheets and intercalated stacks.

Once all model systems were prepared, appropriate surface and volume meshes had to be generated in order to run Palmyra solver and retrieve the macroscopic properties of interest. By applying a displacement-based finite element method to the total mesh, the responses to external deformations were calculated. In order to calculate thermal expansion coefficients, a thermo-elastic solver was used, and a seventh "deformation" (an increase of temperature by 1 K) was applied in order to obtain the linear thermal expansion coefficients. For other physical properties such as electrical conductivity, a Laplace solver was employed, that applies a field in the three main directions to the finite element mesh, and minimizes the energy of the composite.[55]

3.3 Results and discussion

3.3.1 Atomistic simulations

In order to study the effect of PEO molecular weight and of the presence of water molecules on the interactions between polymer and clay platelets, we performed atomistic MD simulations of PEO-based PCNs in a solvated environment using polymers of different chain length but with an approximately constant total number of atoms. Accordingly, we modelled 6 PEO chains with a degree of polymerization DP equal to 19, four chains with DP = 28, two chains with DP = 56, and one chain with DP = 113, respectively, approximately corresponding to a molecular weight of 750, 1100, 2000 and 5000 Da. Figure 3.1(a) and (b) show two MD snapshots of the hydrated MMT/PEO systems with the lowest and highest polymer M_W considered, respectively. The resultant binding energy values between the individual system components are listed in Table 3.4, from which it can be readily seen that the favorable interactions between clay and polymer, as quantified by the term E_{bind}(MMT/PEO), increase with increasing polymer molecular weight. Thermodynamic arguments can be invoked to account for this trend. Indeed, it can be argued that the PEO macromolecules would generally adopt a conformation that allows for maximum segment-surface interactions.[56] For a given amount of polymer, the number of polymer segments can be assumed to be approximately the same. A higher molecular mass PEO possesses the

[55] Gusev, A. A. *Macromolecules* **2001**, *34*, 3081-3093.

[56] Burchill, S.; Hall, P. L.; Harrison, R.; Hayes, M. H. B.; Langford, J. I.; Livingston, W. R.; Smedley, R. J.; Ross, D. K.; Tuck, J. *J. Clay Miner.* **1983**, *18*, 373-397.

potential to realize larger segment/MMT surface contacts, which favour surface adsorption and, ultimately, result in the highest level on polymer intercalation into the silicate galleries.

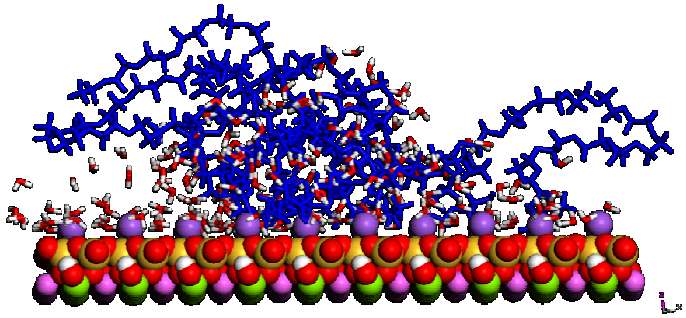

(a)

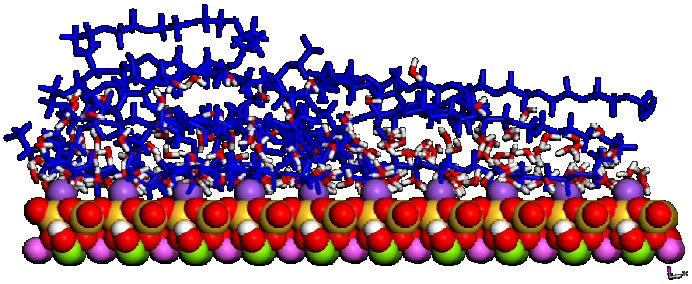

(b)

Figure 3.1. Equilibrated MD trajectory frames for pseudo 2D solvated MMT systems with (a) 6 PEO chains of DP = 19, and (b) 1 PEO chain of DP = 113, respectively. MMT is represented in CKP style, the polymer is depicted in blue stick rendering, and water molecules are shown as atom-colored sticks. Color legend: gold, silicon; red, oxygen; white, hydrogen; purple, Na; pink, Al; light green, Mg.

Polymer	*System MMT/PEO/H_2O*			*N_A*[a]
	E_{bind}(MMT/PEO)	E_{bind}(MMT/H_2O)	E_{bind}(PEO/H_2O)	
PEO19	-695	-5300	-891	810
PEO28	-761	-5276	-861	792
PEO56	-898	-5205	-784	788
PEO113	-1015	-5104	-641	798

Table 3.4. Binding energies in water systems with PEO chains of different molecular weight. All energy values are expressed in kcal/mol. [a]Total number of polymer atoms in each simulation cell.

Also, montmorillonite as a inorganic mineral is generally considered as being hydrophilic.[57] Nonetheless, the basal Si-O groups in the spaces between hydrated cations in the clay interlayers are relatively hydrophobic, and, as results from the inspection of the corresponding density distribution profiles (*vide infra*), and in line with some other

[57] Yan, L. B.; Roth, C. B.; Low, P. F. *J. Colloid Interface Sci.* **1996**, *184*, 663-670.

simulation and convincing experimental evidences,[34,58] PEO tends to adsorb preferentially on these sites. A low molecular mass PEO chain features a higher number of hydrophilic –OH end groups with respect to a high molecular mass one; this, in principle, should facilitate the preferential intercalation and adsorption of the longer PEO chains with respect to the smaller ones, for which, conversely, the contact with the MMT are fewer and the chains tend to cluster, with water, in the middle of the interlayer space.

In harmony with the foregoing discussion, both interaction energy terms between clay and water (E_{bind}(MMT/H_2O) and polymer and water (E_{bind}(PEO/H_2O)) decrease with increasing polymer chain length. Generally speaking, water molecules preferably reside on the surface of the clay, by virtue of strong Coulombic interactions between the water dipoles and the charged MMT surface.

Further, a number of water molecules are engaged in hydrogen bonds with the surface –OH groups of the MMT platelet as well as with the –OH moieties of the PEO chains. As the chain molecular mass increases, however, less MMT surface is available for water contacts due to a more extensive coverage from the long PEO chains; accordingly, E_{bind}(MMT/H_2O) becomes lower. Also, the decreased hydrophilic character of longer PEO macromolecules with respect to shorter ones reflects in the lower interaction energy values (see Table 3.4).

Further molecular dynamics simulations were conducted to derive number density profiles, showing the arrangement polymer molecules in the clay galleries, through a plane normal to the silicate galleries, again as a function of the PEO M_w. Figure 3.2(a) and (b) shows, as an example, the starting configuration and an equilibrated MD frame of the solvated MMT/PEO nanocomposite with PEO chains of molecular mass equal to 750, respectively.

Interestingly, the equilibrium interlayer spacing, or *d*-spacing, is relatively insensitive to the degree of polymerization, being equal to 18.2, 18.0, 17.9, and 17.7 Å, for M_w 750, 1100, 2000, and 5000, respectively. These values are in excellent agreements with both experimental and other simulation studies.[33,54,59] A slightly higher *d*-spacing is obtained for the lowest M_W PEO PCN system, an evidence which could be rationalized by the decreasing concentration of available –OH end groups as M_W increases. Also, the preferential location for smaller chains in the middle region of the interlayer space can account for this (albeit small) larger value of *d* (see Figure 3.2(a)). Interestingly, Na^+ cations in all cases were found located close to the surface of the mineral platelet, although a number of them were also observed at some distance from the MMT sheets (see Figure 3.2(b)), again in agreement with previous studies.[59]

Figure 3.2(c) illustrates the density profiles within the silicate galleries as obtained from all PEO samples considered. As can be inferred from this Figure, the density profiles of the polymer carbon atoms change from those typical of a bilayer structure, featuring maxima near the clay platelets and a flat region in the middle in the intergallery space (highest M_W PEO sample), to those pertaining to a trilayer structure, in which some chains still remain in the vicinity of the mineral surface but a substantial part of the material tends to concentrate in the middle of the MMT interlayer (lowest M_W PEO sample). As discussed above, high mass PEO chains feature the highest binding energy with the MMT surface (see Table 3.4). In line with this evidence, these longer macromolecules tend to align themselves parallel to the clay

[58] Coppin, F.; Berger, G.; Bauer, A.; Castet, S.; Loubet, M. *Chem. Geol.* **2002**, *182*, 57-68.

[59] a) Kuppa, V.; Menakanit, S.; Krishnamoorti, R.; Manias, E. *J. Polym. Sci. B: Polym. Phys.* **2003**, *41*, 3285-3298; b) Strawhecker, K. E.; Manias, E. *Chem. Mater.* **2003**, *15*, 844-849; c) Loyens, W.; Jannasch, P.; Maurer, F. H. J. *Polymer* **2005**, *46*, 903-914; d) Elmahdy, M. M.; Chrissopoupou, K.; Afratis, A.; Floudas, G.; Anastasiadis, S. H. *Macromolecules* **2006**, *39*, 5170-5173; e) Mazo, M. A.; Manevitch, L. I.; Gusarova, E. B.; Shamaev, M. Y.; Berlin, A. A.; Balabaev, N. K.; Rutledge, G. C. *J. Phys. Chem. B* **2008**, *112*, 3597-3604.

wall, so that the highest number of chain segments can line up in a single layer and, thus, maximize the number of favorable contacts with the mineral. Quite an opposite situation is encountered at the other extreme of PEO molecular mass values considered in our study. Indeed, the high number of hydrophilic –OH chain ends tend to limit contacts with the basal Si-O groups, and improve the number of the more favorable water-polymer contacts (see Table 3.4), a situation which can be aptly realized by confining a consistent amount of PEO in the central part of the clay intergallery space. Finally, a smooth, continuum transition between these two extremes is seen for the remaining two intermediate M_W PEO PCN, again in line with the progressively decreasing valued of the corresponding E_{bind}(MMT/PEO) values listed in Table 3.4.

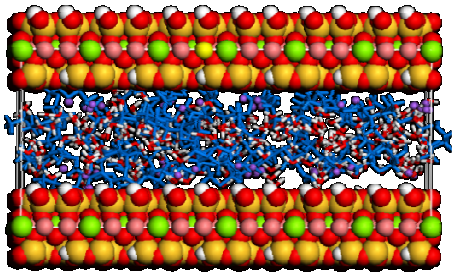

(a)

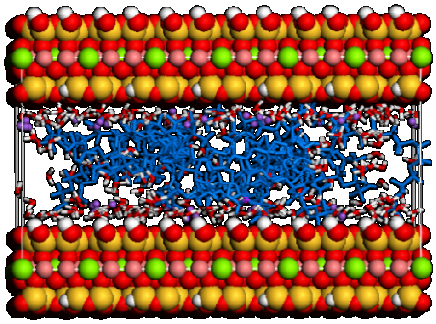

(b)

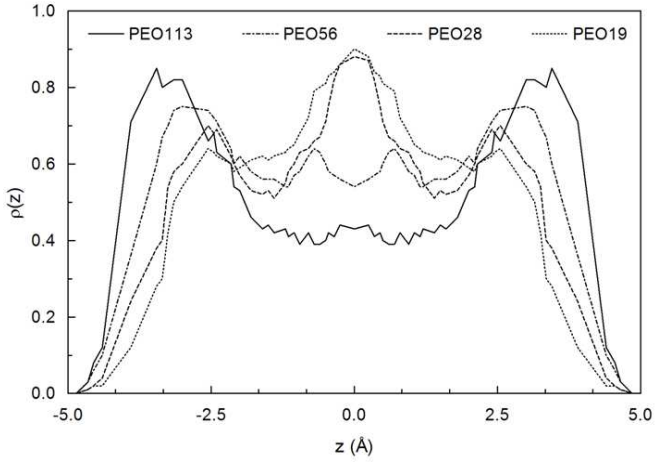

(c)

Figure 3.2. Starting frame (a) and equilibrated MD trajectory frame for a solvated MMT systems with 6 PEO chains of DP = 19. Molecule representation and color scheme as in Figure 3.1. (c) Number density profiles of PEO with different DP in solvated MMT nanocomposites: continuous line, PEO DP = 113; dotted-broken line, PEO DP = 56; broken line, PEO DP = 28; dotted line, PEO DP = 19.

3.3.2 Mesoscopic simulations

By using the *Dissipative Particle Dynamics* approach along with the interaction parameters obtained from lower scale (i.e., atomistic MD) simulations as described previously, we modelled and simulated all solvated MMT/PEO PCNs at a mesoscopic level. In harmony with the MD approach, to mimic polymers of different M_W we simulated four types of PEO chains with different number of beads; the total number of PEO beads, however, was kept constant in all systems. Figure 3.3(a) and (b) illustrates the system morphologies obtained from these simulations for the lowest and highest M_W PEO solvated PCN system, as an example. A cursory comparison of Figure 3.3(b) with Figure 3.2(b) reveals a very good agreement between atomistic and mesoscale predictions. In fact, the highest tendency to flatten onto the MMT surface for the longer PEO with respect to preferred water contacts for chains of lower mass is well preserved at the scale level.

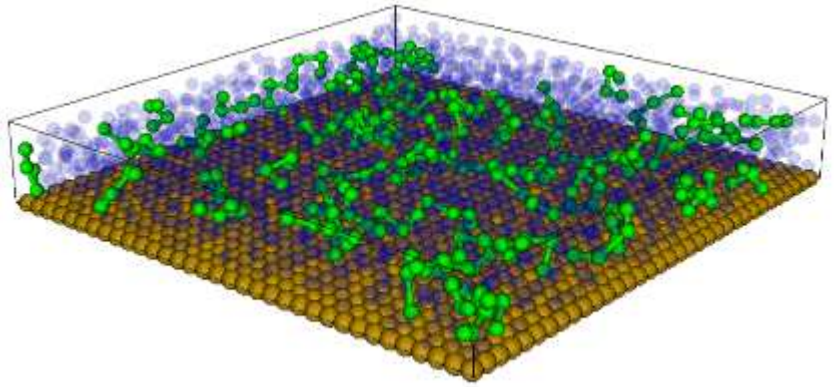

(a)

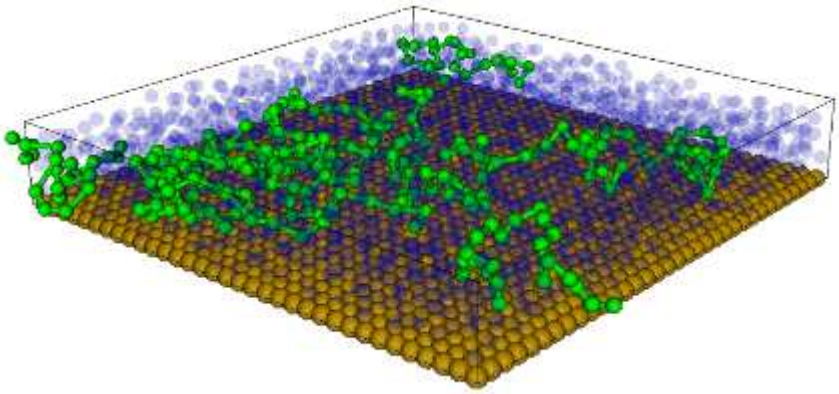

(b)

Figure 3.3. Equilibrated mesoscale morphologies for (a) a solvated MMT systems PEO chains of DP = 19 and (b) a solvated MMT systems with PEO chains of DP = 113. PEO molecules are shows as green sticks-and-balls, MMT walls are portrayed as gold balls, and water molecules are depicted as transparent blue spheres. The top MMT sheet is not shown for clarity.

A quantitative analysis of these systems can be carried out by considering the density profiles along the direction normal to the silicate surface, which are reported in Figure 3.4(a) and (b). The shape of all density curves reveal the high but different affinity of polymer and water molecules for the inorganic surface: indeed, the density of water beads near the MMT surface is higher than that of the polymer chains (see Figure 3.4(a)), in agreement with the results gathered from MD simulations, again indicating that water molecules preferably

reside on the surface of the clay. Also, the density profiles of polymer beads in the DPD simulation box (see Figure 3.4(b)) clearly confirm the predictions obtained from the lower scale simulation that higher molecular weight polymers possess a higher affinity for the MMT surface. In fact, the density of polymer chains near the clay surface increases with increasing polymer chain length. This effect progressively levels out as the polymer chain decreases in length, and a further maximum in the density profile correspondingly appears, located in the clay gallery middle space, in harmony with the corresponding MD quantitative results.

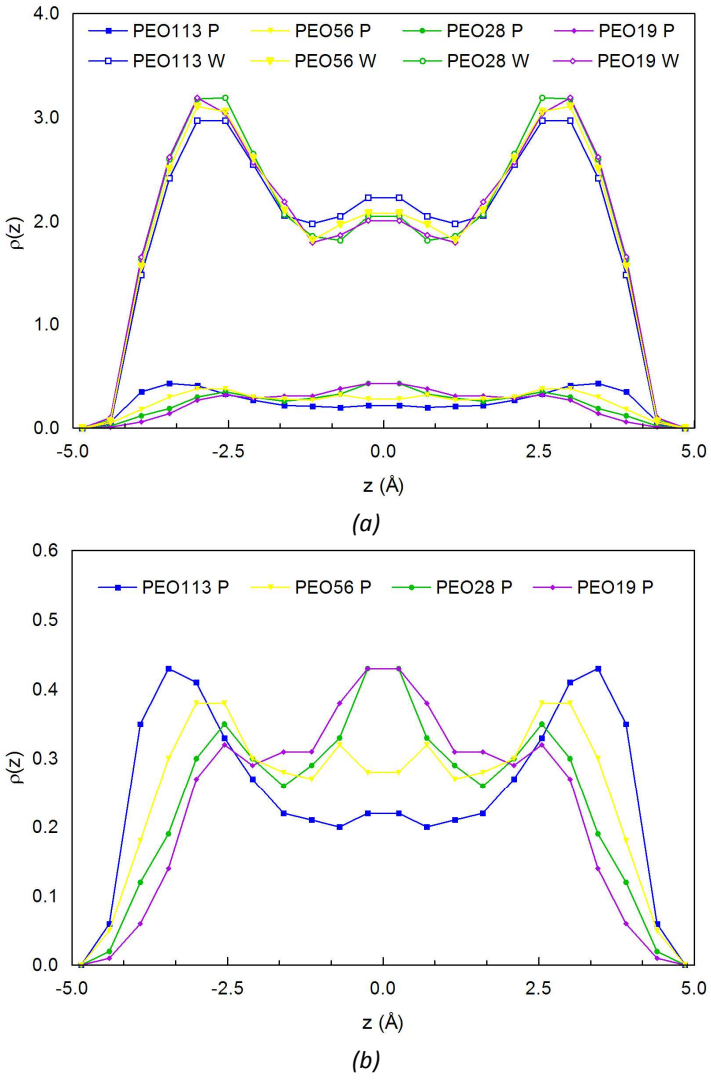

Figure 3.4. (a) DPD mesoscale density profiles of the interlayer polymer/water phase in the direction normal to the clay layers for water and polymer at different molecular weight. (b) Same data but without water curves for a better appreciation of the polymer density distribution. Legend: full symbols, polymer; empty symbols, water.

3.3.3 Finite element simulations

Polymer-clay nanocomposites in which an hydrophilic polymer, such as PEO, is highly intercalated within the sheets of layered silicates such as sodium/lithium MMT show interesting electromechanical responses, rendering them potential candidates for

applications as electrolytes in, for instance, solid batteries.[5-7] Accordingly, for FE calculations we decided to focus on the predictions of those macroscopic properties of PEO/MMT systems most relevant to these practical purposes, i.e., thermal expansion coefficients and electrical conductivity. To this end, we took into consideration the dependence of these properties on the PEO M_w (in the range 750 – 5000 Da) and on the MMT loading (between 1% and 5% w/w). Figure 3.5 (a)-(c) illustrates an intercalated stack in the FE RVE model of the PCN, a global model configuration, and the relative meshed volume used in the FE calculations for the PEO/MMT system with PEO of M_w = 5000 and 5% clay loading, as an example.

The results of the FE calculations for the coefficient of thermal expansion (CTE) for the different PEO/MMT as a function of clay loading are shown in Figure 3.6(a). As can be seen from this image, the values of CTE linearly decrease as MMT loading increases, for all molecular weight PEOs, in agreement with available experimental evidences on closely related systems.[60] The linear thermal expansion of a nanocomposite will greatly depend on the average orientation of the platelets. The effect of inorganic filler orientation on the reduction of linear thermal expansion is similar to the effect on modulus enhancement or reinforcement which has been studied more extensively. Filler geometry can also greatly affect physical properties of composites; e.g. high aspect ratios contribute to greater reduction in thermal expansion.[1,60a)] The high value of the thermal expansion coefficient of polymers is caused by the low energy barrier for the chain conformation to be changed. The thermal expansion coefficient always decreases with increasing aspect ratio and filler loading due to the mechanical constraint of the filler. Enhancement of dimensional stability is expected when a filler with high modulus and low thermal expansion coefficient is dispersed in a matrix of lower modulus and higher thermal expansion coefficient owing to simple mechanical restraints. Layered silicates seem attractive for this purpose owing to their high modulus, high aspect ratio, and low coefficient of thermal expansion; in addition, they are likely to be less detrimental to surface finish and ductility than conventional fillers. The larger constraining effect imposed by dispersed rigid platelets translates into lower thermal expansion coefficients.

The rate of CTE decreasing with increasing clay content is slightly higher for polymers with smaller chains. This observation can be rationalized by considering that, for a given MT loading, the corresponding low molecular weight PEO fractions, characterized by higher chain mobility, should suffer the larger constraining effects imposed by dispersed rigid platelets more than their longer counterparts, and this ultimately translates onto lower thermal expansion coefficients for lower DP PEO/MMT PCNs. Notably, above a certain filler content (between 6 and 8%), the CTE values for all PNCs seems to converge, suggesting that the effect of the polymer molecular mass levels off when a substantial amount of filler is present, and polymer chains undergo comparable constraining effects imposed by the mineral particles independently on their relative length.

Figure 3.6(b) shows the behavior of electrical conductivity σ for all PEO/MMT PCNs as a function of clay loading, as estimated with our multiscale simulation procedure. Although the effect of polymer molecular weight on σ is less pronounced than in the case of CTE, we can still observe that, in particular at lower clay contents, PNCs with shorter PEO chains features higher values of σ with respect to high molecular weight samples.

[60] a) Yoon, P. J.; Fornes, T. D.; Paul, D. R. *Polymer* **2002**, *43*, 6727-6741; b) Jan, I.-N.; Lee, T.-M.; Chiou, K.-C.; Lin, J.-J. *Ind. Eng. Chem. Res.* **2005**, *44*, 2086-2090; c) Lee, K. Y.; Kim, K. H.; Jeoung, S. K.; Ju, S. I.; Shim, J. H.; Kim, N. H.; Lee, S. G.; Lee, S. M.; Lee, J. K.; Paul, D. R. *Polymer* **2007**, *48*, 4174-4183; d) Lee, K. Y.; Hong, S. R.; Jeoung, S. K.; Kim, N. H.; Lee, S. G.; Paul, D. R. *Polymer* **2008**, *49*, 2146-2152; e) Rao, Y. Q.; Blanton, T. N. *Macromolecules* **2008**, *41*, 935-941.

Intuitively, this can be ascribed once more to the higher mobility of smaller PEO chains but, importantly, also to the lower affinity of these shorter macromolecules for the MMT surface (see Table 3.4, Figure 3.1, and discussion above). MMT samples in equilibrium with the atmospheric moisture have water molecules associated with the interlayer cations; accordingly, the enhanced ionic conductivity of these systems can be mainly ascribed to the interlayer cations associated to water molecules.[52] By interacting less tightly with the clay platelet, and being distributed mainly at the center of the interlayer galleries, the low DP PEO chains allows for a higher mobility of the interlayer cations and their hydration shell. In the presence of high molecular weight chains, on the contrary, the high affinity of these macromolecules for the clay surface, and the tendency to adopt chain conformations which maximize polymer segments/clay platelet interactions, ultimately produce a strong association of the interlayer cations and the clay surface oxygens. As a consequence, these metal ions remain entrapped into a highly constrained system where their mobility is prevented, and very high temperatures (e.g., up to 600K) are required to observe ionic conductivity in the range of 10^{-8}–10^{-9} S/cm.[7]

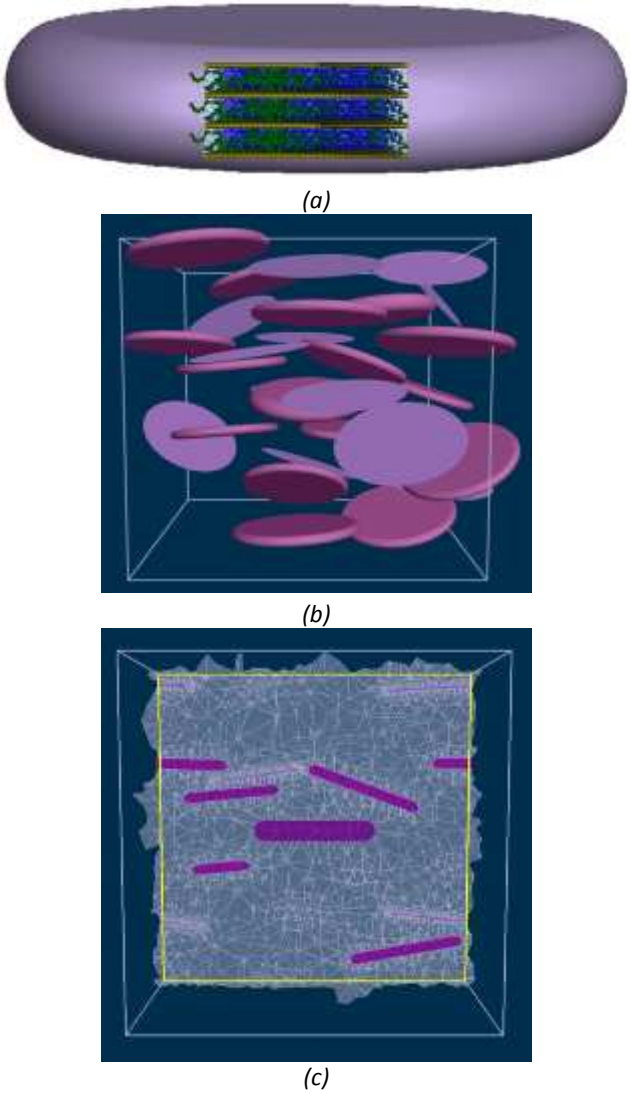

Figure 3.5. Intercalated stack in the FE RVE model of the PEO/MMT PCN (a), global model configuration (b), and relative meshed volume (c) used in the FE calculations for the PEO/MMT system with PEO of M_w = 5000 and 5% clay loading.

PEO intercalation into the MMT galleries, coupled with the presence of water molecules in the sheet spacing produce drastic cation environment modifications that allow appreciable electric conductivity even at ordinary temperature. Following Aranda,[7] and in harmony with the morphologies predicted at all scales in this work, in water-PEO intercalated PCNs the organic polymers with smaller mass chains, by maximizing their density in the interlayer spacing, act as a sort of pillar, causing a permanent separation between the silicate layers on one side and, on the other, reducing the cations mobility restrictions. In addition to this so-call "pillar-effect", other factors, mainly associated with the relaxation of the polymer chains, can also concur to the increase of the cation mobility,[61] although a detailed discussion on these effects is outside the scope of the present study.

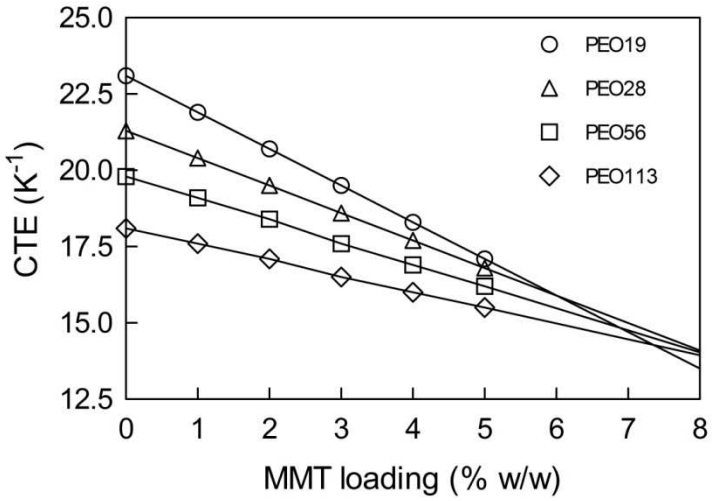

(a)

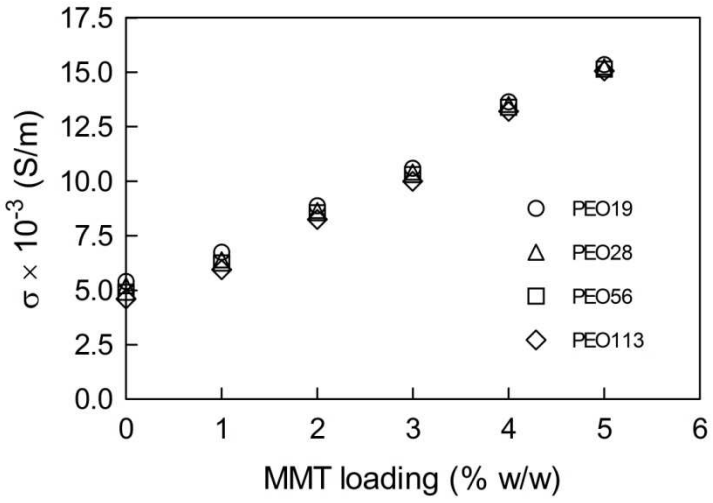

(b)

Figure 3.6. Coefficient of thermal expansion (CTE) (a) and electrical conductivity σ (b) for all PEO/MMT PCNs as a function of clay loading, as predicted from finite element calculations based upon the multiscale modeling procedure developed in this work.

[61] a) Papke, B. L.; Ratner, M. A.; Shriver, D. F. *J. Electrochem. Soc.* **1982**, *129*, 1694-1701; b) Ratner, M. A.; Shriver, D. F. *Chem. Rev.* **1988**, *88*, 109-124; c) Cowie, J. M. G.; Cree, S. H. *Annu. Rev. Phys. Chem.* **1989**, *40*, 85-113.

3.4 Conclusions

There are many levels at which computer-based molecular simulation techniques can be useful, ranging from highly detailed *ab initio* quantum mechanics, through classical, atomistic molecular dynamics, to process engineering modeling. These computations can significantly contribute to reduce wasted experiments, allow products and processes to be optimized, and permit large numbers of candidate materials to be screened *a priori*, even before their synthesis. These techniques are currently used to obtain thermodynamic information about pure or mixed systems. This information obtained by using microscopic properties assumes any system to be homogeneous in composition, structure and density, which is clearly a severe limitation. When a system is complex, comprising several components, eventually sparingly miscible, PCNs being prime examples, peculiar phases with remarkable properties can be observed. These so-called mesophases comprise far too many atoms for atomistic modeling description. Hence, coarse-grained methods are better suited to simulate such structures. One of the primary techniques for mesoscopic modeling is DPD, a particle-based method that uses soft-spheres to represent groups of atoms, and incorporates hydrodynamic behavior via a random noise, which is coupled to a pair-wise dissipation. However, retrieving information on mesophase structures is not enough for predicting macroscopic features of such materials. This is possible if mesophase modeling is coupled with appropriate finite element tools that – provided properties of pure components are given or can be in turn obtained by simulation – allow obtaining a realistic estimation of many nanocomposites features, if integrated with experimental/simulated morphological data.

In this work we presented the derivation and application of a multiscale molecular modeling procedure to characterize polymer-clay nanocomposite materials obtained from water solution intercalation. This approach relies on a step-by step message-passing technique from atomistic to mesoscale to finite element level; thus, computer simulations at all scales are completely integrated, and virtually no experimental data are necessary to characterize the systems, at least at a preliminary stage of the analysis.

The entire computational procedure has been applied to four PCN systems based on montmorillonite and poly(ethylene oxide) with different molecular weights as test materials, and their thermal and electrical macroscopical properties were predicted in excellent agreement with the available experimental data.

The global perspective of our current research in this field is the complete integration of all available simulation scales, in a hierarchical procedure, to provide an efficient and robust simulation protocol for the successful design of PCNs of industrial interest, and the prediction of their final performance. Although the proposed computational recipe could still be refined by considering, for instance, a more precise analysis of different morphologies, matrix morphology next to the single exfoliated platelet surface, to our knowledge this is the first, successful computational procedure applied to water-based PCNs able to predict, with a high degree of confidence, PCNs hierarchical structures and behavior, and to capture all the phenomena taking place on length scales that typically span 5 – 6 orders of magnitudes and time scales encompassing a dozen of orders of magnitude.

Chapter 4

Self-assembly control of nanoparticle mixtures in diblock copolymers

Mixing microphase-separating diblock copolymers and nanoparticles can lead to the self-assembly of organic/inorganic hybrid materials that are spatially organized on the nanometer scale. Controlling particle location and patterns within the polymeric matrix domains remains, however, an unmet need. Computer simulation of such systems constitutes an interesting challenge since an appropriate technique would require the capturing of both the formation of the diblock mesophases and the copolymer-particle and particle-particle interactions, which can affect the ultimate structure of the material. In this work we discuss the application of *Dissipative Particle Dynamics* (DPD) to the study of the distribution of nanoparticles in different copolymer matrices. The DPD parameters of the systems were calculated according to a multiscale modeling approach, i.e., from lower scales (atomistic) simulations. The results show that the positioning and ordering of the nanoparticles depend on several, different factors, including their covering type and volume fraction. Also, the geometrical features of the matrix are found to exert an influence on the particle location and pattern. The overall results provide molecular-level information for the rational, *a priori* design of new polymer-particle nanocomposites with *ad hoc*, tailored properties.

An excerpt of this work is published in Maly, M.; Posocco, P.; Pricl, S.; Fermeglia, M. *Ind. Eng. Chem. Res.* **2008**, *47*, 5023-5038.

4.1 Introduction

The combination of organic polymers and inorganic particles can lead to a composite material whose properties are more useful than those of either of the two individual components. As an example, if the particles are metals or semiconductors, the relevant composite can exhibit both the unique electrical, optical or magnetic properties of the inorganics, and the flexibility, low density and processability of the macromolecules. The

process of fabrication of these nanostructure composites is of paramount importance, as the miniaturization of devices for, say, electronic or biomedical applications is leading to feature sizes that are on the nanometer length scale. One of the most efficient route to prepare such systems is self-assembly, a process in which, in a cooperative fashion, the different components interact and promote the formation of the polymer-particle nanocomposite (PPN). Accordingly, one of the most intriguing – and challenging – scientific and technological goal is to identify critical thermodynamic variables upon which new, alternative paths for driving organic long chain molecules and inorganic nanoparticles to self-assembly into a PPN can be devised. Moreover, another critical step consists in being able to predict the morphology of these hybrid materials, as their macroscopic properties will ultimately depend on their microstructural features.

One way to assess the first challenge is to disperse particles of nanoscopic dimensions in diblock copolymer matrices.[1,2,3] From a theoretical standpoint, the macroscopic phase separation of a copolymer into domains of nanoscale dimensions can be harnessed to template the ordering of the particles in a plethora of structures, ranging from nano-planes to nano-wires or nano-spheres, resulting in materials that are spatially periodic on a length scale of the nanometer. Notwithstanding the variety of methods proposed, however, the real success of controlling the precise location of the nanoparticles within the polymeric domains remains limited.[4,5,6] Recently, a simple procedure to incorporate nanoparticles and control their location within different diblock copolymer domains by controlling the surface chemistry of the particles has been proposed by Chiu et al.[7] According to this idea, to localize particles within the *A*- or *B*- domain of an *A*-*B* diblock copolymer, the particles themselves are coated with either *A*- or *B*-type homopolymer, respectively. To concentrate the particles at the interfaces between the blocks, on the other hand, they should be coated with a mixture of *A*- and *B*-type homopolymers. Using this approach, therefore, the particles position can be fine tuned within either of the two copolymer domains, or at the interface between the blocks.

A further recent strategy for controlling the location of nanoparticles within block copolymer domains involves varying the surface coverage of the nanoparticles by an end-attached homopolymers *A* ligand.[8] As the areal chain density of the *A* chains (i.e. the number of polymer *A* ligands per each particle, divided by the average surface area of the particle) on the nanoparticle decreases, a sharp transition from the case where the particles are located in the A domain to the case where the particles are located at the *A*-*B* interface is observed. Tailoring the surface of the nanoparticles by modifying a single parameter (i.e. the areal chain density of ligand *A*) is then another simple approach for controlling their specific adsorption and localization.

The second, equally important challenge of microstructure prediction is quite ambitious, as the final morphology of these materials will depend on a number of factors, some strictly connected to the nature of the system (i.e., the chemistry and architecture of the blocks, the

[1] Thompson, R. B.; Ginzburg, V. V.; Matsen, M. W.; Balazs, A. C. *Science* **2001**, *292*, 2469-2472.
[2] Lee, J. Y.; Thompson, R. B.; Jasnow, D.; Balazs, A. C. *Macromolecules* **2002**, *35*, 4855-4858.
[3] Thompson, R. B.; Ginzburg, V. V.; Matsen, M. W.; Balazs, A. C. *Macromolecules* **2002**, *35*, 1060-1071.
[4] Lopes, W. A.; Jaeger, H. M. *Nature* **2001**, *414*, 735-738.
[5] Bockstaller, M. R.; Lapetnikov, Y.; Margel, S.; Thomas, E. L. *J. Am. Chem. Soc.* **2003**, *125*, 5276-5277.
[6] Zhang, C. L.; Xu, T.; Butterfield, D.; Mister, M. J.; Ryu, D. Y.; Emrick, T.; Russell, T. P. *Nano Lett.* **2005**, *5*, 357-361.
[7] a) Chiu, J. J.; Kim, B. J.; Kramer, E. J.; Pine, D. J. *J. Am. Chem. Soc.* **2005**, *127*, 5036-5037; b) Kim, B. J.; Bang, J., Hawker, C. J.; Chiu, J. J.; Pine, D. J.; Jang, S. G.; Yang, S.-M.; Kramer, E. J. *Langmuir*, **2007**, *23*, 12693-12703.
[8] a) Kim, B. J.; Bang, J.; Hawker, C. J.; Kramer, E. J. *Macromolecules* **2006**, *39*, 4108-4114; b) Kim, J. B.; Fredrickson, G. H.; Hawker, C. J.; Kramer E. J. *Langmuir* **2007**, *23*2, 7804-7809; c) Kim, J. B.; Fredrickson, G. H.; Kramer E. J. *Macromolecules* **2008**, *4*1, 436-447; d) Kim, J. B.; Fredrickson, G. H.; Bang, J.; Hawker, C. J.; Kramer E. J. *Macromolecules* **2009**, *4*2, 6193-6201.

volume fraction of the nanoparticles, and the strength and type of interactions between the system components, just to name a few), and others bound to process conditions (e.g., temperature or shear). To date, there are few theories to pinpoint the critical parameters or to predict the thermodynamic stability of a PPN system,[9,10,11] substantially forcing synthetic chemists to synthesize all possible mixtures in order to isolate the desired system. Despite the tremendous advances made in the modeling of structural, thermal, mechanical and transport properties of materials at the macroscopic level (finite element (FE) analysis of complicated structures), there remains a tremendous uncertainty about how to predict many critical properties related to performance. The fundamental problem here is that these properties depend on the atomic level of interactions and chemistry, dealing with the electronic and atomic level of description and at a length/time scale of nanometers and nanoseconds. The material designer, however, needs answers from macroscopical modeling (the finite element paradigm) of components having scales of centimeters and milliseconds, if not larger. To substantially advance the ability to design useful high performance materials, it is then essential that we insert the chemistry into the mesoscopic (MS) and macroscopic (FE) modeling. Currently, atomistic level simulations such as molecular dynamics or Monte Carlo techniques allows to predict the structure and properties for systems of considerably large number of atoms and time scales of the order of microseconds. Although this can lead to many relevant results in material design, many critical issues in materials design still require time and length scales far too large for practical MD/MC simulations. Therefore, we need to develop methods treating the mesoscale in between the atomistic length and time scales of MD/MC and the macroscopic length and time scales (microns to millimeters, and microseconds to seconds) pertaining to FE analysis. This linking through the mesoscale, in which we can describe a system microstructure, is probably the greatest challenge to developing reliable first principles methods for practical and effective material design. Indeed, only by establishing this connection from microscale to mesoscale it is possible to build first principles methods for describing the properties of new materials and composites.

One of our major aims is to reach the domain of materials science and engineering by building from fundamental principles of physics and chemistry. Thus, for fundamental predictions to play a direct role in materials innovation and design, it is essential to fill the micro-meso gap. The problem here is that the current methods of coarsening the description from atomistic to mesoscale (as well as MS to FE) are not as obvious as they are from going to the quantum mechanics (QM) to the atomistic level, being strongly system-dependent and, hence, hardly generalizable. Indeed, it is quite clear that the strategy for polymers should be rather different from that adopted for metals, and again different from that conceivable for ceramic systems. Given these concepts, it is than necessary to carry out calculations for realistic time scales fast enough to be useful in design. This requires developing techniques useful to design engineers, by incorporating the methods and results of the lower scales (e.g., MD) to mesoscale simulations.

In this work, we developed a hierarchical procedure for bridging the gap between atomistic and mesoscopic simulation for polymer-particle nanocomposite design. The *Dissipative Particle Dynamics* (DPD)[12] is adopted as the mesoscopic simulation technique, and the interaction parameters of the mesoscopic model are estimated by performing lower

[9] Balazs, A. C.; Singh, C.; Zhulina, E.; Lyatskaya, Y. *Acc. Chem. Res.* **1999**, *32*, 651-657.
[10] Kuznetsov, D.; Balazs, A. C. *J. Chem. Phys.* **2000**, *112*, 4365-4375.
[11] Fornes, T.D.; Paul, D.R. *Polymer* **2003**, *44*, 4993-5013.
[12] a) Hoogerbruge, P. J.; Koelman, J. M. V. A. *Europhys. Lett.* **1992**, *18*, 155–160; b) Koelman, J. M. V.A.; Hoogerbruge, P. J. *Europhys. Lett.* **1993**, *21*, 363.

scale (i.e., atomistic molecular dynamics (MD)) simulations. To test and validate the proposed procedure, we decided to consider the same system used by Kim et al.,[7,8] employing a diblock copolymer poly(styrene-b-2 vinyl pyridine) (PS-PVP) and Au nanoparticles covered either by PS (or PVP) or a mixture of PS and PVP, and considering the influence on nanodispersion of different polymer microstructure morphologies (lamellar, hexagonal, spherical).

4.2 Models and methods

4.2.1 Determination of DPD interaction a_{ij} parameters

There is a close relationship between the soft repulsive sphere model employed in DPD and the well-known Flory-Huggins model for polymer interactions.[13] This relationship allows us to translate the repulsion parameters a_{ij} into the more familiar Flory-Huggins interaction parameter χ_{ij}.

The first step necessary for the determination of the DPD input interaction parameters, a_{AB}, generally consists in defining the DPD bead volume, thus implicitly defining the characteristic length of the system (r_c). As illustrated in Chapter 2, the interaction range r_c sets the basic length-scale of the system; in other terms, r_c is defined as the side of a cube containing an average number of ρ beads. Therefore:

$$r_c = \left(\rho\, V_{DPD}\right)^{1/3} \tag{4.1}$$

where V_{DPD} is the volume of a given DPD bead. Thus, even in a heterogeneous system consisting of several different species, such as PPNs, a basic DPD assumption is that all bead-types (each representing a single species) are of the same volume V_{DPD}.

The basic strategy to calculate V_{DPD} consists in mapping the real polymer chain onto a chain consisting of Kuhn's segments. Consequently, each DPD bead represents a statistically correlated unit or Kuhn segment of the polymer. A DPD chain should, therefore, be made up of n_{DPD} beads, where:

$$n_{DPD} = \frac{N_{mon}}{C_\infty} \tag{4.2}$$

where N_{mon} is the degree of polymerization of the molecular chain, and C_∞ its characteristic ratio, a parameter representing the stiffness of a chain. When a flexible macromolecules is modeled as a Gaussian chain, however, C_∞ represents also the number of monomers making up a Kuhn segment (i.e., contained in a single DPD bead). Therefore, the bead volume V_{DPD} can be simply obtained multiplying the characteristic ratio C_∞ for the monomer volume V_{mon}.

N_{mon} can be obtained knowing the molecular weight of the polymer; C_∞ is an intrinsic property of the chain, and was estimated in this work using a molecular dynamics procedure based on the Rotational Isomeric State (RIS) method highlighted in Figure 4.1.

[13] Groot, R. D.; Warren, P. B. *J. Chem. Phys.* **1997**, *107*, 4423-4436.

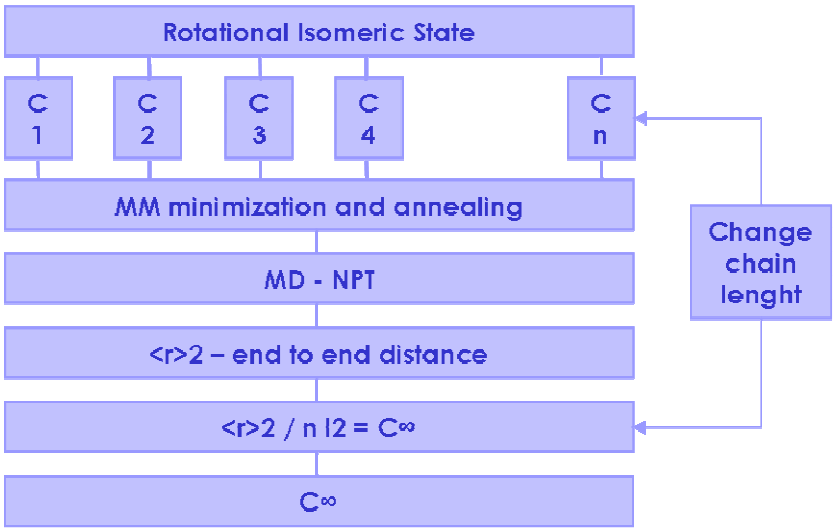

Figure 4.1. Computational procedure to estimate the characteristic ratio C_∞.

Polymer	V_{mol} [a] (cm^3/mol)	V_{mon} [b] (Å^3)	C_∞ [c] (-)	l [d] (Å)	δ [e] (J/cm^3)$^{0.5}$	n_{mon} [f] (-)	V_{DPD} [g] (Å^3)
PS (*A*-type bead)	96.98	161.03	9.90	2.55	19.80	9.90	1610
PVP (*B*-type bead)	92.44	153.50	9.90	2.40	22.12	9.90	1535

Table 4.1. Characteristics of the PS-PVP copolymer building blocks. [a]Monomer molar volume; [b]monomer volume; [c]characteristic ratio; [d]monomer length; [e]solubility parameter, [f]number of monomers of type A (or B) in each DPD bead; [g]volume of one DPD bead.

According to our recipe, a given number of different chain configurations at a fixed N_{mon} – say C_1, C_2, C_3 – are generated via RIS. Each C_i then undergoes independent cycles of molecular mechanics minimization and simulated annealing procedures[14] before running a productive *NVT* MD. After the simulation is done, the end-to-end distance of the chains is estimated, and the C_∞ is calculated. The procedure is repeated, for each configuration at different chain length N_{mon}, until a constant value of C_∞ is obtained. The final value of C_∞ is estimated by averaging over all the configurations considered. The values of the calculated monomer molar volume V_{mol}, monomer volume V_{mon}, characteristic ratio C_∞, and monomer length l are listed in Table 4.1.

Having set the values, the successive, necessary step is the value of the Flory-Huggins interaction parameter χ_{AB}, from which a_{AB} can be determined using the following relationship, as proposed by Glotzer and her group:[15]

$$a_{AB} = a_{AA} + 3.27\left(1 + \frac{3.9}{N_{DPD}^{0.51}}\right)\chi_{AB} \qquad (4.3)$$

where N_{DPD} is the total chain length of the mesoscale model of the *A*-*B* copolymer.

χ_{AB} is defined in terms of solubility parameters of the A and B components as:

[14] Scocchi, G.; Posocco, P.; Fermeglia, M.; Pricl, S. *J. Phys. Chem. B* **2007**, *111*, 2143-2151.
[15] Horsch, M. A.; Zhang, Z., Iacovella, C. R.; Glotzer, S. C. *J. Chem Phys.* **2004**, *121*, 11455-11462.

$$\chi_{AB} = \frac{V_{mon}}{k_B T}(\delta_A - \delta_B)^2 \tag{4.4}$$

where V_{mon} is the volume of one polymer segment corresponding to the bead in DPD, k_B the Boltzmann constant, T the temperature, and δ_i is the solubility parameter of the ith component, which is related to the cohesive energy densities e_{coh} by:

$$\delta = \sqrt{\frac{E_{coh}}{V}} = \sqrt{e_{coh}} \tag{4.5}$$

The solubility parameters for the *A* and *B* homopolymers were obtained from atomistic MD simulations following a validated procedure of our group.[16,17] Briefly, the method comprises the construction of amorphous fluid structures of each homopolymer at experimental density (in the absence of such information, isobaric-isothermal (*NPT*) MD simulations can be performed to equilibrate the system density). Three-dimensional, periodic cells are then generated and MD simulations in the canonical ensemble (*NVT*) are then performed to evolve each system and generate statistically independent structures.

According to Equation 4.5, the solubility parameter δ is defined as the square root of the cohesive energy density; e_{coh}, in turn, is defined as the ratio of the cohesive energy E_{coh} and the molar volume V at a given temperature. Physically, E_{coh} can be seen as the increase in internal energy per mole of substance if all intermolecular forces are eliminated. Since in our simulated systems, each chain is surrounded by other chains that are simply displaced images of the chain itself; accordingly, the cohesive energy is the energy of interactions between these images. The values of E_{coh} can then be simply obtained from simulation by calculating the difference between the non-bonded energy of the periodic structure, $E_{nb\_periodic}$ and the corresponding value for an isolated parent chain *in vacuum* $E_{nb\_isolated}$:

$$E_{coh} = E^{nb}_{isolated} - E^{nb}_{periodic} \tag{4.6}$$

The obtained values of the solubility parameters are listed in Table 4.1.

In contrast to pure diblock copolymer systems, where mapping results from the correspondence between DPD and Flory-Huggins type polymer models and solubility parameters, it is not a straightforward task to map solid particles-diblock interactions.

In this work we decided to obtain these mesoscale interaction parameters from atomistic molecular dynamics binding energies, applying the approach described in details in Chapter 2.

As far as the Au model is concerned, starting from relevant crystallographic coordinates,[18] we built the unit cell using the *Crystal Builder* module of *Materials Studio* (v. 4.4 Accelrys, San Diego, CA).

As our major goal is to estimate the interaction energies between all system elements accurately, and since these quantities are highly sensitive to the nonbonded components of the force field (FF) employed, we decided to adopt here an *ad hoc* modified *Compass* FF, developed recently by Heinz and coworkers.[19]

[16] Fermeglia, M.; Pricl, S. *AIChE J.* **1999**, *45*, 2619-2627.
[17] Pricl, S.; Fermeglia, M. *Fluid Phase Eq.* **1999**, *166*, 21-37.
[18] *CRC Handbook of Chemistry and Physics*; 79th ed.; Lide, D. R., ed.; CRC Press: Boca-Raton, 1998.
[19] Heinz, H.; Vaia, R. A.; Farmer, B. L.; Naik, R. R. *J. Phys. Chem. C* **2008**, *112*, 17281-17290.

As demonstrated by the authors,[19] this accurately derived FF is able to describe the interfacial thermodynamics properties with a deviation from experiment amounting only to 10% in comparison to 100% with earlier models, which constitutes a fundamental step toward quantitative modeling of sensitive interfacial processes involving metal surfaces.

Accordingly, the resulting lattice of our Au model is face centered cubic (fcc) and characterized by the following lattice parameters: $a=b=c=$ 4.0785 Å, and $\alpha=\beta=\gamma=90°$, in excellent agreement with the model validated by Heinz.[19]

Super cells of approximately 2 x 2 x 0.8 nm^3 size (5 x 5 x 2 unit cells) were employed in all MD simulations.

The procedure for the polymer (both PVP and PS) consisted in building and optimizing the polymer constitutive unit using *Compass* FF, which was then polymerized to the desired degree of polymerization. In order to obtain a reasonable sampling of the polymer conformational space, we built 10 different configurations of PVP and PS chains, using *Amorphous Builder* module of *Materials Studio*, which uses a version of the RIS method for generating polymer chain configurations. Each polymeric structure was then relaxed and subjected to a combined molecular mechanics/molecular dynamics simulated annealing (MDSA) protocol.[20]

Resorting to atomistic MD simulations in the *NVT* ensemble allows the retrieval of important information on the interaction and binding energy values between the different components of a PPN system.[20,21,22,23,24,25,26] The technique basically consists in simulating the interface between the gold surface and copolymer by building a cell that is "stretched" along the *c*-direction (up to 150 Å); in this way, even if the model is still 3-D periodic, there are no interactions between the periodic images in the *c* direction, ultimately resulting in a pseudo 2-D periodic system,[27] from which the binding energies between all system components can be calculated.

According to our approach, we created a cell of 150 Å in height and copied each of the 10 configurations of PVP or PS in 10 identical cells, thus obtaining 10 different model systems for each single polymer system (20 systems in total). The NVT molecular dynamics were performed with *Materials Studio Discover* module. Each simulation was run at 298.15 K for 500 ps, applying the Ewald summation method for treating Coulomb interactions; an integration step of 1 fs and Nosé thermostat (Q ratio = 1) were also adopted. The energetic analysis was conducted only on the parts of the trajectory with steady state behavior and mediated over the 10 configurations for each polymer.

The procedure used to calculate the interaction energies and, hence, the binding energy values E_{bind} between all system components, is well estabilished.[20a)-d),22]

For the binding energy E_{bind} calculations, we started from the concept that the binding energy of a system composed, for instance, of poly(styrene) (PS) and gold (Au), may be calculated from the following equation

---

[20] a) Fermeglia, M.; Ferrone, M.; Pricl, S. *Fluid Phase Eq.* **2003**, *212*, 315-329; b) Toth, R.; Coslanich, A.; Ferrone, M.; Fermeglia, M.; Pricl, S.; Miertus, S.; Chiellini, E. *Polymer* **2004**, *45*, 8075–8083; c) Scocchi, G.; Posocco, P.; Danani, A.; Pricl, S.; Fermeglia, M. *Fluid Phase Eq.* **2007**, *261*, 366-374; d) Fermeglia, M.; Ferrone, M.; Pricl, S. *Mol. Simul.* **2004**, *30*, 289-300; e) Scocchi, G.; Posocco, P.; Handgraaf, J.-W.; Fraaije, J. G. E. M.; Fermeglia, M.; Pricl, S. *Chem. Eur. J.* **2009**, *15*, 7586-7592.

[21] a) Kasemägi, H.; Aabloo, A.; Klintenberg, M. K.; Thomas J. O. *Solid State Ion.* **2004**, *168*, 249–254; b) Kasemägi, H.; Klintenberg, M. K.; Aabloo, A.; Thomas J. O. *Solid State Ion.* **2002**, *147*, 367–375.

[22] Toth, R.; Ferrone, M.; Miertus, S.; Chiellini, E.; Fermeglia, M.; Pricl, S. *Biomacromolecules*, **2006**, *7*, 1714–1719.

[23] Tanaka, G.; Goettler, L. A. *Polymer* **2002**, *43*, 541-553.

[24] Gardebien, F.; Bredas, J.-L.; Lazzaroni, R. *J. Phys. Chem. B* **2005**, *109*, 12287–12296.

[25] Katti, K. S.; Sikdar, D.; Katti D. R.; Ghosh, P.; Verma, D. *Polymer* **2006**, *47*, 403-414.

[26] Paul, D. R.; Zeng, Q. H.; Yu, A. B.; Lu, G. Q. *J. Colloid Interface Sci.* **2005**, *292*, 462-468.

[27] Misra, S.; Feming, P. D. III; Mattice, W. L.; *J. Comput.-Aided Mater. Des.* **1995**, *2*, 101-112.

$$E_{bind}(PS/Au) = E_{PS} + E_{Au} - E_{PS/Au} \quad (4.7)$$

where the first two terms represent the energy of poly(styrene) and gold, consisting of both valence and nonbonded energy terms, and the last term is the interaction energy between the two components, made up of nonbonded terms only. By definition, the binding energy E_{bind} is the negative of interaction energy. Next, we deleted the PS molecules, leaving the gold surface alone, and thus calculated the energy of the slab (E_{Au}). Similarly, we deleted the metal layer from the PS-Au system, and calculated E_{PS}.

The remaining binding energy E_{bind}(PVP/Au) can be computed in an utterly analogous fashion from the corresponding energy components.

The detailed procedure for obtaining the mesoscale interaction parameters from atomistic molecular dynamics binding energies is reported in Chapter 2.

The length of the DPD copolymer chain corresponds to N_{DPD} = 14. The bead volume V_{DPD} is taken as the average bead volume of PS/PVP blocks and corresponds to 1573 Å^3; the cutoff radius r_c is calculated from Equation 4.1 using this mean value and is 16.8 Å; the χ_{AB} parameter is derived from Equation 4.4 and found to be equal to χ_{AB}=2.057.

Each DPD gold nanoparticle was considered to have an icosahedral structure, devised as being constituted by a central bead, surrounded by 12 other beads, one of each vertex of the icosahedron (see Figure 4.2). Nanoparticle shape was preserved by employing a high value of the spring constant (i.e., K = 200). In fact, the shape of the icosahedral nanoparticles was monitored during simulations by the radial distribution function between the central and surface beads. It was found that K = 200 was high enough to guarantee icosahedral particle geometry during each simulation. For comparison, the value of the spring constant used for the polymer chain was 4.

The radius of the icosahedron was set equal to $R_i = 0.72 \times r_c$; the equilibrium distance for the bond spring between the surface beads was set equal to r_0=0.76r_c, for the bond spring between the central and surface beads equal to r_0=0.72r_c, and an equilibrium value of r_o=0 was employed for the polymer bonds.

Adapting the recipe described in Chapter 2 to the present system, we set the bead-bead interaction parameter for poly(styrene)-poly(styrene) interaction equal to a_{PSPS}=25.00 according to an appropriate value for a density value of ρ=3.[13] The gold-gold interaction parameter was set to a lower value (i.e. a_{NN}=20.00), in order to mimic the aggregation tendency between bare nanoparticles. Once these two parameters were set, and their values associate with the corresponding values of the self- and mixed rescaled DPD energies, all the remaining bead-bead interaction parameter for the DPD simulation could be easily obtained, starting from the atomistic binding energies (see Chapter 2). The entire set of mesoscale interaction parameters employed in this work is summarized in Table 4.2.

It's known from literature[8a),28] the preferential interaction between gold and PVP, whose nitrogen lone-pair electrons favorably interact with Au atoms of the nanoparticle. This tendency is well reproduced in a lower mesoscale interaction parameter a_{PVPAu} with respect to a_{PSAu} directly derived from lower scale atomistic simulation.

[28] a) Kunz, M. S.; Shull, K. R.; Kellock, A. J. *J. Colloid Interface Sci.* **1993**, *156*, 240-249; b) Ho, R.-H.; Lin, T.; Jhong, M.-R.; Chung, T.-M.; Ko, B.-T.; Chen, Y.-C. *Macromolecules* **2005**, *38*, 8607-8610.

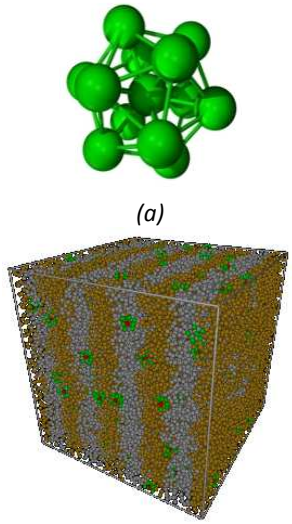

(a)

(b)

Figure 4.2. (a) Geometry and definition of the icosahedral nanoparticles considered in this work: a central core DPD bead N (Au) is surrounded by other 12 DPD beads of type *A* (PS), or *B* (PVP), or *N* (Au), depending of the covering type considered, each on each vertex of the icosahedron. (b) Equilibrated snapshot of a model system with lamellar morphology. The polymer matrix DPD particles of type *A* (PS-blocks) are coloured gold, those of type *B* (PVP-blocks) are depicted in white. In each nanoparticle, the central DPD bead is coloured red, whilst the remaining 12 DPD particles, making up the surface of the real icosahedral nanoparticles, are green.

a_{ij}	*PS (A)*	*PVP (B)*	*Au (N)*
PS (A)	25.00		
PVP (B)	38.55	24.11	
Au (N)	29.76	26.23	20.00

Table 4.2. DPD bead-bead interaction parameters used in this work.

4.2.2 DPD simulation details

The theoretical understanding of the factors that lead to a successful self-assembly of nanocomposites is relatively limited. Hence, it is of paramount importance to develop a general framework for gaining a better insight into the thermodynamics aspect of nanoparticles in ordered microphase-separated domains and for predicting how the nanoparticles will organize into these ordered structures.

In this contribution, we explored the effect of particle loading on the phase behavior of block copolymer/nanoparticles composites. Three different kind of morphologies of the polymeric matrix were considered: lamellar (and perforated lamellar), hexagonal and micellar. Nanoparticles were considered dispersed in the system at a volume fraction in the range of 0.03-0.1.

According to the phase diagram for phase segregation of diblock copolymers,[29,30] to simulate a lamellar morphology the relative amount of the two blocks should be

[29] Groot, R. D.; Madden, T. J. *J. Chem. Phys*. **1998**, *108*, 8713-8724.
[30] Lisal M., Brennan J. K. *Langmuir* **2007**, *23*, 4808-4818.

approximately the same (i.e., 50/50); in our DPD terms, this corresponds to a chain architecture of A_7B_7. According to several, different trials, this DPD chain architecture led to an equilibrium lamellar morphology with all lamellae aligned parallel to one side of the simulation box in the most reasonable CPU time and without the application of shear.[30] The achievement of such condition was necessary to derive accurate 2-dimensional density profiles along the direction perpendicular to the lamellae, which yield information about both nanoparticles and polymeric matrix density distributions.

Perforated lamellae were obtained employing a molecular architecture of A_5B_9, and spherical micelles with a chain of architecture A_2B_{12}.

On the other hand, to obtain a hexagonal matrix morphology, the corresponding DPD architecture should be A_4B_{10}. Again, this DPD chain architecture is the results of a number of different attempts, and represents the best option to obtain an equilibrium hexagonal morphology, having all cylinders aligned along one side of the simulation box, in acceptable CPU time.

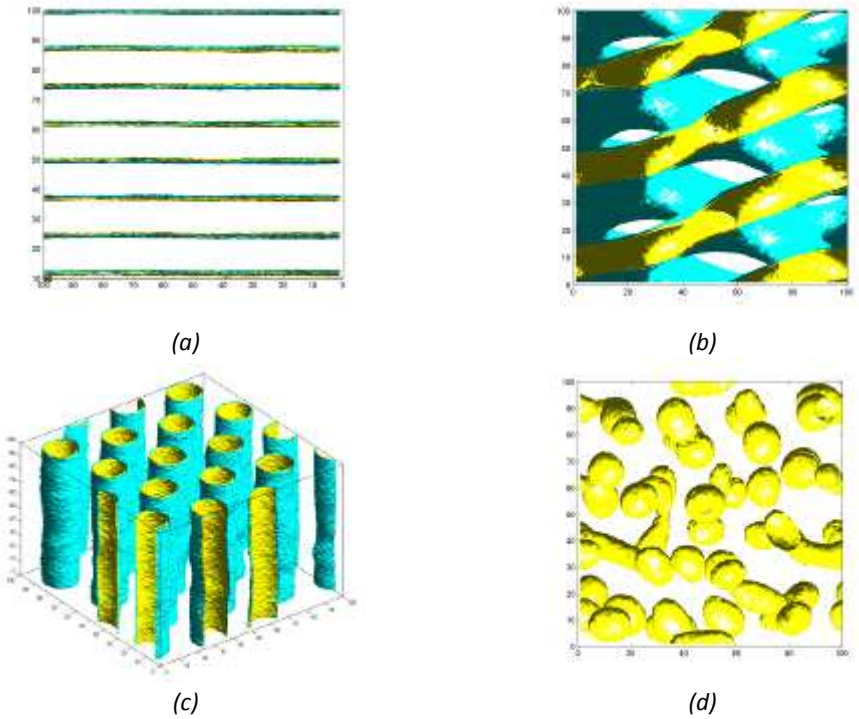

Figure 4.3. Isosurface visualization of the four matrices without nanoparticles. (a) Lamellar morphology simulated employing a model chain architecture of A_7B_7; (b) Perforated lamellar morphology simulated employing a model chain architecture of A_5B_9; (c) Hexagonal morphology simulated employing a model chain architecture of A_4B_{10}; (d) Micellar morphology simulated employing a model chain architecture of A_2B_{12}. The polymer matrix DPD particles of type *A* (PS) are colored yellow; those of type *B* (PVP) are depicted in cyan.

Using the DPD interaction parameter a_{PSPVP} = 38.55, as resulting from the mapping procedure described above, corresponding to χ_{AB} = 2.057 and, thus, to $\chi_{AB} \times N_{DPD}$ = 28.80, the resultant hexagonal and spherical morphology were imperfect, as it could be expected by examining the experimental phase diagram for similar systems.[29,31] Accordingly, it was

[31] Groot, R. D.; Madden, T. J.; Tildesley, D. J. *J. Chem. Phys*. **1999**, *110*, 9739-9749.

necessary to use a higher value of the DPD repulsive parameter which, for a fixed system chemistry (PS-PVP), and a fixed number of DPD beads for each copolymer chain (N_{DPD} = 14), corresponds to decreasing the system temperature or, equivalently, increasing the Flory-Huggins parameter χ_{AB} (and, consequently, $\chi_{AB}\times N_{DPD}$). Further, the nanoparticles also are intuitively expected to exert an influence on the matrix topology. Accordingly, the new $\chi_{AB}\times N_{DPD}$ value should be high enough to guarantee the persistence of a good hexagonal/spherical structure of the matrix. Different trials led us to the choice of the final value of the repulsive DPD parameter a_{PSPVP} = 53.48, which correspond to a χ_{AB} = 4 or, equivalently, to a temperature T = 153K. This only implies that, with such short PS-PVP polymer chains, a PPN nanocomposite with a hexagonal or spherical morphology cannot be achieved at room temperature. In other words, it is $\chi_{AB}\times N_{DPD}$ the key parameter for these simulations, not just χ_{AB}. In fact, should we have used the polymer chain architecture A_6B_{14} in place of A_4B_{10}, the relevant $\chi_{AB}\times N_{DPD}$ value would have been equal to 41.15, corresponding to T = 298 K, which is almost the same value for our A_4B_{10}chain architecture at 153K.

A recent approach in controlling the arrangement of nanoparticles in diblock copolymers template is the end-attaching of short homopolymers ligands to the nanoparticles surface.[7,8] The tailoring of the surface chemistry can be achieved using as mixture of homopolymers of both blocks or chains of one single homopolymer type at different grafting density. This approach exploits enthalpic interaction between the block copolymer and functionalized nanoparticle surface to achieve precise particle placement. Therefore, an understanding of the interaction between the particle surface, ligands on the surface, and the polymer matrix is critical for developing standard rules for controlling 3-dimensional structure of particle-organic hybrid nanomaterials. To begin to address this challenge, a systematic investigation of the effect of surface coverage was conducted in this work using a model system with the following characteristics.

The effect of different covering type of the icosahedral nanoparticles was studied by considering the following surface chemistry: *A*, A_6B_6(*h*), A_6B_6(*r*), A_1B_{11}, A_3B_9, *B,* where homopolymer chains of PS (*A*) or PVP(*B*) are supposed to completely shield the Au core from the interactions with the external environment (*full coverage*), or A_1N_{11}, A_2N_{10}, A_3N_9, A_4N_8, where only type *A* homopolymer chains are chemically attached onto the surface at different grafting density (*partial coverage*) and N bead is representing the bare Au surface. Different areal chain densities were modeled varying the number of *A* bead type on the icosahedron surface, i.e. n=1, 2, 3, 4, thus representing an increasing content of polymer in the shell around the Au core. The remaining beads represent bare Au particle surface exposed to the matrix interactions.

According to this notation, for instance, a surface architecture A_3B_9 identifies a nanoparticle covering in which three beads on the icosahedron vertices are of type *A* and the remaining nine are of type *B*, whereas, the letters *h* and *r* stand for homogeneous and random distribution of the *A* and *B* type beads, respectively.

The DPD simulation box length was set equal to $L = 25\times r_c$. The simulation of the initial structure was created starting from a random space distribution of polymer chains and nanoparticles. 2×10^5 DPD steps (integration time step Δt = 0.03) were used to equilibrate the system and a total of more than 6×10^5 DPD time steps were used to reach the final structure.

All simulations were performed at the University of Trieste on the Tartaglia cluster of 60 CPUs, 120 GB RAM, 2 TB disk space with a computing power of 245 Gflops (benchmark High-Performance Linpack in HPCC). The commercial software *Materials Studio* (v. 4.4, Accelrys,

San Diego, CA, USA) was used for both molecular mechanics (MM) and molecular dynamics (MD) simulations. An in house developed version of the DPD code (M. Maly, unpublished) was employed for the mesoscopic calculations.

4.3 Results and discussion

4.3.1 Lamellar matrix morphology in presence of fully covered nanoparticles

As the first step to study the self-assembly of nanoparticles in diblock copolymers, we considered the case of a lamellar matrix morphology and nanoparticles compatible only with block *A* or *B*, alternatively. The volume fraction of the nanoparticles VF embedded in the matrix is set equal to 0.05. The particles exhibit a remarkable tendency to segregate to the center of the corresponding domain, in perfect agreement with the corresponding experimental evidences.[7a),b)] Figure 4.4 (a) illustrates the DPD bead density profiles along a direction perpendicular to the lamellar orientation, from which it is clearly seen that, for icosahedral particles covered by *A*-type beads the particle concentration is higher at the center of the compatible (PS) domain. Analogously, the *B*-type covering beads distribute throughout the corresponding compatible (PVP) domain, again with a marked tendency for concentrating at the center of the preferred domain. Figure 4.4 (b) shows the two-dimensional density distribution of the particle central (*core*) bead *N*. Figure 4.4 (d) and (e) reports the three-dimensional density matrices for *A*- and *B*-type polymer matrix beads, respectively, from which we can clearly see how nanoparticles can influence the thickness of the lamellae. *A*-type lamellae are wider, and characterized by a lower density value in their centers due to the presence of the *A*-type covering nanoparticle beads. On the other hand, *B*-type lamellae are compressed the same reason. Figure 4.4 (c) finally shows a detailed view of a section perpendicular to the lamellar orientation of the same system.

Figures 4.4 illustrate clearly the self-assembled lamellar phase where particles gather in the center of the *A*-block and form nanosheets. This structure is in good agreement with the "center-filled lamellar" (CFL) predicted by Balazs et al. using a SCFT/DFT combined model.[32] CFL phase can be easily recognized by the deficit of *A* monomers in the middle of the *A* region due to the presence of nanoparticles in the center of the domain.

Intuitively, the driving forces for particle location and assembly stem from the repulsion between the particles themselves and the incompatible block component. By segregating into the corresponding domain of the block copolymer, the particles covered by a compatible, small homopolymer lower their enthalpy. Moreover, by concentrating at the center of the likely domain, where the polymer chain ends are located, the chains can accommodate particles by only moving apart, rather than undergoing substantial deformations. The particle localization in any case ultimately results in a decrease of their translational entropy; however, an even more substantial penalty resulting from large chain stretching and deformation due to particle distribution along the entire domain is avoided.

[32] Thompson, R. B.; Ginzburg, V. V.; Matsen, M. W.; Balazs, A. C. *Macromolecules* **2002**, *35*, 1060-1071.

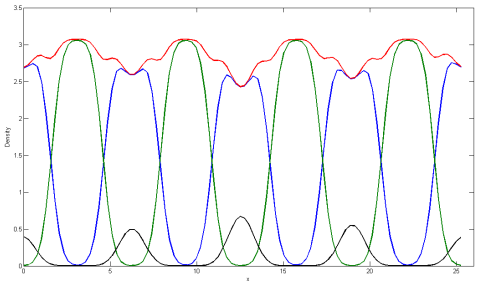

(a)

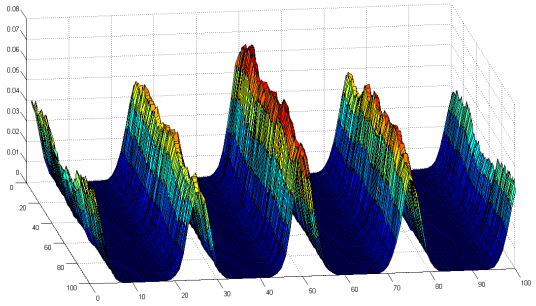

(b)

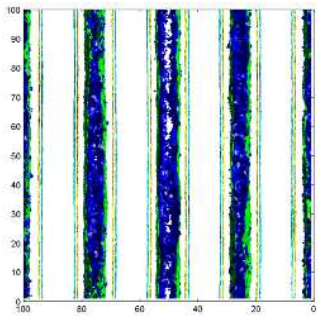

(c)

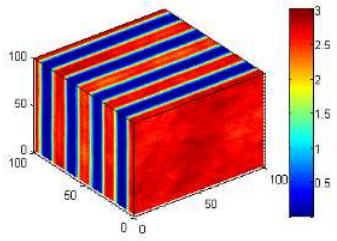

(d)

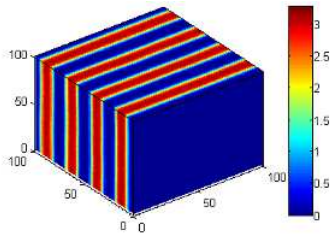

(e)

Figure 4.4. (a) One dimensional bead density profiles of the simulated PPN with lamellar morphology and particles covered by *A*-type covering only in direction perpendicular to the lamellae. Color code: blue: *A*-type polymer matrix beads; green: *B*-type polymer matrix beads; red: total *A*- and *B*-type polymer matrix beads; black: total icosahedral nanoparticle beads. (b) Central particle bead *N* density distribution along a direction perpendicular to the lamellar orientation for the same system (color code: blue, minimum, red maximum density value). (c) Detailed view of a section perpendicular to the lamellar orientation of the same system. The polymer matrix *A*- type beads are colored yellow whilst those of *B*-type are cyan. All nanoparticles beads are colored green, except the central particles of the icosahedrons *N* which are highlighted in blue. Three-dimensional bead density of (d) *A*-type and (e) *B*-type polymer matrix beads.

When the nanoparticles are covered by an equal mixture of *A*- and *B*-type homogeneous covering ($A_6B_6(h)$), and mixed in the copolymer matrix at VF=0.05, an opposite trend is revealed: the nanoparticles manifest a tendency to locate at the interfaces between the *A*-*B* blocks, as well evidenced in Figure 4.5 (a) and (b) (compare with Figure 4.4). Figure 4.5 (c) and (d) shows a detailed view of a section perpendicular to the lamellar orientation of the same system and a snapshot of the simulated PPN structure, respectively.

When the particle surface is roughly neutral with respect to the blocks, nanoparticles tend to be found at the block copolymer interface since displacing them into either block involves a free energy penalty consisting of the interfacial energy of the block copolymer times the projected area of the adsorbed particle.

Moreover, the distribution of the covering type on the particle surface does not significantly influence this behavior, as nicely evidenced by the results obtained for particles with the same covering but with a random pattern, i.e., the $A_6B_6(r)$ system reported in Figure 4.6. Regardless of how the *A* and *B* homopolymer chains are distributed on the Au surface, the surface remains neutral in composition and nanoparticles are expected to be located along the interface.

Intuitively, when only a small amount of the covering is of one type (say *A* or *B*), and the remaining of the other type (*B* or *A*), a particle distribution utterly similar to the case of full *B* (*A*) coverage is obtained. This is illustrated in Figure 4.7 for the system A_1B_{11} (VF=0.05). Indeed, the differences between these two cases are mainly quantitative, and concern the heights and thickness of the nanoparticle density peaks. In the case of *A*-type covering only, the peaks are higher and thinner than in the case of the A_1B_{11} system, revealing a greater ordering and better positioning of the nanoparticles in the center of the corresponding compatible domain in the single-type particle covering. This can be fully appreciated by comparing the 2D density profiles of the particle central bead *N* in Figure 4.7 (b) with those of Figure 4.4 (b).

The final case of covering considered, A_3B_9 (VF=0.05), shows a 'hybrid' behavior, as it could be intuitively expected. In fact, Figures 4.8 reveals that, although most of the particles are still located in the corresponding compatible domain (the *B*-block in this case), the maxima of the nanoparticle density are located at the block interfaces. Clearly, gold particles coated with a mixture of PS and PVP ligands are less selective for the PS and PVP domains and tend to be directed toward the interface.

It is noteworthy that the lamellar morphology remains unchanged at the considered nanoparticle volume fraction (VF=0.05) despite the relative amount of *A* and *B* homopolymer chains chemically attached onto the Au surface.

These results are in very good agreement with the matrix morphology and nanoparticle distributions experimentally predicted by Kim et al. on comparable PS-PVP /Au hybrid composites.[7a)-b)]

4.3.2 Hexagonal matrix morphology in presence of fully covered nanoparticles

In order to analyze the influence of the matrix morphology on the nanoparticles self-assembly, we then selected to study also a case in which the polymer matrix microstructure was characterized by a hexagonal geometry.

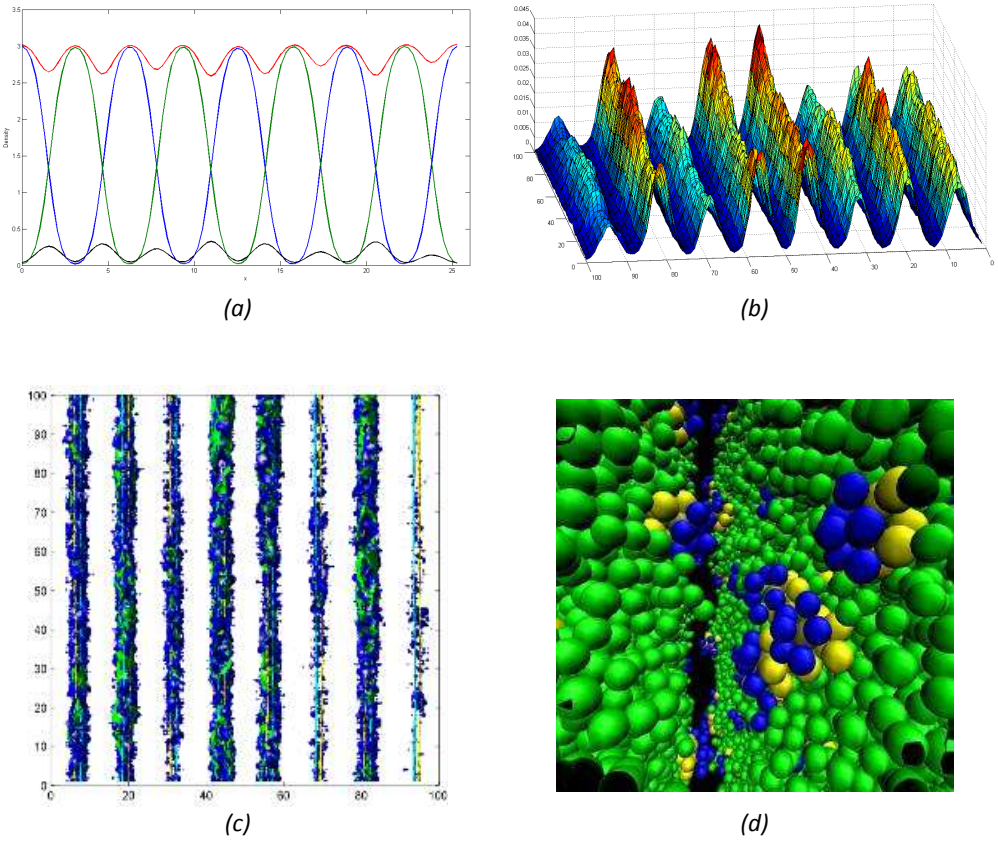

Figure 4.5. (a) One dimensional bead density profiles of the simulated PPN with lamellar morphology and particles covered by a 50-50 *A*-*B* type covering with an homogeneous distribution (A_6B_6(h)) along a direction perpendicular to the lamellae. Color code: blue: *A*-type polymer matrix beads; green: *B*-type polymer matrix beads; red: total *A*- and *B*-type polymer matrix beads; black: total icosahedral nanoparticle beads. (b) Central particle bead *N* density distribution along a direction perpendicular to the lamellar orientation for the same system (color code: blue, minimum, red maximum density value). (c) Detailed view of a section perpendicular to the lamellar orientation of the same system. The polymer matrix *A*-bead type are colored yellow, whilst those of *B*-type are cyan. All nanoparticles beads are colored green; the central particles of the icosahedrons *N* are highlighted in blue. (d) Snapshot of the simulated PPN structure. Matrix *A*-type bead (PS) are colored green, whilst particle covering type *A* (PS) and *B* (PVP) are colored yellow and blue, respectively. Matrix *B*-type beads are omitted for clarity.

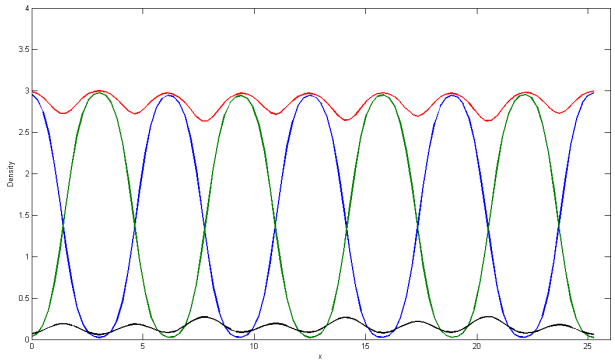

(a)

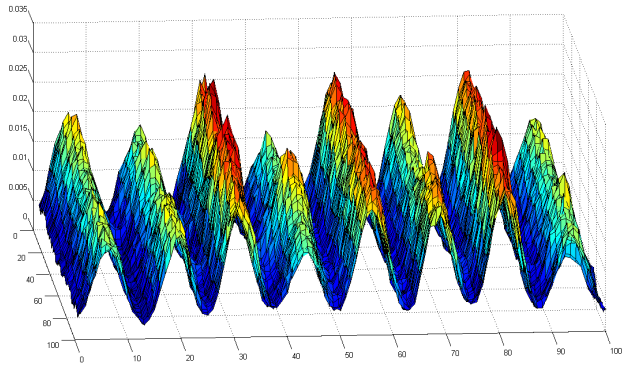

(b)

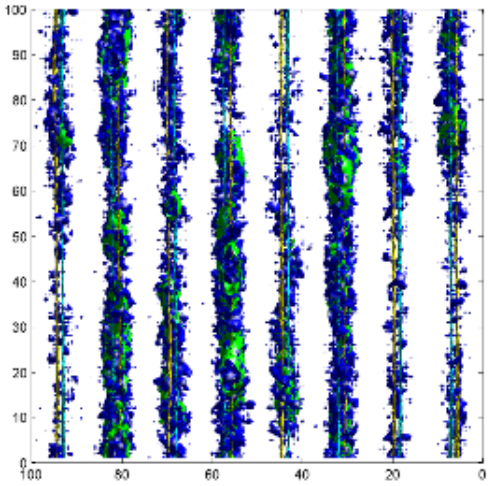

(c)

Figure 4.6. (a) One dimensional bead density profiles, (b) central particle bead *N* density distribution, and (c) detailed view of a section perpendicular to the lamellar orientation for the simulated PPN with lamellar morphology and particles covered by a 50-50 *A*-*B* type covering with a random distribution (A_6B_6(r)). Color code as in Figure 4.5.

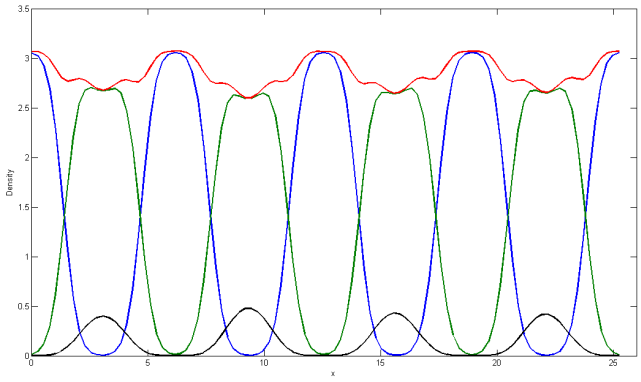

(a)

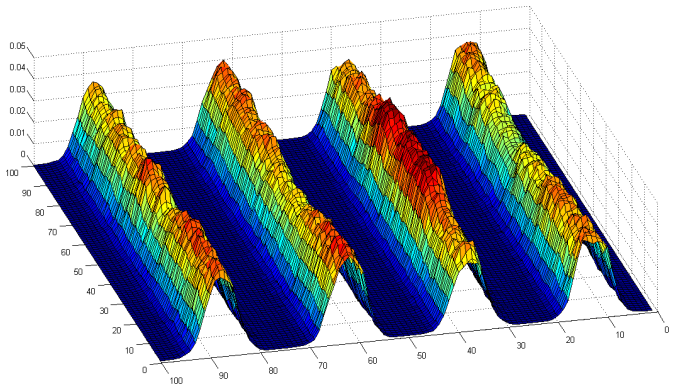

(b)

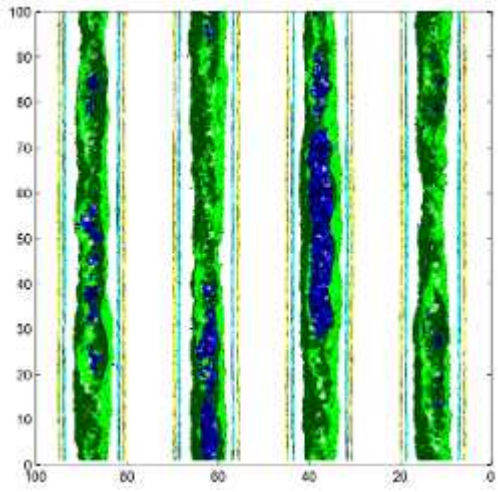

(c)

Figure 4.7. (a) One dimensional bead density profiles, (b) central particle bead *N* density distribution, and (c) detailed view of a section along a direction perpendicular to the lamellar orientation for the simulated PPN with lamellar morphology and particles covered by one *A*- type bead covering and the remaining bead covering of type B (A_1B_{11}). Color code as in Figure 4.5.

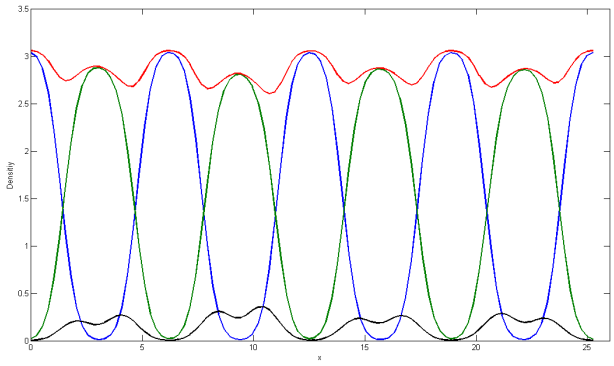

(a)

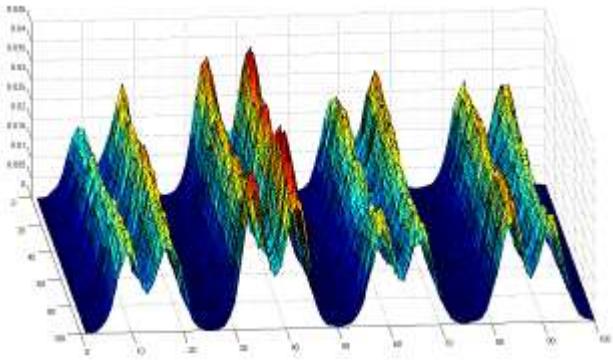

(b)

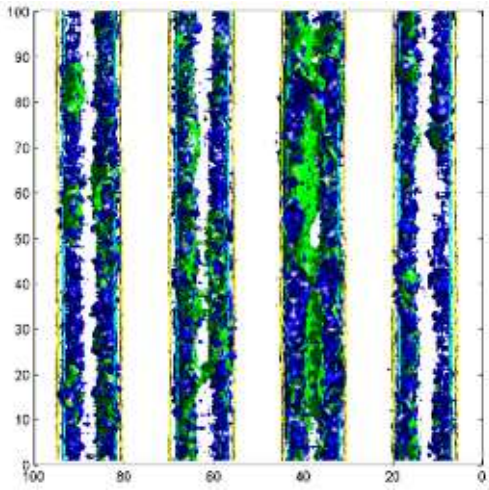

(c)

Figure 4.8. (a) One dimensional bead density profiles, (b) central particle bead *N* density distribution, and (c) detailed view of a section along a direction perpendicular to the lamellar orientation for the simulated PPN with lamellar morphology and particles covered by A_3B_9 type covering along a direction perpendicular to the lamellar orientation. Color code as in Figure 4.5.

Again, we started our investigation by considering a single type of particle covering (either *A* or *B*) for the nanoparticles dispersed in a cylindrical *A*-*B* matrix. Figures 4.9 and 4.10 show that, in analogy with the lamellar morphology, the nanoparticles segregate in the center of the corresponding compatible domain.

However, a careful observation of Figure 4.9 reveals a minor deformation of the cylinders, which could sensibly be ascribed to the slightly unfavorable ratio of the particle/cylinder diameters. Should this be the case, this negative effect could be practically reduced by either increasing the value of the repulsive parameter a_{AB} or decreasing the particle volume fraction VF. Indeed, Figure 4.10 shows the same system simulated at VF = 0.03, where a much lesser perturbation of the cylindrical geometry is indeed observed.

Interesting, when a mixed homogeneous *A*-*B* nanoparticles covering type is considered (i.e., $A_6B_6(h)$), we assist to a progressive modification of the hexagonal geometry of the matrix leading to a final, well-oriented lamellar morphology, in which the particles are ultimately segregated at the block interfaces. Figure 4.11 shows the final snapshot of the DPD simulation of the $A_6B_6(h)$ system, obtained with a VF=0.05 and a_{AB}=53.84. The critical role played by the nanoparticle volume fraction in changing the matrix morphology is well illustrated by the results obtained simulating the same system at a lower VF value equal to 0.03, as reported in Figure 4.12. In fact, in this case the final situation yielded by the simulation is utterly analogous to that realized in the presence of a lamellar morphology, since the $A_6B_6(h)$ covered nanoparticles locate at the interface between the blocks, and the cylindrical morphology is fully preserved.

Another interesting difference ascribable to the distinct matrix microstructure is revealed by simulating a A_1B_{11} system. Recalling that, in the presence of lamellae, the effect of a very small percentage of *A*-type covering beads among a plethora of *B*-type covering beads did not result in any major difference from the single-type covering case, and, accordingly, the particles did segregate in the center of the compatible domain, in the case of cylinders one single *A*-type bead is sufficient to lead all particles to locate themselves at the interfaces between the blocks. Figure 4.13 highlights this by showing the comparison between the results obtained for the A_1B_{11} and the *B*-type covering only systems, respectively.

4.3.3 Lamellar and perforated lamellar matrix morphology in presence of partially covered nanoparticles

The location of nanoparticles within a block copolymer matrix is primarily influenced by the compatibility of the nanoparticles with each constituent of the block copolymer microstructure.

Therefore, surface modification of the nanoparticle is required not only to prevent their aggregation but also to tune their interactions with each block copolymer domain.

A simple strategy to control the location of polymer-coated gold nanoparticles within *A*-*B* block copolymer domains is the variation of a single parameter, the surface coverage of gold nanoparticles by a homopolymer *A* ligand.

As the areal chain density of *A* chains on the nanoparticle decreases, a sharp transition from the case where the nanoparticles are located in the *A* domain to the case where the nanoparticles are located at the *A*-*B* interface is observed.

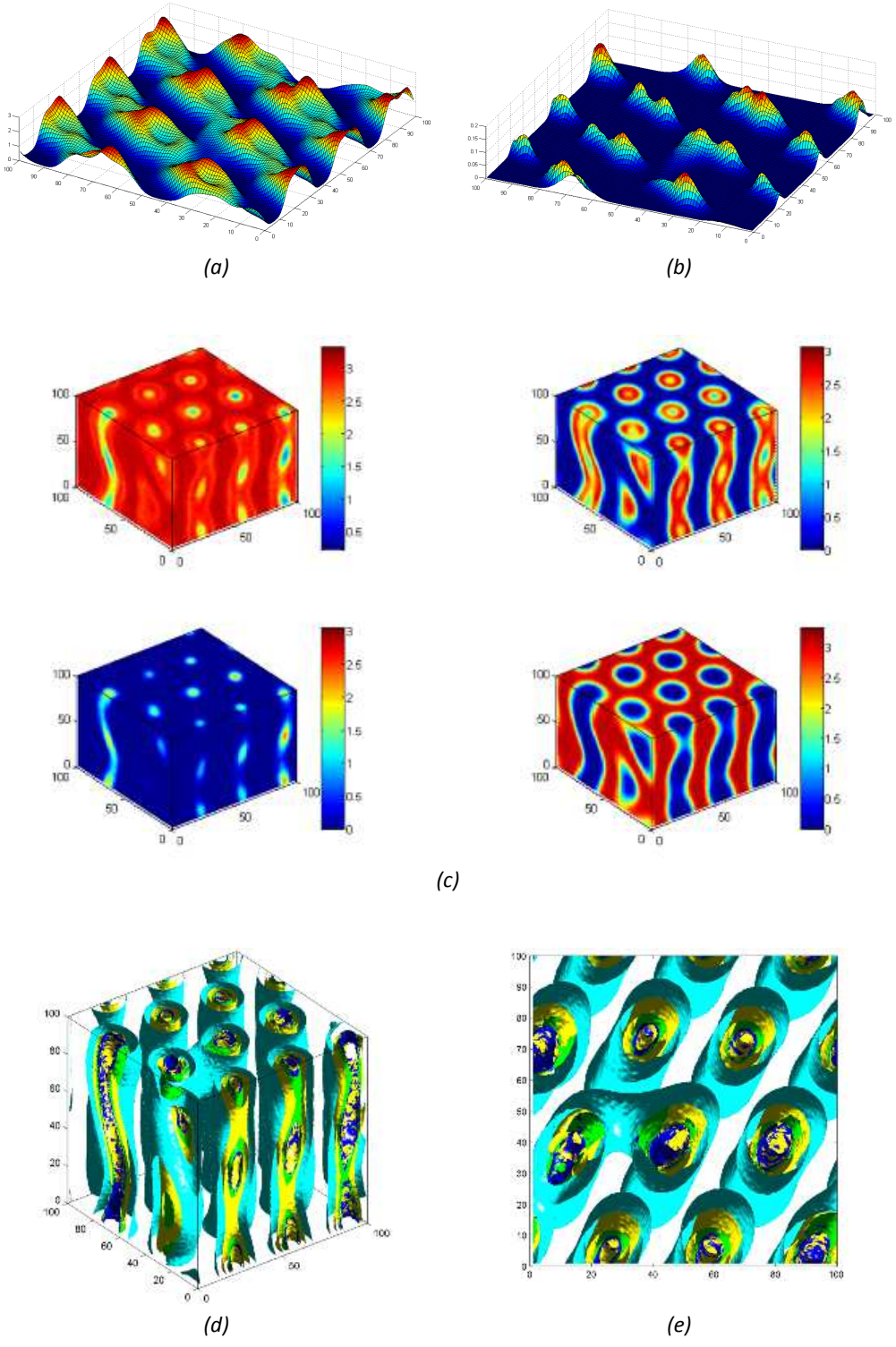

Figure 4.9. (a) Two dimensional bead density profile for *A*-type polymer matrix beads for the simulated PPN structure with hexagonal morphology and particles covered by *A*-type covering only. (b) Central particle bead *N* density distribution for the same system (color code: blue, minimum, red maximum density value). (c) Three-dimensional bead density representation: top, left: *A*- and *B*-type polymer matrix beads; top, right, *A*-type polymer matrix beads; bottom, left: total nanoparticle beads; bottom, right, *B*-type polymer matrix beads. (d) Three-dimensional and (e) top isosurface visualization of the simulated PPN structure with hexagonal morphology and particles covered by only *A*-type covering. The polymer matrix *A*-type beads are colored yellow whilst those of *B*-type are cyan. All nanoparticles beads are colored green; the central particles of the icosahedrons *N* are highlighted in blue.

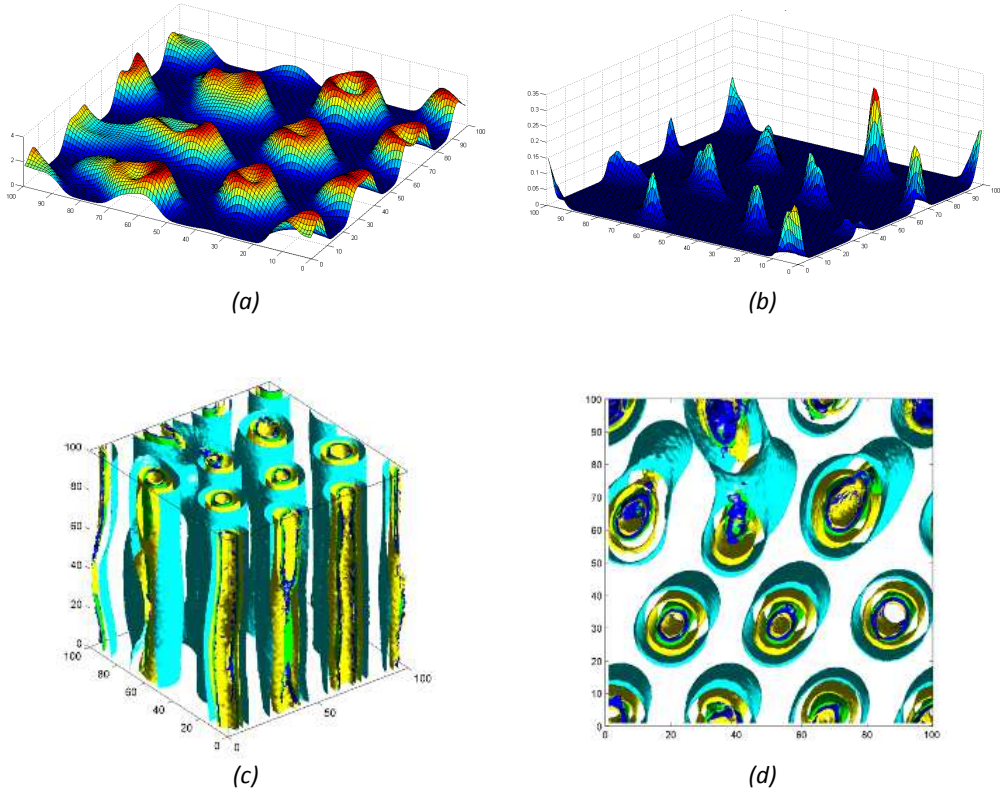

(a) *(b)*

(c) *(d)*

Figure 4.10. Same system of Figure 4.9 but simulated at a lower volume fraction (VF=0.03). Legend and color code as in Figure 4.9.

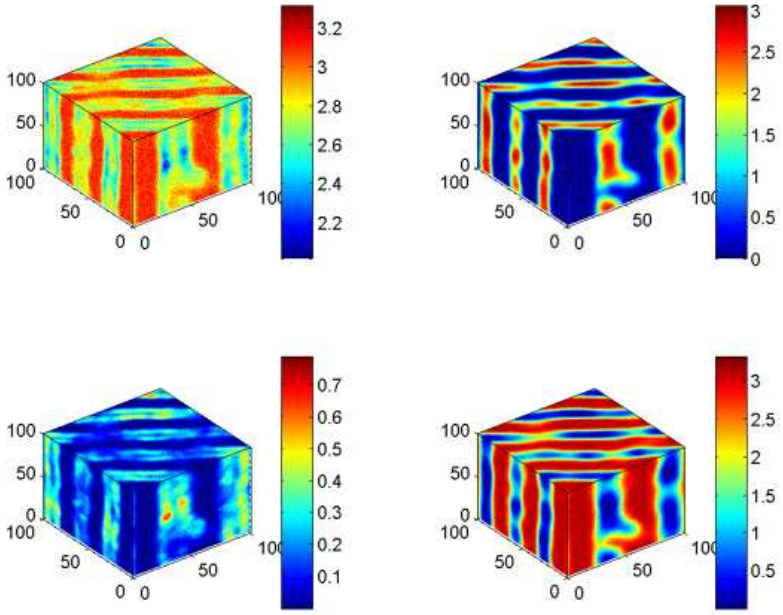

(a)

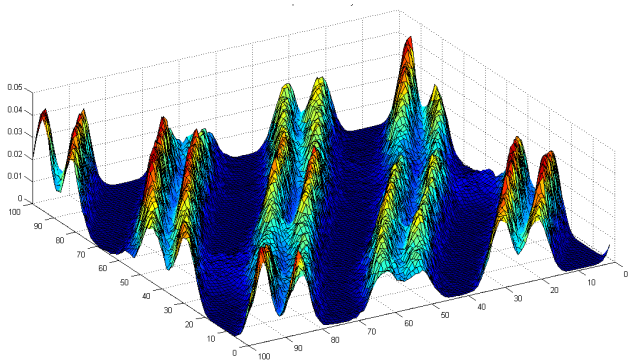

(b)

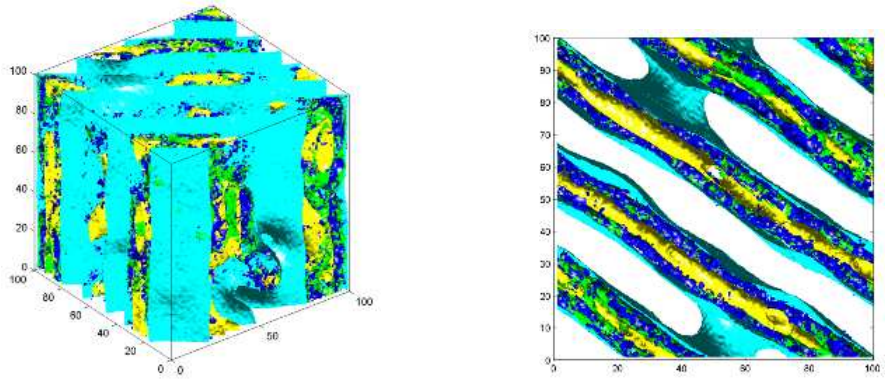

(c) *(d)*

Figure 4.11. (a) Three-dimensional bead density representation of the simulated PPN structure with initial hexagonal morphology and particles covered by 50-50 *A*-*B* type covering with an homogeneous distribution (A_6B_6(h)) and VF=0.05 and a_{AB}=53.84: top, right, *A*-type polymer matrix beads; bottom, left: total nanoparticle beads; bottom, right, *B*-type polymer matrix beads. The final lamellar geometry is well evident. (b) Central particle bead *N* density distribution for the same system. (c) Three-dimensional and (d) top isosurface visualization of the corresponding simulated PPN structure. Color code as in Figure 4.9.

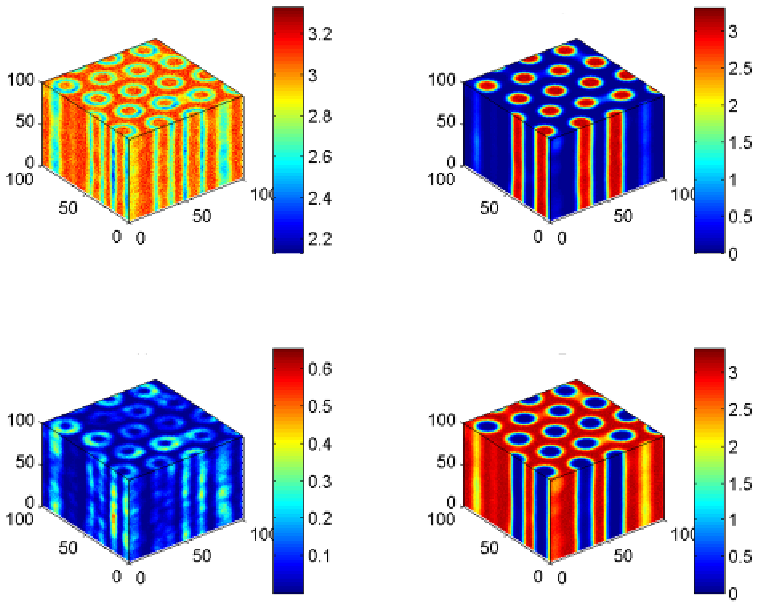

(a)

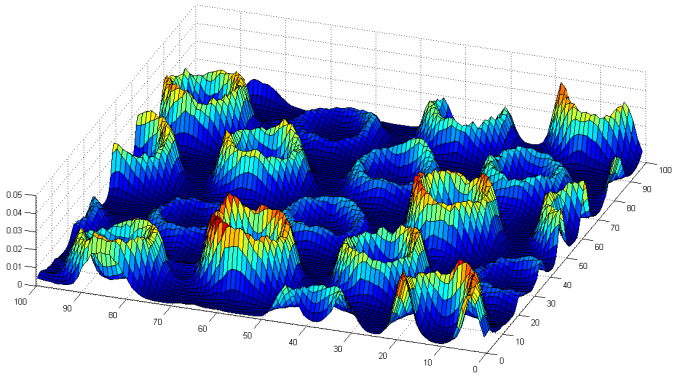

(b)

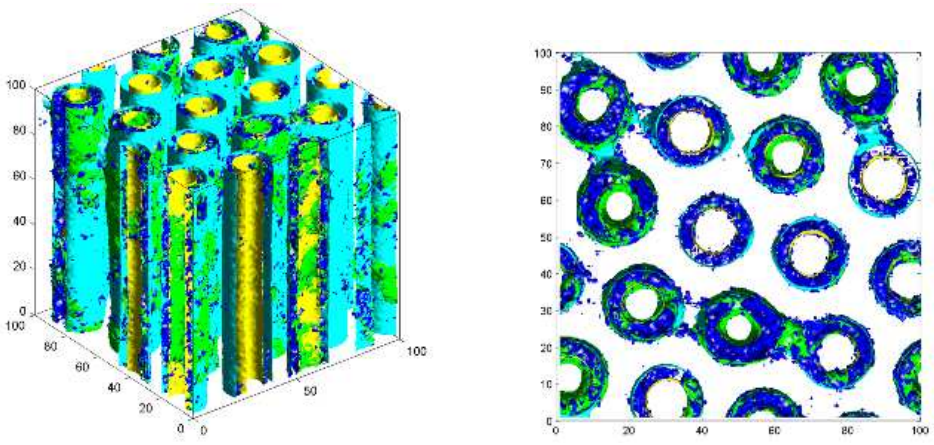

(c) *(d)*

Figure 4.12. Same system of Figure 4.11 but simulated at a lower volume fraction (VF=0.03). Legend and color code as in Figure 4.9.

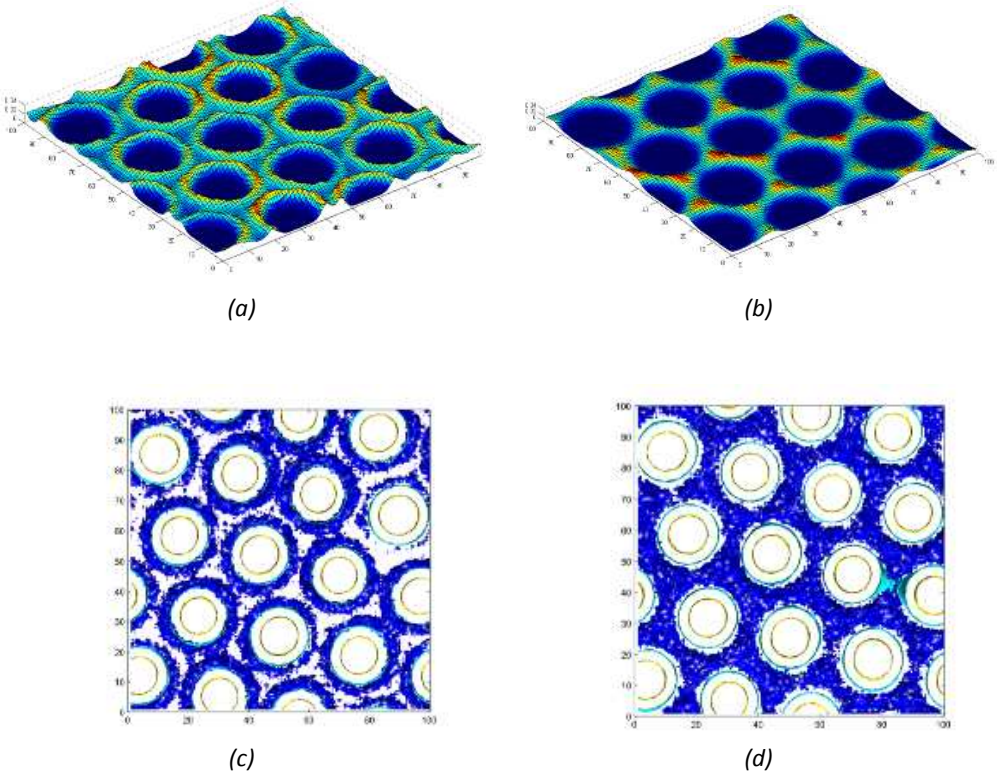

(a) *(b)*

(c) *(d)*

Figure 4.13. Comparison between the A_1B_{11} (left) and *B*-type covering only (right) cases in the hexagonal matrix. (a) and (b) Central particle bead *N* density distributions; (c) and (d) Isosurface visualization of the corresponding simulated PPN structure. Color code: yellow, *A*-type polymer matrix beads; cyan, *B*-type polymer matrix beads; blue, central particle bead *N* only. The density isosurface of all nanoparticle beads was omitted here for better highlighting the differences between the two covering cases.

To systematically investigate this aspect, the nanoparticle location within the block copolymer template was studied as a function of the polystyrene coverage surface using a set of four different coverage percentages represented by four different architectures: A_1N_{11}, A_2N_{10}, A_3N_9, A_4N_8. As an example of the notation employed, the A_1N_{11} models describes an icosahedron nanoparticle where 1 bead on the surface is of type *A* (PS) and the remaining 11 beads are of type *N* (Au). The central bead is always of type *N*.

From Figure 4.14, it is clear that nanoparticles coated with a high percentage of PS (A_4N_8, VF=0.05) are mostly located near the center of the PS domain.

As the particle grafting density decreases, virtually all nanoparticles are located at the interface between PS and PVP block domain, as shown in Figure 4.17 (A_1N_{11}, VF=0.05).

Au-PS nanoparticles with intermediate coverage remain close to the interface as shown in Figure 4.16 (A_2N_{10}, VF=0.05), and the nanoparticles are directed to the PVP domain at a coverage corresponding to A_3N_9 (Figure 4.15).

The change of PS grafting density induces a transition of nanoparticle location from PS domain to the PS-PVP interface. A rational for this behavior is that nanoparticles with minor PS areal chain density do not fully shield the Au nanoparticle surface from interacting with the PVP block of the PS-PVP matrix. There is a favourable interaction between gold and PVP, while the PS-gold interaction is relatively weaker.

These low areal chain density PS-Au nanoparticles thus segregate to the interface due to the inability of the low-density surface chains to screen the favourable interaction between the PVP block chains and the bare Au surface.

Of particular note is that the segregation of PS coated nanoparticles at the PS/PVP interface is observed over a range of PS fraction on the Au surface.

To quantitatively reinforce the qualitative impressions derived from the visual inspection of the Figures 4.14-17, we plot density distributions of nanoparticles, *A* and *B* component in the direction perpendicular to the lamellae (Figure 4.18).

The diagram clearly shows the occurrence of a single peak in the particle density distribution at the center of the PS domain when particles have a relatively high grafting coverage, where the unfavourable interaction between the PS ligands of the particle surface and the PVP domain is dominant.

Decreasing the grafting density, the particle density distribution exhibits three different peaks, one at the center of the PS domain and the other two at the PS/PVP interface. Upon further decrease in surface coverage, the particles are stack at the interface and the peak at the PS center disappears.

The trend in the dramatic change of the particle location from the center of PS domain to the interface is preserved when the particle concentration is increased up to VF=0.1.

Three dimensional density representation and isosurface visualization of PS-PVP block copolymer containing gold nanoparticles coated by a higher chain density are shown in Figure 4.19. Particles with high (areal) chain density are mostly located within the PS domain, while most gold particles with a minor coverage of the surface are shown to be segregated to the PS/PVP interface (Figure 4.22). Intermediate coverages are shown in Figure 4.20 and 4.21.

Diagrams of the density distribution of nanoparticles, *A* and *B* component in the direction perpendicular to the lamellae reflecting this transition of particle location in the PS-PVP template at VF=0.1, are shown in Figure 4.23.

For both VF=0.05 and 0.1 the morphology of the matrix is preserved, and only in presence of a higher nanoparticles concentration (i.e. VF=0.1) a slightly bending the lamellar interface can be observed.

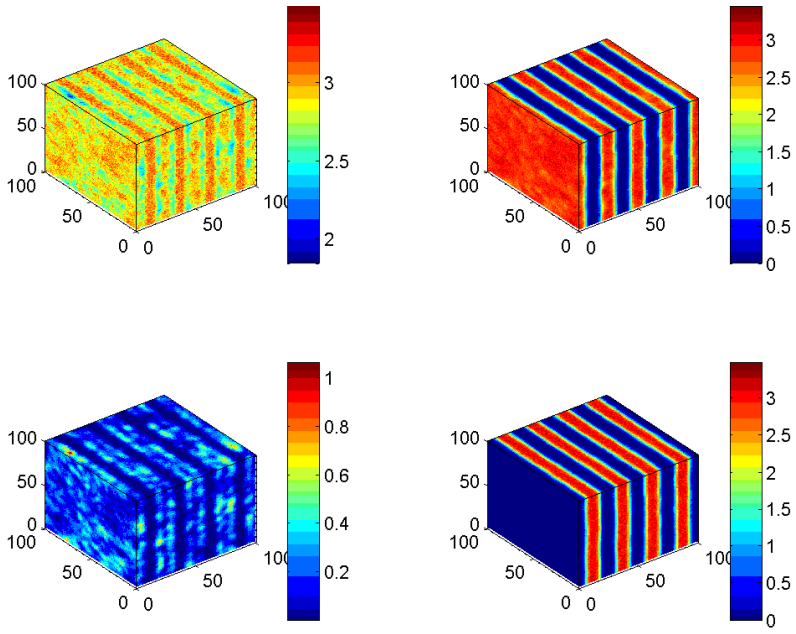

(a)

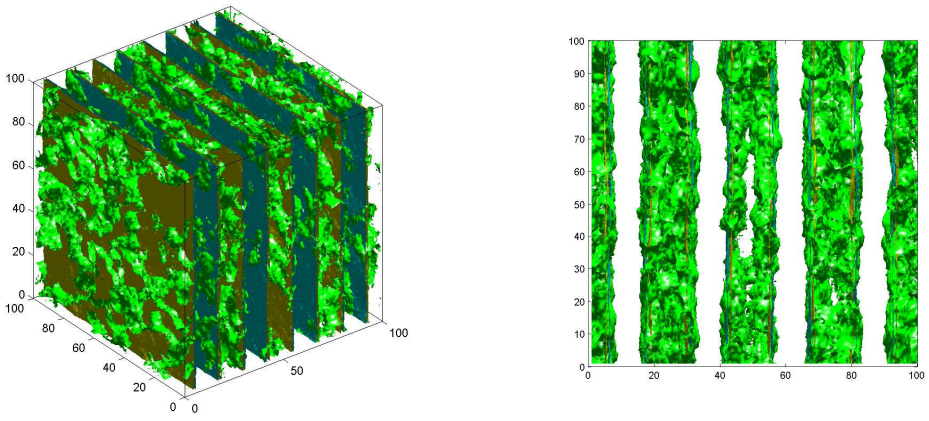

(b) *(c)*

Figure 4.14. (a) Three-dimensional bead density representation: top, left: *A*- and *B*-type polymer matrix beads; top, right, *A*-type polymer matrix beads; bottom, left: total nanoparticle beads; bottom, right, *B*-type polymer matrix beads. (b) Three-dimensional and (c) lateral isosurface visualization of the simulated PPN structure with lamellar morphology and particles covered by a A_4N_8 type covering at VF=0.05. The box length was set equal to $31r_c$. The polymer matrix *A*-type beads are colored yellow whilst those of *B*-type are cyan. All nanoparticles beads are colored green.

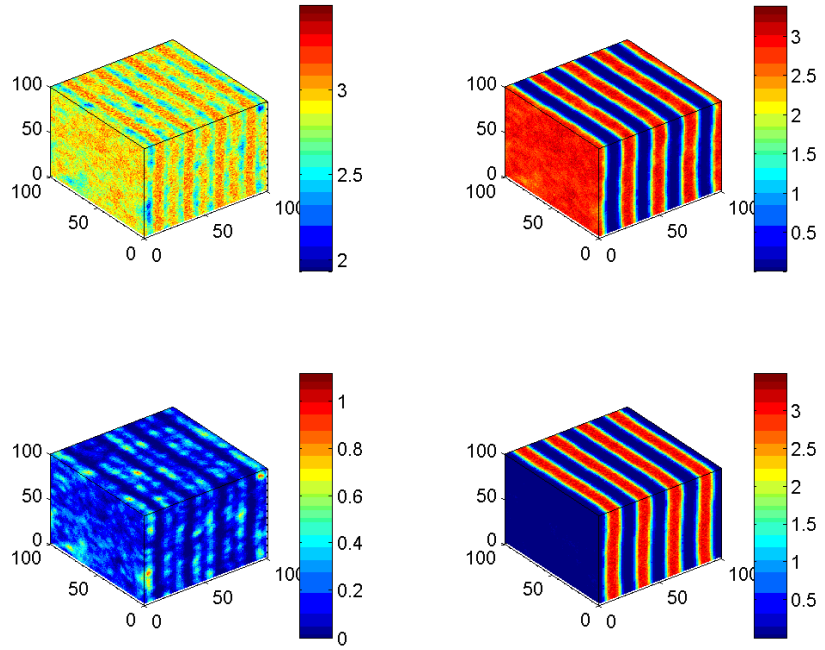

(a)

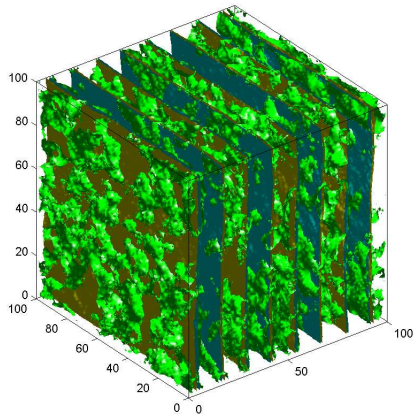

(b)

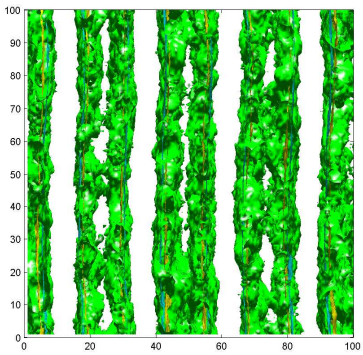

(c)

Figure 4.15. (a) Three-dimensional bead density representation: top, left: *A*- and *B*-type polymer matrix beads; top, right, *A*-type polymer matrix beads; bottom, left: total nanoparticle beads; bottom, right, *B*-type polymer matrix beads. (b) Three-dimensional and (c) lateral isosurface visualization of the simulated PPN structure with lamellar morphology and particles covered by a A_3N_9 type covering at VF=0.05. The box length was set equal to $31r_c$.The polymer matrix *A*-type beads are colored yellow whilst those of *B*-type are cyan. All nanoparticles beads are colored green.

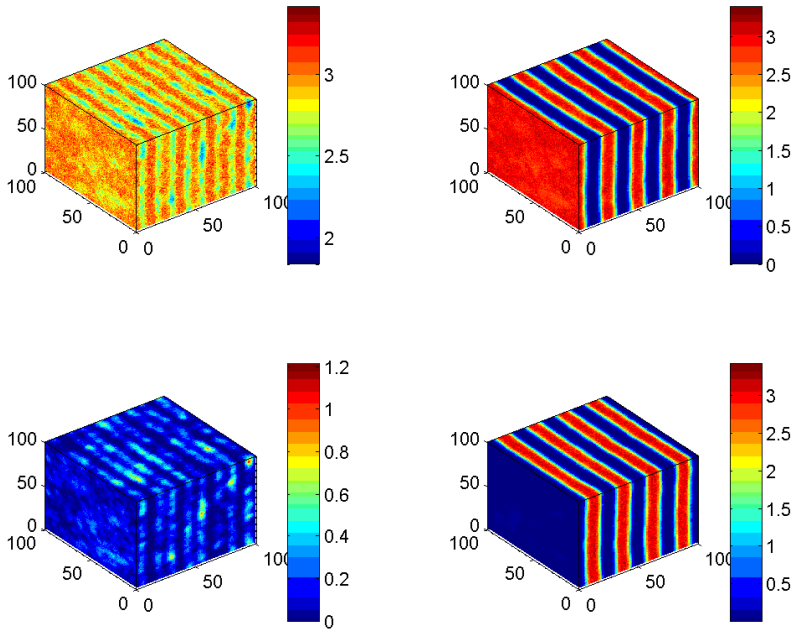

(a)

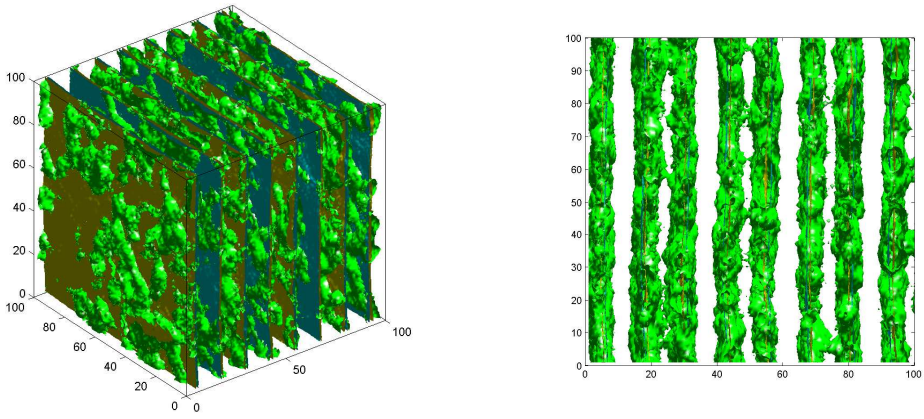

(b) *(c)*

Figure 4.16. (a) Three-dimensional bead density representation: top, left: *A*- and *B*-type polymer matrix beads; top, right, *A*-type polymer matrix beads; bottom, left: total nanoparticle beads; bottom, right, *B*-type polymer matrix beads. (b) Three-dimensional and (c) lateral isosurface visualization of the simulated PPN structure with lamellar morphology and particles covered by a A_2N_{10} type covering at VF=0.05. The box length was set equal to $31r_c$.The polymer matrix *A*-type beads are colored yellow whilst those of *B*-type are cyan. All nanoparticles beads are colored green.

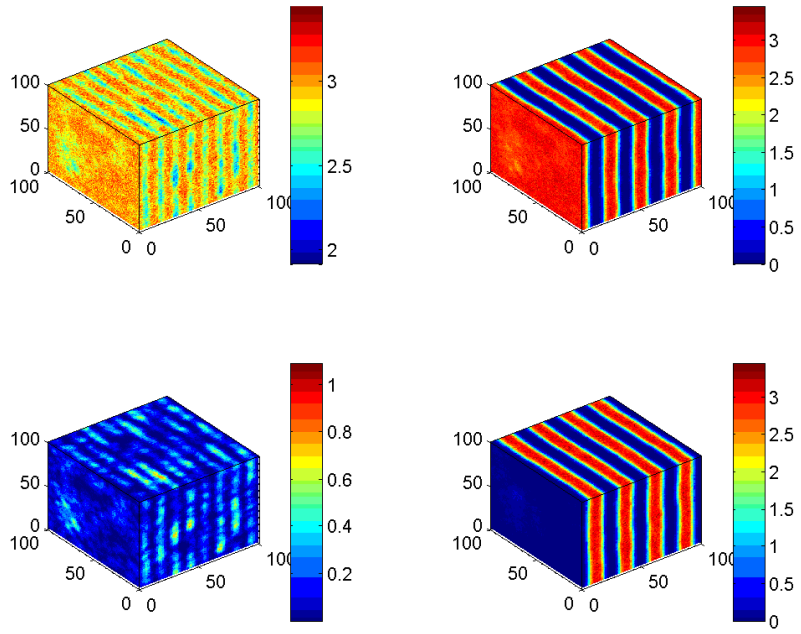

(a)

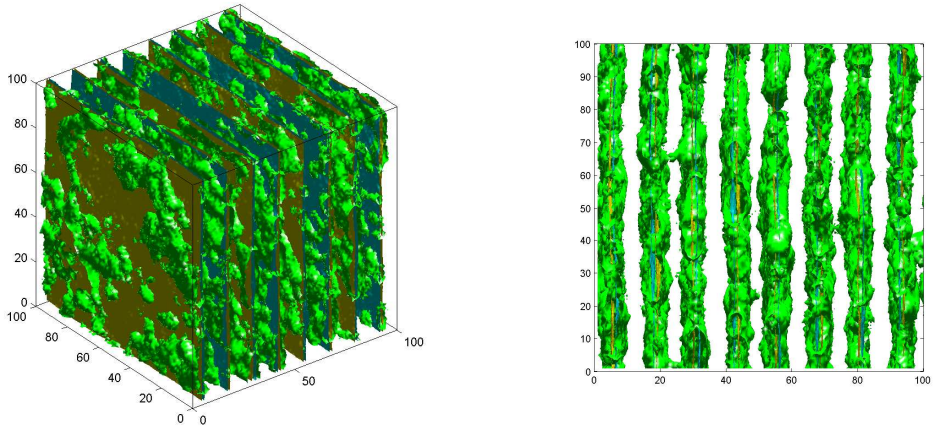

(b) *(c)*

Figure 4.17. (a) Three-dimensional bead density representation: top, left: *A*- and *B*-type polymer matrix beads; top, right, *A*-type polymer matrix beads; bottom, left: total nanoparticle beads; bottom, right, *B*-type polymer matrix beads. (b) Three-dimensional and (c) lateral isosurface visualization of the simulated PPN structure with lamellar morphology and particles covered by a A_1N_{11} type covering at VF=0.05. The box length was set equal to $31r_c$.The polymer matrix *A*-type beads are colored yellow whilst those of *B*-type are cyan. All nanoparticles beads are colored green.

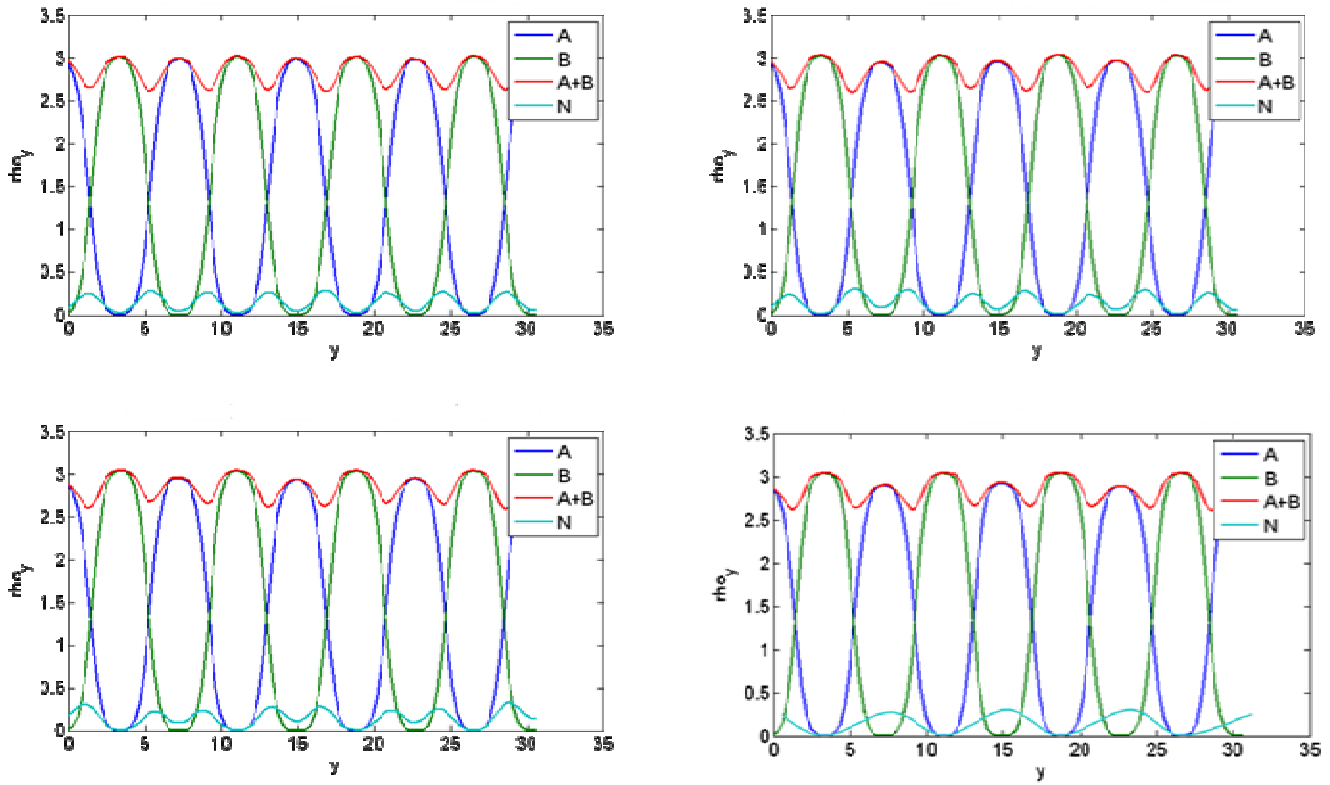

Figure 4.18 One dimensional bead density profiles of the simulated PPN with lamellar morphology and particles at VF equal to 0.05 in direction perpendicular to the lamellae. Nanoparticles coverage architecture: top left, A_1N_{11}; top right, A_2N_{10}; bottom left, A_3N_9; bottom right, A_4N_8. Color code: blue: *A*-type polymer matrix beads; green: *B*-type polymer matrix beads; red: total *A*- and *B*-type polymer matrix beads; light blue: total icosahedral nanoparticle beads.

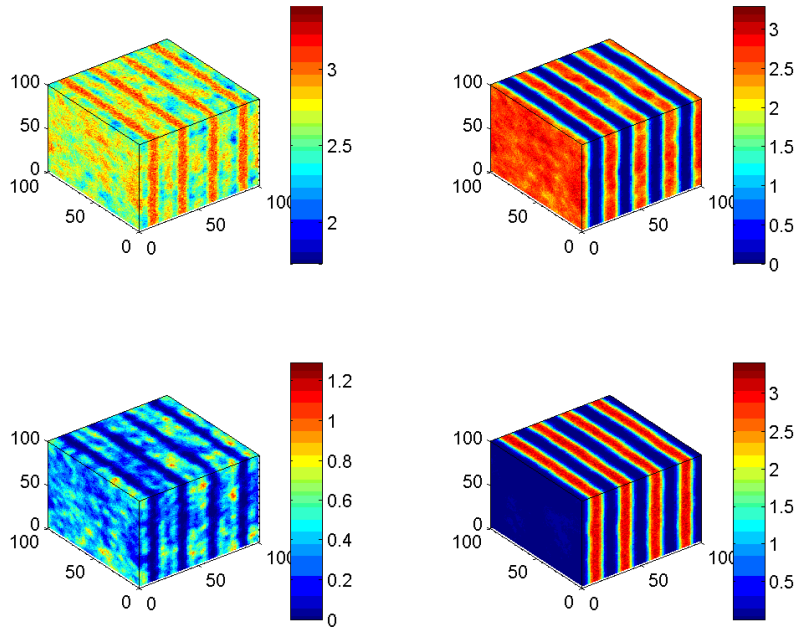

(a)

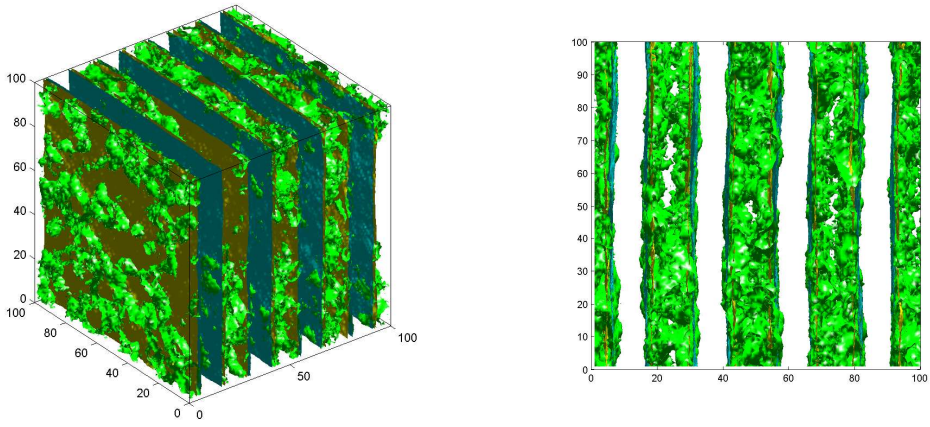

(b) *(c)*

Figure 4.19. (a) Three-dimensional bead density representation: top, left: *A*- and *B*-type polymer matrix beads; top, right, *A*-type polymer matrix beads; bottom, left: total nanoparticle beads; bottom, right, *B*-type polymer matrix beads. (b) Three-dimensional and (c) lateral isosurface visualization of the simulated PPN structure with lamellar morphology and particles covered by a A_4N_8 type covering at VF=0.1. The box length was set equal to $31r_c$.The polymer matrix *A*-type beads are colored yellow whilst those of *B*-type are cyan. All nanoparticles beads are colored green.

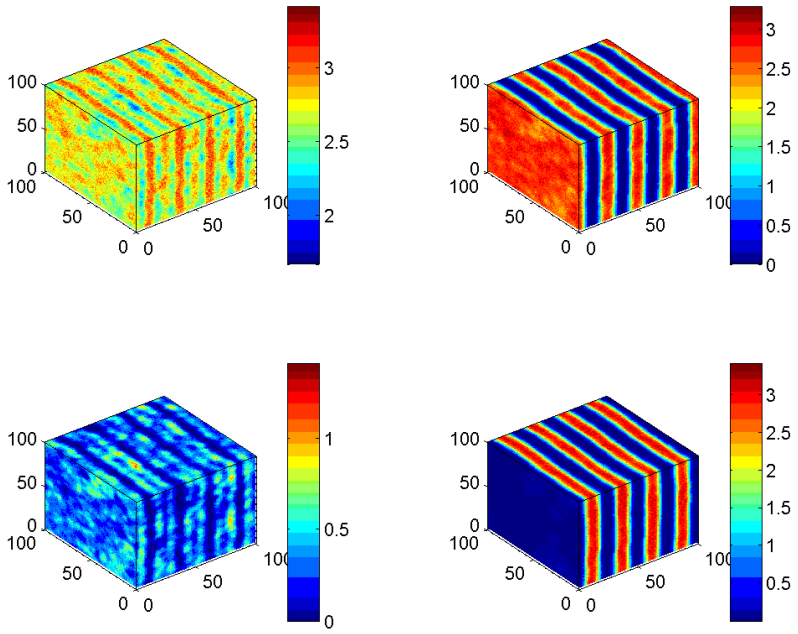

(a)

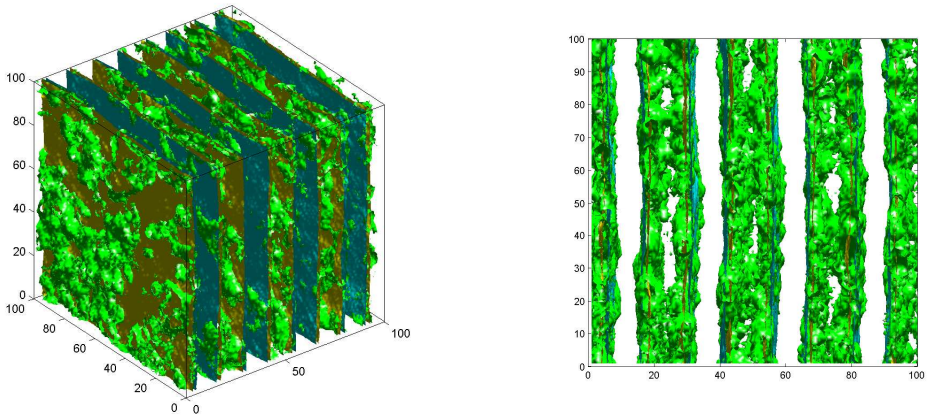

(b) *(c)*

Figure 4.20. (a) Three-dimensional bead density representation: top, left: *A*- and *B*-type polymer matrix beads; top, right, *A*-type polymer matrix beads; bottom, left: total nanoparticle beads; bottom, right, *B*-type polymer matrix beads. (b) Three-dimensional and (c) lateral isosurface visualization of the simulated PPN structure with lamellar morphology and particles covered by a A_3N_9 type covering at VF=0.1. The box length was set equal to $31r_c$. The polymer matrix *A*-type beads are colored yellow whilst those of *B*-type are cyan. All nanoparticles beads are colored green.

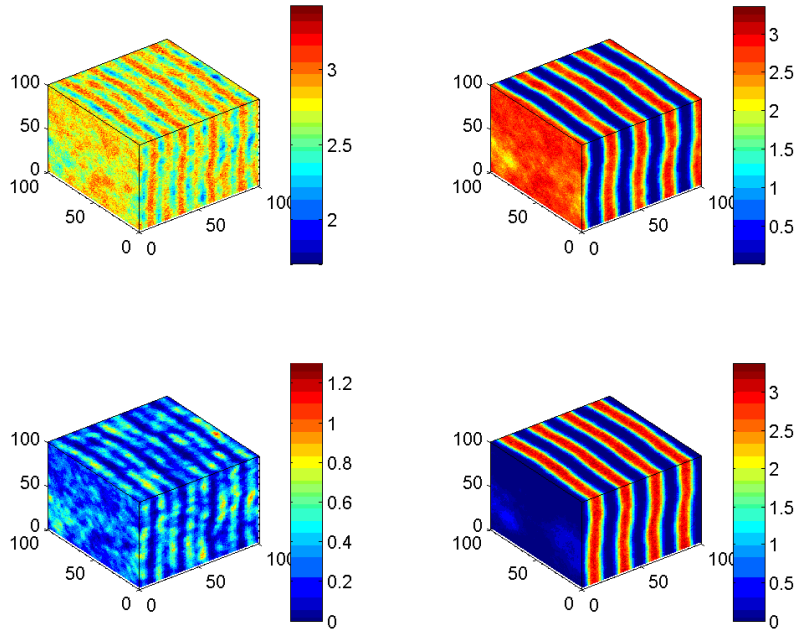

(a)

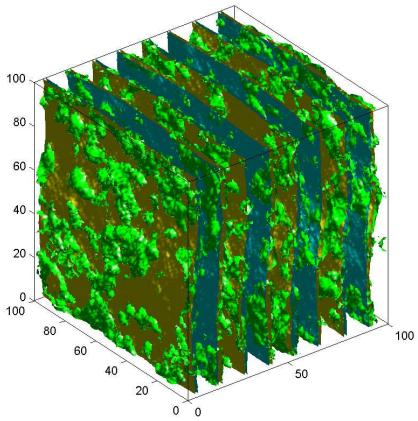

(b)

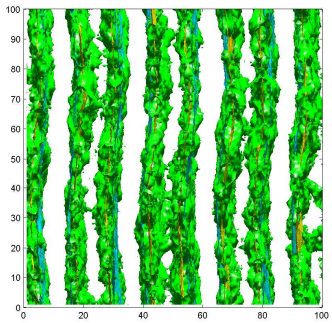

(c)

Figure 4.21. (a) Three-dimensional bead density representation: top, left: *A*- and *B*-type polymer matrix beads; top, right, *A*-type polymer matrix beads; bottom, left: total nanoparticle beads; bottom, right, *B*-type polymer matrix beads. (b) Three-dimensional and (c) lateral isosurface visualization of the simulated PPN structure with lamellar morphology and particles covered by a A_2N_{10} type covering at VF=0.1. The box length was set equal to $31r_c$.The polymer matrix *A*-type beads are colored yellow whilst those of *B*-type are cyan. All nanoparticles beads are colored green.

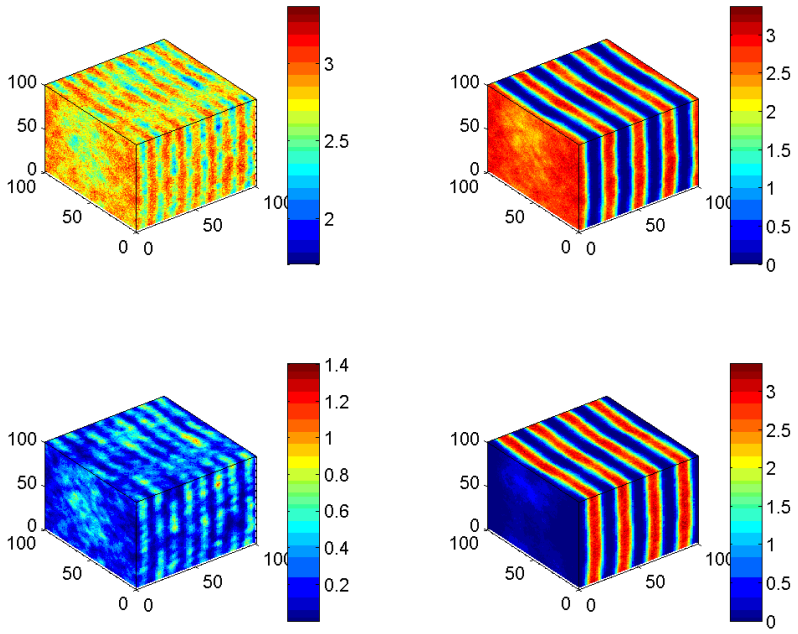

(a)

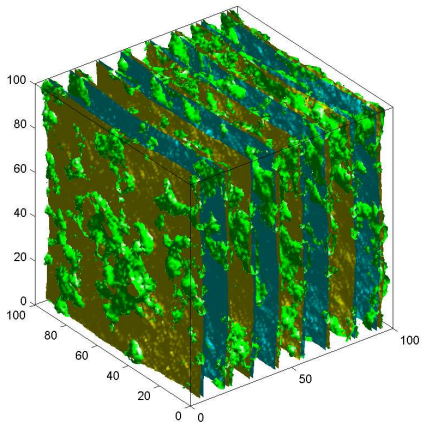

(b)

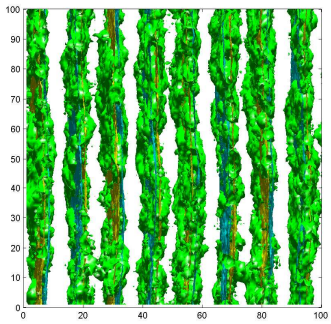

(c)

Figure 4.22. (a) Three-dimensional bead density representation: top, left: *A*- and *B*-type polymer matrix beads; top, right, *A*-type polymer matrix beads; bottom, left: total nanoparticle beads; bottom, right, *B*-type polymer matrix beads. (b) Three-dimensional and (c) lateral isosurface visualization of the simulated PPN structure with lamellar morphology and particles covered by a A_1N_{11} type covering at VF=0.1. The box length was set equal to $31r_c$. The polymer matrix *A*-type beads are colored yellow whilst those of *B*-type are cyan. All nanoparticles beads are colored green.

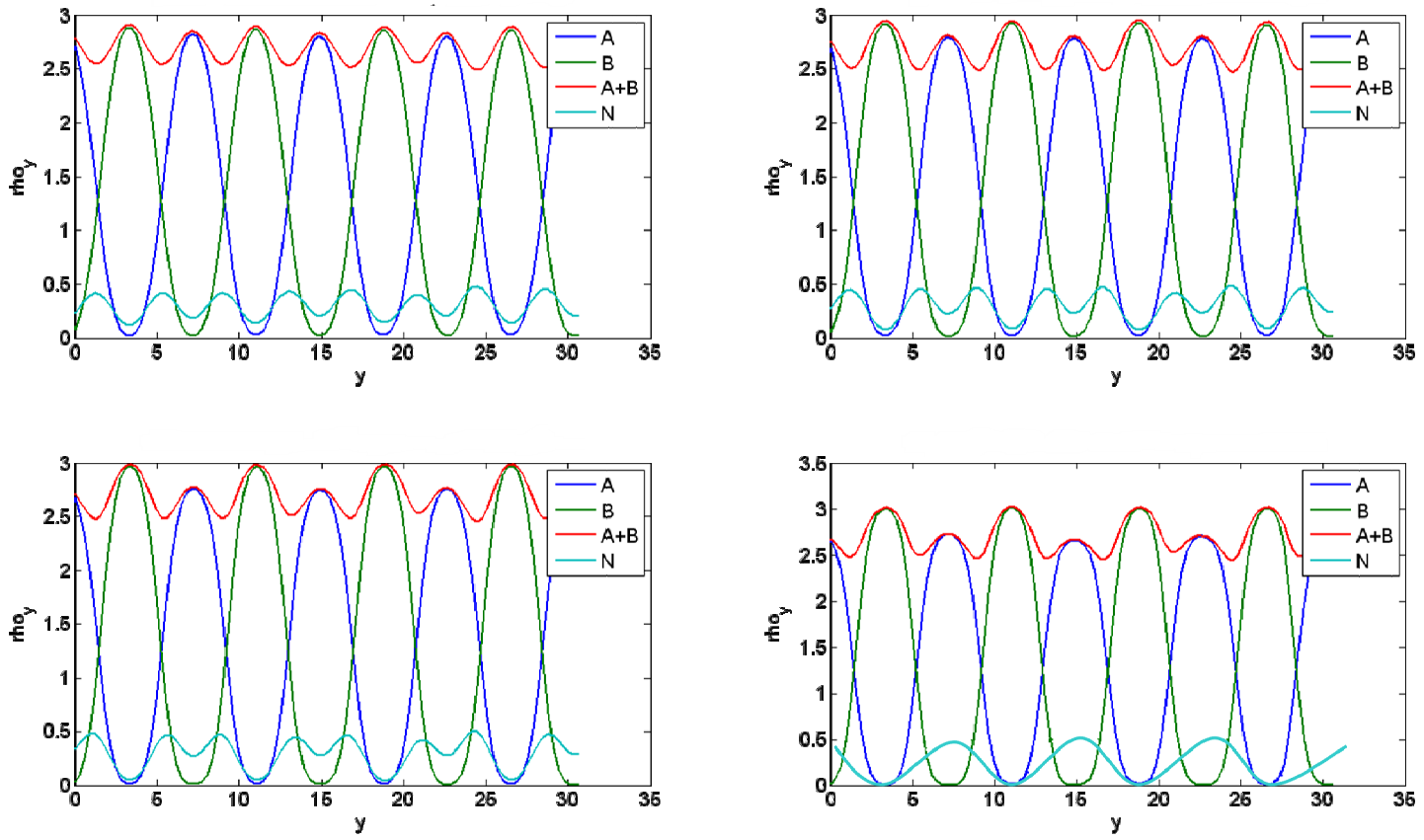

Figure 4.23 One dimensional bead density profiles of the simulated PPN with lamellar morphology and particles at VF equal to 0.1 in direction perpendicular to the lamellae. Nanoparticles coverage architecture: top left, A_1N_{11}; top right, A_2N_{10}; bottom left, A_3N_9; bottom right, A_4N_8. Color code: blue: *A*-type polymer matrix beads; green: *B*-type polymer matrix beads; red: total *A*- and *B*-type polymer matrix beads; light blue: total icosahedral nanoparticle beads.

In the presence of the nanoparticles in the PS domain, the PS chains surrounding the particles have to alter their conformation to accommodate the nanoparticles, and this required additional energy expense. The PS chains normal to the interface have to stretch to release the energy, while the PVP chains normal to the interface will contract. Thus, the position of the PS-PVP interface strongly depends on the balance between the stretching of the PS chains and the contracting of the PVP chains. This behavior induces local fluctuations and the composite forms distorted lamellar structures.

To complete the analysis of the effect of the incorporation of Au nanoparticles differently covered in a PS-PVP lamellar template, we decided to consider a perforated lamellar morphology. In some circumstances the entropic contribution to the free energy outweighs the energy penalty for the presence of pores, and one has an equilibrium phase of perforated lamellae. Perforated lamellae exist in a narrow range along the lamella-cylindrical phase boundary.

Figure 4.24 illustrates three-dimensional distribution and isosurface visualization of A_4N_8 nanoparticle dispersed a perforated lamellar matrix at a volume fraction of VF=0.5. Due to the unfavourable interaction between the PVP blocks and PS ligands, moderate segregation of particles at the interface can be observed at this value of coverage.

The decrease in coverage has the effect of increasing the attractive interaction between the bare Au surface not shielded by the *A* ligands and the PVP block of the diblock copolymer.

As a result, particles tend to stay close to the interface between the PS-PVP block, and finally a interfacial segregation occurs (Figure 4.25).

The trend in the sharp transition of the particle location from the center of PS domain to the interface is preserved when the particle concentration is increased up to VF=0.1 (Figure 4.26 and 4.27).

At both volume fraction considered in this work the morphology of the diblock copolymer matrix is preserved and no macrophase separation is observed in this range of concentration.

4.3.4 Spherical matrix morphology in presence of partially covered nanoparticles

Nanodots or nanospheres can be formed in addition to nanowires and nanosheets employing a spherical phase as template.

Once again, the PS chains grafted to the Au particle surface cause a net attraction between the nanoparticles and the PS domain of the copolymer: hence, at higher density of grafting the nanoparticles are segregated to the lamellar domains.

From Figure 4.28 it is clear that the higher areal chain density nanoparticles are principally dispersed into the PS domains.

In direct contrast, lower areal density nanoparticles are localized at the interface between the PS-PVP blocks (Figure 4.29), as the nanoparticles are not sufficiently covered by the PS ligands.

This tendency can be observed both at VF=0.05 and VF=0.1 (Figures 4.30 and 4.31).

We did not observe any macrophase separation for each concentration of particle and nanoparticles are seen strongly localized at the PS-PVP interfaces or within the PS domains according to the coverage of the nanoparticle surface.

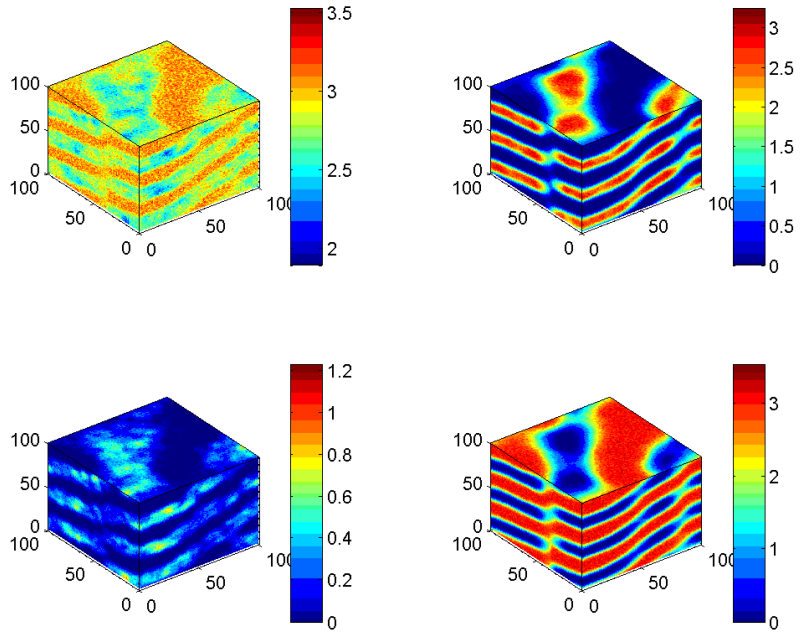

(a)

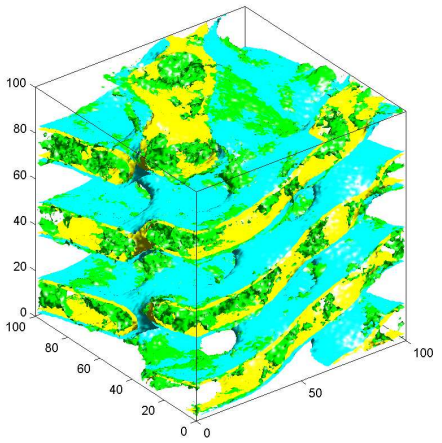

(b)

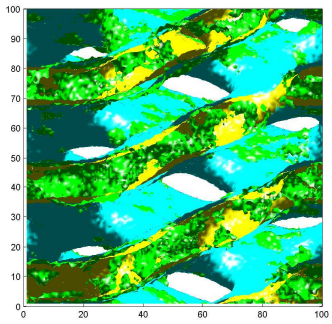

(c)

Figure 4.24. (a) Three-dimensional bead density representation: top, left: *A*- and *B*-type polymer matrix beads; top, right, *A*-type polymer matrix beads; bottom, left: total nanoparticle beads; bottom, right, *B*-type polymer matrix beads. (b) Three-dimensional and (c) lateral isosurface visualization of the simulated PPN structure with perforated lamellar morphology and particles covered by a A_4N_8 type covering at VF=0.05. The polymer matrix *A*-type beads are colored yellow whilst those of *B*-type are cyan. All nanoparticles beads are colored green.

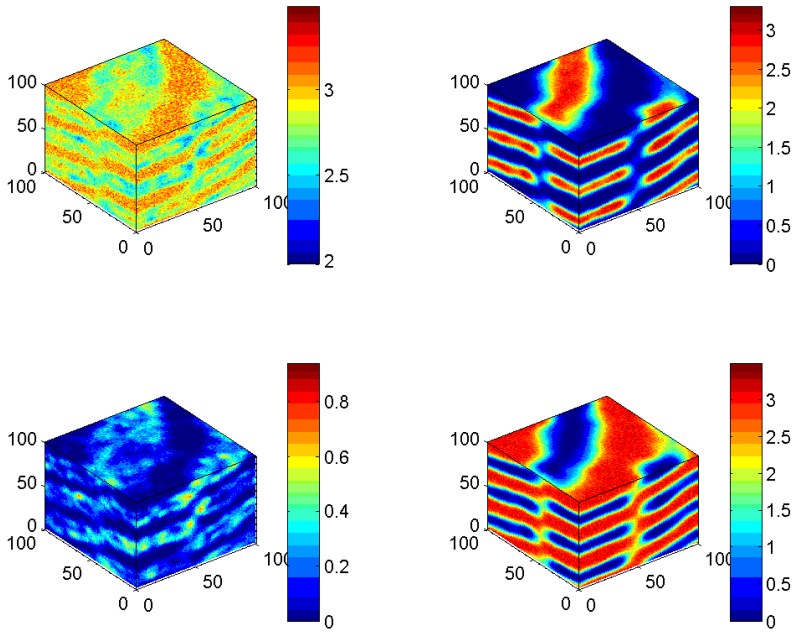

(a)

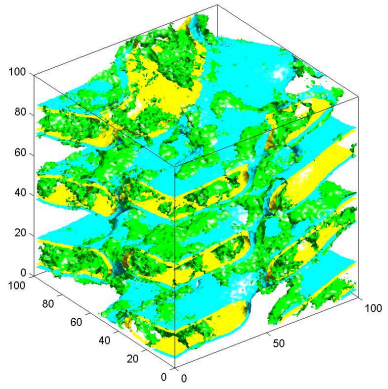

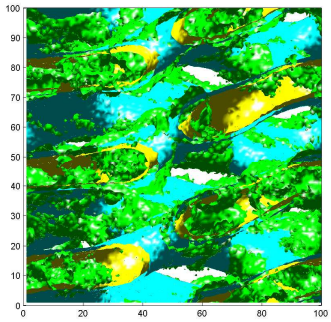

(b) *(c)*

Figure 4.25. (a) Three-dimensional bead density representation: top, left: *A*- and *B*-type polymer matrix beads; top, right, *A*-type polymer matrix beads; bottom, left: total nanoparticle beads; bottom, right, *B*-type polymer matrix beads. (b) Three-dimensional and (c) lateral isosurface visualization of the simulated PPN structure with perforated lamellar morphology and particles covered by a A_1N_{11} type covering at VF=0.05. The polymer matrix *A*-type beads are colored yellow whilst those of *B*-type are cyan. All nanoparticles beads are colored green.

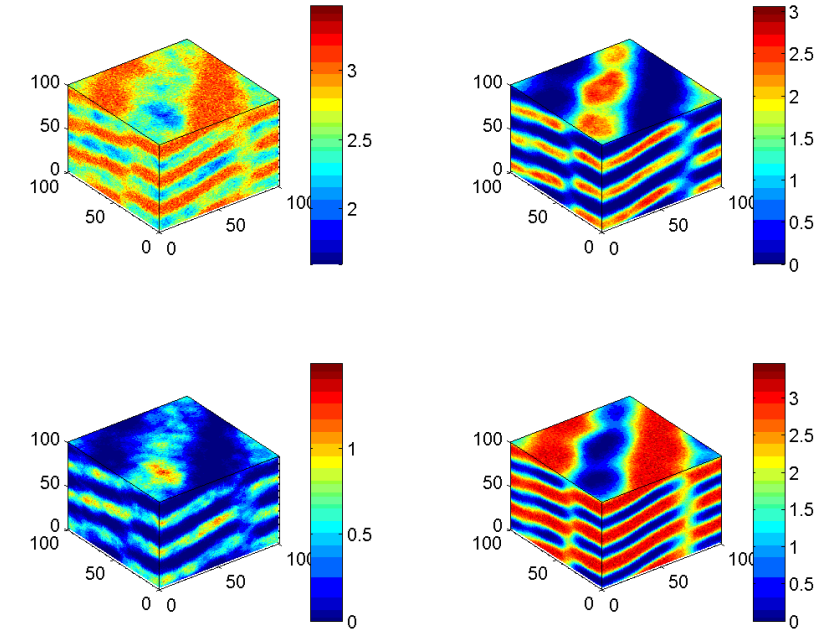

(a)

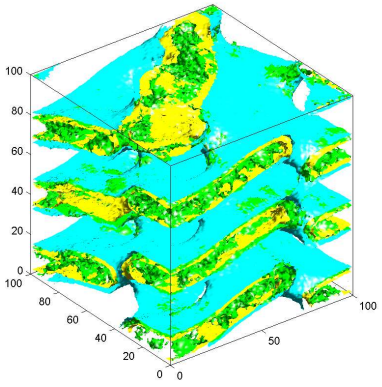

(b)

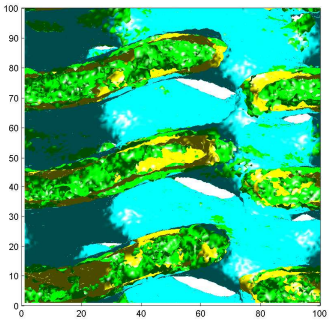

(c)

Figure 4.26. (a) Three-dimensional bead density representation: top, left: *A*- and *B*-type polymer matrix beads; top, right, *A*-type polymer matrix beads; bottom, left: total nanoparticle beads; bottom, right, *B*-type polymer matrix beads. (b) Three-dimensional and (c) lateral isosurface visualization of the simulated PPN structure with perforated lamellar morphology and particles covered by a A_4N_8 type covering at VF=0.1. The polymer matrix *A*-type beads are colored yellow whilst those of *B*-type are cyan. All nanoparticles beads are colored green.

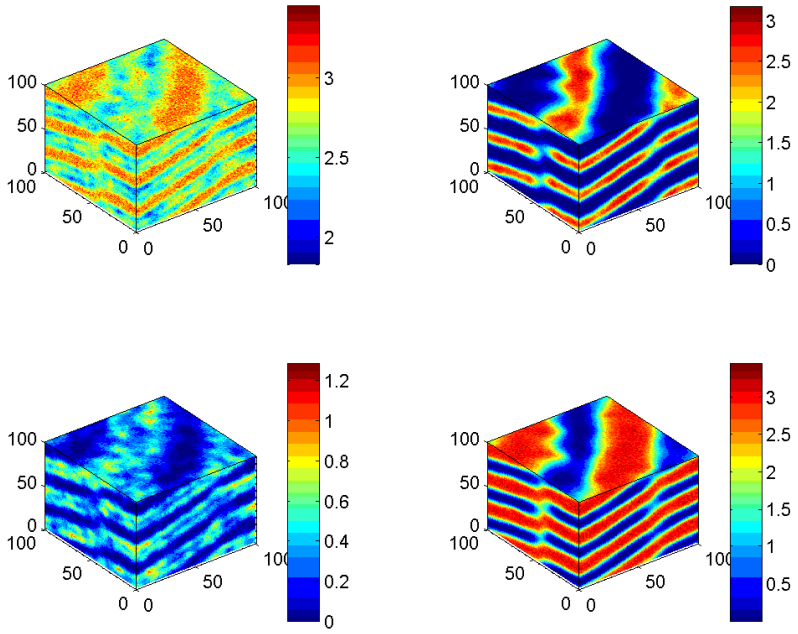

(a)

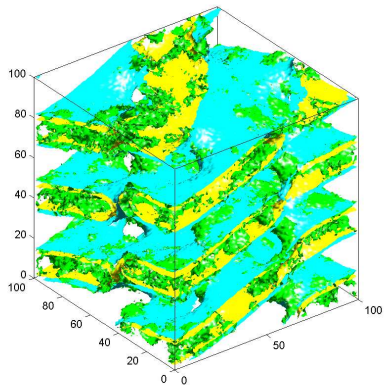

(b)

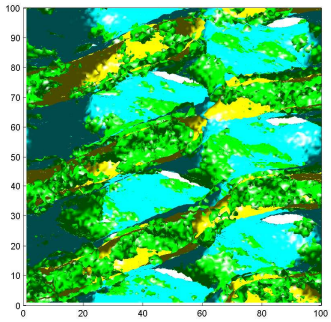

(c)

Figure 4.27. (a) Three-dimensional bead density representation: top, left: *A*- and *B*-type polymer matrix beads; top, right, *A*-type polymer matrix beads; bottom, left: total nanoparticle beads; bottom, right, *B*-type polymer matrix beads. (b) Three-dimensional and (c) lateral isosurface visualization of the simulated PPN structure with perforated lamellar morphology and particles covered by a A_1N_{11} type covering at VF=0.1. The polymer matrix *A*-type beads are colored yellow whilst those of *B*-type are cyan. All nanoparticles beads are colored green.

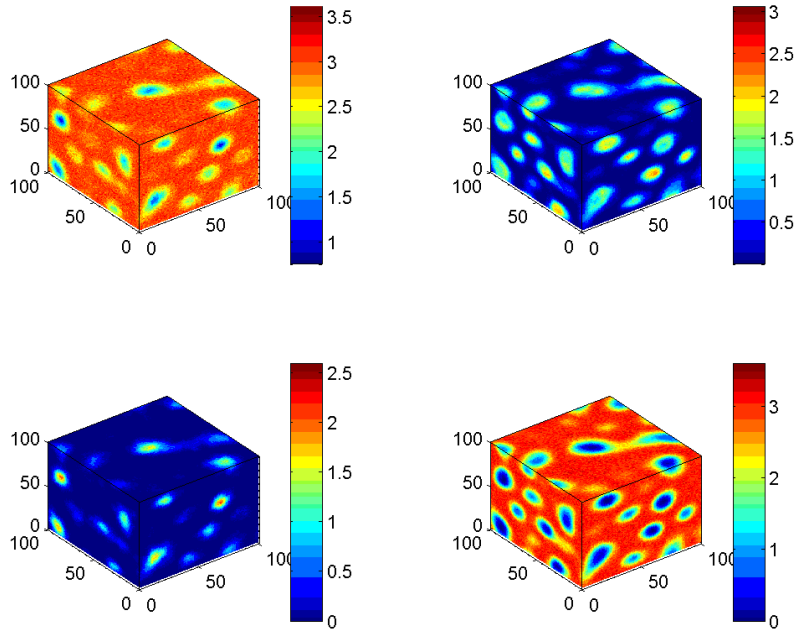

(a)

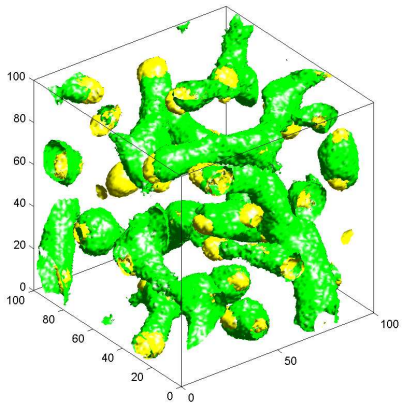

(b)

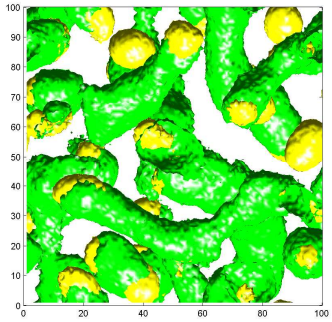

(c)

Figure 4.28. (a) Three-dimensional bead density representation: top, left: *A*- and *B*-type polymer matrix beads; top, right, *A*-type polymer matrix beads; bottom, left: total nanoparticle beads; bottom, right, *B*-type polymer matrix beads. (b) Three-dimensional and (c) lateral isosurface visualization of the simulated PPN structure with spherical morphology and particles covered by a A_4N_8 type covering at VF=0.05. The polymer matrix *A*-type beads are colored yellow whilst those of *B*-type are cyan. All nanoparticles beads are colored green.

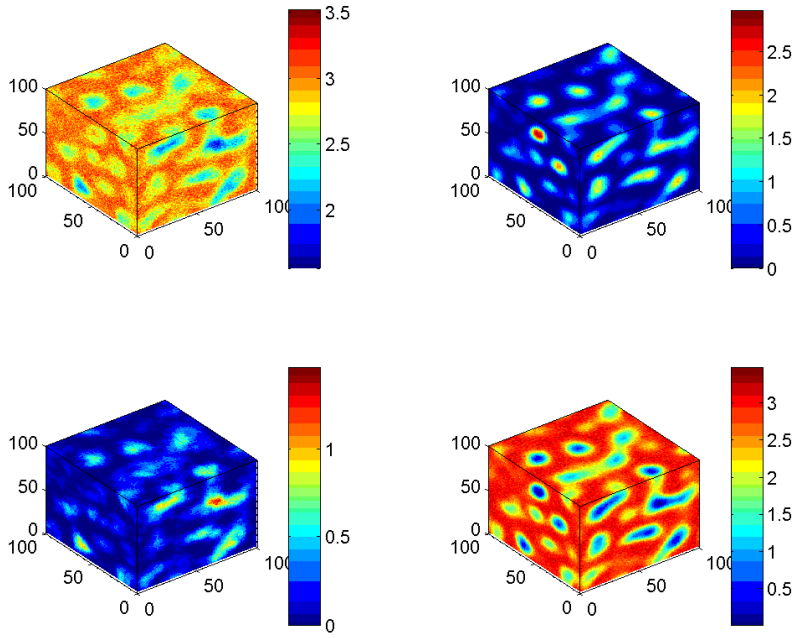

(a)

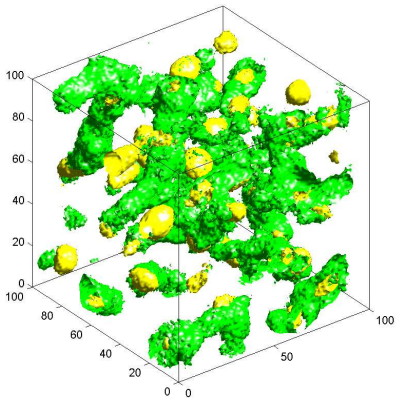

(b)

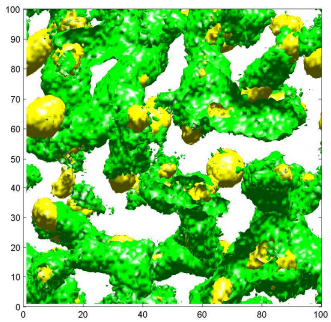

(c)

Figure 4.29. (a) Three-dimensional bead density representation: top, left: *A*- and *B*-type polymer matrix beads; top, right, *A*-type polymer matrix beads; bottom, left: total nanoparticle beads; bottom, right, *B*-type polymer matrix beads. (b) Three-dimensional and (c) lateral isosurface visualization of the simulated PPN structure with spherical morphology and particles covered by a A_1N_{11} type covering at VF=0.05. The polymer matrix *A*-type beads are colored yellow whilst those of *B*-type are cyan. All nanoparticles beads are colored green.

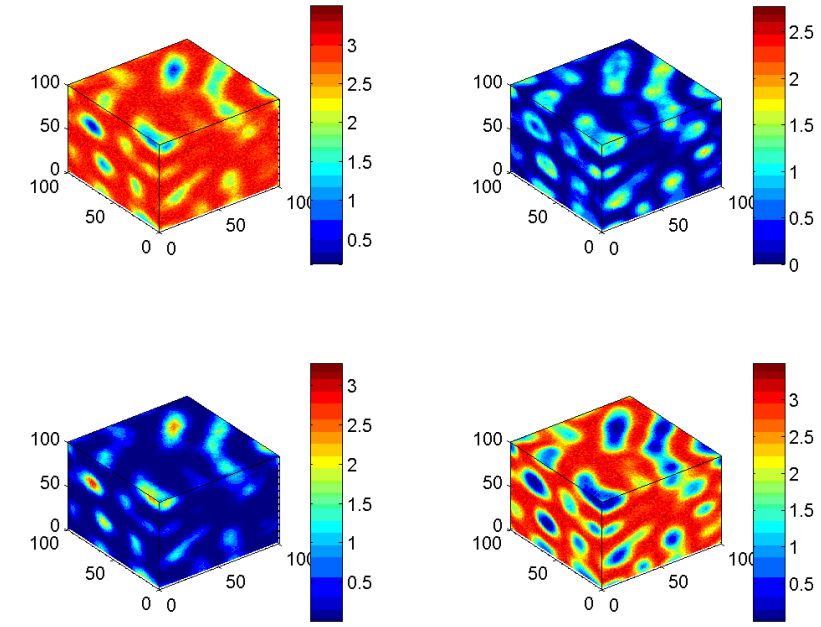

(a)

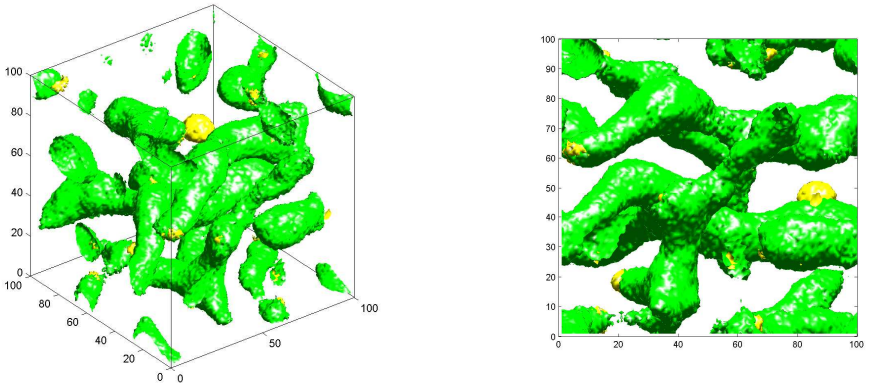

(b) *(c)*

Figure 4.30. (a) Three-dimensional bead density representation: top, left: *A*- and *B*-type polymer matrix beads; top, right, *A*-type polymer matrix beads; bottom, left: total nanoparticle beads; bottom, right, *B*-type polymer matrix beads. (b) Three-dimensional and (c) lateral isosurface visualization of the simulated PPN structure with spherical morphology and particles covered by a A_4N_8 type covering at VF=0.1. The polymer matrix *A*-type beads are colored yellow whilst those of *B*-type are cyan. All nanoparticles beads are colored green.

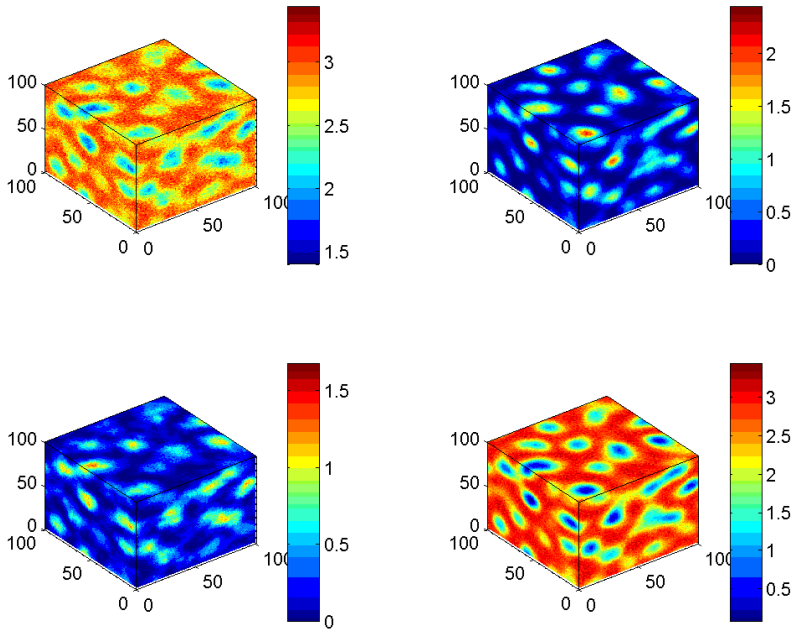

(a)

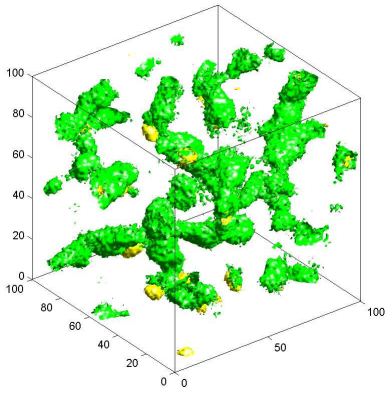

(b)

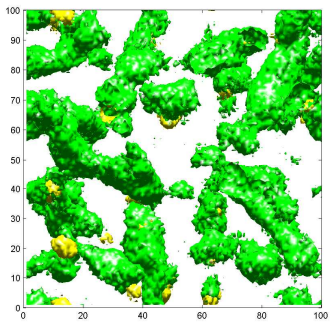

(c)

Figure 4.31. (a) Three-dimensional bead density representation: top, left: *A*- and *B*-type polymer matrix beads; top, right, *A*-type polymer matrix beads; bottom, left: total nanoparticle beads; bottom, right, *B*-type polymer matrix beads. (b) Three-dimensional and (c) lateral isosurface visualization of the simulated PPN structure with spherical morphology and particles covered by a A_1N_{11} type covering at VF=0.1. The polymer matrix *A*-type beads are colored yellow whilst those of *B*-type are cyan. All nanoparticles beads are colored green.

As the filling fraction of the nanoparticles increases, the distributions become narrower. At higher concentration of particles in the diblock copolymer matrix, dispersion of particles in the PS domain becomes increasingly unfavourable as the PS chains must stretch further to accommodate more nanoparticles. This increase in stretching penalty cannot be offset by particle translational entropy, and thus particles are prevented from spreading throughout the PS domains. To accommodate higher volume of particles without incurring in a lager stretching penalty, more particles localize near the center of the compatible PS domain. As a result, the width of the particle distribution in the PS domain profile narrows as the filling fraction increases.

4.4 Conclusions and future perspectives

Macromolecular self-assembly has the potential to address the ever-growing demand for arranging nanostructures that serve as building blocks for sensors, photonic, and nanobiodevices, just to name a few. Block copolymer films and bulk samples, in particular, have been used to spatially organize nanoparticles, thus creating polymer-particle nanocomposites (PPNs) with outstanding thermophysical properties. Yet, to fully utilize their advantageous magnetic, electronic, catalytic and optical properties, PPNs must be patterned and accessed over large areas with nanoscale precision and selectivity, and these issues still constitute key, critical steps in the large scale production of these systems.

Molecular simulations provide an excellent opportunity to directly study the influence of nanoparticles the structure and dynamics of polymeric matrices, since detailed information on the properties near a nanoparticle surface is difficult to obtain experimentally. Accordingly, in this work we used *Dissipative Particle Dynamics* (DPD), a recently developed mesoscopic simulation technique, to model and characterize the morphology, self-assembly, and distribution of nanoparticles in different *A*-*B* diblock copolymer matrices. The DPD parameters of the systems were calculated according to a multiscale modeling approach.

In summary, we designed a system consisting of an *A*-*B* diblock copolymer matrix containing nanoparticles whose surfaces were chemically modified to be energetically similar to one of the blocks or amphiphilic with respect to the two blocks.

Upon incorporating the particles into the copolymer matrix, we demonstrated precise control of the location of the nanoparticles within the matrix simply by varying the composition of the ligands on the particle surfaces, in agreement with some experimental evidences.

Particles with a mixture of PS and PVP chains attached to the surface adsorb principally at the interface between PS and PVP blocks. In these cases, for instance, if the copolymer matrix was to be dissolved from the system, the remaining inorganic phase could give origin to a nanoporous material, with a regular arrangement of uniform pores, which could find applications, for instance, in separation or catalytic processes.

On the other hand, particle with only PS and PVP chains attached to the surfaces segregate near the center of the compatible domain or at the interface according to the grafting density of the ligands. If particles are localized near the centers of the corresponding compatible domains (being these lamellae or cylinders for instance), they form nanowire-like structures that extend throughout the material. In effect, the interplay between microphase separation and favorable interactions do result in the self-assembly of spatially ordered nanocomposites. Should these particles be, for instance, metals or semiconductors, these

systems could constitute a sort of nanoelectrode array, which could be utilized to fabricate organized nanodevices.

Further, the control of nanoparticle location by varying composition and areal chain density of ligands on the particle surfaces is a simple and versatile method that can be extended to other block copolymer and particle systems.

The results also indicate that the morphologies of the organic/inorganic hybrid materials can be tailored by adding particles of specific size and chemistry. The findings highlight the fact that, in such complex mixtures, it is not simply the ordering of the copolymers that templates the spatial organization of the particles: the particles do not play a passive role and can affect the self-assembly of the polymeric chains. In fact, we detected a phase transition from the hexagonal to lamellar morphology induced by a non–selective (i.e., A_6B_6) block-particle interaction, indication that the particles actively contribute to the determination of the system structure.

In conclusion, the proposed multiscale computational approach, which combines atomistic and mesoscale simulations, can yield important information for the design of PPNs with desired morphology for novel applications.

In this contribution we clearly demonstrated that the ability to precisely control nanoparticle location within a block copolymer matrix relies on the enthalpic interactions between the particle surface, the polymer ligands, and the block copolymer template, interaction that depends on the fraction and on the areal chain density of the polymer ligands. Thus, the surface chemistry and the areal chain density are critical parameters for controlling the nanoparticle location within the PS-PVP template.

In particular, the ability of the PS chains ligands to shield the surface of the gold nanoparticles from PVP block chains logically depends on the character of the PS chains assembled on the gold nanoparticle.

Further, the size effect of selective particles in a block copolymer matrix has been investigated theoretically[33] and experimentally,[34] showing that the particles size is one of the major factors influencing the particles location within a block copolymer matrix. While the behavior of selective particles has been studied intensively, the effect of the size of nanoparticles that are attracted enthalpically to the interface has not been fully investigated.

The model proposed in this work for the nanoparticle –i.e. a icosahedron whose surface can be tailored varying the nature of the constituents- was able to correctly reproduce the different arrangements of the nanoparticles in a block copolymer template as function of the surface chemistry of the nanoparticle. More, this model highlights, in agreement with some experimental evidences, a transition in the distribution of the nanoparticles from the compatible domain when the particle is completely shielded from the interactions, to the interface between the two blocks of the copolymer, when the particle is partially exposed.

Nevertheless, a deeper insight into the enthalpic and entropic phenomena governing the local spatial arrangement of the nanoparticles within a block copolymer matrix can be achieved by the employ of a more sophisticated model. This model will able to evaluate the effect of nanoparticle size on the ultimate morphology of the matrix and on the dispersion of

[33] a) Thompson, R. B.; Ginzburg, V. V.; Matsen, M. W. Balazs, A. C. *Science* **2001**, *292*, 2469-2472; Thompson, R. B.; Ginzburg, V. V.; Matsen, M. W.; Balazs, A. C. *Macromolecules* **2002**, *35*, 1060-1071.

[34] a) Bockstaller, M. R.; Lapetnikov, Y.; Margel, S.; Thomas, E. L.; *J. Am. Chem. Soc.* **2003**, *125*, 5276-5277; b) Spontak, R. J.; Shankar, R.; Bowman, M. K.; Krishnan, A. S.; Hamersky, M. W.; Samseth, J.; Bockstaller, M. R.; Rasmussen, K. O. *Nano Lett* **2006**, *6*, 2115-2120.

the particles. The distribution and the mobility of the ligand chains attached on the Au surface will be also explicitly taken into account.

A preview of the nanoparticle model we are currently working on is shown in Figure 4.32.

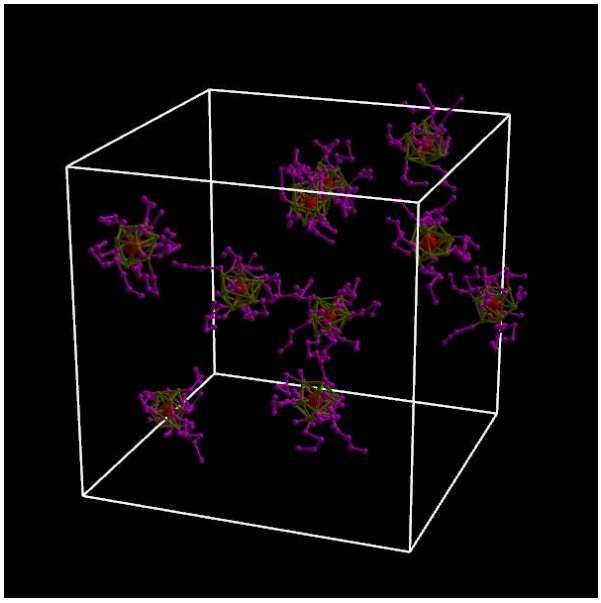

Figure 4.32. Future improvement of the nanoparticle model proposed in this work. Explicit ligand chains attached to the surface are colored in purple.

The explicit introduction of the ligands chains chemically bound to the Au surface will allow a more effective description of the environments surrounding the core of the nanoparticle, will estimate the effects of the mobility of the chains in shielding the interaction, will include the molecular weight of the ligands chains, providing an even more powerful instrument for the investigation of nanocomposite systems with grafted nanoparticles.

Chapter 5

Multiscale property prediction of hybrid organic-inorganic nanocomposites

A current challenge of physical, chemical and engineering sciences is to develop theoretical tools for predicting structure and physical properties of hybrid organic inorganic nanocomposite from the knowledge of a few input parameters. However, despite all efforts, progress in the prediction of macroscopic physical properties from structure has been slow. Major difficulties relate to the fact that (a) the microstructural elements in multiphase materials are not shaped or oriented as in the idealizations of computer simulations, and more than one type can coexist; (b) multiple length and time scales are generally involved and must be taken into account, when overall thermodynamic and mechanical properties wish to be determined, and finally (c) the effect of the interphases/interfaces on the physical properties is often not well understood and characterized. As a consequence, their role is often neglected in the development of new theoretical tools or they are treated in a very empirical way. In this work, we focused on issues (b) and (c) in a multiscale molecular simulation framework, with the ultimate goal of developing a computationally-based nanocomposite designing tool. In particular, we developed a hierarchical procedure in which lower scale (i.e., QM, MD and /or MC) simulations are performed to obtain parameters for higher scale (i.e., mesoscopic and/or finite element) calculations, from which the bulk properties of the hybrid nanocomposite material can be ultimately estimated.

An excerpt of this work is published in Maly, M.; Posocco, P.; Fermeglia, M.; Pricl, S. *Molecular Simulation* **2008**, *34*, 1215-1236.

5.1 Introduction

Nanoscience and nanotechnology are opening new avenues in the fields of chemistry and physics of matter. In particular, the chance to create new, *smart* substances starting from a molecular level clearly constitutes an appealing way to design materials which possess targeted and well-defined macroscopic properties. In this scenario, the molecular building

block – a nano-object – is usually an isolated entity (e.g., a molecule or an ensemble of nanoparticles) prepared at the nanometric scale which exhibits a specific chemical and/or physical property. Sol-gel formation technique constitutes one of the most actual, promising and convenient way to prepare nanomaterials, as it can be produced by using one-step processes which are flexible, efficient, and can be carried out in a wide range of operative conditions.[1] Moreover, different devices characterized by different shapes – matrices, fibers, etc. – can be easily obtained. With this well-established synthesis technique inorganic materials (glassy or ceramic) and hybrid inorganic-organic (I/O) polymers or nanocomposites can be processed to form (nano)particles, coatings, fibers, or bulk materials. Inorganic-organic sol-gel-derived materials had been investigated and commercialized a few decades ago and, due to the profound understanding of the underlying chemical and technical processes, are still present as important examples of large-scale applications of the sol-gel technology.[2]

These hybrid materials combine the advantages of their constituents, like high transparency, high refractive index, good chemical resistance (glass-like), low weight, flexibility, good impact resistance, low processing temperatures (polymer-like), sufficient thermal stability (silicone-like), and are easily accessible because of an unique availability of the respective precursors (commercially available metal alkoxides and organo(alkoxy)silanes as well as nanoparticles). Besides the simple metal or silicon alkoxides that - after hydrolysis - lead to the formation of an inorganic oxidic network, organo(alkoxy)silanes can be used to incorporate polymerizable organic substituents (epoxy, vinyl, or methacryloxy groups) into the final product, because the Si-C bonds in these molecules are stable under the mild conditions of sol-gel processing. The polymerization reactions of the functional organic groups can be induced by thermal or photochemical means, thereby cross-linking the preformed nanosized inorganic moieties.

Inorganic-organic hybrids can be grossly divided into two major classes.[3] In *class I*, organic molecules, pre-polymers or even polymers are embedded in an inorganic matrix. These materials are synthesized by carrying out the hydrolysis and condensation of the inorganic compound, i.e., the formation of the inorganic network, in the presence of the organic compound or by polymerizing organic monomers in porous inorganic hosts. Only weak bonds exist between both phases. In *class II*, the inorganic and organic components are connected by covalent bonds. This approach requires molecular precursors that contain a hydrolytically stable chemical bond between the element that will form the inorganic network during sol-gel processing and the organic moieties.

If the hybrid system is not built up from nanocrystalline components, the intricate mixture of inorganic and organic phases in most cases leads to amorphous materials. Further, because of the complexity of the possible chemical reactions and the numerous parameters influencing the hydrolysis and condensation of organo-(alkoxy)silanes (pH, temperature, catalyst, water/silane ratio) a more or less broad distribution of dimers, oligomers, and higher condensation products can be expected. The results can be interpreted in the sense of initial formation of small clusters or oligomers, which grow to larger polycondensates presumably by a cluster-cluster aggregation mechanism. The peripheral positions of the organic substituents are important to allow subsequent polymerization reactions to crosslink the individual inorganic condensates and embedding them into an organic matrix. The high

[1] Brinker, C. J.; Scherer, G. W.; *Sol-Gel Science, The Physics and the Chemistry of Sol-Gel Processing*, Academic Press, New York, USA, 1990.

[2] Schottner, G. *Chem. Mater.* **2001**, *13*, 3422-3445.

[3] Judeistein, P.; Sanchez, C. *J. Mater. Chem.* **1996**, *6*, 511-525.

transparency of the resulting hybrid polymers is a further hint to their submicrometer or nanostructural phase size.

Compared to other chemical elements, silicon is one of the most convenient and productive element for the preparation of the organically modified alkoxides required for the design and synthesis of hybrid organic-inorganic (O/I) materials. A plethora of reasons speak in favor of the peculiar character of silicon, among which the transparency, thermal, and chemical stability of Si-O-Si networks, and the "sweet chemistry" involved in their synthesis are just a few.[4,5] Generally speaking, the polycondensation reaction of alkoxysilanes results in a variety of structures, ranging from monodisperse silica particles to polymer networks, depending of the reaction conditions involved.[6] In addition, copolymerization of alkoxysilanes of different functionalities makes it possible to tailor the ultimate material structure and performance. For example, tetrafunctional alkoxysilanes form densely crosslinked silica structure SiO_2, trifunctional monomers polymerize to branched polysilsesquioxanes (PSSQOs) of the general formula $RSiO_{3/2}$, whilst bifunctional alkoxysilanes generally yield linear polymer chains $(R_2SiO)_n$. Ring formation is also a peculiar feature of alkoxysilanes polymerization reactions; clearly, the presence and amount of cyclic structures exert an influence on the ultimate structure and performances of the O/I hybrids.[7,8,9,10]

Properties of the microheterogeneous organic-inorganic hybrids depend, to a good extent, on an interphase interaction determining the morphology. Strong interactions, for instance, leads to a reduction of the size of inorganic domains in the organic medium, and often improve the properties. Therefore, organofunctional trialkoxysilane monomers are used to prepare hybrid polymers and are employed as coupling agents, mainly in coating materials. 3-glycidyloxypropyltrimethoxysilane (GPTMS) is an organofunctional alkoxysilane monomer that can undergo both the sol-gel polymerization of the alkoxy groups and curing of the epoxy functionality to form a hybrid network with covalent bonds between organic and inorganic phases. Routinely, however, polymerization of GPTMS is carried out by a sol-gel process which leads to the formation of PSSQO structures with pendant, unreacted epoxy functionalities that are prone to later, eventual curing.[7] O/I hybrid materials based on GPTMS have several important applications, including antiscratch coatings,[11] contact lens materials,[12] passivation layers for microelectronics,[13] multifunctional coatings,[14] and optical devices.[15,16,17] GPTMS-based optical waveguides, in particular, are very promising materials because of the possibility to incorporate optically active organic molecules in a matrix that is dense at low temperature and with a high degree of microstructural homogeneity.[18,19] Accordingly, this extensive range of applications continues to attract various studies on

[4] Sanchez, C.; Soler-Illia, G. J. d. A. A.; Ribot, F.; Lalot, T.; Mayer, C. R.; Cabuil, V. *Chem. Mater.* **2001**, *13*, 3061-3083.
[5] Livage, J.; Sanchez, C. *J. Non-Cryst. Solids* **1992**, *145*, 11-19.
[6] Kelts, L. W.; Armstrong, N. J. *J. Mater. Res.* **1989**, *4*, 423-433.
[7] Mateika, L.; Dukh, O.; Brus, J.; Simonsick, W. J. Jr.; Meissner, B. *J. Non-Cryst. Solids* **2000**, *270*, 34-37.
[8] Eisenber, P.; Erra-Balsells, R.; Ishikawa, Y.; Lucas, J. C.; Mauri, A. N.; Nonami, H.; Riccardi, C. C.; Williams, R. J. J. *Macromolecules* **2000**, *33*, 1940-1947.
[9] Matejka, L.; Dukh, O.; Hlavata, D.; Meissner, B.; Brus, J. *Macromolecules* **2001**, *34*, 6904-6914.
[10] Brus, J.; Spirkova, M.; Hlavata, D.; Strachota, A. *Macromolecules* **2004**, *37*, 1346-1357.
[11] Nass, R.; Arpac, E.; Glaubitt, W.; Schmidt, H. *J. Non-Cryst. Solids* **1990**, *121*, 370-374.
[12] Philipp, G.; Schmidt, H. *J. Non-Cryst. Solids* **1984**, *63*, 283-292.
[13] Popall, M.; Kappel, J.; Pilz, M.; Schulz, J.; Feyder, G. *J. Sol-Gel Sci. Technol.* **1994**, *2*, 157-160.
[14] Schmidt, H. *J. Non-Cryst. Solids* **1994**, *178*, 302-312.
[15] Sorek, Y.; Zevin, M.; Reisfeld, R.; Hurvits, T.; Rushin, S. *Chem. Mater.* **1997**, *9*, 670-676.
[16] Knobbe, E. T.; Dunn, B.; Fuqua, P. D.; Nishida, F. *Appl. Opt.* **1990**, *29*, 2729-2733.
[17] Sorek, Y.; Reisfeld, R.; Tenne, R. *Chem. Phys. Lett.* **1994**, *227*, 235-242.
[18] a) Guglielmi, M.; Brusatin, G.; Della Giustina G. *J. Non-Cryst. Solids* **2007**, *353*, 1681-1687; b) Della Giustina, G.; Brusatin, G.; Guglielmi M.; Romanato F. *Mat. Sci. Eng. C* **2007**, *27*, 1382-1385; c) Brusatin, G.; Della Giustina, G.; Guglielmi, M.; Casalboni, M.; Prosposito, P.; Schutzmann S.; Roma G. *Mat. Sci. Eng. C* **2007**, *27*, 1022-1025.
[19] Zevin, M.; Reisfeld, R. *Opt. Mater.* **1997**, *8*, 37-41.

GPTMS hybrid O/I systems. These nanocomposites have received broad attention for optical applications in both fundamental and applied research in recent years, due to their outstanding physical and chemical properties resulting from their hybrid nature.

The incorporation of inorganic particles into polymers allows one to integrate new functions inside polymer matrices. For transparent plastics, of interest for optical applications, modification of the matrix by dispersing a second inorganic component into the polymer typically results in a significant loss of transparency due to scattering from large particles or agglomerates. A novel approach for the functionalization of transparent plastics is the incorporation of high refractive index (RI) building block (such as TiO_2, ZrO_2, PbS, ZnS) on the nanoscale. In particular, ZnS semiconductors and their nanoparticles have been widely used in flat-panel displays, electroluminescence devices, light-emitting diodes, nonlinear optical devices and infrared window materials.[20] Two approaches, *in situ* formation of nanoparticles in pre-synthesized polymer and direct blending of pre-made nanoparticles and polymer or polymer precursors (*ex situ*), have been developed to prepared nano-ZnS/polymer nanocomposites. The latter provides full synthetic control over both the nanoparticles and the matrix, and is a more effective way for preparing nanocomposites.[21]

For the design of nanocomposites for optical applications, one of the technical challenges is the requirement to retain transparency whilst avoiding phase separation between organic and inorganic moieties. Control over particle size and size distribution as well as uniform dispersion of the building blocks at the nanometre scale within the matrix is a critical issue for improving the transparency and overall properties of these nanocomposites. This is also a technological challenge for the design and synthesis of high RI organic–inorganic nanocomposites because nanoscale building blocks, such as nanoparticles with high specific surface energies and inherent hydrophilicity, are prone to aggregation, even before incorporation into an organic-inorganic matrix. Hence, the prerequisites for synthesizing high RI transparent nanocomposites, especially those with high nanophase content, are: the appropriate design and tailoring for the nanoscale building blocks and matrices, such as surface engineering of nanoparticles; the fabrication approaches of nanocomposites and the improvement of the compatibility between the inorganic domains and the matrix.

To obtain optimized formulations and efficient technological processes, however, extensive experimental campaigns must be carried out; further, some sound theories in conjunction to experiments must be developed, in order to gain some fundamental knowledge about the physical/chemical phenomena at the basis of the properties of these materials. On the other hand, on the spur of actual industrial competition, the number of lengthy and costly experiments must be drastically reduced, and the establishment of reliable, accurate theories is urgently needed, to be able to design molecular systems with fine-tuned, targeted properties.

Computer-based molecular simulation nowadays constitutes a versatile, efficient and reliable tool to achieve these goals. Indeed, these techniques can be of great help in reducing experimental hard work by sorting out useless trials and addressing the synthesis and characterization to more productive efforts. Accordingly, in this work we developed a computational strategy to obtain realistic molecular models of crosslinked polymer networks based nanocomposites. We consider a model system based on a GPTMS network; “pre-

[20] a) Lü, C.; Cui, Z.; Wang, Y.; Li, Z.; Guan, C.; Yang, B.; Shen J. *Mater. Chem.* **2003**, *13*, 2189 – 2195; b) Zhao, Y.; Wang, F.; Fu, Q.; Shi, W. *Polymer* **2007**, *48*, 2853-2859; c) Duttaa, K.; Mannab, S.; Deb, S. K. *Synthetic Metals* **2009**, *159*, 315–319; d) Burunkova, J. E.; Denisyuk, Y. D.; Williams T. R. *Journal of Applied Polymer Science* **2010**, *116*, 1857–1866.

[21] Lu, C.; Cheng, Y.; Liu, Y.; Liu, F.; Yang, B. *Adv. Mater.* **2006**, *18*, 1188-1192.

made" nanoscale building blocks, i.e. ZnS nanoparticles, are dispersed in the sol-gel derived hybrid system. This is intended to mimic the so called "*ex-situ*" sol-gel route, one of the more suitable synthesis methods for large scale industrial applications. The nanoparticles are chemically modified with (3-mercaptopropyl)trimethoxysilane (MPTMS), in order to evaluate the influence of the surface engineering on the interface energies between nanoparticles and matrix and ultimately on their aggregation behavior.

Briefly, our procedure consists in: (*a*) development of a molecular dynamics (MD) Perl script to mimic the formation of 3D hybrid O/I networks based on the condensation reaction of GPTMS under acid conditions; (*b*) quantum/force-field based atomistic simulation to derive molecular interaction energies between GPTMS matrix and ZnS nanoparticle; (*c*) mapping these values onto mesoscopic *Dissipative Particle Dynamics* (DPD) parameters; (*d*) mesoscopic simulations to determine system density distributions, nanoparticle dispersion, and morphologies; a Reactive *Dissipative Particle Dynamics* approach is employed to reproduce the reticulation of the polymer matrix at mesoscale level; (*e*) simulations at finite-element level to calculate the relative macroscopic properties of the nanocomposite.

5.2 Computational methods

5.2.1 Atomistic model and details of the GPTMS matrix simulation

Model building and general computational recipe

A fully hydrolyzed GPTMS molecule was selected as the starting monomer, and its condensation reaction under acid conditions was considered. This practically corresponds to a situation in which only the creation of Si-O-Si bonds between the available Si-O-H moieties takes place, leaving the epoxy groups unreacted (see Figure 5.1).[9]

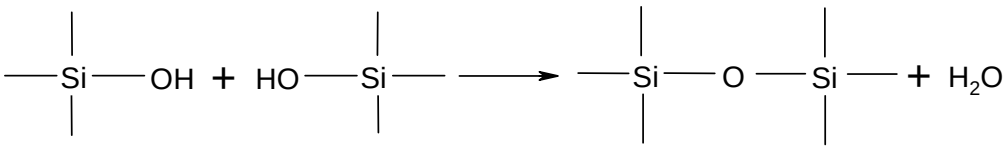

Figure 5.1. Scheme reaction leading to the Si-O-Si network formation.

For the generation of the final crosslinked system, the following general computational recipe (script details in Appendix A) was applied:

Step 1. The molecular model of the hydrolyzed GPTMS molecule was built, and its atoms were typed and charged using the *Compass* forcefield (FF).[22,23] The molecular geometry was then optimized again using *Compass* FF. In order to test the eventual influence of the partial charge distribution on the physical properties of the final crosslinked system, we also assigned to the previously geometry optimized molecule a partial charge scheme obtained recharged using the quantum semi empirical method *AM1-ESP* as implemented in the *Vamp* toolbox of *Materials Studio*. At the end of ***Step 1***, then, two molecular models of the

[22] Sun, H.; Rigby, D. *Spectrochim. Acta Part A* **1997**, *53*, 1301-1323.
[23] Sun, H. *Macromolecules* **1995**, *28*, 701-712.

hydrolyzed GPTMS monomer with the identical shape but different partial charges were obtained and used for further calculations.

Step 2. 100 hydrolyzed GPTMS molecules were packed into a simulation box under periodic boundary conditions using the *Amorphous Cell* builder modulus of *Materials Studio*. The initial density of the liquid mixture was set to 1.57 g/cm^3, a value estimated from the average experimental density of the final crosslinked system assuming an ideal case of 100% condensation (1.35 g/cm^3).[24] To start the condensation reaction/networking process from a representative initial system, 100 different simulation boxes were independently created for each charge scheme considered (i.e., 200 3D cells were obtained overall). After geometry relaxation of each 3D box, the one with the lowest energy value was selected, - namely structures I - one for each charge scheme, for running the molecular dynamics (MD) simulations. Finally, in order to determine the eventual influence of the choice of the initial structure on the simulation results, two further, independent MD simulations for each charging case on structures characterized by approximately the same energy value of structure I after relaxation – namely structures II, were also conducted and analyzed.

Step 3. The selected 3D boxes containing the initial GPTMS monomer systems were first subjected to a geometry optimization (2000 steps); then simulated annealing procedure was applied[25,26,27,28,29,30] (8 cycles of 1000 MD steps, temperature range 200K - 500K). 5000 steps of molecular dynamics a room temperature (298 K) were carried out. All simulations were conducted in the canonical (*NVT*) ensemble. After preliminary trials, an integration time step of 0.2 fs finally was selected, giving a total annealing time of 1.6 ps, and an overall MD time of 1 ps.

Step 4. The distances between the reactive atoms (O and H atoms from each OH group linked to the Si atom, see Figure 5.1) were measured and ordered in an increasing order. The three closest pairs of reactive atoms whose distances were smaller than the selected reactive cut-off distance (3 Å) were identified, and between the corresponding Si atoms new Si-O-Si bonds were created. An equivalent number of water molecules were deleted from the system (see Figure 5.2). The reactive cut-off distance was increased during the networking formation from 3 Å to 6 Å. Since the presence of small, strained rings (i.e., with less than 4 Si atoms) in the final system is not found experimentally in hybrid O/I systems based on GPTMS,[7,31] the necessary restrictions were implemented in the corresponding script, as described in details in Appendix A.

Step 5. Steps 3 (referred to the actual cell) and ***4*** were repeated until no more pairs of reactive atoms satisfying all criteria were detected in the system.

After the GPTMS 3D network, structures were built starting from the two partial charge schemes and applying the script protocol (i.e., two structures I and two structures II), each system was subjected to further annealing cycles up to 600K. The minimum energy structure for each system was selected for further *NVT* and *NPT* molecular dynamics simulation at 300K for data collection. The velocity Verlet algorithm was used for integration in all MD simulations. A time step of 0.2 fs, and the Nosè/Berendsen thermostat were employed for *NPT* and *NVT* MD simulations, respectively. The cut-off for non-bond interactions was set at 9.50 Å.

---

[24] Brusatin, personal communication, 2007.
[25] Scocchi, G.; Posocco, P.; Fermeglia, M.; Pricl, S. *J. Phys. Chem. B* **2007**, *111*, 2143-2151.
[26] Fermeglia, M.; Cosoli, M.; Ferrone, M.; Piccarolo, S.; Mensitieri, G.; Pricl, S. *Polymer* **2006**, *47*, 5979-5989.
[27] Fermeglia, M.; Ferrone, M.; Pricl, S. *Mol. Simulation* **2004**, *30*, 289-300.
[28] Toth, R.; Coslanich, A.; Ferrone, M.; Fermeglia, M.; Pricl, S.; Miertus, S.; Chiellini, E. *Polymer* **2004**, *45*, 8075-8083.
[29] Fermeglia, M.; Ferrone, M.; Pricl, S. *Fluid Phase Equilib.* **2003**, *212*, 315-329.
[30] Fermeglia, M.; Pricl, S. *AIChE J.* **1999**, *45*, 2619-2627.
[31] Fidalgo, A.; Ilharco, L. M. *J. Non-Cryst. Solids* **2001**, *283*, 144-154.

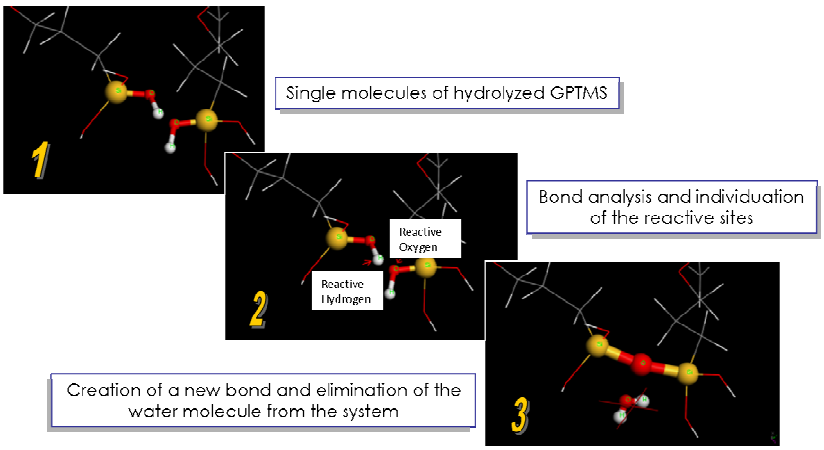

Figure 5.2. Details of the GPTMS molecular modeling showing, in stick-and-ball representation, the reactive atom pairs (top), and the newly formed Si-O-Si bond and the corresponding deleted water molecule (bottom). All other atoms are in line rendering. Color code: Si, gold; O, red; C, gray, H, white.

The final density of the MD equilibrated systems corresponding to the two different atomic partial charge schemes, *AM1-ESP* and *COMPASS*, respectively, is reported in Table 5.1. As can be seen from Table 5.1, the equilibrated network densities obtained from initial structure modelled with both partial charge schemes are utterly similar; further, starting from two different annealed initial GTPMS 3D boxes (i.e., structure I and structure II), leads to the same network final density values, thus validating the initial structure selection protocol.

Atomic partial charge scheme	Initial structure I ρ (g/cm^3)	Initial structure II ρ (g/cm^3)
AM1-ESP	1.368	1.369
COMPASS	1.371	1.368

Table 5.1. MD equilibrated density values ρ for the 3D GPTMS-based O/I network structures obtained from the simulations.

Mechanical properties (elastic constants) determination

The mechanical behavior of a given molecular system can be described by using continuum mechanics. Since, however, any molecular system has a discrete structure, the model to be employed for the estimation of the elastic constants is an equivalent-continuum model,[32] in which the overall mechanical response of representative volume elements to an applied set of boundary conditions is equivalent to the response of the molecular representative volume system subjected to the same set of boundary conditions. The equivalent-continuum is assumed to have a linear-elastic constitutive behavior. The generalized constitutive equation of the equivalent continuum hence is given by:

[32] Odegard, G. M.; Gates, T. S.; Nicholson, L. M.; Wise, K. E. *Compos. Sci. Technol.* **2002**, *62*, 1869-1880.

$$\sigma_{ij} = C_{ijkl}\,\varepsilon_{kl} \tag{5.1}$$

where σ_{ij} are the components of the stress tensor (i,j =1,2,3), C_{ijkl} are the components of the linear-elastic stiffness tensor, and ε_{kl} are the components of the strain tensor. It is further assumed that the system has isotropic material symmetry.

In atomistic calculation, the internal stress tensor in a system can be obtained using the virial expression:

$$\sigma = -\frac{1}{V_0}\left[\left(\sum_{i=1}^{N} m_i\left(\mathbf{v}_i\,\mathbf{v}_i^T\right)\right)+\left(\sum_{i<j} r_{ij}\,\mathbf{f}_{ij}^T\right)\right] \tag{5.2}$$

where index i runs over all particles through N, m_i and $\mathbf{v}_i$ are the mass and the velocity of the particle, respectively, $\mathbf{f}_i$ is the force acting on the particle, and V_0 is the undeformed system volume.

Basically, two classes of methods for calculating material elastic constants using molecular simulations are available in literature at present. Consistently, the static method (i.e., based on molecular mechanics) was found to be more practical and reliable than the one based on molecular dynamics.[33] Thus, a constant strain minimization method, belonging to the class of static methods, was applied to the equilibrated 3D O/I network system. Accordingly, after an initial system energy minimization, three tensile and three pure shear small deformations (to remain within elastic limits) are applied. The system is then again energy minimized following each deformation. The stiffness matrix is calculated from the second derivative of the potential energy U with respect to strain ε as follows:

$$C_{ij} = \frac{1}{V}\frac{\partial^2 U}{\partial\varepsilon_i\,\partial\varepsilon_j} = \frac{\partial\sigma_i}{\partial\varepsilon_j} = \frac{\sigma_{i+}-\sigma_{i-}}{2\varepsilon_j} \tag{5.3}$$

where σ_i is the ith component of the internal stress tensor, and σ_{i+} and σ_{i-} are the components associated with the stress tensor under tension and compression, respectively.[34] The Lamé constants for the structure - λ and μ - can in turn be calculated from the related stiffness matrix:

$$\lambda = \frac{1}{3}\left(C_{11}+C_{22}+C_{33}\right)-\frac{2}{3}\left(C_{44}+C_{55}+C_{66}\right) \tag{5.4}$$

$$\mu = \frac{1}{3}\left(C_{44}+C_{55}+C_{66}\right) \tag{5.5}$$

For isotropic materials, the stress-strain behavior can be finally be described in terms of the Lamé constants according to the equations:

$$E = \mu\frac{3\lambda+2\mu}{\lambda+\mu} \tag{5.6}$$

[33] Raaska,T.; Niemela, J. S.; Sundholm, F. *Macromolecules* **1994**, *27*, 5751-5757.
[34] Theodorou, D. N.; Suter, U. W. *Macromolecules* **1986**, *191*, 139-154.

$$G = \mu \tag{5.7}$$

$$B = \lambda + \frac{2}{3}\mu \tag{5.8}$$

$$\nu = \frac{\lambda}{2(\lambda + \mu)} \tag{5.9}$$

where *E*, *G*, *B*, and *v* represent Young's modulus, shear modulus, bulk modulus and Poisson's ratio, respectively.

Constant pressure heat capacity determination

Statistical fluctuations about the mean values of quantities measured during the course of an MD simulation can be directly related to thermodynamic properties. Beside common average quantities like density, pressure, or energy, the analysis of fluctuations allows to determine properties like heat capacities, compressibility, thermal expansion coefficient, or the Joule-Thomson coefficient. Specific heat capacity at constant pressure C_P, for instance, is obtained from the fluctuations of energy in the isothermal-isobaric ensemble (*NPT*) according to:

$$C_P = \frac{1}{kT^2}\left\langle \partial(K + U + pV)^2 \right\rangle \tag{5.10}$$

where *k* is the Boltzmann constant, *K* and *U* denote the instantaneous values of the kinetic and potential energy, respectively, and *T*, *P*, and *V* are the familiar thermodynamic state variables. In addition, the notation δX stands for X-<X>, where <X> denotes the ensemble average value of a given quantity *X*.

5.2.2 Atomistic model and details of the GPTMS+ZnS simulation

All atomistic simulations were performed using *Materials Studio* (v 4.1 Accelrys, San Diego, CA). a=5.4093. As far as the ZnS (sphalerite) model is concerned, starting from relevant crystallographic coordinates,[35] we built the unit cell using the *Crystal Builder* module of *Materials Studio*. Accordingly, the resulting lattice is cubic, space group F43*m*, with a unit cell of *α*=*b*=*c*=5.4093 Å, and *α*=*β*=*γ*=90°, in excellent agreement with experimental prediction. We chose sphalerite as it is recognized as the most stable phase of zinc sulphide polymorphs, and for the same reason we selected the (110) surface. We replicated the basic cell in order to obtain a super cell of approximately 3.2 x 3.2 x 1.1 nm^3 size (6 x 6 x 2).

Then, we modelled the surface modifier, chosen to be a (3-mercaptopropyl) trimethoxysilane (MPTMS) molecule. The modifier conformational search was carried out using *Compass* FF, and applying our validated combined molecular mechanics/molecular dynamics simulated annealing (MDSA) protocol.[25-30,36] The choice of the *Compass* FF resulted

[35] Smith, F. G. *American Mineralogist* **1955**, *4O*, 658-675.

[36] a) Fermeglia, M.; Ferrone, M.; Pricl, S. *Bioorg. Med. Chem.* **2002**, *10*, 2471-2478; b) Felluga, F.; Pitacco, G.; Valentin, E.; Coslanich, A.; Fermeglia, M.; Ferrone, M.; Pricl, S. *Tetrahedron: Asymmetry* **2003**, *14*, 3385-3399; c) Pricl, S.; Fermeglia, M; Ferrone, M.; Asquini, A. *Carbon* **2003**, *41*, 2269-2283; d) Metullio, L.; Ferrone, M.; Coslanich, A.; Fuchs, S.; Fermeglia,

from a compromise between good accuracy and availability of FF parameters for all atom types present in the molecular model. The relaxed molecular structure is subjected to repeated temperature cycles using constant volume/constant temperature (*NVT*) MD conditions. At the end of each annealing cycle, the structure is again energy minimized, and only the structure corresponding to the minimum energy is used for further modeling.

Resorting to atomistic MD simulation in NVT ensemble allows the retrieval of important information on the interaction and binding energies values between the different components of a nanocomposite system.[27,28,29,37,38,39,40,41] The technique basically consists in simulating the interface between the zinc sulfide surface and the GPTMS network by building a cell that is stretched along the *c*-direction (up to 150 Å); in this way, even if the model is still 3-D periodic, there are no interaction between the periodic images in the *c*-direction, ultimately resulting in a pseudo 2-D periodic system,[42] from which the binding energies between all system components can be calculated.

According to this approach, we created a cell of 150 Å in height, and we copied and chemically linked a certain number of MPTMS molecules (15 molecules) to the surface and finally we added the GPTMS network to the system.

The *NVT* molecular dynamics were performed with *Materials Studio Discover* module. Each simulation was run at 298 K for 550 ps, applying the Ewald summation method for treating Coulomb interactions; an integration step of 1 fs and Nosé thermostat (Q = 1) were also adopted. The energetic analysis was conducted only on the parts of the trajectory with steady state behavior. During each MD ZnS layers were treated as rigid bodies by fixing their position in time.

The procedure used to calculate the interaction energies and, hence, the binding energies values between all system components is well established.[27,28,29,36g),l)]

By definition, the binding energy E_{bind} is the negative of the interaction energy. As an example, to calculate the binary binding energy term E_{bind}(GPTMS/MPTMS), we can first created a GPTMS–MPTMS system deleting the ZnS surface from the equilibrated MD trajectory frames, and then calculated the potential energy of the system $E_{GPTMS/MPTMS}$. Next, we deleted the MPTMS molecules, leaving the GPTMS network alone, and thus calculated the energy of the GPTMS matrix, E_{GPTMS}. Similarly, we deleted GPTMS from the GPTMS–MPTS system, and calculated E_{MPTMS}. Then, the binding energy E_{bind}(GPTMS/MPTMS) is simply obtained from the following equation:

$$E_{bind}\left(GPTMS/MPTMS\right) = E_{GPTMS} + E_{MPTMS} - E_{GPTMS/MPTMS} \qquad (5.11)$$

The remaining binding energy terms E_{bind}(GPTMS/ZnS) and E_{bind}(MPTMS/ZnS), can be calculated in an utterly analogous fashion from the corresponding energy components.

M.; Paneni, M. S.; Pricl, S. *Biomacromolecules* **2004**, *5*, 1371-1378; e) Toth, R.; Ferrone, M.; Miertus, S.; Chiellini, E.; Fermeglia, M.; Pricl, S. *Biomacromolecules*, **2006**, *7*, 1714–1719; f) Posocco, P.; Ferrone, M.; Fermeglia, M.; Pricl, S. *Macromolecules* **2007**, *40*, 2257-2266; g) Scocchi, G.; Posocco, P.; Danani, A.; Pricl, S.; Fermeglia, M. *Fluid Phase Eq.* **2007**, *261*, 366-374; h) Mensitieri, G.; Larobina, D.; Guerra, G.; Venditto, V.; Fermeglia, M.; Pricl, S. *J. Polym. Sci. B: Polym. Phys.* **2008**, *46*, 8-15; i) Cosoli, P.; Scocchi, G.; Pricl, S.; Fermeglia, M. *Micropor. Mesopor. Mater.* **2008**, *1*, 169-179; l) Scocchi, G.; Posocco, P.; Handgraaf, J.-W.; Fraaije, J. G. E. M.; Fermeglia, M.; Pricl, S. *Chem. Eur. J.* **2009**, *15*, 7586-7592.

[37] a) Kasemägi, H.; Aabloo, A.; Klintenberg, M. K.; Thomas J. O. *Solid State Ion.* **2004**, *168*, 249–254; b) Kasemägi, H.; Klintenberg, M. K.; Aabloo, A.; Thomas J. O. *Solid State Ion.* **2002**, *147*, 367–375.

[38] Tanaka, G.; Goettler, L. A. *Polymer* **2002**, *43*, 541-553.

[39] Gardebien, F.; Bredas, J.-L.; Lazzaroni, R. *J. Phys. Chem. B* **2005**, *109*, 12287–12296.

[40] Katti, K. S.; Sikdar, D.; Katti D. R.; Ghosh, P.; Verma, D. *Polymer* **2006**, *47*, 403-414.

[41] Paul, D. R.; Zeng, Q. H.; Yu, A. B.; Lu, G. Q. *J. Colloid Interface Sci.* **2005**, *292*, 462-468.

[42] Misra, S.; Feming, P. D. III; Mattice, W. L.; *J. Comput.-Aided Mater. Des.* **1995**, *2*, 101-112.

Importantly, the binding energies between the individual components of each nanocomposite system estimated using the procedure outlined above will also constitute the input parameters for the higher level, mesoscale simulations, as described later on.

5.2.3 Reactive *Dissipative Particle Dynamics* (RxDPD)

At the mesoscale level, we employed the so called Reactive *Dissipative Particle Dynamics* (RxDPD) simulation technique. The RxDPD method is primarily intended for the prediction of the system composition and the thermodynamic properties of reaction equilibrium polymer systems. The RxDPD formulation has been developed and validated recently by Lisal and coworkers.[43]

This approach combines elements of *Dissipative Particle Dynamics* (DPD)[44] and reaction ensemble Monte Carlo (RxMC)[45,46] for the mesoscale simulation of reaction equilibrium polymer systems, and utilizes the concept of a fractional particle.[47] The fractional particle is coupled to the system via a coupling parameter that varies between zero (no interaction between the fractional particle and the other particles in the system) and one (full interaction between the fractional particle and the other particles in the system). The time evolution of the system is governed by the DPD equations of motion, accompanied by changes in the coupling parameter. The coupling-parameter changes are either accepted with a probability derived from the grand canonical partition function or governed by an equation of motion derived from the extended Lagrangian. The coupling-parameter changes mimic forward and reverse reaction steps, as in RxMC simulations. The RxMC method is a powerful molecular-level simulation tool for studying reaction equilibrium mixtures. The method requires as input only the interaction potentials and the ideal-gas properties of the reaction species that are present. Most notably, the method does not require a reactive type potential that mimics bond breakage and formation. Reactions are simulated by performing forward and reverse reaction steps according to the RxMC algorithm which guarantees that the reaction equilibrium conditions are satisfied.

In a RxDPD simulation, the system is simulated using *Dissipative Particle Dynamics* (DPD). DPD mesoscopic beads are defined by a mass m_i, position r_i, and velocity v_i, and interact with each other via a force $\mathbf{f}_i$ that is written as the sum of a conservative force ($\mathbf{F}_{ij}^{C}$), dissipative force ($\mathbf{F}_{ij}^{D}$), and random force ($\mathbf{F}_{ij}^{R}$)

$$\mathbf{f}_i = \sum_{i \neq j} \left(\mathbf{F}_{ij}^{C} + \mathbf{F}_{ij}^{D} + \mathbf{F}_{ij}^{R} \right) \tag{5.12}$$

where the sum extends over all particles within a given distance r_c from the ith particle. $\mathbf{F}_{ij}^{C}$ is given as the negative derivative of a particle coarse-grain potential, u^{CG}, and the remaining two forces, $\mathbf{F}_{ij}^{D}$ and $\mathbf{F}_{ij}^{R}$, arise from degrees-of-freedom neglected by coarse-graining.

The DPD simulation of cross-linked polymeric matrices and nanoparticles requires incorporating a non-crossing condition by adding bond-bond repulsion to the model.[48] The distance of closest approach between two bonds, *D*, is computed and a repulsive interaction

[43] a) Lisal, M.; Brennan, J. K.; Smith, W. R. *J. Chem. Phys.* **2006**, *125*, 164905, *15 pages;* b) Lisal, M.; Brennan, J. K.; Smith, W. R. *J. Chem. Phys.* **2009**, *130*, 104902, *15 pages*.

[44] Groot, R. D.; Warren, P. B. *J. Chem. Phys.* **1997**, *107*, 4423-4435.

[45] Smith, W. R.; Triska, B. *J. Chem. Phys.* **1994**, *100*, 3019-3027.

[46] Johnson, J. K.; Panagiotopoulos, A. Z.; Gubbins, K. E. *Mol. Phys.*, **1994**, *81*, 717-733

[47] Çagin, T.; Pettitt, B. M. *Mol. Simul.* **1991**, *6*, 5-26

[48] Kumar, S.; Larson, R. G. *J. Chem. Phys.* **2001**, *114*, 6937–6941.

is then applied based on D. The form of the bond-bond repulsion potential, $u_{rep}(D)$, avoiding artificial bond crossing in DPD simulation was given by Pan and Manke[49]

$$u_{rep}(D) = \frac{K_{rep}}{2} D_c \left(1 - \frac{D}{D_c}\right)^2 \qquad (D < D_c) \qquad (5.13)$$

where K_{rep} is the bond-bond repulsion constant, D_c is the bond-bond cut-off distance and $\boldsymbol{D}=\boldsymbol{P}_i+t_i\boldsymbol{R}_i-(\boldsymbol{P}_j+t_j\boldsymbol{R}_j)$; $\boldsymbol{P}_i$ and $\boldsymbol{P}_j$ are midpoints of bonds i and j, respectively, $\boldsymbol{R}_i$ and $\boldsymbol{R}_j$ are the vectors characterizing the direction and length of each bond, and t_i and t_j are parameters which indicate where we are along each bond. The bond-bond cut-off distance was set approximately equal to $0.15r_c$, and the bond-bond repulsion constant to $\approx a_{ij}$ of the specie involved in the bonds.

Crosslinking of polymeric matrix wais mimicked by a reactive potential

$$u_{reac} = \varepsilon \exp\left[-\frac{\left(r_{ij} - r_w\right)^2}{\lambda^2}\right] \qquad (5.14)$$

where ε is the Gaussian well (ε=2), and r_w and λ is its position and width, respectively. The polymer Gaussian-well position corresponds to r_w=0.6 and the polymer Gaussian-well width λ to $(\lambda/r_c)^2$=0.003.

The mass of DPD beads m_i, r_c and kT were used as the unit of the mass, length, and energy, respectively; k is the Boltzmann constant and T is the temperature.

5.2.4 Finite element calculation of macroscopic properties

The prediction of macroscopic properties of GPTMS/ZnS nanocomposites considered in this work, as a function of metal loading, is the final step of the proposed multiscale procedure. To this aim, finite element (FE) calculations were performed using the module *Mesoprop* included in the software Palmyra (v. 2.5, MatSim, Zürich, CH). This software has been validated on different composite material morphologies by several authors,[36l),50,51,52] yielding reliable results.

Mesoprop technique is a method based on finite elements for estimating properties of complex materials starting from the density distribution at the mesoscale. *MesoProp* links the physical properties of pure materials to the properties of multicomponent bulk materials systems. The method uses the results of a mesoscale simulation under the form of three dimensional density maps, and transforms such information into a fixed grid for the integration of the equations to determine macroscopical properties.

It uses a numerical method to determine the overall properties of composites with arbitrary morphologies from the properties of the components based on small homogeneous grid elements. The morphology is defined by a number of phases in a periodically continued base cell of cubic or orthorhombic shape where the phases may consist of any material. The resolution depends solely on the number of grid elements used.

---

[49] Pan, G.; Manke C. W. *Int. J. Mod. Phys. B* **2003**, *17*, 231–235.

[50] a) Gusev, A. A. *J. Mech. Phys. Solids* **1997**, *45*, 1449-1459; b) Gusev, A. A. *J. Mech. Phys. Solids* **1997**, *45*, 1449-1459; c) Gusev, A. A. *Macromolecules* **2001**, *34*, 3081-3093; Heggli, M.; Etter, T.; Wyss, P.; Uggowitzer, P. J.; Gusev, A. A. *Adv. Eng. Mater.* **2005**, *7*, 225-229.

[51] Osman, M. A.; Mittal, V.; Lusti, H. R. *Macromol. Rapid Commun.* **2004**, *25*, 1145-1149.

[52] a) Fermeglia, M.; Ferrone, M.; Pricl, S. *Mol. Simul.* **2004**, *30*, 289-300; b) Scocchi, G.; Posocco, P.; Danani, A.; Pricl, S.; Fermeglia, M. *Fluid Phase Eq.* **2007**, *261*, 366-374.

For each of the grid elements it is possible to specify the fraction of each phase contained in that particular position. By applying a displacement-based finite element method to the volume mesh, the responses to external deformations are calculated. In order to calculate mechanical properties an elastic solver is used. It applies six different infinitesimally small deformations to the composite and minimizes the total strain energy for each of these deformations in order to calculate the elastic composite properties.

The properties of the nanoparticles were taken from the available literature referring to typical characteristics,[53] and those of the matrix from our atomistic calculation.

Integration between these methods (from mesoscale to macroscale) is of paramount importance for the estimation of the properties of the materials.

5.3 Results and discussion

5.3.1 Atomistic results

Structural analysis

Figure 5.3 shows the geometry optimized molecular model of the GPTMS molecule, along with the atom labelling used in this work. For this monomer, the relevant structural parameters are listed in Table 5.2. These include the Si-O and Si-C1 bond lengths, and the O-Si-O and O-Si-C bond angles, which were estimated to be 1.670 Å, 1.909 Å, 108.4°, and 109.5°, respectively. Unfortunately, experimental X-ray diffraction or other spectroscopy data for GPTMS are not available to date. Therefore, to further validate the geometrical features of our model we applied the same model building/optimization procedure to structurally related molecules, for which such information could be retrieved from the literature. The relevant names, structural formulas and geometrical parameters are listed in Table 5.3.

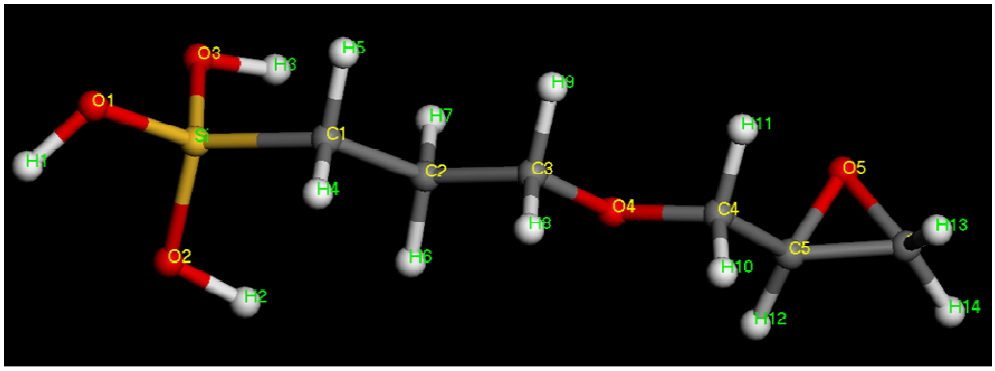

Figure 5.3. Geometry optimized molecular model of the GPTMS molecule, along with the atom labelling used in this work. All atoms are in stick-and-ball representation, using the same color code of Figure 5.2.

[53] a) Binny, T.; Abdulkhadar, M. *Solid State Communications* **1995**, *94*, 205-210; b) Harris, D. C.; Baronowski, M.; Henneman, L.; LaCroix, L. V.; Wilson, C.; Kurzius, S. C.; Burns, B.; Kitagawa, K.; Gembarovic, J.; Goodrich, S. M.; Staats, C.; Mecholsky, J. J. Jr. *Optical Engineering* **2008**, *47*, 114001-114012.

Si-O1(O2,O3)/Å	1.670	O1-Si-O2	108.4°
Si-C1/Å	1.909	H1-O1-Si	109.5°
H1-O1/Å	1.110	Si-C1-C2	114.7°
C1-C2/Å	1.531	C1-C2-C3	115.1°
C2-C3/Å	1.527	C2-C3-O4	106.6°
C3-O4/Å	1.419	C3-O4-C4	114.2°
O4-C4/Å	1.419	O4-C4-C5	105.9°
C4-C5/Å	1.495	C4-C5-C6	125.4°
C5(C6)-O5/Å	1.428	C5-O5-C6	60.2°
C5-C6/Å	1.439	H6-C2-H7	107.2°
H4-C1/Å	1.104	H13-C6-H14	112.2°
H12-C5/Å	1.098		

Table 5.2. Geometrical parameters of the GPTMS molecular model after geometry optimization with COMPASS ff. Atom numbering as in Figure 5.3.

Name	Geometrical parameters					
Dimethyl ether	C-O/Å 1.412 (1.416)	C-H/Å 1.124° (1.121°)	C-O-C 111.8° (112°)	H-C-C 108.3° (108°)		
Ethylene oxide	C-C/Å 1.459 (1.466)	C-H/Å 1.096 (1.085)	C-O/Å 1.428 (1.431)	C-O-C 60.4°	C-C-H 116.5° (116.6°)	
Propylene oxide	$C(H_3)$-C(H)/Å 1.527 (1.510)	C(H)-$C(H_2)$/Å 1.452	C-O/Å 1.426	C-O-C 60.4°	C-C-C 122° (121°)	
Propyl Methyl Ether	C-O/Å 1.415 (1.418)	C-C/Å 1.527 (1.520)	C-H/Å 1.115 (1.118)	C-O-C 112.3° (111.9°)	O-C-C 109.7° (109.4°)	H-C-H 109.2° (109°)
Disiloxane	Si-O/Å 1.635 (1.63)[a]	Si-H/Å 1.485 (1.490)	Si-O-Si 151.3° (151.2°)[b]	H-Si-H 109.8°		
Hexamethyl-disiloxane	Si-O/Å 1.639 (1.638)	Si-C/Å 1.862 (1.869)	H-C/Å 1.101 (1.104)	C-Si-O 108.3° (109.0°)	Si-O-Si 149.7° (151.3°)	C-Si-C 110.8°
Methoxysilane	Si-C/Å 1.421	Si-O/Å 1.669	H-C/Å 1.101	H-Si/Å 1.476	C-O-Si 122.6°	H-Si-H 110.8°
Tetramethylsilane	Si-C/Å 1.880 (1.875)	H-C/Å 1.110 (1.115)	C-Si-C 109.5°	H-C-H 109.7° (109.8°)		

Table 5.3. Computed geometrical data for molecules structurally related to GPTMS. Experimental available data[54] are reported in parenthesis for comparison.

[54] a) Lide D. R., *Handbook of Chemistry and Physics*, Ed., 79th ed., CRC Press, Boca Raton, FL, USA, 1999; b) Barrow, M. J.; Ebsworth, E. A.; Harding, M. M. *Acta Crystal.* **1979**, *B35*, 2091-2099; c) Koput, J.; Wierzbicki, A. *J. Mol. Spectrosc.* **1983**, *99*, 116-132.

By comparing the value listed in Tables 5.2 and 5.3, given the differences in molecular species and the fact that, whilst FF calculations are performed on an isolated molecule *in vacuum* the corresponding experimental quantities are obtained either from single-crystal or spectroscopic studies, we can conclude that all our results are in good agreement with the literature data.

In order to check the influence of the atomic partial charges on the final properties of the system, the GPTMS optimized structure was also assigned a partial charge distribution as derived from AM1-ESP calculations (see Table 5.4). Generally, speaking, a common procedure to estimate atomic partial charges is via Mulliken analysis.[55] However, since the results may be strongly dependent on the basis set employed, and there is no unambiguous method to assign charge to two atoms within a given bond,[56] we tried to bypass the problem by fitting the point charges at pre-selected positions to the electrostatic potential surface (ESP).[57,58] On the other hand, the partial charge scheme thus obtained may be, in turn, dependent on the specific molecular conformation considered.[59] To verify whether this was our case, we tested the obtained charge distribution by calculating molecular dipole moments and standard enthalpies of formation for all molecules listed in Table 5.3, and compared them with the corresponding experimental values, where available (see Table 5.5). As results from this Table, once again the agreement between calculate and experimental quantities is good, thus confirming the validity of the adopted approach.

According to the procedure outline above, a hybrid O/I 3D system based on GPTMS was successfully generated with high conversion. It is well known that a 100% conversion is rarely achieved experimentally because of gel transition at later stage.[60] Although other systems with a different (lower) conversion degree α could be generated by changing, for instance, the distance between close contacts up to a reasonable value of 10 Å, the amount of unreacted group in the actual simulated molecular systems is, on average, equal to 10%, yielding $\alpha = 0.9$.

The central unit cells of the initial GPTMS monomers, and the final network systems obtained from both structures I and II are shown in Figures 5.4 and 5.5, respectively. As can be seen from Figure 5.5, the 3D network structure is characterized by the presence of both chemical and physical crosslinks. Some bonds clearly connect to image cells across the boundary, and thus extend throughout the periodic system. Due to the scarcity of experimental characterization, which by the way accounts for the small number of simulation studies on crosslinked polymeric systems,[61,62,63] only a few comparisons between experimental and simulation can be attempted based on the main structural features of the systems.

As mentioned in the introduction, PSSQOs are the generic products obtained by the hydrolytic condensation of monomers such as GPTMS. Strictly speaking, the term refers to fully condensed structures of formula $(RSiO_{3/2})_n$ (n = even number), also denoted T_n.

[55] Mulliken, R. S. *J. Chem. Phys.* **1955**, *23*, 1833-1840.
[56] Singh, U. C.; Kollman, P. A. *J. Comput. Chem.* **1984**, *5*, 129-145.
[57] Weiner, S. J.; Kolmann, P. A.; Nguyen, D. T.; Case, D. A. *J. Comput. Chem.* **1986**, *7*, 230-252.
[58] Weiner, S. J.; Kolmann, P. A.; Case, D. A.; Singh, U. C.; Ghio, C.; Alagona, G., Profeta, S.; Weiner, P. J. *J. Am. Chem. Soc.* **1984**, *106*, 765-784.
[59] Reynolds, C. A.; Essex, J. W.; Richards, W. J. *J. Am. Chem. Soc.* **1992**, *114*, 9075-9079.
[60] Girard-Reydet, E.; Riccardi, C. C.; Sautereau, H.; Pascault, J. P. *Macromolecules*, **1995**, *28*, 7599-7607.
[61] Fan, H. B.; Yuen, M. M. F. *Polymer* **2007**, *48*, 2174-2178.
[62] Wu, C.; Xu, W. *Polymer* **2006**, *47*, 6004-6009.
[63] Yarowsky, I.; Evans, E. *Polymer* **2002**, *43*, 963-969.

Atom name	Si	O1	O2	O3	O4	O5	C1
Compass	0.80	-0.47	-0.47	-0.47	-0.32	-0.32	-0.24
AM1_ESP	0.72	-0.27	-0.32	-0.30	-0.10	-0.099	-0.25

Atom name	C2	C3	C4	C5	C6
Compass	-0.11	0.054	0.054	0.11	0.054
AM1_ESP	-0.20	-0.22	0.14	-0.12	-0.052

Atom name	H1	H2	H3	H4	H5	H6	H7
Compass	0.25	0.25	0.25	0.053	0.053	0.053	0.053
AM1_ESP	0.13	0.12	0.12	0.045	0.064	0.10	0.093

Atom name	H8	H9	H10	H11	H12	H13	H14
Compass	0.053	0.053	0.053	0.053	0.053	0.053	0.053
AM1_ESP	0.084	0.096	0.016	-0.014	0.070	0.076	0.072

Table 5.4. Partial charges on GPTMS atoms as assigned by *Compass* and obtained from AM1-ESP calculations. Atom numbering as in Figure 5.3.

Name	μ_{calc} (D)	μ_{exp} (D)	$\Delta H_{form,calc}$ (kcal/mol)	$\Delta H_{form,exp}$ (kcal/mol)
Dimethyl ether	1.36	1.30	-44.66	-44.00
Ethylene oxide	1.95	1.89	-13.61	-12.57
Propylene oxide	2.06	2.01	-21.68	-22.63
Propyl Methyl Ether	1.13	1.11	-55.08	-56.91
Disiloxane	0.34	0.24	-65.22	–
Hexamethyldisiloxane	0.38	–	-182.01	-185.87
Methoxysilane	1.1	1.15	-53.98	–
Tetramethylsilane	0.00	0.00	-57.99	-57.12

Table 5.5. Computed dipole moment and standard enthalpy of formation for molecules structurally related to GPTMS.

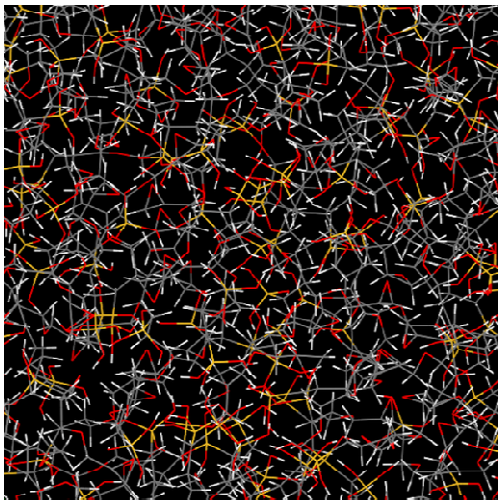

Figure 5.4. Central unit cell of the initial GPTMS monomers. Color code as in Figure 5.2.

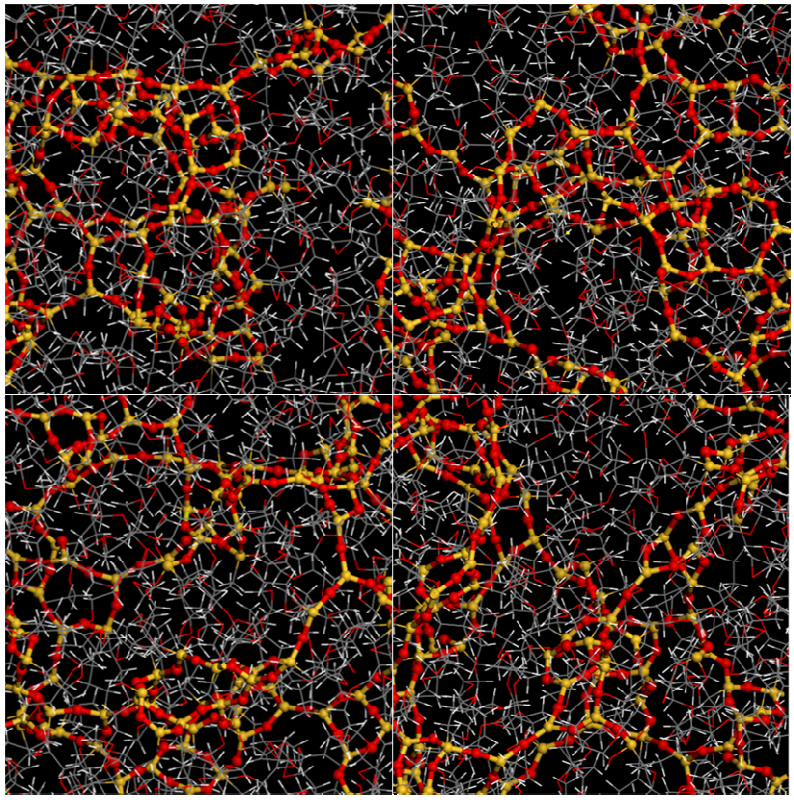

Figure 5.5. Hybrid O/I 3D network structures obtained starting from GPTMS models bearing atomic partial charges calculated with the AM1-ESP method (structure I, top left, structure II, top right), and assigned by the *Compass* FF (structure I, bottom left, structure II, bottom right). (see text for details). Crosslinked Si and O atoms are highlighted in Stick-and-Ball. Color code as in Figure 5.2.

But the term is frequently extended to denote partially condensed structures, $[RSiO_{3/2-x}(OH)_{2x}]_m$ or $T_n(OH)_m$, where m = 0, 2, 4…(2+n) for n = even number and m = 1, 3, 5 … (2+n) for n = odd number. Keeping this definition, PSSQO structures may vary from perfect polyhedra, incompletely condensed polyhedral, ladder polymers, open structures, linear polymers, and all possible combinations thereof.

Generally speaking, then, according to the polymerization conditions employed different structures for the resulting networks are proposed, such as randomly connected three-dimensional networks of trifunctional monomers, “ladder” structures, and a combination of linear, “ladder” and cage-like fragments.[64]

As the presence and relative amount of the structures described above significantly affect the network final structure, homogeneity and, ultimately, the mechanical properties of the resulting hybrids, the different reaction steps can be optimized to obtain final materials with targeted properties. Experimentally, it has been found that, under acid conditions, only a very small amount of cage-like structures are formed in the GPTMS polymerization, the intermolecular condensation being the preferred mechanism of network growth.[9] Accordingly, a high-molecular weight branched PSSQO grows, until a gel system is formed at a conversion degree approximately equal to 0.7. The corresponding composition of the gel state exhibits a considerable amount of silicon atoms involved in triple intermolecularly branched units representing the cross-links in the network. Further SAXS experiments revealed also that, under acid catalysis, no microphase separation resulting in self-assembly

[64] Boury, B.; Corriu, R. *Chem. Rec.* **2003**, *3*, 120-132.

of regularly arranged domains is present.[9] Contrarily, a broad distribution of high-molecular weight PSSQOs with dangling organic substituents is formed, the structure not promoting any ordering. The inspection of the 3D structures obtained from our simulation procedure compare well with the network picture described above. Indeed, the overall network structure is linear and extends in all three directions, the presence of unstrained rings with a number of Si atoms greater than 4 are present. To further confirm the quality of the network structures, Table 5.6 lists the mean values of some geometrical parameters, as obtained from initial structure I with the *Compass* atomic partial charges scheme by averaging over 10 MD frames. By comparing these data with the corresponding geometrical features of the GPTMS monomer model reported in Table 5.2, we can see that the differences are rather small, indeed confirming that crosslinking does not result in considerable geometrical modifications, and no substantial strain is induced in the final network (compare Figures 5.4, 5.5 and 5.6).

Si-O/Å	Si-C1/Å	O-Si-O	O-Si-C	Si-C-C	Si-O-Si
1.660	1.928	124.1°	104.3°	123.5°	142.8°

Table 5.6. Mean geometrical parameters of the GPTMS 3D network obtained from structure I with the *Compass* atomic partial charges scheme by averaging over 10 MD frames.

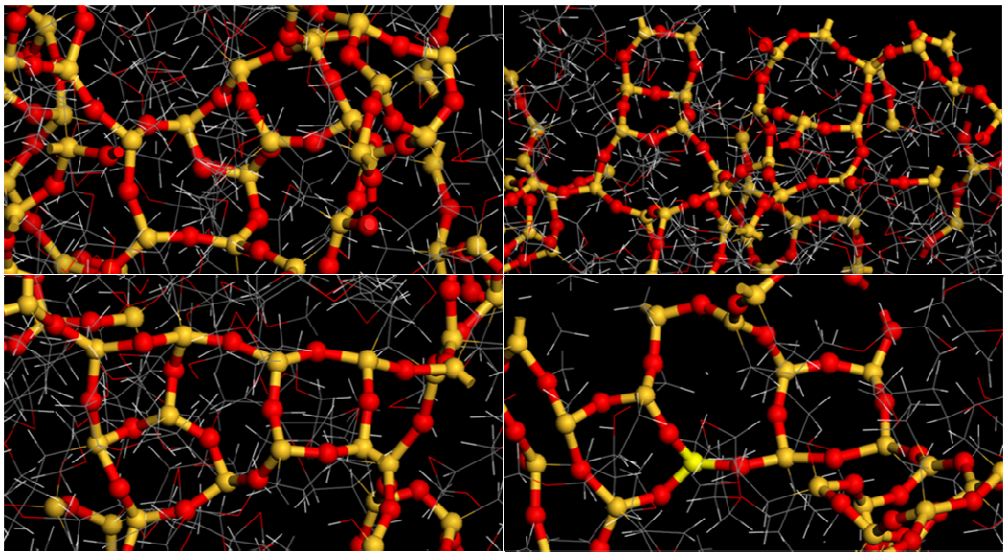

Figure 5.6. Details of the hybrid O/I 3D network structures obtained starting from GPTMS models bearing atomic partial charges calculated with the AM1-ESP method (structure I, top left, structure II, top right), and assigned by the *Compass* FF (structure I, bottom left, structure II, bottom right). (see text for details). Crosslinked Si and O atoms are highlighted in Stick-and-Ball. Color code as in Figure 5.2.

Mechanical properties

The mechanical properties calculated using the 3D network structures obtained from the MD simulations are reported in Table 5.7. The second column refers to the properties of the network structures simulated with the partial charge scheme obtained using the AM1-ESP

approach, whilst the third column lists the same quantities resulting from the 3D structures bearing the partial charges as assigned by the *Compass* FF (see Table 5.4). In the last column of this Table, the range of experimental values of the corresponding mechanical properties[65,66] is also reported for comparison.

Mechanical properties	Structure I AM1-ESP	Structure II AM1-ESP	Structure I *Compass*	Structure II *Compass*	Experimental data[a]
E (GPa)	2.85	3.00	3.52	3.96	1.9-4.5
B (GPa)	1.89	2.00	2.58	2.66	2.5-7
G (GPa)	1.14	1.20	1.38	1.58	0.9-1.5
ν	0.25	0.27	0.27	0.25	0.3-0.4
λ (GPa)	1.13	1.20	1.66	1.61	-
μ (GPa)	1.14	1.20	1.38	1.58	-

Table 5.7. Young's modulus E, bulk modulus B, shear modulus G, Poisson ratio ν, and Lamé constants λ and μ for the 3D GPTMS-based O/I network structures obtained from MD simulations. [a] Average values for crosslinked networks.

Specific heat capacity	Structure I AM1-ESP	Structure II AM1-ESP	Structure I COMPASS	Structure II COMPASS	Experimental data[a]
c_P (kJ/kgK)	1.16	1.23	1.64	1.49	1.1-2.2

Table 5.8. Specific constant pressure (c_P) heat capacity for the 3D GPTMS-based O/I network structures obtained from the MD simulations. [a] Average values for crosslinked networks.

The data in Table 5.7 indicate that the charging method has a certain impact on the mechanical properties of the final material. Indeed, in the case of the AM1-ESP partial charging scheme the values obtained from the simulation are located close to the lower limit of the expected range, if not below. With the *Compass* FF charge scheme, the mechanical characteristic of the GPTMS network lay in the expected range. Although no experimental measures are available for our systems, as a conclusion we could say that the predictions obtained by using a standard force field satisfactorily reproduce the available mechanical experimental data.

Heat capacities

The specific heat capacities at constant volume and constant pressure, c_V and c_P, calculated for the GPTMS-based O/I network are reported in Table 5.8. Again, these properties were obtained for structure bearing the two different partial charge schemes (see second and third column of Table 5.8 for AM1-ESP and *Compass* charge scheme, respectively). In the last column, the experimental data range available in literature for similar systems is also shown for comparison.[65,66]

As seen for the mechanical properties, all data calculated starting from structures bearing atomic partial charges derived from the AM1-ESP approach lay in the lower limit of the experimental data range, whilst those obtained from the *Compass* partial charge set fall better within the interval of observed values.

[65] Van Krevelen, D.W., *Properties of polymers*, Elsevier, Amsterdam, The Netherlands (1990).
[66] Bicerano, J., *Prediction of polymers properties*, M. Dekker, New York, USA (1996).

5.3.2 Mesoscale results

Molecular dynamics simulations (MD) were used to predict the equilibrium conformation and the interactions energies value for the GPTMS-MPTMS/ZnS nanocomposite. Figure 5.7 shows one snapshot taken along the equilibrated MD trajectory as an example.

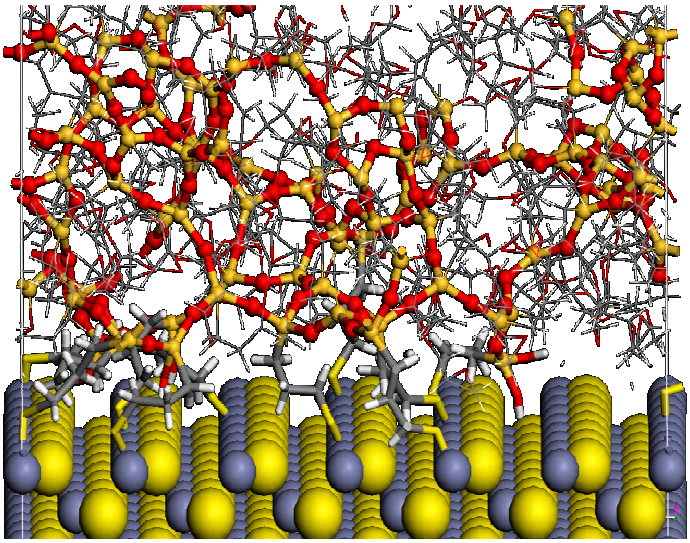

Figure 5.7. Frame extracted from the equilibrated MD trajectory of a system made up of a ZnS surface chemically modified with MPTMS molecules and a crosslinked GPTMS matrix.

As the simulation proceeds in time, the modifier molecules partially shield the surface from the interaction with the matrix and at the same time interpenetrate the polymeric network by virtue of favorable interaction energies. Following our previous work originally based on Tanaka's approach,[25,29,35l)] we derived interaction energies as well as the binding energies from the equilibrium conformation of the corresponding MD simulations. The values obtained are reported in Table 5.9.

E_{bind}		
GPTMS-ZnS	GPTMS-MPTMS	MPTMS-ZnS
-80.14	-158.25	-60.24
(±3.57)	(±8.19)	(±4.56)

Table 5.9. Equilibrium binary binding energies. All energies are expressed in kcal/mol and standard deviations are reported in parentheses.

The binding energies between the individual components constitute the input parameters for the calculation of the mesoscopic interaction parameters.

In this work we employed a recently developed technique called Reactive *Dissipative Particle Dynamics* (RxDPD) to model crosslinked polymeric matrices and nanoparticles at mesoscale level. Generally speaking, in a mesoscale representation, the actual material is modeled as a collection of particles that represent lumps of the material.

Our mesoscopic system consists of coarse-grained polymers and coarse-grained nanoparticles. Nanoparticles are modelled by icosahedrons, i.e., an assembly of 13 mesoscopic beads connected by harmonic spring potentials. Figure 5.8 shows schematically mesoscopic model for the nanoparticles. This effectively represents a uniformly dispersed set of nanoparticles of approximately 5-6 nm in diameter. Ideally, inorganic particles for optical applications should have a diameter below 10 nm; this is because the presence of even a small percentage of particles or aggregates larger than 100 nm results in strong light scattering in the visible region, causing haze or even turbidity.[67] Consequently, the size of inorganic nanoparticles employed for fabricating high RI nanocomposites is frequently below 10 nm.

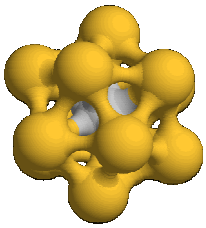

Figure 5.8. Mesoscopic model for the nanoparticle used in this work.

The polymer is represented by a chain of mesoscopic connected beads; the polymer chains can crosslink via a reactive potential and originate a 3-D amorphous network. A ring of four GPTMS monomers constitutes the basic unit, i.e. single DPD bead, for the GPTMS network model at mesoscale. Figure 5.9 shows the mesoscopic model for the GPTMS matrix used in this work.

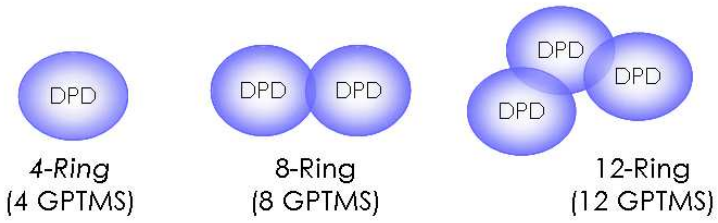

Figure 5.9. Mesoscopic model for the GPTMS matrix used in this work.

Assuming this as the basic mesoscale unit for the polymer, we simulated the network using the RxDPD technique and we compared the final structure of the network predicted after mesoscale runs to that yielded by atomistic simulations. As shown in Figure 5.10, predicted structures resulting from mesoscale crosslinking agree quite well with those obtained by atomistic simulations. The probability to find cyclic structures of 4, 8, 12 units in the atomistic network is colored in grey while the corresponding probability for the mesoscale network is depicted in red. The agreement between the two distributions means

[67] a) Caseri, W. *Macromol. Rapid Commun.* **2000**, *21*, 705-722; b) Ramaswami, R.; Sivarajan, K. *Optical Networks: A Practical Perspective*, Morgan Kaufmann, San Francisco, 2001.

that the mesoscale model chosen for representing the network fits well the atomistic one, thus validating the choice for the mesoscale unit of the matrix.

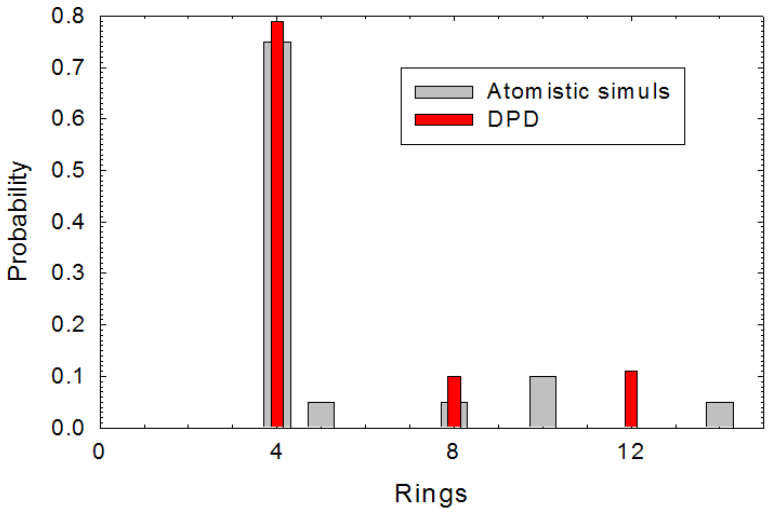

Figure 5.10. Atomistic/mesoscale comparison of crosslinking resulting structures in GPTMS systems.

As it is easy to understand from the probability distribution, our mesoscale network was essentially constituted by 79 mol% of 4-rings, 10 mol% of 8-rings and 11 mol% of 12-rings.

Once defined and optimized the mesoscale models and mesoscale species for the constituents, the next important issue is the determination of the bead interaction parameters. The detailed procedure for obtaining the mesoscale interaction parameters from atomistic molecular dynamics binding energies is reported in details in Chapter 2.

Adapting the recipe to the present system, we set the bead-bead interaction parameter for the polymer matrix equal to a_{GPTMS}=25.00 according to an appropriate value for a density value of ρ=3.[44] As, according to our procedure, we needed one more point as reference, we firstly calculated the Flory-Huggins interaction parameter for GPTMS and MPTS $\chi_{GPTMS\text{-}MPTMS}$ following a validated procedure derived by our group,[30,68] and described in Chapter 4, and then we derived the $a_{GPTMS\text{-}MPTMS}$ interaction parameter using the relation proposed by Groot[44] linking the Flory-Huggins interaction parameter χ_{ij} to the mesoscopic interaction a_{ij}. From our calculations, the Flory-Huggins interaction parameter results to be $\chi_{GPTMS\text{-}MPTMS}$=0.11 and the corresponding DPD interaction parameter $a_{GPTMS\text{-}MPTMS}$=25.34.

Once these two parameters were set, and their values associate with the corresponding values of the self- and mixed rescaled DPD energies, all the remaining bead-bead interaction parameter for the RxDPD simulation could be easily obtained, starting from the atomistic binding energies (see Chapter 2). According to this procedure, the interaction parameters were set to $a_{ZnS\text{-}GPTMS}$=26.04 and $a_{ZnS\text{-}ZnS}$=27.01, incorporating the effect of MPTMS covering into the ZnS contribution.

Generally speaking, the macroscopic properties of a composite material intrinsically depend not only on the properties of each constituent, but also on the characteristics of the composite morphology, interfacial interactions and nanoparticle loading. To elucidate these critical issues, we varied the nanoparticle loading from 2 to 15% in volume and we analyzed

[68] Pricl, S.; Fermeglia, M. *Fluid Phase Eq.* **1999**, *166*, 21-37.

the morphology of the resulting composites and the dispersion of the semiconductor in the matrix after crosslinking reaction occurred.

Figure 5.11 shows clustering analysis of ZnS nanoparticles as a function of nanoparticle loading. We found that up to 5%vol, the nanoparticles are quite well distributed in polymeric matrix and then they start clustering. Most likely, the modifier attached on the metal surface is not sufficient to completely shield the ZnS nanoparticles to favourably interact and consequently they tend to aggregate when the concentration is increasing.

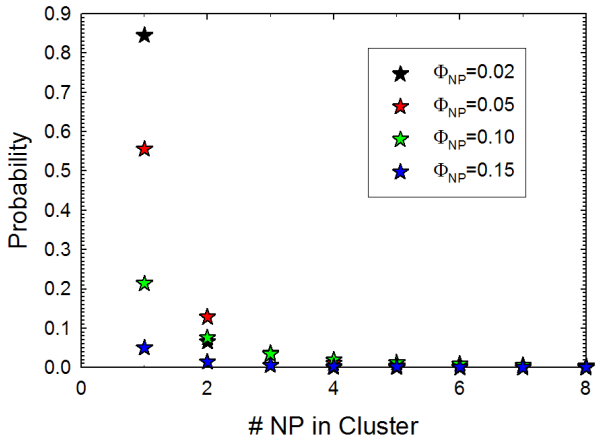

Figure 5.11. Clustering analysis in GPTMS-ZnS+MPTMS systems from reactive DPD.

In order to avoid nanoparticle aggregation and favour dispersion of the nanoparticles in the polymeric matrix, an accurate control and the increase of MPTMS modifier content in the system could improved the dispersion of the metal.

Figure 5.12 shows the dispersion of the nanoparticles at 2% in concentration as obtained from RxDPD simulations as an example of the mesoscale prevision.

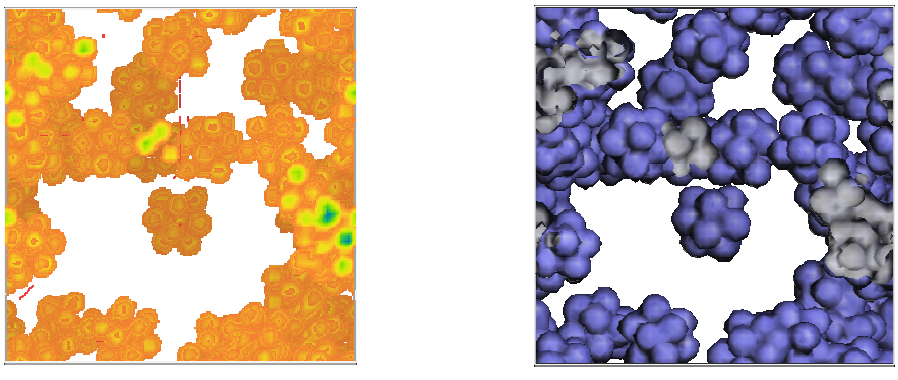

(a) *(b)*

Figure 5.12. 3-D density field (a) and isodensity surface (b) visualization of a GPTMS-MPTMS/ZnS system containing 2% vol of nanoparticle. GPTMS matrix is not visible for clarity.

5.3.3 Macroscopic properties

The problem of obtaining nanocomposites having good optical and mechanical properties, like typical thermoplastic or UV-curable polymers, and high nanoparticle concentration at the same time, i. e. with no limitation on thickness of the film, has not been solved till now.

Mechanical properties should permit the making of optical elements and/or coatings using current industrial methods suitable for polymer materials; the material should be processable in any form: coating, layer up to some hundreds of microns, and bulk. In addition, as far as optical properties is concerned, the requirement of retain transparency obliges to a strict control of dispersion to avoid any phase separation or even small aggregation phenomena, especially when high inorganic loadings are needed.

In particular, the mechanical properties of a nanocomposite resin can be different from those of the matrix polymer due the presence of the nanoparticles and the local physical interactions near the particle surface. Because of larger surface-to-volume ratio of nanoparticles over traditional fillers, these effects are expected to be more prominent for a given filler volume fraction. Nanoparticles can significantly alter the mechanical properties of the polymer close to the particle surface due to changes in chains mobility. Toughness has been attributed to the suppression of polymer chain mobility at the nanoparticle surface from attractive interactions. If one designs strong interactions between nanoparticles and the polymer matrix to avoid coagulation (for example use of surface active polymers with active groups), the modulus of the system will certainly increase, but simultaneously the coating (if it is not thin) will crack due to the rise of local mechanical stresses during the material production. Furthermore, since cracking and mechanical deformation occurs at dimensions larger than the isolated nanoparticles, it is important to understand the composite morphology at length scales larger than the size of the nanoparticles. Thus, characterization of the multiscale morphology of dispersed nanoparticles is important to understand the properties of a nanocomposite resin.

One of the goals of the mesoscale simulations is to generate density maps for polymeric matrix-nanoparticle systems to be used for prediction of macroscopic properties by finite elements methods. In this way, lower scale molecular information is passed as input to upper scale continuum calculation. The morphology of the systems at different metal loading as obtained fro mesoscale simulation in form of 3-D density distributions were transferred to the microFEM simulation for the calculation of relevant macroscopic properties. Examples of a 3D density distribution are reported in Figures 5.13 for lower (2%vol) and upper (5%vol) content of nanoparticles.

Accordingly, the macroscopic mechanical properties of the GPTMS-MPTMS/ZnS nanocomposite as calculated from FE analysis are reported in Table 5.10 as function of nanoparticle loading.

Volume loading (%)	2	5	10	15
Young's modulus (GPa)	2.22	2.30	2.36	2.52
Poisson ratio (-)	0.27	0.27	0.27	0.27
Shear modulus (GPa)	0.87	0.91	0.93	0.99
Bulk modulus (GPa)	1.61	1.67	1.71	1.83
Density (g/cm^3)	1412	1473	1577	1680

Table 5.10. Mechanical properties of GPTMS-MPTMS/ZnS nanocomposite as function of nanoparticle loading obtained from FE calculation.

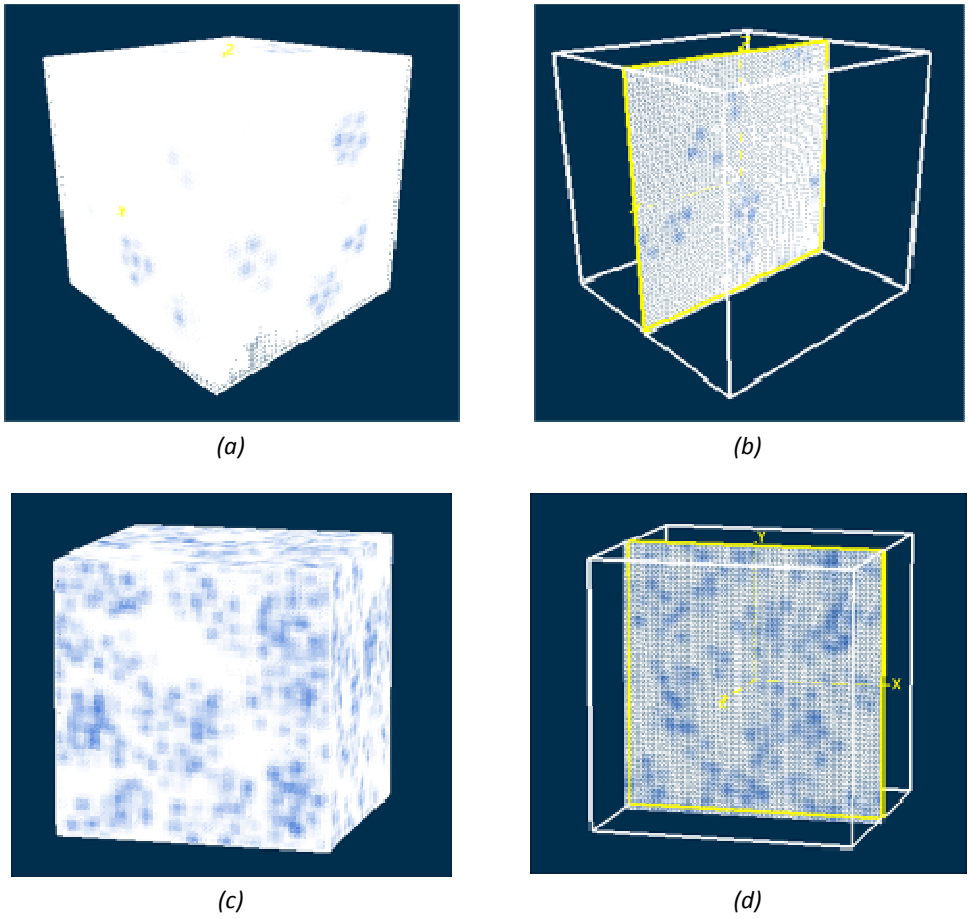

Figure 5.13. 3-D density distribution of GPTMS-MPTMS/ZnS nanocomposite at 2%vol, (a) and (b), and 15%vol, (c) and (d), of metal. Particle density is colored in blue and matrix density in white. Two different visualizations are reported, full cell view (Figures (a) and (c)), and cut-plane (Figures (b) and (d)). In all pictures is visible the grid mesh employed for FEM calculation.

Predicted values of mechanical characteristics are in good agreement with those expected for similar or comparable systems.[69] The results shown here demonstrate that only 2-5%vol ZnS incorporation into the GPTMS matrix was effective in enhancing the mechanical strength of the material. The reason for that is the high mechanical strength of ZnS (approximately E=70GPa) and its smaller size allow for a greater surface area to be available for the polymer/filler interaction and adhesion.

When the loading is low, due an attractive interaction between the nanoparticles modified and the surrounding polymer, the interphases region has decreased molecular mobility over that of the bulk polymer, and this consequently results in an increase in modulus. Further, the molecular structure of the shell material (MPTMS) provides the compatibilization of the nanoparticles with the polymer to prevent coagulation.

When the nanoparticle loading is increased, this shielding effect is no longer sufficient to avoid particle interaction and aggregation occurs. The presence of clusters at higher percentage of loading explains why the increasing of the mechanical properties with the addition of the semiconductor is much lower than the value expected. The presence of

[69] a) Wong, C. P.; Bollampally, R. S. *J. Appl. Pol. Sci.* **1999**, *74*, 3396-3403; b) Chen, C.; Justice, R. S.; Schaefer, D. W.; Baur, J. W. *Polymer* ***2008***, *49*, 3805-3815; c) Knör, N.; Gebhard, A.; Haupert, F.; Schlarb A. K. *Mechanics of Composite Materials* **2009**, *45*, 199-206.

clusters in the matrix reduces the volume-to-surface ratio, and the composite behaves as a traditional micro-composite rather than a nano-composite.

5.4 Conclusions

Hybrid organic–inorganic nanocomposites have attracted significant attention since their structure and properties can be easily manipulated, even at the molecular level, by the precise design and tailoring of the nanoscale building blocks and organic matrix. Although the promising applications of these nanocomposites have facilitated the rapid development of this area in both fundamental and applied research, there are still lots of questions that need to be addressed. The greatest obstacle to the industrial-scale production and commercialization of these nanocomposites is the dearth of cost-effective strategies for controlling the homogeneous dispersion of the nanoscale building blocks in polymer hosts, especially when high inorganic loading is used. The *ex situ* method is still considered to be a facile and feasible route for the generation of high RI nanocomposites, nevertheless the key challenge is to carry out the large-scale preparation of high RI nanoparticles with good compatibility with polymer matrices or monomers. Another hurdle to the broader use of the high RI nanocomposites is the lack of a structure–property relationship (SPR) because there are limited property databases for these nanocomposites. Thus, greater efforts are needed to correlate the structure of the nanocomposites with their macroscopic performance, including optical properties, thermal and mechanical properties, light stability, and processability, which is very important for the precise design of nanomaterials with excellent balanced properties.

In this study, we tried to contribute to this strong request fro SPR by proposing a computational recipe that can constitute a useful tool for a systematic design and development of new hybrid O/I systems with specific structural/chemico-physical properties.

Chapter 6

Morphology prediction of block copolymers for drug delivery

Polymeric drug carriers have traditionally been considered important for enhancing drug stability and solubility, and improving transport properties of pharmaceutical molecules. Drug carriers in the form of microspheres, nanoparticles, solution-dispersed polymeric micelles, hydrogels, or polymer–drug conjugates have been used to encapsulate hydrophobic drugs and other bioactive molecules, which are released in a controlled manner over a long period of time. Two polymers extensively studied in this regard are poly (lactide) (PLA) and poly (ethylene oxide) (PEO). Both polymers are biodegradable, adapt well to biological environments, and do not have adverse effects on blood and tissues. Due to such unique properties, copolymers of PLA/PEO with AB and ABA architectures have generated broad interest in nanomedicine applications. Nonetheless, a systematic investigation of the main structural and physical factors influencing the ultimate morphology and structure of the block polymer nanoscopic aggregates is still lacking, as it understandably requires a enormous experimental effort. Molecular simulation techniques, as time and cost efficient tools, can not only complement experimental works, but also eventually give a preview of phenomena prior to experiments. In this work we report the results of a complete study on the self-assembly of (DL)-PLA/PEO di/triblock copolymers in aqueous environment and in the presence of a model drug based on a multiscale molecular modeling recipe. In details, atomistic molecular dynamics simulations were used to obtain *Dissipative Particle Dynamics* (DPD) input parameters, and this mesoscale technique was employed to derive the entire phase diagrams for these systems.

6.1 Introduction

Despite remarkable progress in the past century, acute and chronic maladies such as bacterial and viral infections, cancer, cardiovascular disease, and strongly debilitating central nervous system afflictions continue to take a significant toll around the world. Various types

of drugs and gene therapy strategies are currently employed for the treatment of diseases based on differences between the normal and pathological tissues. These differences can be subtle and in remote areas of the body at the organ, tissue, cell, or sub-cellular levels. As pathological knowledge is leading to the molecular distinction between normal and abnormal tissue, it is predicted that more therapeutic targets will emerge at all these levels. However, the use of a specific carrier system that can overcome biological barriers and provide optimum drug concentration at the disease target at each level is required.

Nanoscale drug delivery systems – or *nanovectors* – are ideal candidates to provide essential solutions to the time-honoured problem of optimizing the therapeutic index for a treatment (i.e., to maximize efficacy while reducing health-adverse side effects).[1] Three main aspects neatly summarize the essential breakthrough opportunities for nanovector delivery; i) selective cells and tissue targeting; ii) ability to reach disease sites where the target cells and tissues are located, and iii) capacity to deliver even multiple active agents on site. The use of nanoparticle-based pharmaceutical carriers has well established itself over the last decade both at the pharmaceutical research and clinical settings. Nonetheless, many issues are to be solved before one new such material can reach the stage of clinical routine.

Soft materials, which have characteristic fluid-like disorder on short scale and high order at longer length scale, are increasingly drawing the attention of both scientists and engineers as possible nanocarriers systems. Much of the interest in soft matter, which include colloids, surfactants, membranes, (bio)polymers and their composites, stems from the inherent capacity for many of these materials to self-assemble into nanostructures. Self-organization is a powerful means to fabricate useful nanostructured materials and is currently heavily exploited by nature in many of its systems.[2] From the standpoint of pharmaceutical technology (PT), whose main goal is the design of technologically optimal vehicles for the administration of drugs, self-assembly represents a low-cost, fast, and easily scalable process.

Among the plethora of polymeric systems with promising potential as nanoscale drug delivery systems,[3] block copolymers (BCPs) have been widely studied as long-circulating carrier for hydrophobic drugs. BCPs are composed of two or more chemically distinct, and most frequently immiscible, polymer blocks covalently bound together. In the myriad of ways in which blocks can be linked to one another, the simplest and most widely employed categories so far are the AB diblock copolymers - composed of a linear chain of type A monomers bound to one end to a linear chain of type B monomers - and the ABA triblock copolymers, in which a linear chain of type B monomers is bound to both ends to a linear chain of type A monomers (see Figure 6.1(a) and (b)). Thermodynamic incompatibility between the A and B blocks drives a collection of AB or ABA copolymers to self-organize via microphase separation in which the contacts between like and unlike entities tends to be maximized and minimized, respectively.

---

[1] a) Ferrari, M. *Nat. Rev. Cancer* **2005**, *5*, 161-171; b) Kommareddy, S.; Tiwari, S. B.; Amiji, M. M. *Technol. Cancer Res. Treat.* **2005**, 4, 615-625; c) Ferrari, M. *Curr. Op. Chem. Biol.* **2005**, *9*, 343-346; d) Torchilin, V. P. *Adv. Drug Deliv. Rev.* **2006**, *58*, 1532-1555; e) Sengupta, S.; Sasisekharan, R. *Br. J. Cancer* **2007**, *96*, 1315-1319.

[2] Ball, P. *The Self-made Tapestry: Pattern Formation in Nature*, Oxford University Press, New York, 1999.

[3] a) Dhal, P. K.; Polomoscanik, S. C.; Avila, L. Z.; Holmes-Farley, S. R.; Miller, R. J. *Adv. Drug Deliv. Rev.* **2009**, *12*, 1121-1130; b) Gaspar, R.; Duncan, R. *Adv. Drug Deliv. Rev.* **2009**, *61*, 1220-1231; c) Hu, X.; Jing, X. *Expert Opin. Drug Deliv.* **2009**, *6*, 1079-1090; d) Khemtong, C.; Kessinger, C. W.; Gao, J. *Chem. Commun.* **2009**, *28*, 3497-3510; e) Belting, M.; Wittrup, A. *Mol. Biotechnol.* **2009**, *43*, 89-94; f) Venugopal, J.; Prabhakaran, M. P.; Low, S.; Choon, A. T.; Deepika, G.; Dev, V. R.; Ramakrishna, S. *Curr. Pharm. Des.* **2009**, *5*, 1799-1808; g) Singh, R.; Lillard Jr, R. J. W. *Exp. Mol. Pathol.* **2009**, *86*, 215-223; h) Soussan, E.; Cassel, S.; Blanzat, M.; Rico-Lattes, I. *Angew. Chem. Int. Ed. Engl.* **2009**, *48*, 274-288, i) Mintzer, M. A.; Simanek, E. E. *Chem. Rev.* **2009**, *109*, 259-302; j) Branco, M. C.; Schneider, J. P. *Acta Biomater.* **2009**, *5*, 817-831; k) Kim, S.; Kim, J. H.; Jeon, O.; Kwon, I. C.; Park, K. *Eur. J. Pharm. Biopharm.* **2009**, *71*, 420-430; l) Torchilin, V. P. *Eur. J. Pharm. Biopharm.* **2009**, *71*, 431-444.

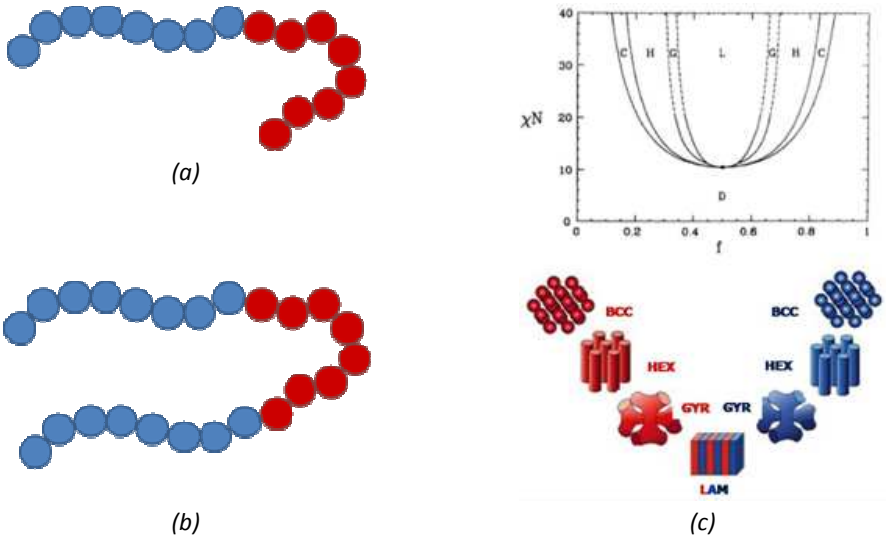

Figure 6.1. Schematic representation of the AB (a) and ABA (b) architecture of block copolymers. A-type monomers are depicted as light blue spheres, whilst B-type monomers are shown as orange spheres. Note that in the particular AB type copolymer shown as example, the A-block length is equal to the B-block length. In such case the copolymer is symmetric, and $f_A = f_B = 1/2$. In the case of the illustrated triblock copolymer ABA, the fraction of A-type monomer is double with respect to that of B-type monomers, that is $f_A = 0.67$ and $f_B = 0.33$. (c) Representative phase diagram for conformationally symmetric diblock melts (top) and cartoon of the corresponding microphase-segregated copolymer morphologies (bottom). Phases are labeled as follows: L/LAM (lamellar), G/GYR (gyroid), H/HEX (hexagonal cylinders), C/BCC (spheres), D (disordered). Dashed lines denote extrapolated phase boundaries, and the dot denotes the critical point.

Macrophase separation is prevented by entropic forces stemming from the covalent bonds between the A- and B-blocks, and the system ultimately reaches a compromise between mixing and separation. The tendency to microphase segregation and the free energy cost of bringing into contact unlike monomers are accounted for by the corresponding values of the well known temperature-dependent Flory-Huggins parameter χ_{AB}.[4] Two additional parameters concur to determine the ultimate morphology of a microphase segregated copolymer system: the overall degree of polymerization N, and the relative composition fractions, f_A and f_B, where $f_A = N_A/N$ and $f_A + f_B = 1$. In the case of a triblock copolymer ABA, a further parameter, i.e., the relative length of the three blocks, must also be considered.

Even in the simplest case, i.e., AB diblock copolymers in bulk, a rich assortment of ordered phases has been documented (see Figure 6.1 (c)).[4] For nearly symmetric diblocks ($f_A = f_B = 1/2$), a *lamellar* (L) phase occurs. For moderate asymmetries, a complex bicontinuous state, known as the *gyroid* (G) phase, has been observed in which the minority blocks form domains consisting of two interweaving threefold-coordinated lattices. Another complex structure, the *perforated lamellar* (PL) phase, may occur when the minority-component layers of the L phase develop a hexagonal arrangement of passages. At yet higher asymmetries, the minority component forms *hexagonally packed cylinders* (C) and then *spheres* (S) arranged on a body-centered cubic lattice. Eventually, as $f \rightarrow 0$ or 1, a *disordered* phase results. When a solvent component is added to the melt, and in particular if the solvent is selective for one of the copolymer blocks, the resulting system can have an

[4] a) Leibler, L. *Macromolecules* **1980**, *13*, 1602-1617; b) Fredrickson, G. H.; Leibler, L. *Macromolecules* **1989**, *22*, 1238-1250; c) Bates, F. S.; Fredrickson, G. H. *Annu. Rev. Phys. Chem.* **1990**, *41*, 525-557; d) Darling, S. B. *Prog. Polym. Sci.* **2007**, *32*, 1152-1204.

extremely complicated phase diagram that may differ entirely from that of the pure melt. For instance, other phases, which include the *micellar* phase (M), usually appear. On the other hand, if the solvent is a good solvent of roughly equal affinity for all of the blocks, one can expect that the copolymer system will have thermodynamics similar to that of the pure melt.

Poly(D-L lactide) (PLA) and poly(ethylene oxide) (PEO) are two polymers which have both been extensively investigated for applications as drug delivery systems (DDSs). Both are biodegradable, biocompatible, adapts well to biological environments, and do not have severe adverse effects on blood and tissues. Due to such unique properties, copolymers of PEO/PLA with an AB and ABA architecture have generated broad interest for use in biomedical applications.[5] Also, depending on the volume ratio between the less soluble (PLA) and soluble (PEO) blocks (the so-called *insoluble soluble ratio* (ISR)) and independently of whether the different hydrophilic and hydrophobic parts are arranged as AB or ABA, these copolymer are expected to generate the entire collection of allowed microstructures – spheres, cylinders, lamellas up to micelles – as a result of balancing the different interactions between the two block types and the solvent.

Thermodynamically and kinetically stable copolymeric microstructures, even when encapsulating an active payload, may retain their integrity in the biological environment for long periods and, more effectively, avoid uptake by the reticuloendothelial system (RES) and elimination through the kidney and possibly change the normal organ distribution of an encapsulated drug the same way. At the same time, it can be easily conceived that different microstructures can result in quite diverse nanostructures which, in turn, can perform rather differently in terms, for instance, of drug loading capacity, cellular localization and uptake, cargo release efficiency, and toxicity. The *a priori* knowledge of the phase diagram of a given di/triblock copolymer-based nanocarrier, in particular in the presence of water and/or of an active principle, would therefore constitute an invaluable piece of information in the process development of these DDSs.

To this purpose, it is essential to develop theoretical and computational approaches sufficiently fast and accurate that the structure and property of the materials can be predicted for various conditions. A particular advantage of molecular simulation techniques is that the properties of new materials can be predicted in advance of experiments. This allows the system to be adjusted and refined (or designed) so as to obtain the optimal properties before the arduous experimental task of synthesis and characterization. However, there are significant challenges in using theory to predict accurate properties for nanoscale materials, especially when (bio)macromolecules are involved. Indeed, despite the tremendous advances made in molecular modeling and simulation techniques, there remains a remarkable uncertainty about how to predict many critical properties related to material final performance. The main problem lies in the fact that most of these properties depend on the interactions and chemistry taking place at the atomic level, involving electronic and atomic descriptions at the level of nanometers in the length scale, and picoseconds in the timescale. Conversely, the PT designer needs answers from microscopic modeling of components having scales of the order of tens/hundreds of nanometers, and of

[5] a) Kissel, T.; Li, Y.; Unger, F. *Adv. Drug Deliv. Rev.* **2002**, *54*, 99-134; b) Agrawal, S. K.; Sanabria-Delong, N.; Coburn, J. M.; Tew, G. N.; Bhatia, S. R. *J. Control. Release* **2006**, *112*, 64-71; c) Lee, W. C.; Li, Y. C.; Chu, I. M. *Macromol. Biosci.* **2006**, *6*, 846-854; d) Sanabria-Delong, N.; Agrawal, S. K.; Bhatia, S. R.; Tew, G. N. *Macromolecules* **2007**, *40*, 7864-7873; e) Agrawal, S. K.; Sanabria-Delong, N.; Jemian, P. R.; Tew, G. N.; Bhatia, S. R. *Langmuir* **2007**, *24*, 5039-5044; f) Agrawal, S. K.; Sanabria-Delong, N.; Tew, G. N.; Bhatia, S. R. *Langmuir* **2008**, *18*, 13148-13154; g) Agrawal, S. K.; Sanabria-Delong, N.; Tew, G. N.; Bhatia, S. R. *Macromolecules* **2008**, *41*, 24, 1774-1784; h) Garric, X.; Garreau, H.; Vert, M.; Molès, J. P. *J. Mater. Sci. Mater. Med*. **2008**, *19*, 1645-1651.

phenomena taking place in a time range of milliseconds or much larger. Thus, to achieve a dramatic advancement in the skill of designing innovative, highly-performing materials, it is mandatory that we link the atomistic to the microscopic modeling.

Molecular modeling and simulation combines methods that cover a range of size scales in order to study material systems. All together, quantum mechanics (QM), molecular mechanics (MM), molecular dynamics (MD) and Monte Carlo (MC) methods, and mesoscale techniques cover many decades of both length and time scale, and can be applied to arbitrary materials: solids, liquids, interfaces, self-assembling fluids, gas phase molecules and liquid crystals, to name but a few.[6] There are a number of factors, however, which need to be taken care of to ensure that these methods can be applied routinely and successfully. First and foremost of course are the validity and usability of each method on its own, followed by their interoperability in a common and efficient user environment. Of equal importance is the integration of the simulation methods with experiment. Multiscale simulation can be defined as the enabling technology of science and engineering that links phenomena, models, and information between various scales of complex systems. The idea of multiscale modeling is straightforward: one computes information at a smaller (finer) scale and passes it to a model at a larger (coarser) scale by leaving out (i.e., coarse-graining) degrees of freedom The ultimate goal of multiscale modeling is then to predict the macroscopic behavior of a chemical-physical process from first principles, i.e., starting from the quantum scale and passing information into molecular scales and eventually to process scales. The MD level allows predicting the structures and properties for systems much larger in terms of number of atoms than for QM, allowing direct simulations for the properties of many interesting systems. This leads to many relevant and useful results in materials design; however, many critical problems in this field still require time and length scales far too large for practical MD. Hence, the need to model the system at the mesoscale (a scale between the atomistic and the macroscopic) using information retrieved at the atomistic (lower) scale.

This linking through the mesoscale in which the microstructure can be described over a length scale of tens to hundred nanometers is probably the greatest challenge to develop reliable first principles method for practical material design applications.[6] Only by establishing this connection from atomistic to mesoscale it is possible to build first principles method for describing the properties of new materials. The problem here is that the methods of coarsening the description from atomistic to mesoscale is not as obvious as it is going from electrons to atoms. For example, the strategy for polymers seems quite different from that applicable to metals, which in turn differs from those employed in the case of ceramics or semiconductors. In other words, the coarsening from QM to MD relies on basic principles and can be easily generalized in a method and in a procedure, while the coarsening at higher scales is more system specific for polymer materials due to the larger range of length and time scales that characterize macromolecules.

Scale integration in specific contexts in the field of polymer modeling can be done in different ways. Any recipe for passing information from one scale to another (upper) scale is based on the definition of multiscale modeling which considers objects that are relevant at

[6] a) Fermeglia, M.; Pricl, *AIChE J.* **1999**, *45*, 2619-2627; b) Fermeglia, M.; Pricl, *Fluid Phase Eq.* **1999**, *166*, 21-37; c) Pricl, S.; Ferrone, M.; Fermeglia, M.; Amato, F.; Cosentino, C.; Cheng, M. M.; Walczak, R.; Ferrari, M. *Biomed. Microdevices* **2006**, *8*, 291-298; d) Scocchi, G.; Posocco, P.; Fermeglia, M.; Pricl, S. *J. Phys. Chem. B* **2007**, *111*, 2143-2151; e) Cosoli, P.; Scocchi, G.; Pricl, S.; Fermeglia, M. *Micropor. Mesopor. Mater.* **2008**, *107*, 169-179; f) Scocchi, G.; Posocco, P.; Handgraaf, J.-W.; Fraaije, J. G.; Fermeglia, M.; Pricl, S. *Chem. Eur. J.* **2009**, *15*, 7586-7592; g) Fermeglia, M.; Pricl, S. in IUTAM Symposium on Modelling Nanomaterials and Nanosystems, Vol. 1, Eds: R. Pyrz, R. C.d Rauhe, Springer-Verlag, Berlin, **2009**, 261-270.

that particular scale, disregard all degrees of freedom of smaller scales, and summarize those degrees of freedom by some representative parameters. As mentioned above, mesoscopic simulations are performed using a coarse-grained molecular model: the particle in mesoscopic simulation is related to a group of several atoms in the atomistic simulation. *Dissipative Particle Dynamics* (DPD)[7] is one of the best established mesoscopic simulation techniques, according to which a set of particles moves according to Newton equation of motion, and interacts dissipatively through simplified force laws. In the DPD model, individual atoms or molecules are not represented directly by the particle, but they are coarse-grained into beads. These beads represent local "fluid packages" able to move independently. DPD thus offers an approach that can be used for modeling physical phenomena occurring at larger time and spatial scales than some other coarse-grained methods as it utilizes a momentum-conserving thermostat and soft repulsive interactions between the beads representing clusters of atoms/molecules. In their seminal work of 1997,[7c)] Groot and Warren made a fundamental contribution to this method by establishing a relationship between the main parameter in DPD a_{ij}, i.e., the maximum repulsion between beads of different material type i and j, and the Flory-Huggins parameter χ_{ij}.

In this work we present the results obtained from the application of a multiscale simulation procedure to the prediction of the phase diagrams of racemic PLA and PEO copolymers characterized by AB and ABA architectures in the presence of water. It is important to observe here the choice of the poly(D-L lactide) instead of one of the two pure enantiomeric blocks (L or D), as it has recently been verified that DDSs in which the ABA copolymers contain a racemic mixture of D- and L-lactide are characterized by amorphous PLA domains.[5g)] This, in turn, results into systems with different, more tunable drug delivery behavior. Also, as a proof-of-concept demonstration of the utility of these techniques in the formulation of structure-activity relationships for these DDSs, the self-assembly and microsphere formation of PLA-PEO and PLA-PEO-PLA carriers and a model drug (Nifedipine, a poorly soluble drug widely used as calcium channel blocker) under defined compositions is presented and discussed. The DPD method is adopted as the mesoscale modeling technique, and all necessary parameters of the mesoscopic model are estimated by a two-step procedure involving i) the matching of the atomistic and mesoscopic pair correlation functions to determine the best mesoscopic topology for polymers, and ii) the estimation of the DPD interaction parameters via the χ_{ij} values obtained from atomistic molecular dynamics simulations.

6.2 Computational details

In order to simulate AB and ABA copolymers of PLA and PEO of practical interest for the PT, the following macromolecules were chosen as proof-of-concept systems: PLA_xPEO_y with x=720–6480 and y=704–6336 for the diblock, and $PLA_{5875}PEO_{8448}PLA_{5875}$ for the triblock copolymer, respectively. The first step in the computational recipe applied in this work then consisted in the determination of the coarse-grained models for the PLA and PEO polymers, respectively. Following our previous work on different systems,[6f)] at first atomistic molecular dynamics (MD) simulations were performed on the di- and triblock copolymer chains. Using the relevant MD trajectories, the pair correlation functions were calculated using the following formula:

[7] a) Hoogerbrugge, P. J.; Koelman, J. M. V. A. *Europhys. Lett.* **1992**, *19*, 155-160; b) Español, P.; Warren, P. B. *Europhys. Lett.* **1995**, *30*, 191-196; c) Groot, R. D.; Warren, P. B. *J. Chem. Phys.* **1997**, *107*, 4423-4435.

$$P_{IJ}\left(\mathbf{r}_I\mathbf{r}_J\right)=\sum_i\sum_j\theta_{Ii}\theta_{Jj}\left\langle\delta\left(\mathbf{r}_I-\mathbf{R}_i\right)\delta\left(\mathbf{r}_J-\mathbf{R}_j\right)\right\rangle \tag{6.1}$$

where the sum runs over all atoms *i* and *j* in the molecular fragments *I* and *J*, and the square brackets indicate a thermal average. θ_{Ii} is a simple step function defined as:

$$\theta_{Ii}\begin{cases}1 \text{ if } i \text{ is of type } I\\ 0 \text{ if } i \text{ is not of type } I\end{cases}. \tag{6.2}$$

Coarse-grained *Dissipative Particle Dynamics* (DPD) simulations were then performed for each polymer using a repulsion parameter a_{ij} of 25 for all bead-bead interactions and, similarly to MD, the corresponding pair correlations between the different beads were computed.

The optimal overlap of the pair correlation functions obtained between the MD and the coarse-grained models was achieved with 10 PLA monomers and 16 PEO monomers per each PLA and PEO DPD bead, respectively. This mapping in turn resulted in the following mesoscopic copolymer architectures: PLA_nPEO_m with $n + m = 10$ for the AB copolymer, and $PLA_8PEO_{12}PLA_8$ for the ABA copolymer. Once these models were defined, the basic DPD assumption that all bead-types should be of comparable volume ultimately led to the coarse-graining of the entire molecule of Nifedipine into one DRUG bead, and 48 water molecules in each SOLVENT bead, respectively.

The successive, necessary step in the multiscale modeling procedures relied on the estimation of the value of the Flory-Huggins interaction parameter χ_{ij}, from which, in turn, the main DPD interaction parameter a_{ij} can be obtained using the following relationship recently proposed by Glotzer et al.[8] as a modification of the original equation of Groot and Warren[7c)] to better account for the polymer chain length:

$$a_{ij}=a_{ii}+3.27\left(1+\frac{3.9}{N_{DPD}^{\ 0.51}}\right)\chi_{ij} \tag{6.3}$$

χ_{ij} is defined in terms of the solubility parameters of the *i* and *j* components as:

$$\chi_{ij}=\frac{V_{DPD}}{k_BT}\left(\delta_i-\delta_j\right)^2 \tag{6.4}$$

where V_{DPD} is the volume of one polymer segment corresponding to a DPD bead, k_B the Boltzmann constant, *T* the temperature, and δ_i is the solubility parameter of the *i*th component, which is related to its cohesive energy density through the well-known relation $\delta_i = e_{coh}^{\ 0.5}$. Therefore, the solubility parameters for all system components were obtained from atomistic MD simulations following our validated procedure.[6a),b)]

The values of the resulting interaction parameters a_{ij} for all DPD species defined above and used for the mesoscale simulations are listed in Table 6.1.

[8] Horsch, M. A.; Zhang, Z.; Iacovella, C. R.; Glotzer, S. C. *J. Chem Phys.* **2004**, *121*, 11455-11462.

a_{ij}	PLA	PEO	SOLVENT	DRUG
PLA	25			
PEO	50.2	25		
SOLVENT	69.1	25	25	
DRUG	25.3	34	66.3	25

Table 6.1. DPD interaction parameters a_{ij} used in the mesoscale simulations.

The simulations were performed in a $20^3 r_c$ box and in a $30^3 r_c$ box for the AB and ABA systems, respectively. A density value ρ=3 was considered, and periodic boundary conditions were applied in all directions. The dimensionless time step of 0.05 was employed and more than 500000 steps have been adopted to get a steady state at a constant temperature of 308.15K.

6.3 Results and discussion

The entire phase diagram of aggregate morphology for the PLA-PEO copolymer with AB architecture as a function of the PLA fraction f_{PLA} in the copolymer is shown in Figure 6.2. Corresponding to distinctly different structures and morphologies of the aggregates, the diagram is divided into nine, well defined regions. The first one, spanning the entire range of f_{PLA} and a copolymer concentration in water ϕ up to ~0.2 v/v is characterized by the presence of micelles, in which the interior core is constituted by the hydrophobic portion of the copolymer (PLA) and the outer corona is decorated by the hydrophilic PEO blocks (*vide infra*). Interestingly, such morphology (particularly important in the formulation of DDSs) is predicted to exist at all ϕ values for f_{PLA} up to about 0.1. Moving along the f_{PLA}-axis, as the copolymer concentration ϕ increases above ~0.3 v/v, the correct sequence of phases is predicted progressively: PLA spheres (BCC), PLA cylinders (HEX), and the PLA gyroid phase (GYR). In correspondence of f_{PLA}=0.5, the phase diagram displays the appearance of the lamellar phase, typical of symmetrical diblock copolymers which, depending of ϕ, can persist up to f_{PLA}=0.8. Finally, the right-hand side of the phase diagram shows the region of existence of the reverse-phase morphologies, in the order: PEO GYR, PEO HEX, and PEO BCC, as expected. Interestingly, the ninth region in this phase diagram pertains to what it is usually defined a disordered phase, that a system for which no canonical or well defined structures can be identified.

Figures 6.3 and 6.4 show a selection of pictorial evidences for each of the phases described above in the case of a PLA-PEO copolymer of the AB type as a function of f_{PLA} and at ϕ = 0.9 and 0.2 v/v, respectively.

In the case of the triblock copolymer PLA-PEO-PLA with the linear architecture ABA sketched in Figure 6.1(b), the corresponding phase diagram is more complicated, with the appearance of a hydrogel phase for intermediate value of polymer concentration ϕ.

As an example, Figure 6.5 illustrates the aggregate morphologies obtained from the application of the multiscale simulation procedure developed in this work to ABA copolymer characterized by a f_{PLA} of 0.57. As can be readily seen from the images, for this system the simulation reveals the existence of well separated micelles, with an inner PLA core surrounded by a corona of the hydrated PEO block only in a narrow range of ϕ.

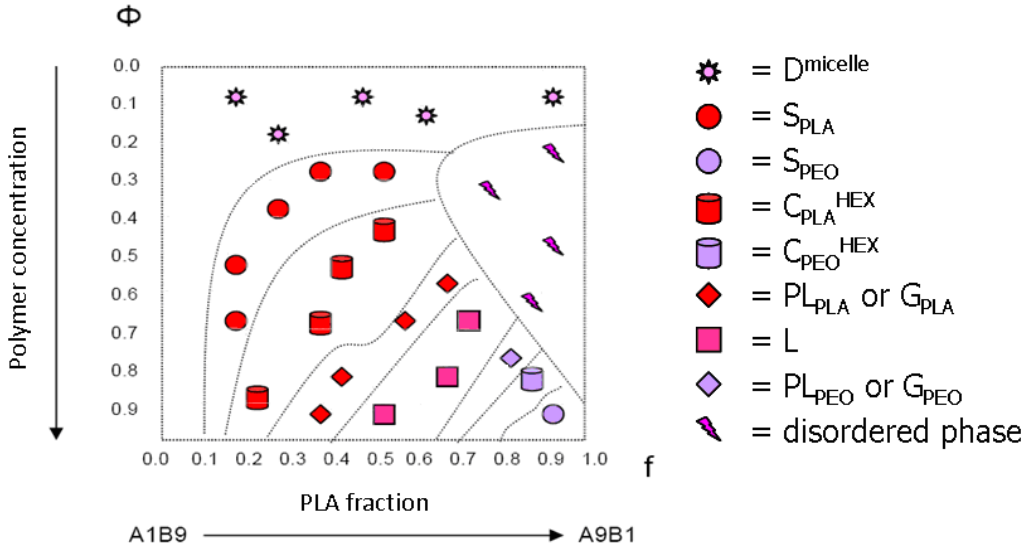

Figure 6.2. Phase diagram of the PLA-PEO diblock copolymer of AB architecture in water as obtained from the application of the multiscale molecular simulation procedure developed in this study.

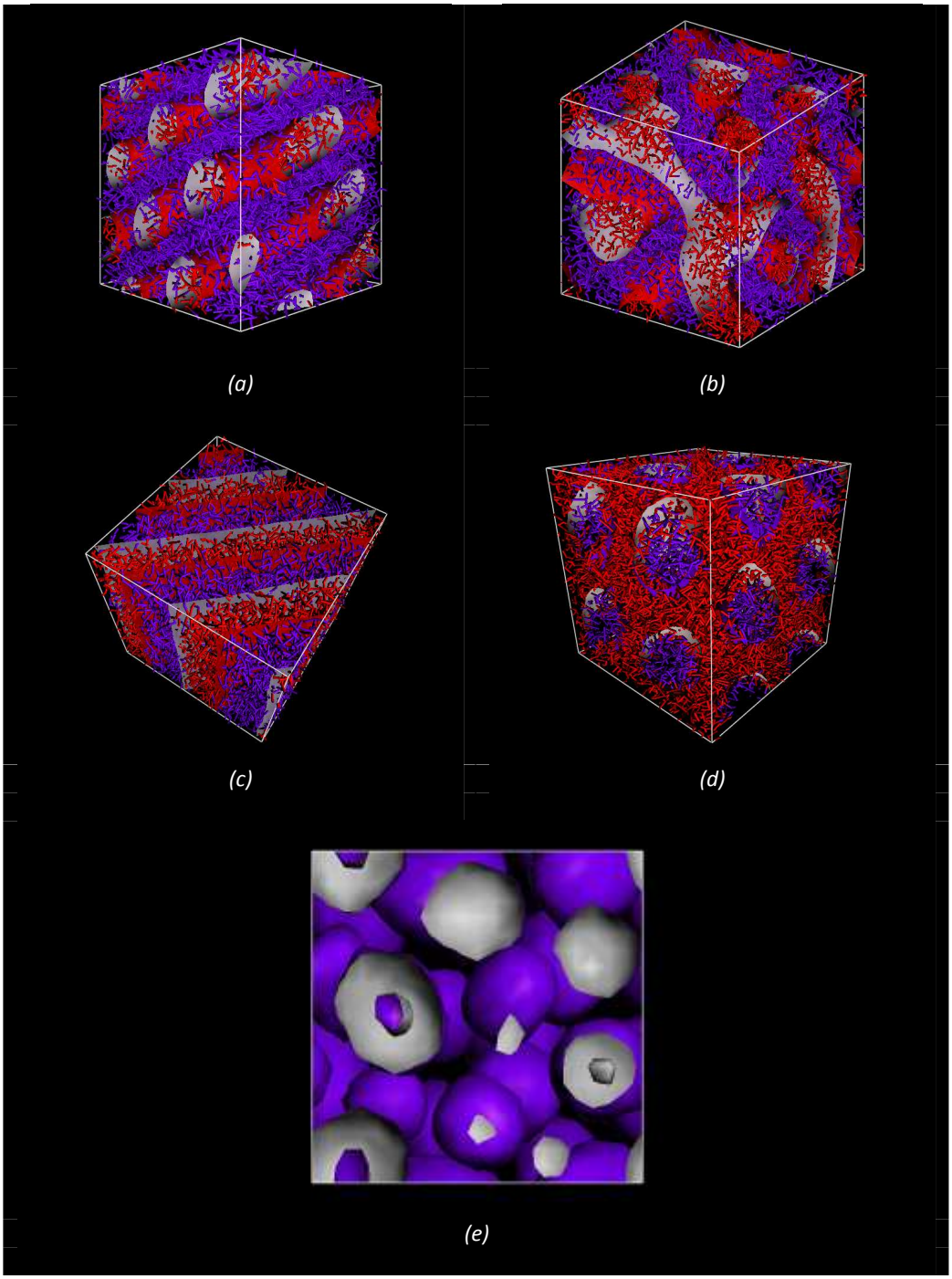

Figure 6.3. Predicted phase morphologies for a PLA-PEO diblock copolymer in water at ϕ = 0.9 v/v and different f_{PLA} values: (a) f_{PLA}=0.2; (b), f_{PLA}=0.4; (c), f_{PLA}=0.5; (d), f_{PLA}=0.8; (e), f_{PLA}=0.9. Color legend: red, PLA blocks; purple, PEO blocks. Water molecules not displayed for clarity.

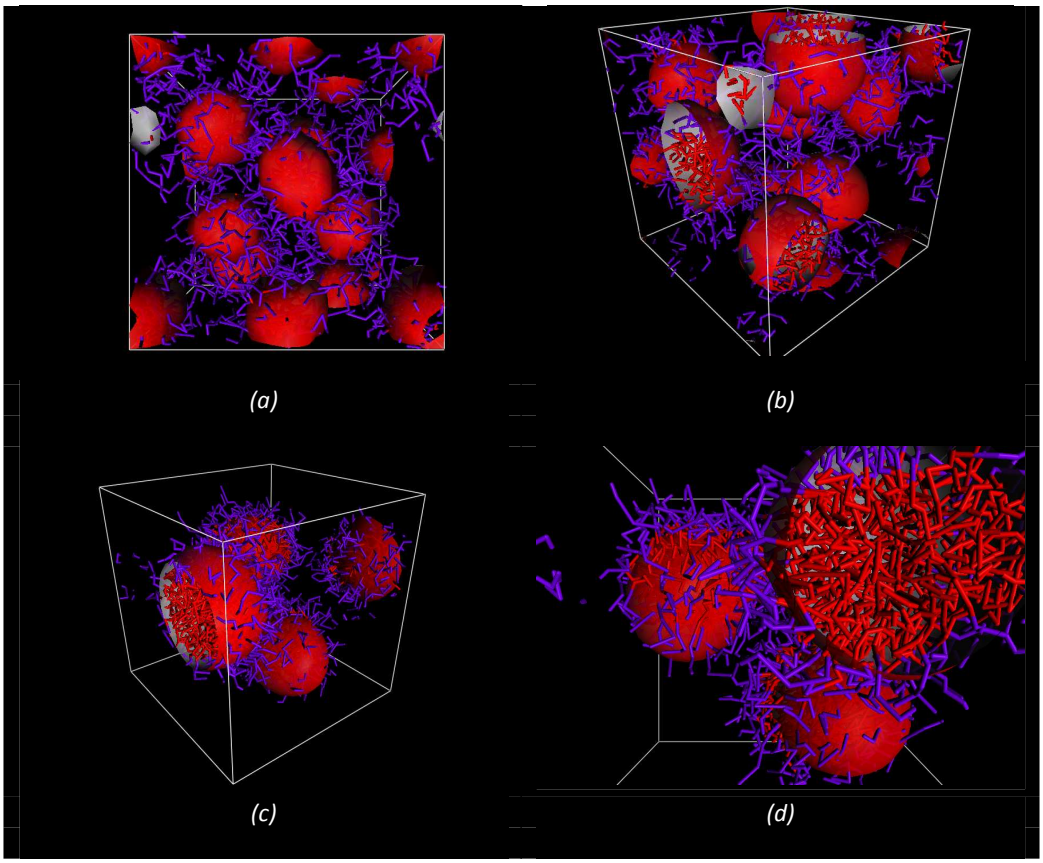

Figure 6.4. Predicted phase morphologies for a PLA-PEO diblock copolymer in water at ϕ = 0.2 v/v and different f_{PLA} values: (a) f_{PLA}=0.3; (b), f_{PLA}=0.4; (c), f_{PLA}=0.6. Panel (d) is a zoomed vision of the micelles for the system with f_{PLA} = 0.6. Color legend: red, PLA blocks; purple, PEO blocks. Water molecules not displayed for clarity.

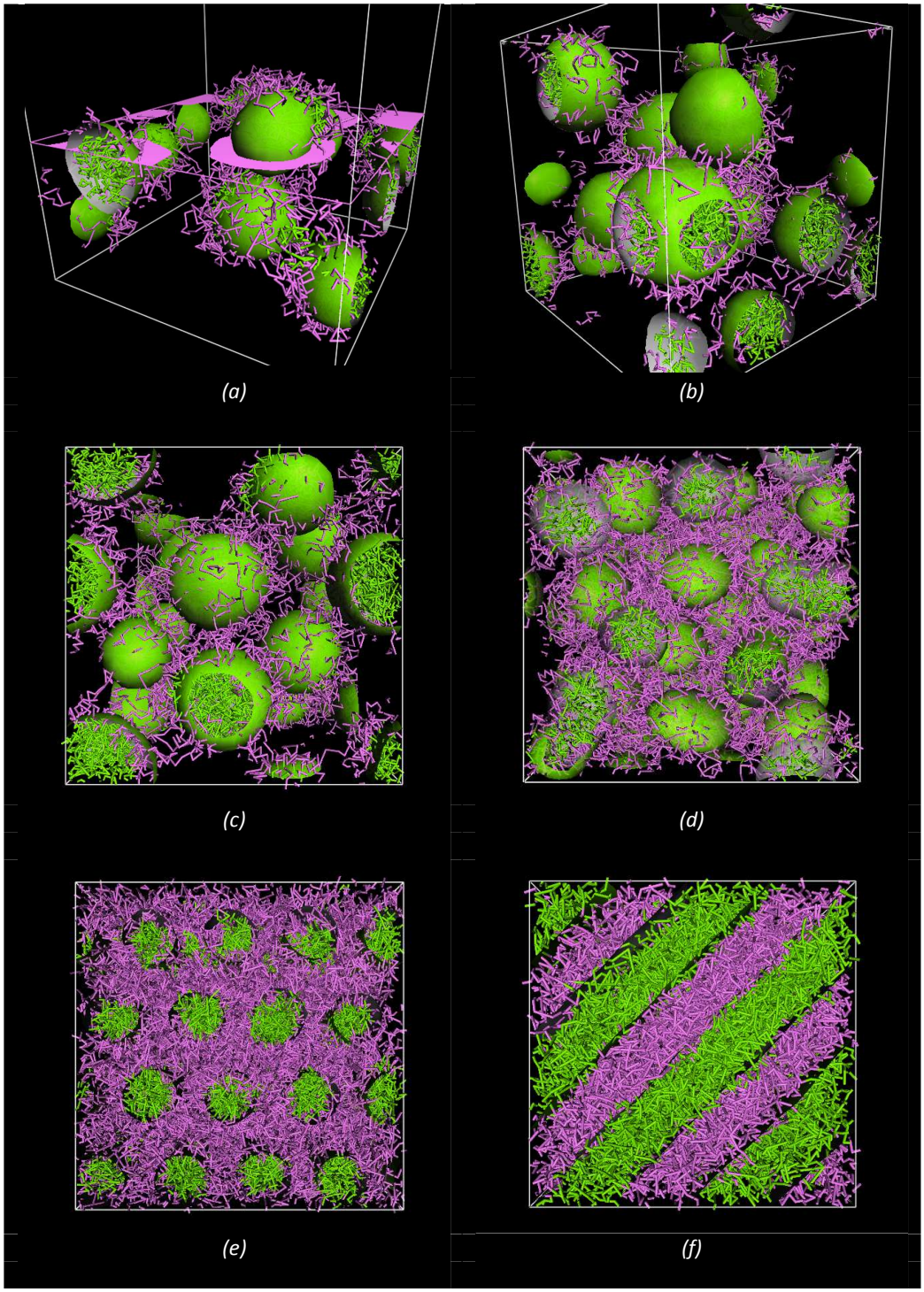

Figure 6.5. Predicted phase morphologies for a PLA-PEO-PLA triblock copolymer in water at f_{PLA} = 0.57 and different ϕ values: (a), ϕ = 0.1 v/v; (b), ϕ = 0.15 v/v; (c), ϕ = 0.22 v/v; (d), ϕ = 0.35 v/v; (e), ϕ = 0.5; (f), ϕ = 0.6. Color legend: green, PLA blocks; lavender, PEO blocks. Water molecules not displayed for clarity. In panel (a), a cut-plane is highlighted for graphical purposes.

Upon increasing ϕ, the transition to a *flowerlike* micellar morphology is observed, which persist up to ϕ ~0.15 v/v. At still higher values of ϕ, bridging between micelles takes place, leading to formation of a three-dimensional network and gelation. The junction points formed are temporary and reversible, and therefore, they break and re-form frequently over the time scale of the simulation. For a polymer concentration of ~0.5 the hexagonal geometry characterizes the predicted morphology which, upon further increasing of ϕ, undergoes a phase transition to the lamellar one.

Importantly, this predicted behavior is in excellent agreement with the recent experimental results obtained by Agrawal and his group,[5b),d),e),f),g)] and thus deserves a deeper comment. In the last of a series of elegant and thorough studies,[5g)] these authors have verified that PLA-PEO-PLA triblock copolymers characterized by amorphous PLA domains form spherical micelles at very low concentration in water solution. The end PLA blocks, which are poorly compatible if at all with the solvent, make up the micellar core, whilst the hydrophilic midblock generated the micellar corona (see Figure 6.6(a)). As the polymer concentration increases, the micelles begin to interact by virtue of the intensive hydrophobic attraction among the core phases: the intermicellar spacing progressively decreases while the flowerlike micelles become more closely packed and the bridges of PEO blocks among them increase in number (see Figure 6.6(b)). Further increasing the bridging density eventually leads to the point where all micelles are connected into a network in solution, namely the percolation threshold, thereby resulting in the formation of a gel at high concentration (see Figure 6.6(c)).

Another interesting piece of evidence of a good match between simulated and experimental results stems from the estimation of the micelle dimensions. Taking the systems with ϕ = 0.22 v/v as a proof of principle, the average estimated values of the micelle PLA core radius R_c as extracted from the DPD simulations is 6.4 ± 0.6 nm whilst the average radius of an entire micelle R_m amounts to 9.7 ± 0.8 nm. Accordingly, the thickness of the PEO shell S_{th} is equal to 3.3 nm. These values are in utter agreement with previously reported experimental studies on closely related PLA-PEO-PLA water systems.[5g),9] Two other parameters can be used to further characterize these micellar structures: the aggregation number N_a, i.e., the number of PLA blocks forming the core, and the degree of the hydration shell, φ_{sh}. These two quantities can be calculated, at first approximation, using the following relationships:[5g),10]

$$N_a = \frac{4/3\pi {R_c}^3}{V_{PLA}} \tag{6.5}$$

$$\varphi_{sh} = 1 - \frac{N_a V_{PEO}}{4/3\pi\left({R_m}^3 - {R_c}^3\right)} \tag{6.6}$$

in which V_{PLA} and V_{PEO} are the molecular volumes of PLA and PEO, respectively. Applying Equations 6.5 and 6.6 to the PLA-PEO-PLA systems with ϕ=0.22 v/v as an example results in an average N_a value of 179 and a value for φ_{sh}=0.32, again in astounding agreement with the corresponding estimates reported in the literature for analogous systems.[5g),9]

[9] Riley, T.; Heald, C. R.; Stolnik, S.; Garnett, M. C.; Illum, L.; Davia, S. S.; King, S. M.; Heenan, R. K.; Purkiss, S. C.; Barlow, R. J.; Gellert, P. R.; Washington, C. *Langmuir* **2003**, *19*, 8428-8435.

[10] a) Goldmints, I.; von Gottberg, F. K.; Smith, K. A.; Hatton, T. A. *Langmuir* **1997**, *13*, 3659-3664; b) Yang, L.; Alexandridis, P.; Steytler, D. C.; Kositza, M. J.; Holzwarth, J. F. *Langmuir* **2000**, *16*, 8555-8561.

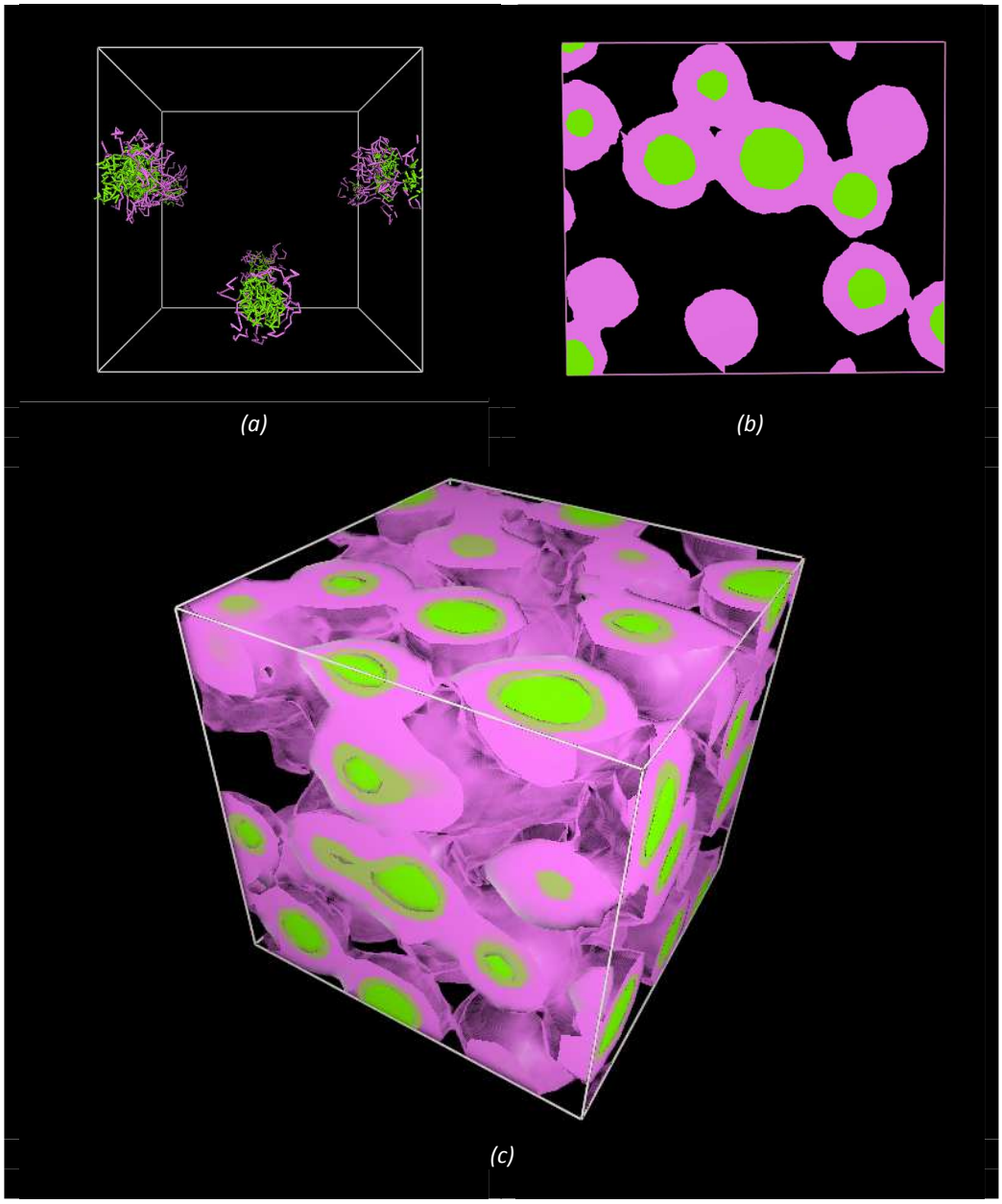

Figure 6.6. Evolution micellar aggregation for the PLA-PEO-PLA copolymer as a function of polymer concentration ϕ at constant PLA fraction f_{PLA} = 0.57. (a), ϕ = 0.02 v/v; (b), ϕ = 0.22 v/v; (c), ϕ = 0.35 v/v. Color legend: green, PLA blocks; lavender, PEO blocks. Water molecules not displayed for clarity. In panel (b), a volume representation in a plane cut along the simulation cell is shown. In panel (c), a three-dimensional volume representation is chosen to highlight the percolating connectivity in the hydrogel.

It is worth noting that the substantial value of N_a is in harmony with the morphological evidences that the big PLA domains tend to be strongly phase-separated in the micellar core and, also, support that fact that these large segregated hydrophobic domains tend to interact strongly among themselves, ultimately leading to the formation of the micellar network. Under this condition, where the micelles are expected to be densely packed, the center-to-center distance between any two adjacent micelles should in principle be equal to the micelle diameter. This seems to be almost the case for the PLA-PEO-PLA systems with ϕ = 0.35 v/v and f_{PLA}=0.57, (see Figures 6.5(d) and 6.6(c)). On the other hand, at lower copolymer concentrations the intermicellar radii are mostly seen to be larger than R_m (see, for example, Figure 6.6(b)), indicating that the close-packing condition and, hence, the percolation threshold, is far from being reached for these systems. In passing, we also note that calculated degree of hydration of 32% for the above mentioned system is in line the expected balance between a good hydration level and the partial engagement of these blocks in bridging the flowerlike micelles through the solution.

To test the ability of the adopted methodology to account for the effect of drug-loading on the nanocarrier aggregated morphology, further simulations were performed both on the di- and tri-block copolymer systems containing the model drug Nifedipine in concentration and composition intervals of PT interest. Figures 6.7(a)-(c) show the evolution of the morphology for the system PLA-PEO characterized by ϕ=0.15 and f_{PLA}=0.3 upon different drug loading. As can be seen from these Figures, upon addition of the active principle up to ~12% v/v, the micellar morphology, although characterized by bigger dimensions, can still be observed, with the drug fully and well dispersed into the PLA hydrophobic core (Figure 6.7(b)). A further increase in drug loading up to 22% v/v leads to the formation of columnar micelles (Figure 6.7(c)). This concentration threshold seems then to mark the maximum payload the considered copolymer nanocarrier can take on under the selected conditions.

Considering now the triblock PLA-PEO-PLA copolymer, an analogous morphology evolution upon drug loading is envisaged, although the payload concentration at which the useful, micellar morphology is substantially altered is quite lower than in the case of the PLA-PEO diblock counterpart. As illustrated in Figure 6.8(a)-(e) for the ABA copolymer system with ϕ=0.22 and f_{PLA}=0.57 as an example, the nanocarrier is able to accommodate the drug within the PLA core up and without an appreciable alteration of the micellar morphology up to a concentration of 3%. At 4% a transition to columnar or wormlike micelles is observed and, finally, in correspondence to a drug load of 7%, the fusion of the micelles into a bilayer membrane is predicted. In other words, as the drug concentration increases, the local packing of the hydrophobic entities (i.e., PLA blocks and drug molecules) changes, and progressively leads to a decrease of the local curvature. Thus, those systems which at low drug concentrations still form spherical aggregates will rearrange their assembly into cylindrical or eventually membrane-like aggregate (consisting of two monolayers of block copolymers aligned so as to form a sandwich-like membrane: soluble block-insoluble block with interspersed drug-soluble block) as the payload amount increases.

6.4 Conclusions

Novel approaches to drug delivery and formulation using nanotechnology are revolutionizing the future of medicine.

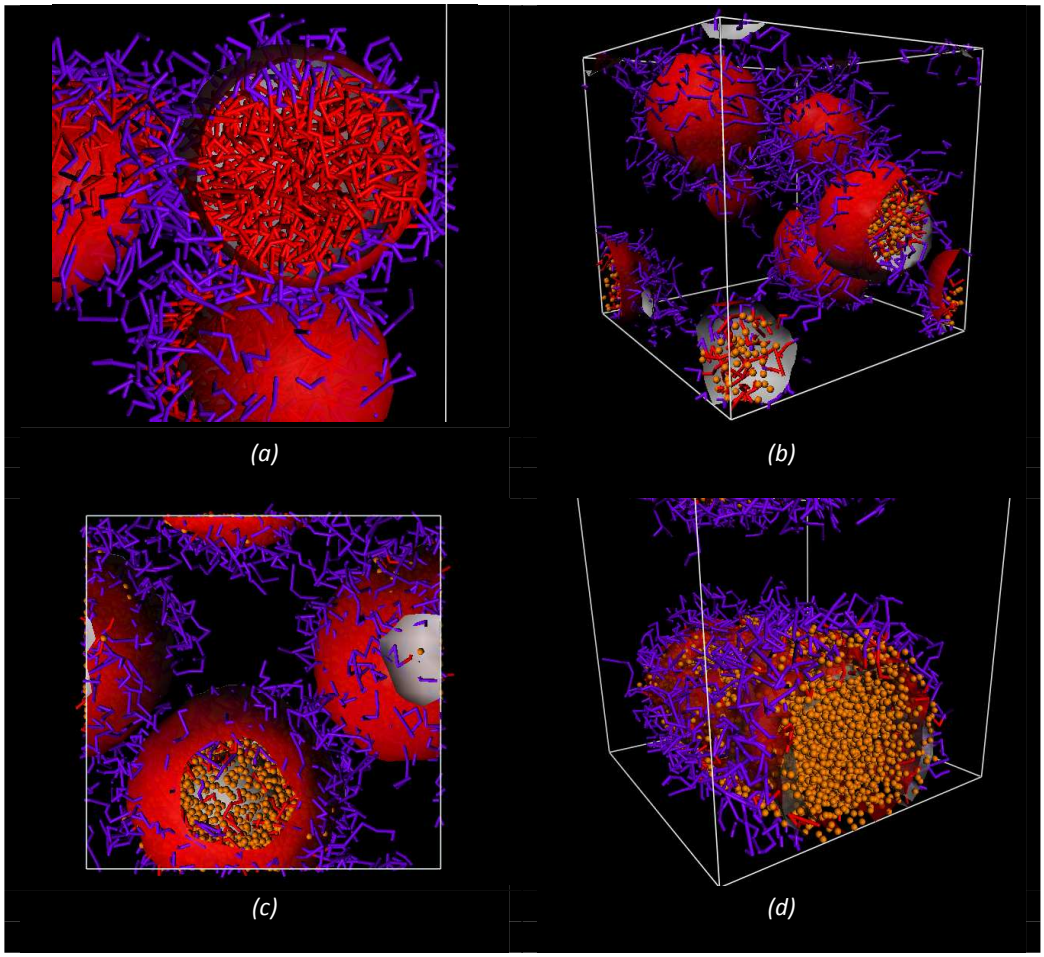

Figure 6.7. Evolution of the micellar aggregate morphology for the PLA-PEO copolymer at ϕ = 0.15 v/v and f_{PLA} = 0.3 as a function of Nifedipine loading (% v/v). (a), no drug loading; (b), 4%; (c), 12%; (d) 17%. Color legend: purple, PLA blocks; red, PEO blocks, orange, drug. Water molecules not displayed for clarity.

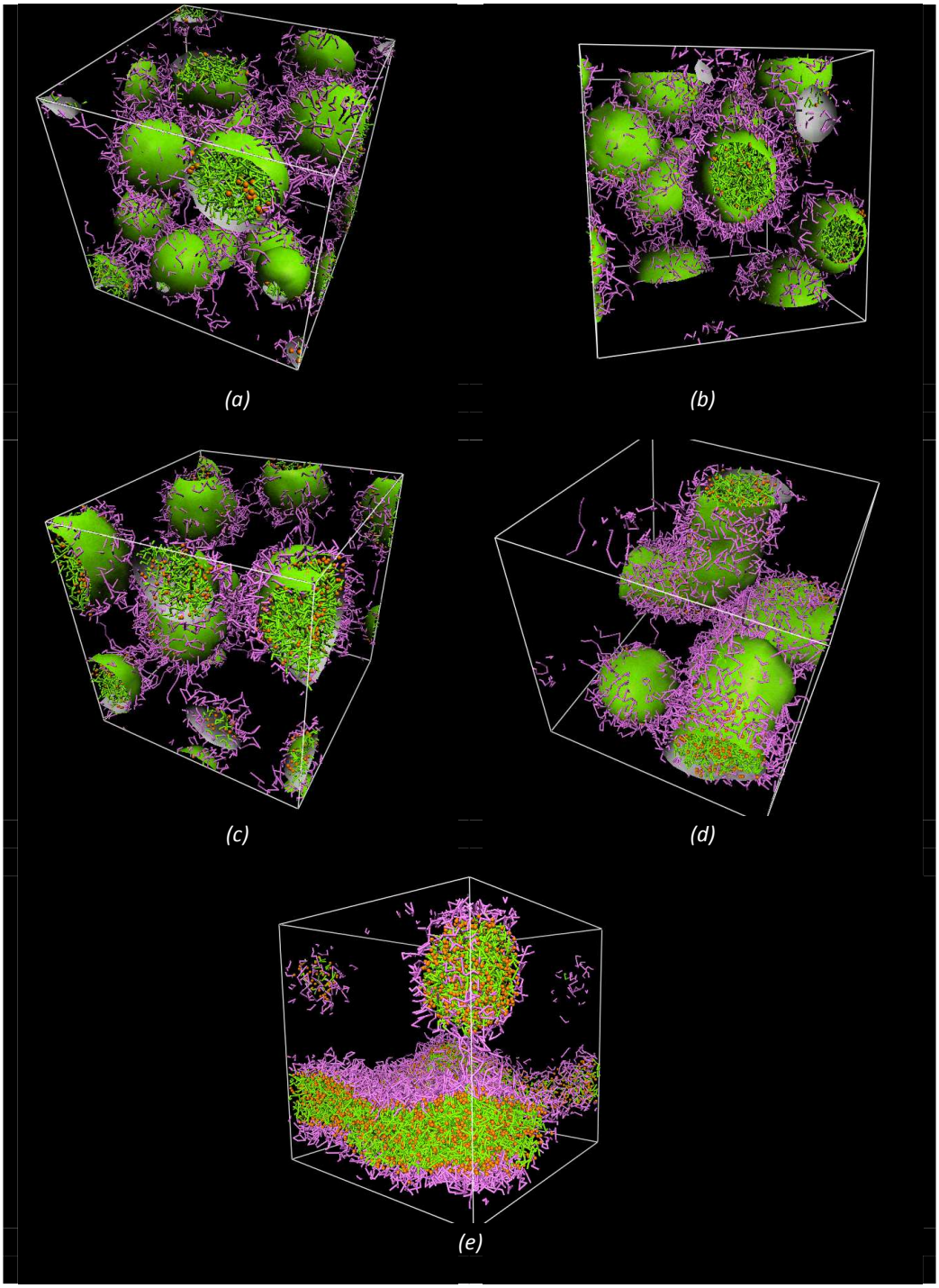

Figure 6.8. Evolution of the micellar aggregate morphology for the PLA-PEO-PLA copolymer at ϕ = 0.22 v/v and f_{PLA}=0.57 as a function of Nifedipine loading (% v/v). (a), 1%; (b), 2%; (c), 3%, (d) 4%; (e) 7%. Color legend: green, PLA blocks; lavender, PEO blocks, orange, drug. Water molecules not displayed for clarity.

At the time of writing, nanomedicine - the medical application of nanotechnology - offers the promise of an endless range of applications from biomedical imaging to drug delivery and therapeutics which, coupled to genomic tailoring, may soon spawn the much-anticipated and highly-pursued individualized medicine. The specific area of nanoformulations includes the creation of many different nanoscale DDs such as those discussed in the present work, which can be created from a countless combination of materials and active principles. These nanovectors can be tailored for working in specific tissues or individual patients, and may eliminate the need for conditional administration of drugs, thereby promoting patient compliance and maximizing therapeutic effects.

Being able to formulate an *a priori* quantitative structure-property (QSPR) or structure-activity relationship (QSAR) for a novel nanocarrier in a given solvent and in the eventual presence of a drug cargo – possibly even before the nanoformulation preparation is attempted in the laboratory – would constitute a giant leap towards an advancement in PT. Time, economical resources, and human efforts could then be minimized and focused on the most promising DDs systems designed on the basis of the application of these computer-assisted QSPRs/QSARs. The procedure and the results presented in this work, based on the application of a multiscale molecular modeling recipe for the phase diagram prediction for block copolymers in water and in the presence of a model drug, represent one example of this grand challenge. Hopefully, the outstanding agreement between predicted and experimental morphologies obtained for these DDSs may pave the way for these *in silico* approaches to become part of the arsenal of techniques used every day in PT, the only limitation being human creativity.

Chapter 7

Conclusions

This Chapter reports the main conclusions about the present research and an overview of future perspectives.

7.1 Conclusions and future perspectives

The development of new and tailored nanomaterials necessitates a comprehensive understanding of the phenomena at different time and length scales.

In the past, this need has significantly stimulated the development of computer modeling and simulation, either as a complementary and alternative technique to experimentation. In this context, many traditional simulation techniques (i.e., Monte Carlo, Molecular Dynamics, Brownian Dynamics, Lattice Boltzmann, Ginzburg–Landau theory, micromechanics and Finite Element Methods) have been employed, and some novel simulation techniques (e.g., Dissipative Particle Dynamics, equivalent-continuum and self-similar approaches) have been developed to study more effectively novel nanomaterials. These techniques indeed represent approaches at various time and length scales from molecular scale (e.g., atoms), to microscale (e.g., coarse-grains, particles, monomers) and then to macroscale (e.g, domains), and have shown success to various degrees in addressing many aspects of nanomaterials.

The simulation techniques developed thus far have different strengths and weaknesses, depending on the need of research. For example, molecular simulations can be used to investigate molecular interactions and structure on the scale of 0.1–10 nm. The resulting information is very useful to understanding the interaction strength at nanoparticle–polymer interfaces, for instance, and the molecular origin of mechanical improvement. However, molecular simulations are computationally very demanding, thus not so applicable to the prediction of mesoscopic structure and properties defined on the scale of 0.1–10 μm, for example, the dispersion of nanoparticles in polymer matrix and the morphology of polymer nanocomposites.

To explore the morphology on these scales, mesoscopic simulations such as coarse-grained methods, Dissipative Particle Dynamics and dynamic mean field theory are more

effective. On the other hand, the macroscopic properties of materials are usually studied by the use of mesoscale or macroscale techniques such as micromechanics and Finite Element Methods. But these techniques may have limitations when applied, for instance, to polymer nanocomposites because of the difficulty to deal with the interfacial nanoparticle–polymer interaction and the morphology, which are considered crucial to the mechanical improvement of nanoparticle-filled polymer nanocomposites.

Therefore, despite the progress over the past years, there are a number of challenges in computer modeling and simulation. In general, these challenges represent the work in two directions. First, there is a need to develop new and improved simulation techniques at individual time and length scales.

Secondly, it is important to integrate the developed methods at wider range of time and length scales, spanning from quantum mechanical domain (a few atoms) to molecular domain (many atoms), to mesoscopic domain (many monomers or chains), and finally to macroscopic domain (many domains or structures), to form a useful tool for exploring the structural, dynamic, and mechanical properties, as well as optimizing design and processing control of nanocomposites.

In this work the power of integrating modeling across different scales and with experimental data has been demonstrated over several examples of industrial interest and application. Further, we proposed an alternative and promising route, system independent, linking through the scales.

Developing such a multiscale method is very challenging but indeed represents the future of computer simulation and modeling, whatever the target field of application is.

New concepts, theories and computational tools should be developed in the future to make truly seamless multiscale modeling a reality. Such development is crucial in order to achieve the longstanding goal of predicting particle–structure–property relationships in material design and optimization.

Appendix A

The whole network formation procedure was achieved by writing a Perl script using the object library available in *Materials Studio* v. 4.1. In what follows, for the sake of clarity and brevity, we will limit the description to the most important technical parts of the final version of the script. Each condensation simulation starts by loading the initial structure obtained at ***Step 2*** and its association to a proper variable to be used for accessing all objects present in the structure itself. The corresponding command is:

```
my $doc = $Documents{"name.xsd"};
```

The next action consists in deleting all existing sets in the initial structure, i.e.:

```
my $sets = $doc->UnitCell->Sets;
foreach my $set (@$sets) {
$set->Delete;
}
```

This is an important issue as, in some of the next steps, some new sets will be created with respect to predefined reactive atoms; these sets, in turn, will be used to create the relevant close contacts and, ultimately, bonds. Accordingly, the presence of other sets has to be avoided.

Since the simulations are performed under 3D periodic conditions, one of the filters **DisplayRange**, **UnitCell** or **AsymmetricUnit** should be applied to access any object in the document. These filters define finite sets of accessible objects in the document. For example, the **DisplayRange** filter allows to access the items which are displayed when the document is viewed in the *Materials Studio Visualizer*, whilst the **UnitCell** filter returns objects which are unique with respect to periodic translation of the lattice. Having tested both the **UnitCell** and **DisplayRange** filters, we selected to use the former. From preliminary tests performed on the considered systems, it follows that both filters can be employed for scripting. The results are very similar in terms of physical properties of the final structures,

and a criterion for the alternative choice of these filters will be the subject of a more detailed study.

It is useful to create a simple variable which will maintain all the atoms instead using

$doc->UnitCell->Atoms;

This association is done by this command:

my $atoms = $doc->UnitCell->Atoms;

Another fundamental step that has to be undertaken is proper labelling of all the important chemical entities which, for the specific system considered here, are the linked Si-O-H atoms. Accordingly, all silicon atoms were labelled **Si**, the oxygen atoms covalently bonded to it **O**, and the reactive hydrogens **H**. The whole Perl code for this action is listed below:

```
foreach my $atom (@$atoms){
  if($atom->ElementSymbol eq "Si"){
    $atom->Name = "Si";
foreach my $atom1 (@{$atom->AttachedAtoms}){
if( $atom1->ElementSymbol eq "O" && $atom1->Name ne "RO"){$atom1->Name = "O";
foreach my $atom2 (@{$atom1->AttachedAtoms}){
  if( $atom2->ElementSymbol eq "H"){$atom2->Name = "H";}
                }
               }
              }
             }
            }
```

The **RO** label was chosen for the oxygen atoms bridging two Si atoms (i.e., Si-O-Si). Since it may be necessary to restart the whole script several times, it is essential to avoid relabelling **RO** oxygens to **O**, and this justifies the choice of the label **RO** in the above piece of code.

Before performing any calculation, all relevant parameters for Geometry Optimization (GO), Annealing (AN) and Molecular Dynamics (MD) must be set, and each proper setting saved to a file (*.xms). This setting file must be placed later in the same directory where the Perl script is located. Then, the command for loading the parameter file:

Modules->Forcite->LoadSettings("name");

must be included in the script. This avoids the tedious repeating of setup operations. As can be seen from the command above, the *Forcite* module of *Materials Studio* was employed in the calculations performed in this work, as scripting cannot be implemented in the *Discover* engine available in version 4.1 of *Materials Studio*.

Direct commands inside the script are then used to set some important calculation parameters for running the calculations. The settings and running commands for GO, AN, and MD calculations employed in the present study are reported below:

Modules->Forcite->ChangeSettings(["ChargeAssignment"=>"Use current"]);

```
Modules->Forcite->Calculation->Run($doc,Settings(Task=>"GeometryOptimization",
MaxIterations =>2000));
Modules->Forcite->Calculation->Run($doc,Settings(Task=>"Anneal",TimeStep=>0.2,
AnnealCycles=>8, EnergyDeviation=>2000000 ));
Modules->Forcite->Calculation->Run($doc,Settings(Task=>"Dynamics",TimeStep=>0.2,
Ensemble3D =>"NVT", NumberOfSteps=>5000, EnergyDeviation=>2000000 ));
```

When a trajectory file (*.xtd) is created as output of the AN and MD simulations, the **$doc** variable is automatically reinitialized, and from that moment it represents the whole trajectory of the system. Since just the last frame from each of these trajectories is needed as input for subsequent calculations, this last fame is used for reinitializing the document variable **$doc** after each AN/MD run. Furthermore, in the case of MD runs (after which ***Step 4*** is applied, see above), another important reason to update **$doc** variable to the last frame of the trajectory can be envisaged. Since some atoms are to be deleted from the system during the condensation reaction leading to network formation, (i.e., H_2O molecules, see Figure 5.2), the atomistic file (*.xsd) and not the trajectory file (*.xtd) has to be used as, once the number of atoms in actual frame is altered, the entire trajectory is invalidated. The complete sequence of commands in AN, MD part of our script is as follows:

```
Modules->Forcite->Calculation->Run($doc,Settings(Task=>"Anneal",TimeStep=>0.2,
AnnealCycles=>8, EnergyDeviation=>2000000 ));

my $numFrames = $doc->Trajectory->NumFrames;
$doc->Trajectory->CurrentFrame = $numFrames;
my $LastFrame = Documents->New("After-ANN.xsd");
  $LastFrame -> CopyFrom($doc);
$doc -> Discard;
$doc = $LastFrame;

Modules->Forcite->Calculation->Run($doc,Settings(Task=>"Dynamics",TimeStep=>0.2,
Ensemble3D=>"NVT", NumberOfSteps=>5000, EnergyDeviation=>2000000 ));

my $numFrames = $doc->Trajectory->NumFrames;
$doc->Trajectory->CurrentFrame = $numFrames;
my $LastFrame = Documents->New("After-MD.xsd");
  $LastFrame -> CopyFrom($doc);
$doc -> Discard;
$doc = $LastFrame;
```

On the first line of the **$doc** updating code, the new variable **$numFrames** is created, and the number of frames of the considered trajectory is assigned to it. Then, the last frame of the trajectory is set as the actual one. Afterwards, the empty atomistic file is created (**After-ANN.xsd or After-MD.xsd** in the above routine) and associated to the variable **$LastFrame**. In the next line of the code, the last frame of the actual trajectory is copied into the new atomistic file; subsequently, the current trajectory variable is discarded, clearing this document (i.e., the trajectory file) from the computer memory. This obviously does not imply that the trajectory file which is represented by this variable is deleted. Each trajectory file, together with the corresponding (**After-ANN.xsd or After-MD.xsd)** files, are saved in the

corresponding *Materials Studio* project. The last step is updating the document variable **$doc** by variable **$LastFrame**, where the last frame from the previous trajectory is stored.

Since ***Steps 3*** and **4** are repeated several time during the entire simulation recipe, the **After-ANN.xsd** and **After-MD.xsd** files are automatically numbered (e.g., **After-ANN (2), After-ANN (3)** etc.) by *Materials Studio*. The same automatic procedure is applied to the corresponding trajectories files. No saving instructions then need to be implemented since *Materials Studio* includes all created files automatically into the open project.

Now let us describe a little more in details ***Step 4***, which includes i) the analysis of the distances of the pairs of reactive atoms, ii) the creation of new Si-O-Si bonds, and iii) the deletion of H_2O molecules from the system. In order to make the system react, the optimal close contacts between the atoms involved in the condensation reaction have to be realized; accordingly, the atom pairs between which close contacts should take place have to be defined. Given the chemistry of the systems considered in this work, where condensation takes place between Si-O-H¨H-O-Si groups (see Figure 5.1), only O–H close contacts are needed, where O is the name for the oxygens bound to the Si atoms, and H designs the hydrogens linked to the O oxygens. The part of our script that creates these close contacts is written below:

```
# Create arrays to store the reactive atoms in
my @reactive_O;
my @reactive_H;
foreach my $atom (@$atoms) {
 if ($atom->Name eq "O" ) {
   push (@reactive_O, $atom);
 } elsif ($atom->Name eq "H" ) {
   push (@reactive_H, $atom);
 } else {
   push (@reactive_O, $atom);
   push (@reactive_H, $atom);
 }
   }
```

The above piece of code creates two atom arrays, **reactive_O** and **reactive_H**, which, intuitively, store all atoms except atoms named **H** and named **O**, respectively. Since close contact restrictions can be applied only to sets, however, it is necessary to create relevant sets based on previously created atomic arrays. This can be done by the following commands:

```
my $reactive_O_set=$doc->CreateSet("reactive_O",\@reactive_O);
my $reactive_H_set=$doc->CreateSet("reactive_H",\@reactive_H);
```

Then, the **ExclusionMode** is set to **'Set'** value, which should guarantee that creation of close contacts between atoms inside each defined set is forbidden. Clearly in this study only the close contacts between atoms named **O** and **H** are expected, since these atoms are in different sets. The command that make the above described exclusion mode setting is the following:

```
Tools->BondCalculation->ChangeSettings([ExclusionMode => 'Set']);
```

Unfortunately, this elegant trick works perfectly only under non-periodic conditions (e.g., a non-periodic superstructure). In the case of a system under periodic boundary conditions, such as in the present work, it is necessary to introduce some further filtering to eliminate all the non **O–H** close contacts (see the code part for the creation of **GoodCloseContacts** array listed below). Nevertheless, given the 3D symmetry characteristics of our system, this approach can be successfully applied, ultimately resulting in a substantial reduction computer memory.

The last step necessary for calculating close contacts is the setting of **DistanceCriterionMode, MinAbsoluteDistance** and **MaxAbsoluteDistance** parameters. In our case, the following setting was employed:

```
Tools->BondCalculation->ChangeSettings(Settings(DistanceCriterionMode
=>"Absolute", MinAbsoluteDistance => 0.0, MaxAbsoluteDistance => 3));
```

At this point, predefined close contacts can be calculated according to:

```
$doc->CalculateCloseContacts;
```

Again, it is appropriate to create a variable(s) which will represent the set of created close contacts: **$CloseContacts**:

```
my $CloseContacts = $doc->UnitCell ->CloseContacts;
```

For the next procedure, mainly in order to save significant time and memory in loop operations, the creation and use of an arrays, such as **GoodCloseContacts**, in which all the necessary information can be stored, needs to be created:

```
my @GoodCloseContacts;
```

The code for the initialization of the **GoodCloseContacts** array is listed below:

```
foreach my $CloseContact (@$CloseContacts) {
  my $Name1=  $CloseContact->Atom1->Name;
  my $Name2 = $CloseContact->Atom2->Name;
  my $Atom1 = $CloseContact->Atom1;
  my $Atom2 = $CloseContact->Atom2;
  if ( ($Name1 eq "O") && ($Name2 eq "H") || ($Name1 eq "H") && ($Name2 eq "O") ) {
    push(@GoodCloseContacts,[1,$Name1,$Name2,$Atom1->X,$Atom1->Y,$Atom1-
>Z,$Atom2->X,
  $Atom2->Y,$Atom2->Z,$CloseContact->Length,$CloseContact->Atom1,$CloseContact-
>Atom2]);
                    }
    }
```

In the above code, each element of the **GoodCloseContacts** array has the structure **[status**, **Name1**, **Name2**, **x1**, **y1**, **z1**, **x2**, **y2**, **z2**, **Length**, **Atom1**, **Atom2]**, where **status** represents a variable which denotes if a given close contact can take place or not at a given instant. **Name1** and **Name2** are the names of the atoms which belong to that given close

contact. **x1**, **y1**, **z1**, **x2**, **y2**, **z2** are the coordinates of these atoms, **Length** denotes the length of the given close contact, and finally **Atom1** and **Atom2** are the atom objects which belongs to the close contact. The names of these atoms are stored in the array as separate variables (i.e., **Name1** and **Name2**); however, they are accessible through the atom objects. This last action was taken just to save some time, since atom names will be frequently used in the analysis section (see below).

It is also worthwhile to note that the filtering of non **O**–**H** close contacts discussed previously is included in the piece of code listed above; accordingly, the **GoodCloseContacts** array contains only **O**–**H** close contacts. However, in order to simulate a network-forming condensation reaction, only those **O**–**H** close contacts which are created between two different GPTMS molecules must be taken into account. Therefore, it is necessary to filter out the **O**–**H** close contacts which are created between O and H atoms belonging to the same GPTMS molecule. This can be simply achieved by analyzing the array **GoodCloseContacts** and checking whether the species **Atom1** and **Atom2** belong to the same GPTMS molecule or not. In the affirmative, the variable **status** must be changed from 1 to –1, and all the subsequent analysis must be carried out only on those close contacts which have variable **status** equal to 1.

The way to identify the molecular object to which a given atom belongs is using:

$atom1->Ancestors->Molecule

Unfortunately, at present, there is no direct method to obtain the index of any given molecule in a molecular model. Thus, a way to circumvent the problem is to identify two different molecules by their different center of mass. To access the coordinates of the center of mass of any given molecule, the following construction can be used:

```
my $x1 = $atom1->Ancestors->Molecule->Center->X;
my $y1 = $atom1->Ancestors->Molecule->Center->Y;
my $z1 = $atom1->Ancestors->Molecule->Center->Z;
```

Finally, the **GoodCloseContacts** is ordered by increasing close contact length which, in each element of this array, is represented by the **Length** variable.

At this point, the new Si-O-Si bonds building procedure can begin. As the whole code for this section is long, and the detailed description of each part will exceed the scope of this work, it will only be summarized and briefly commented below.

The first close contact (by index) in the array **GoodCloseContacts** which has the **status** variable equal to 1 (i.e., the shortest one, see above) is chosen. Two new variables **$O** and **$H** are created, which are initialized by the atoms **Atom1** and **Atom2** from the selected **GoodCloseContacts** element. All the remaining atoms involved in the bond formation are then identified, and assigned to the proper variables (**$H1**, $**O1**, **$Si**, and **$Si1**, respectively). Figure A.1 illustrates the association of these variables to the corresponding atoms.

According to the bonding scheme of Figure A.1, at the beginning only the two atoms which belongs to the chosen close contact (**$O** and **$H**, respectively) are considered. Next, the hydrogen atom **$H1**, which will be deleted together with atoms **$O** and **$H**, from the system due to the formation of a H_2O molecule, must be identified (see Figure A.1). It is important to note that, in the real process, the water formed during the condensation reaction remains in the reaction environment, and eventually contributes to the hydrolysis of non hydrolyzed GPTMS molecules. In the system considered here, however, the GPTMS

monomers were fully hydrolyzed (a realistic condition which can be easily achieved experimentally). Therefore, water plays no additional role in the process, and does not need to be further considered.

Next, atoms **$O1**, **$Si**, and **$Si1** must be identified, in order to create the new bond **$Si-$O1** (see Figure A.1).

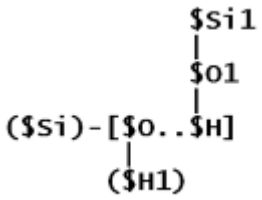

Figure A.1 Atom/variable association in the bonding scheme considered in this work.

This identification process can be carried out resorting to the **AttachedAtoms** function. Below, the piece of code for the identification of the **$H1** and **$Si** atoms is listed, as an example:

```
my $Si;
my $H1;
foreach my $at (@{$O->AttachedAtoms}){
if($at->Name eq "Si"){$Si=$at;} else {$H1=$at;}
        }
```

As mention in Chapter 5, although the structure of a GPTMS-based hybrid O/I network obtained under acid catalysis is similar to that of a crosslinked polymer network, some cyclic structures can be present.[1,2] In order to apply some restrictions related to ring size in the formation of eventual cyclic structures, a check whether the bonding between the **$Si** and **$O1** atoms will not result in the closure of a strained ring (i.e., with less than 4 Si atoms) must be performed. This leads to the necessity of identifying atom **$Si1** (see Figure A.1); this operation could also serve graphical purposes: for example, the need of changing graphical style for both bonds **$Si-$O1** and **$O1-$Si1** in order to differentiate them, for example, from other bonds.

Should every condition described above be satisfied, the new bond **$Si - $O1** is created at this stage with the command:

```
$doc->CreateBond($Si, $O1, "Single");
```

Otherwise, the next available close contact in the **GoodCloseContacts** array is selected, and the whole procedure outlined above is repeated.

As said, once the new Si-O bond is created, a water molecule is released. In our model, this corresponds to deleting atoms **$O**, **$H**, and **$H1** from the system. To accomplish this goal, instead of deleting the required atoms directly (e.g., using commands such as **$O->Delete**, etc., which can generate problems, especially when using periodic boundary

[1] Mateika, L.; Dukh, O.; Brus, J.; Simonsick, W. J. Jr.; Meissner, B. *J. Non-Cryst. Solids* **2000**, *270*, 34-37.
[2] Fidalgo, A.; Ilharco, L. M. *J. Non-Cryst. Solids* **2001**, *283*, 144-154.

conditions, as once some individual atoms are deleted, all its periodic images are also deleted from the set of close contact atoms).

```
push (@AtomsToDelete,$H);
push (@AtomsToDelete,$O);
push (@AtomsToDelete,$H1);
```

After the end of the **$i** loop, a set based on the **AtomtoDelete** array is created, and all the atoms which are deleted from the system according to the reaction scheme will be cancelled at once and in a safe way, according to:

```
my $AtomsToDelete_Set=$doc->CreateSet("AtomsToDelete",\@AtomsToDelete);
$AtomsToDelete_Set->Items->Delete;
```

Once the atoms **$O**, **$H**, and **$H1** are added to **AtomsToDelete** array, and the **$Si - $O1** bond is created, it is appropriate to analyze the whole **GoodCloseContacts** array from the actual index **$i** to the end, and switch the variable **status** to –1 in all those cases in which some of the atoms **$O**, **$O1**,**$H**, and **$H1** are periodically equivalent to **Atom1** or **Atom2.**

For checking periodic equivalence of two atoms, the following function was created:

```
sub AtomsArePeriodicEquivalent {
  my ( $A1, $A2) = @_;
  if($A1->Name ne $A2->Name){ return 0;}
  my @dA = ($A2->X - $A1->X,$A2->Y - $A1->Y,$A2->Z - $A1->Z);
  my @length = ($lengthX,$lengthY,$lengthZ);
  for(my $i=0;$i<3;$i++){
  if(abs($dA[$i])!=0 && abs($dA[$i])!=$length[$i]) {return 0;}
  }
  return 1;
}
```

#The variables **$lengthX, $lengthY** *and* **$lengthZ** *denotes the length of the sides of the periodic box*.

Figure A.2 shows that, if the mentioned **GoodCloseContacts** revision is checked only for equality and not for periodic equivalence of relevant atoms, unrealistic valences of oxygen and silicon atoms are generated.

There can be several configurations which originate these problems, and example of which is illustrated in Figure A.3. In the left part of Figure A.3 it can be seen that, when more reactive centers are in close proximity, we can see some “collision” possibility if more reactive centers is in proximity. For example, suppose that the O-H contact (i.e., black O and blue H) is shorter than the other O-H contact (i.e., green O and blue H). Under this condition, the bond between the blue O and black Si is created (red line). If no check of the remaining **GoodCloseContacts** elements is performed, then also the Si-O bond between the green Si and blue O is created. If only equality check after creation of the blue O and black Si bond is performed, no problem arises if the configuration corresponds to the portrayed on the left side of Figure A.3. However, if the position of the green molecule is shifted to the periodic image position, then both O-H atoms (the green O and the small blue H atom) are not equal to any other atom (the black and large blue H atom, and the black and the blue O atom), but

the small blue H atom is periodically equivalent to that large one, which is a sufficient condition for creating the Si-O bond (blue O and green Si atoms) which is interrupted by the periodic cell boundary but can be clearly seen using the **InCell** viewtype. This situation is nicely illustrated in Figure A.4, taken from the real system of Figure A.2.

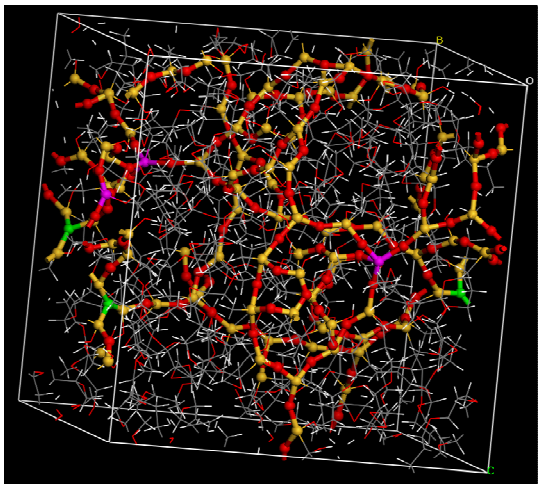

Figure A.2 GPTMS crosslinked structure created using only equality (not equivalence) check of the atoms during the **GoodCloseContacts** revision. The unrealistic oxygen atoms forming three bonds with Si are highlighted in green, whilst the Si atoms with 4 oxygen bonds are highlighted in violet.

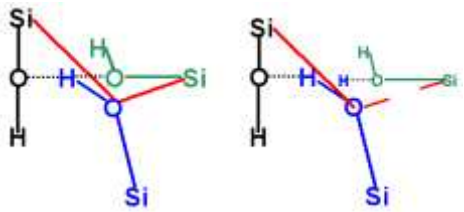

Figure A.3 Scheme of one problematic configuration leading to unrealistic valences of O and Si atoms (see text for details).

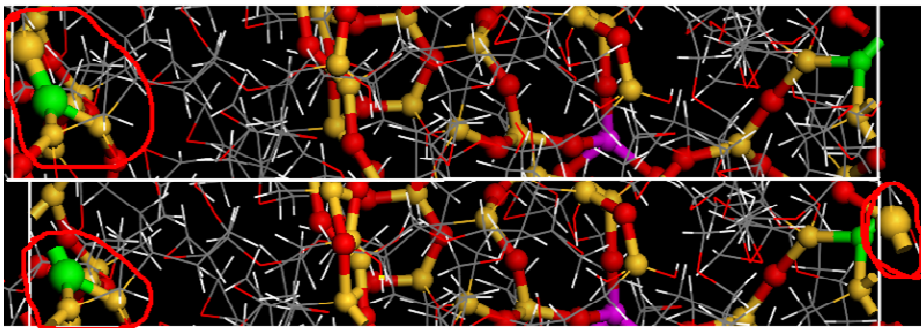

Figure A.4 Details of the real system illustrated in Figure A.2. Top: **InCell** lattice display style view; bottom: **default** lattice display style view.

Then, the bonding procedure with respect of the next O–H close contact from array **GoodCloseContacts** which has **status** equal to 1 (or, more precisely, the **GoodCloseContacts[$i][0]** element) must be repeated.

After a desired number of bonds (**$MaxNumBond**) is reached, or at the end of the **GoodCloseContacts** array is reached, all sets created and populated in the previous steps must be deleted to release computer memory. Also, renaming of the bridging oxygens (**$O1**) must be performed, since these atoms must not enter the next **$I** loop for creating new O-H close contacts.

To give a final overview of the entire procedure, the most critical steps are summarized below using a pseusdocode:

****START OF THE SCRIPT****

#Loading of the structure (.xsd)*

my $IterMax=50; #number of the main loops
my $MaxNumBond=3; #maximum number of created bonds in one **I** loop

#Main loop

for(my $I=0;$I<$IterMax;$I++){

Loading of the setup file (.xms)*
Geometry Optimization
Annealing
Molecular Dynamics
Creation of the reactive atom arrays and sets
Close contacts calculation
Creation of **GoodCloseContacts** *array and close contacts filtering*
Ordering of the **GoodCloseContacts** *elements by increasing close contact length*
for(my$i=0;(($NumOfCreatedBonds<$MaxNumBond)&&
($i<=$#GoodCloseContacts));$i++){

Identification of all the atoms **$O**, **$H**, **$H1**, **$O1**, **$Si** *and* **$Si1**
Creation of **$Si-$O1** *bond*
Addition of atoms **$O, $H, $H1** *to array* **AtomsToDelete**
GoodCloseContacts *array revision*

} #end of the **$I** loop (***Step 4***)

#Deletion of reacted atom sets

$reactive_O_set->Delete;
$reactive_H_set->Delete;

#Deletion of all calculated close contacts

$CloseContacts->Delete;

#*Creation of the set* **$AtomsToDelete_Set** *from the array* **AtomsToDelete** *and appropriate deletion of all the atoms marked in previous steps for deletion*

#the **if** *statement excludes attempt to create set from the empty array*

```
if($#AtomsToDelete + 1>=1){
my $AtomsToDelete_Set=$doc->CreateSet("AtomsToDelete",\@AtomsToDelete);
$AtomsToDelete_Set->Items->Delete;
}
```

#Renaming of oxygen atoms involved in the formation of Si-O-Si bonds (i.e., accessed using the variable **$O1**) *from* "**O**" *to* "**RO**"

```
foreach my $atom (@$atoms })
{
if($atom->Name eq "O"){
  my $NumOfSi=0;
  foreach my $atom1 (@{$atom->AttachedAtoms})
  {
  if($atom1->Name eq "Si"){$NumOfSi++;}
  }#end $atom1
if($NumOfSi==2){$atom->Name="RO";}
}
#end of if($atom->Name eq "O"
}
#end of loop $atom
}
```

#end of **I** loop (main loop, which should be repeated **$IterMax times**)

****END OF THE SCRIPT****

At the very end it may be worth noticing that, despite we release all computer memory properly in each **$I** loop, during each script run the memory used by the computer is slowly and progressively increasing, so that, after a number of **$I** loops, the limit of accessible memory is reached and calculations have to be manually restarted. The number of successfully accomplished **$I** loops clearly depends upon the available RAM of a given computer, but also on the amount of close contacts which are created during each **$I** loop. That is the reason why we increased **MaxAbsoluteDistance** from 3 to 6 Å.